Aspects of research at Risø. A collection of papers dedicated to Professor T.Bjerge on his seventieth birthday

Research Establishment Risø, Roskilde

Publication date:
1972

Document Version
Publisher's PDF, also known as Version of record

Risø Report No. 256

Risø Report No. 256

Danish Atomic Energy Commission
Research Establishment Risø

Aspects of Research at Risø

A Collection of Papers dedicated to Professor T. Bjerge on his Seventieth Birthday

January 1972

Sales distributors: Jul. Gjellerup, 87, Sølvgade, DK-1307 Copenhagen K, Denmark

Available on exchange from: Library, Danish Atomic Energy Commission
Risø, DK-4000 Roskilde, Denmark

January 1972 Risø Report No. 256

ASPECTS OF RESEARCH AT RISØ

A Collection of Papers Dedicated to Professor T. Bjerge
on his Seventieth Birthday

Danish Atomic Energy Commission
Research Establishment Risø
Roskilde

CONTENTS

Page

PREFACE

In 1956, Risø was a peaceful and sparsely inhabited peninsula in Roskilde Fjord. By 1969, there had developed on this site a research establishment with a staff of about 800 and a wide range of scientific and technological activities. During these years of fruitful growth, Risø was directed by Professor Torkild Bjerge, whose wise judgement, breadth of interest, and commitment to the highest ideals of scientific research are reflected in the pattern of the establishment today.

According to the law by which it was founded, Risø has the task of furthering the peaceful uses of atomic energy for the benefit of society. The variety of natural phenomena associated with atomic energy and its ramifications has resulted in a corresponding variety of activities within basic and applied research, while the modest size of the establishment has made necessary the virtue of close collaboration with a host of research institutes, industrial companies, universities, and scientific laboratories, both in Denmark and in other countries. The structure of Risø, which is composed of about a dozen interrelated departments with a wide range of experience, has proved to be well suited to tackling complex problems involving expertise in different fields, and the interdisciplinary character of its research is one of the establishment's principal strengths.

In this volume are collected a series of papers chosen to give an impression of the character of Risø today. Accordingly, there are reports on research in reactor technology, non-nuclear applications, especially within medicine, and basic studies with long-range goals. The research of the establishment is greatly influenced by the special facilities which are available. The use of the reactors in materials testing, basic research, isotope production, and activation analysis is illustrated in this volume, while the utilization of other radiation sources, especially the electron accelerators, in both applied and basic research, is also described.

Papers 1-6 are concerned with various aspects of reactor technology, although the last two of these deal with modern developments in materials science and systems analysis which have general application in non-nuclear technology. Papers 7-9 describe the application to practical problems of expertise in the generation and detection of various kinds of radiation, while 10-12 are concerned with technical developments in the medical field. The protection of the population against excessive exposure to radiation was the primary motivation of the plant studies discussed in papers 13 and 14, while the study of the dispersion of radioactivity through the atmosphere provided

the initial impetus for meteorological studies of the type described in paper 15, although again this work has proved to have wide application in other fields. Finally, papers 16 and 17 describe basic research on the chemical and physical properties of matter, carried out using electrons and neutrons respectively.

For over a decade, Risø has been occupied with developing the peaceful uses of modern science in collaboration with many other institutions. It has established a place in the scientific and technological life of the country and become an internationally respected research institution. In appreciation of his outstanding contribution to the development of the establishment, this volume is gratefully dedicated to Professor Bjerge on his seventieth birthday by his colleagues at Risø, who have benefitted so greatly from his efforts.

A. R. Mackintosh

The Development of Three-Dimensional Calculations in Reactor Physics Experience with Flux Synthesis

by

H. Larsen and B. Micheelsen

Reactor Physics Department

Abstract

Three-dimensional overall calculations of flux and power are necessary for detailed reactor calculations. The approximative flux synthesis method is fast and well suited for calculations of repetitive nature.

A three-dimensional flux synthesis burn-up program SYNTRON was developed. SYNTRON uses a variational, single-channel, flux synthesis technique. Calculations are performed with SYNTRON for comparison with a conventional difference equation program.

1. INTRODUCTION

In reactor physics three-dimensional overall calculations are necessary to give an accurate description of the flux and power distributions over the reactor core. For example, boiling in a boiling-water reactor creates different void contents throughout the reactor core and makes three-dimensional calculations essential.

The flux distribution in the reactor core is most conveniently determined by the use of diffusion theory in the form of the difference equation technique. However, three-dimensional calculations by that technique for a whole reactor core are costly in computing time and unacceptably expensive for many purposes such as calculation of critical control rod configuration. For this reason several approximate methods have been suggested, and two of the best known are the nodal theory and flux synthesis.

With the nodal theory the necessary number of flux points are reduced by introducing some fitting parameters through the coupling coefficients. The fitting parameters must then be determined outside the program. In the flux synthesis method the number of flux points is not reduced, but instead the existence of a certain separability between the vertical and the horizontal fluxes in many typical reactor calculations is used.

Flux synthesis has undergone great development during the past fifteen years. One of the methods first suggested was Meyer's single-channel flux synthesis[4], where the neutron flux was assumed to be, piece by piece, separable in the vertical and horizontal directions. The single-channel synthesis was extended to the multi-channel flux synthesis by Wachspress[5]. He divided each horizontal plane into a number of subregions and performed a synthesis in each of these subregions. Another extension of the single-channel synthesis is the variational flux synthesis developed by Kaplan[3]. In this formalism the three-dimensional flux at each vertical elevation is found by mixing a set of two-dimensional (horizontal) flux shapes, called trial functions. Later, some more sophisticated flux synthesis methods have appeared, as for example variational flux synthesis with discontinuous trial functions, i. e. different trial functions at each z-elevation[6], and methods with pseudo-discontinuous trial functions[7].

The SYNTRON program uses a variational, single-channel flux synthesis formalism with continuous trial functions. The discontinuous formalism is not used because it is rather complicated and slow (in computing time). Another problem in the discontinuous formalism is that the user must beforehand know the solution of the problem fairly well to specify the

trial functions, and this knowledge cannot in general be assumed avilable.

2. SYNTRON

The three-dimensional flux synthesis program SYNTRON[2] uses a variational, single-channel flux synthesis formalism primarily based on Kaplan's method. The three-dimensional group flux $\varphi^g(z, y, x)$ is found by means of the following expansion:

$$\varphi^g(z, y, x) = \sum_{k=1}^{K_g} Z_k^g(z) \cdot H_k^g(y, x) . \qquad (1)$$

where

K_g = number of trial functions in group g

$H_k^g(y, x)$ = trial function number k in group g

$Z_k^g(z)$ = mixing function number k in group g.

If the trial functions $H_k^g(y, x)$ are assumed to be known, the problem is how to find the mixing functions.

The SYNTRON program includes an ordinary difference equation routine called DIFFERENS. By means of this routine it is possible, inside the program, to set up calculations of the necessary two-dimensional flux shapes (horizontal) for the trial function set to be used as expansion functions.

If the flux expansion eq. (1) is substituted into the group diffusion equation, we have:

Diffusion equation:

$$-D^g \cdot \nabla^2 \varphi^g + \Sigma_a^g \cdot \varphi^g = Q^g . \qquad (2)$$

Synthesis equation:

$$(-D^g \nabla^2 + \Sigma_a^g) \left(\sum_{k=1}^{K_g} Z_k^g(z) \cdot H_k^g(y,x) \right) =$$

$$\sum_{g'=1}^{GR} \sum_{i=1}^{K_{g'}} (\Sigma_s^{g \leftarrow g'} + XI^g \cdot \nu \Sigma_f^{g'} / k_{eff}) \cdot Z_i^{g'}(z) \cdot H_i^{g'}(y,x) \,, \tag{3}$$

where

D^g = diffusion coefficient

Σ_a^g = absorption cross section

$\Sigma_s^{g \leftarrow g'}$ = scattering cross section from group g' to group g

XI^g = neutron fission spectrum

$\nu \cdot \Sigma_f^g$ = neutron production cross section

GR = number of energy groups

$1 \leq g \leq GR$ = energy group index

k_{eff} = effective multiplication factor

Q^g = source term.

Equation (3) is the basic equation for finding the unknown mixing functions $Z_k^g(z)$. For the solution of eq. (3) a new function set called the weighting function set $W_j^g(y,x)$ is introduced, cf. [2]. In the SYNTRON program the weighting functions may be either the trial functions (Galerkin weighting) or the adjoint trial functions. The following treatment is independent of the method used.

Equation (3) is multiplied by $W_j^g(y,x)$, and an integration over the (y, x) plane is performed.

A typical integration term is:

$$A^g_{kj}(z) = \int_y \int_x \Sigma^g_a \cdot H^g_k(y,x) \cdot W^g_j(y,x)\, dydx, \tag{4}$$

which is the (y, x) integrated absorption term.

The most complicated term is the radial leakage term:

$$DBZ^g_{kj}(z) = \int_y \int_x D^g \cdot W^g_j(y,x) \cdot \nabla^2_{yx} H^g_k(y,x)\, dydx\,. \tag{5}$$

The practical integration is performed by a difference approximation technique[2, 8].

According to the transformations above, eq. (3) is replaced by:

$$\sum_{k=1}^{K_g} (-DZ^g_{kj}(z) \cdot \nabla^2_z + DBZ^g_{kj}(z) + A^g_{kj}(z)) \cdot Z^g_k(z) =$$

$$\sum_{g'=1}^{GR} \sum_{i=1}^{K_{g'}} (SP^{gg'}_{ij}(z) + XIF^{gg'}_{ij}(z)/k_{eff}) \cdot Z^{g'}_i(z)\,, \tag{6}$$

which is the basic equation to be solved with the synthesis program.

The terms $SP^{gg'}_{ij}(z)$ and $XIF^{gg'}_{ij}(z)$ are integration terms for scattering in and fission contribution to group g from group g'. They have the same form as in (4).

We now return to the problem of finding the z-dependence of the mixing functions. In the z-direction, the vertical direction, the reactor is divided into axial zones or a coarse mesh. The axial zones are selected so that there are no variations in the cross sections in the z-direction in each axial zone.

The mixing equations (6) are solved approximately by a finite difference method. The axial zones are subdivided into a fine-mesh structure, and the mesh point is chosen in the middle of each mesh. Eq. (6) is transformed into a set of difference quations by means of an integration over the remaining direction, z.

In this program a semi-iterative technique is used for solving the synthesis equation. The solution technique used is similar to that of the line

difference technique, only the elements in the matrix equation are here submatrices. The direct inversion method[9] is used, and as it is possible to invert the submatrices once before the iterations are started, little computation is necessary at each iteration, and the solution is very fast, cf. [2]. The eigenvalue, k_{eff}, the effective multiplication factor, is found with an overall neutron balance equation.

When the mixing functions have been found, it is easy to calculate the three-dimensional flux distribution from eq. (1).

3. CRITICALITY SEARCH

In reactor physical calculations one is often interested in the flux and power distributions for the critical reactor rather than in the distribution for a system held artificially critical by an effective multiplication factor k_{eff}. The criticality options of greatest interest would be those directly simulating the operation of modern power reactors, i. e. critical poison search and direct iteration on the control rod positions. No feature in the flux synthesis formalism makes it more convenient to use this formalism in preference to any other for critical poison search, but for direct iteration on the control rod positions the flux synthesis is very convenient. Control rod movement in the vertical z-direction can be simulated by internal boundary displacement between the axial zones.

In the SYNTRON program two different dimension control search options are implemented, one for iteration on the dimensions, and one for internal boundary displacement with fixed outer dimensions (control rod movement).

3.1. Critical Dimensions

The synthesis, eq. (6), can at each z-elevation and in each group formally be written as

$$\text{LEAK} + \text{ABS} = \text{SOUR} , \tag{7}$$

where

LEAK = leakage term, ABS = absorption term, SOUR = source term.

In order to determine the size, i. e. the length in the z-direction, of one or more axial zones at which the reactor is critical, for example axial zone No. 1, an eigenvalue must be associated with the height L_1^o of axial zone No. 1.

In realistic, three-dimensional synthesis calculations the most time-consuming calculations, besides the trial function calculations, are the integration of the matrix elements, particularly the leakage term DBZ, eq. (5). This is the case if the fast solution method mentioned in section 2 is used. During the integrations no assumption is made about the size of the mesh in the z-direction. The absorption and the source elements are directly proportional to the length, and the axial leakage elements are to a certain degree inversely proportional to the length. If the dimension dependence of the leakage terms is dropped - i. e. the leakage terms are held constant - and an eigenvalue is associated with the absorption and source terms, eq. (7) will, for the zones to be altered, be:

$$\text{LEAK} + \text{ABS} \cdot \lambda = \text{SOUR} \cdot \lambda . \tag{8}$$

The eigenvalue λ is found by an overall neutron balance equation.

When the mixing functions and λ have been found, the dimensions of the axial zones are now $L_1 = L_1^o \cdot \lambda$, while L_2^o and L_3^o remain unchanged. With these new dimensions new leakage terms, new mixing functions, and λ are calculated, and only one or two such leakage term recalculations are normally required for the convergence of this system ($\lambda = 1$). The extra cost in computer time for finding the critical dimensions instead of k_{eff} is small.

3. 2. Internal Boundary Search

Internal boundary displacement means that the internal dimensions are altered in such a way that the outer dimensions become fixed. If we want to find the critical position of the control rod in the test example in fig. 1, this may be done by associating an eigenvalue λ with the axial length of the zone with a control rod

$$\text{LEAK} + \text{ABS} \cdot \lambda = \text{SOUR} \cdot \lambda , \tag{9}$$

while the equation for the axial zone below without control rod becomes

$$\text{LEAK} + \text{ABS} \cdot (1 - \lambda) = \text{SOUR} \cdot (1 - \lambda) . \tag{10}$$

The calculation method is then the same as for dimension search.

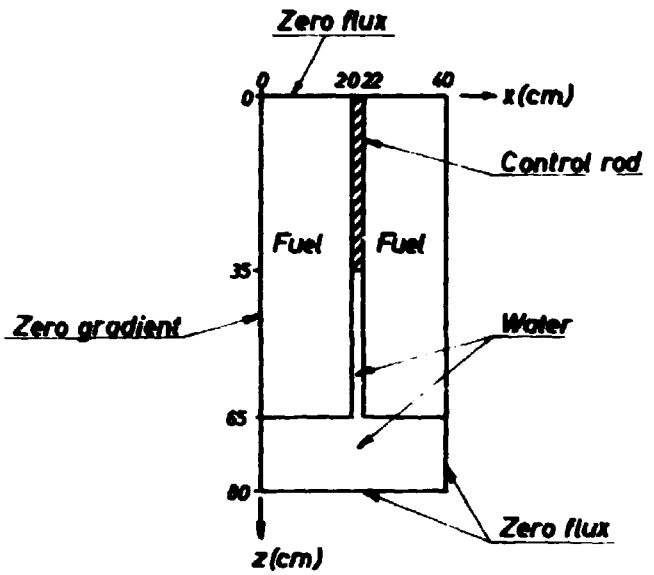

Fig. 1.

3.3. A Two-Dimensional Example with Internal Boundary Search

For illustration of the capability of the synthesis approximation, a calculation for a simple, two-dimensional example was made with the SYNTRON program. The example is from Kaplan's original paper[3]. The synthesis calculations were compared with calculations by a difference equation code, DIFFERENS. The geometry of the example is shown in fig. 1. The calculations were made in two energy groups. A 43 x 40 fine-mesh structure was used. The two-dimensional synthesis calculations were performed with two one-dimensional trial functions for each flux group. The trial functions were found by one-dimensional difference equation calculations: one at the upper rod-in fuel zone, and one at the lower rod-out fuel zone.

The eigenvalue, the effective multiplication factor k_{eff}, was found to be 1.020 by the reference calculation method and 1.018 by the synthesis method.

The example from fig. 1 is used to illustrate the method of direct iteration on the control rod position. In fig. 1 some thermal flux curves are shown calculated with SYNTRON and test calculations with DIFFERENS. A k_{eff} is put into the SYNTRON program, and the program is asked to find the control rod position which gives the specified k_{eff}. Afterwards the calculated dimensions are put into the static difference equation code DIFFERENS to check the flux distribution and k_{eff}. This is done for critical reactor case II, an over-critical reactor case I, and an under-critical case III,

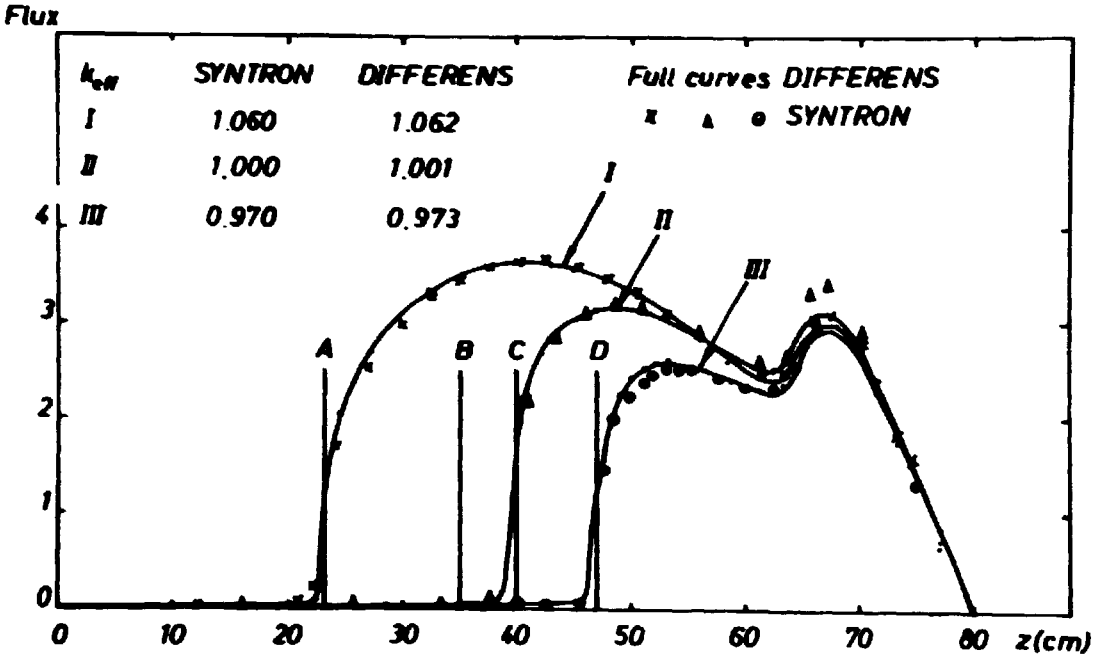

Fig.2 INTERNAL BOUNDARY SEARCH. AXIAL FLUX at X=21(cm)

cf. fig. 2. The letters A, B, C, and D give the control rod position, B is the original position and also the guessed position for the start value in cases I, II, and III.

3.4. A Three-Dimensional Calculation Example with Internal Boundary Search

The reactor core configuration in fig. 3 a and b represents a large light-water reactor with 25 control absorbers (P) partly inserted (in the whole core). The SYNTRON program was used in three-dimensional, two-group calculations, with a 20 x 20 x 24 mesh.

Calculation 1 with the control absorbers inserted one quarter of the core length - as shown in fig. 3 b - gave $k_{eff} = 1.0169$. The calculation with internal boundary search, varying the insertion L of the control absorbers, gave criticality at L = 250.0 cm. (No comparison with detailed, three-dimensional difference equation calculations was possible). Calculation times for a B 6700 (which is 1.2 times faster than an IBM 7094) are:

Calculation 1: Trial functions = 90 s. Synthesis = 25 s. Total = 183 s.

Calculation 2: Trial functions = 90 s. Synthesis = 53 s. Total = 219 s.

Fig.3 LWR calculation

a. Horizontal cross section at core midplane (z=200 cm)

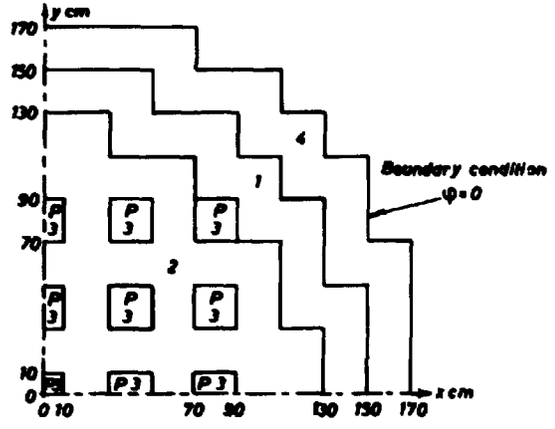

b. Vertical cross section (y=0)

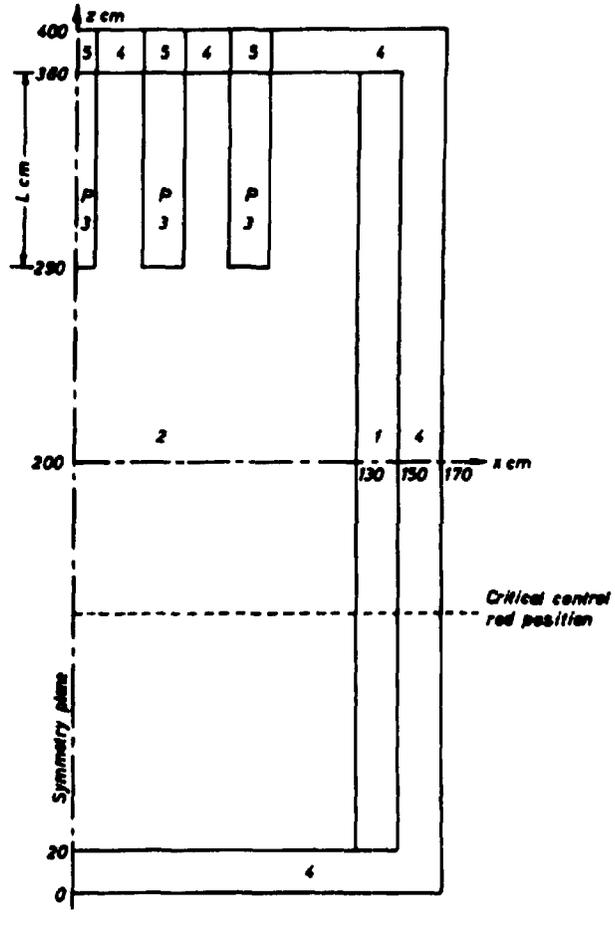

x=0 and y=0 are symmetry planes

Region 1 — high K_∞ fuel

Region 2 — low K_∞ fuel

Region 4 — reflector

Region 3 — fuel boxes with control absorber

P — control absorber partly inserted

A fuel box is 20×20 cm

One quarter of a core has:

14 fuel boxes type 1

27 fuel boxes type 2 without control absorber

$6\frac{1}{4}$ fuel boxes type 2 with partly inserted control absorber

16 reflector boxes

4. SUMMARY

The main conclusions of these investigations are that variational flux synthesis gives reasonable results if a suitable set of trial functions is used, and that flux synthesis is well suited for calculations with a criticality search on dimensions or control rod positions.

REFERENCES

1) K. E. Lindstrøm Jensen, Development and Verification of Nuclear Calculation Methods for Light-Water Reactors. Risø Report No. 235 (1970) 161 pp.

2) H. Larsen, SYNTRON, A Three-Dimensional Flux Synthesis Programme. Risø-M-1346 (1971) 33 pp.

3) S. Kaplan, Some New Methods of Flux Synthesis. Nucl. Sci. Eng. 13 (1962) 22-31.

4) J. E. Meyer, Synthesis of Three-Dimensional Power Shapes - a Flux-Weighting Synthesis Technique. In: Proceedings of the 2nd United Nations International Conference on the Peaceful Uses of Atomic Energy, Geneva, 1-13 September 1958, 11 (United Nations, Geneva, 1958) 519-522.

5) E. L. Wachspress et al., Multichannel Flux Synthesis. Nucl. Sci. Eng. 12 (1962) 381-389.

6) J. B. Yasinsky and S. Kaplan, Synthesis of Three-Dimensional Flux Shapes Using Discontinuous Sets of Trial Functions. Nucl. Sci. Eng. 28 (1967) 426-437.

7) E. L. Wachspress, On the Use of Different Radial Trial Functions in Different Axial Zones of a Neutron Flux Synthesis Computation. Nucl. Sci. Eng. 34 (1968) 342-343.

8) S. Kaplan et al., Equations and Programs for Solutions of the Neutron Group Diffusion Equations by Synthesis Approximations. WAPD - TM - 377 (1963) 67 pp.

9) R. S. Varga, Matrix Iterative Analysis. (Prentice-Hall, Inc., Englewood Cliffs, N. J., 1962) 194-196.

A Cold-Neutron Source in the DR 3

by

J. A. Leth

Reactor Engineering Department

Abstract

A general description of the cold-neutron source in the DR 3 is given together with a short introduction to cold neutrons and the history of cold-neutron sources in reactors. The main difference between the DR 3 cold-neutron source and other cold sources is in the use of supercritical hydrogen as moderator, which permits adjustment of the effective hydrogen thickness by changing the temperature of the cryogenerators.

1. INTRODUCTION

1.1. Cold Neutrons

Cold neutrons may be defined as neutrons with energies below 5 meV, corresponding to de Broglie wave lengths longer than 4 Å.

The average kinetic energy of fission neutrons is approximately 5 MeV. In a thermal reactor these fission neutrons are moderated to become thermal neutrons, mainly as a result of inelastic scattering reactions with the moderator. The thermal-neutron spectrum achieved is nearly a Maxwellian distribution corresponding to the moderator temperature. The average energy of the thermal neutrons is approximately 25 meV. Of the thermal neutrons only 1 - 2% have energies below 5 meV, i. e. are cold neutrons.

In order to obtain a higher cold-neutron flux from an experimental hole, a chamber filled with a moderator which can be cooled to low temperatures is placed in the hole. For most cold-neutron sources liquid hydrogen is chosen as the moderating material.

Cold neutrons have longer wave lengths than thermal neutrons, which makes them more suitable for investigations of structures with large atomic spacings. As examples may be mentioned structures of complex chemical combinations and molecules, structures of biochemical supermolecules, defects in crystals, and magnetic defects in magnetic alloys.

Because of wave length - longer than 4 Å - and velocity - below 1000 m/s - cold-neutron scattering has also proved a most useful method for dynamic investigations. As examples may be mentioned phonon life times, magnon life times, dynamics of magnetic phase transformations, diffusion in liquids, and molecular rotations which because of symmetry characteristics cannot be studied by means of conventional methods.

An introduction to cold neutrons has previously been given in[1].

1.2. History of Cold-Neutron Sources in Reactors

Interest in cold neutrons was first aroused at Harwell in the early 1950's. After studies of different hydrogenous moderators outside the reactor, the world's first cold-neutron source was built in the Harwell BEPO reactor in 1957.

In 1959 a cold source was installed in the EL3 reactor at Saclay, and the following year the Harwell Dido source was commissioned[2].

Two cold sources are in operation in Germany. One in the FR-2 at Karlsruhe since 1968[3], and one in the FRJ-2 at Jülich since 1969[4].

Cold sources have also been installed in the low-flux reactors BR1 at Mol and FiR1 at Helsinki.

A cold source for the high-flux reactor in Grenoble RHF is being built and is expected to be operating by the end of 1972[5].

The project for a cold source in the DR 3 was started late in 1968, and the source is expected to be operational about the middle of 1972.

2. THE COLD-NEUTRON SOURCE IN THE DR 3

2.1. General Description

In principle the cold-neutron source in the DR 3 consists of a hydrogen-filled moderator chamber placed in the horizontal beam hole 7TL-3 of the reactor, see fig. 1. The moderator chamber, made of aluminium alloy AlMg3, is placed inside the vacuum casing, which is made of the same aluminium alloy. Vacuum is used to insulate the cold parts, and the vacuum containment further acts as a second containment in a triple containment system, see 2.3. The annulus between the vacuum containment and the liner in the beam hole and the rest of the liner are filled with helium at a small positive pressure.

Hydrogen is used as moderating material and as moderator chamber coolant at a pressure of 15 bars, which is above the critical pressure, see 2.2. The hydrogen is circulated between the moderator chamber and the two Philips-Stirling cryogenerators by means of a fan. Another fan is a standby. The moderator temperature is expected to be about 22°K at a reactor power of 10 MW.

From an intermediate stage the cryogenerators may provide cooling at a nominal temperature of 80°K. This cooling capacity is used to cool the neutron filters with a flow of cold helium circulated by a fan. The helium flow passes round the filter blocks in a spiralled groove. This cooling jacket is insulated by means of a vacuum annulus which is in connection with the vacuum in the rest of the plug.

The cryogenerators are connected to the system through a joint box which contains the four fans and eight cryogenic valves. The cryogenerators and the joint box are placed just above the beam hole. The moderator chamber and the cooling jacket for the neutron filter are connected to the joint box by means of transfer lines. The cryogenerators and joint box are shown in fig. 2.

The only equipment placed outside the reactor shell is the hydrogen buffer and supply system.

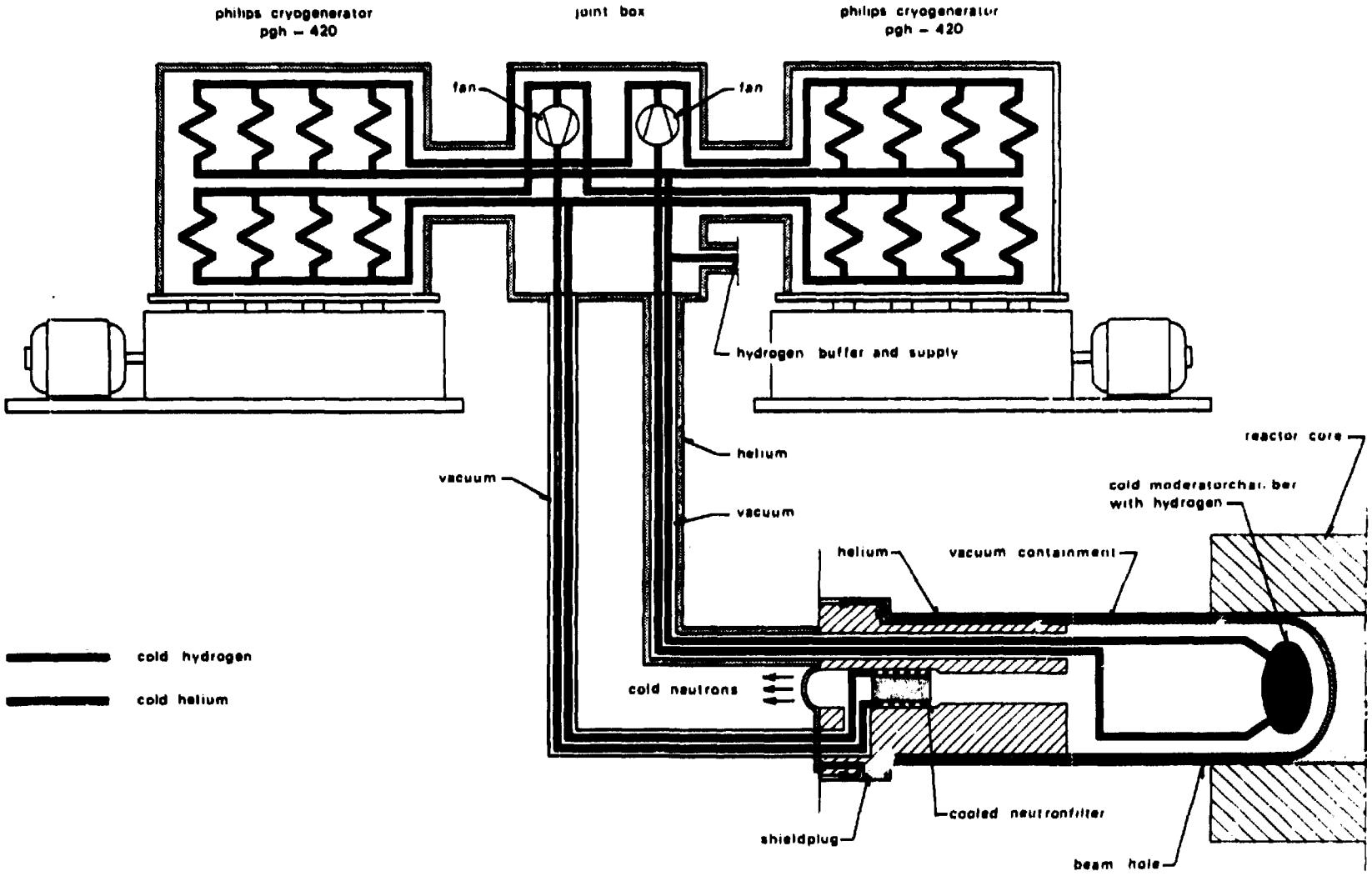

Fig. 1. Simplified diagram of the cold-neutron source.

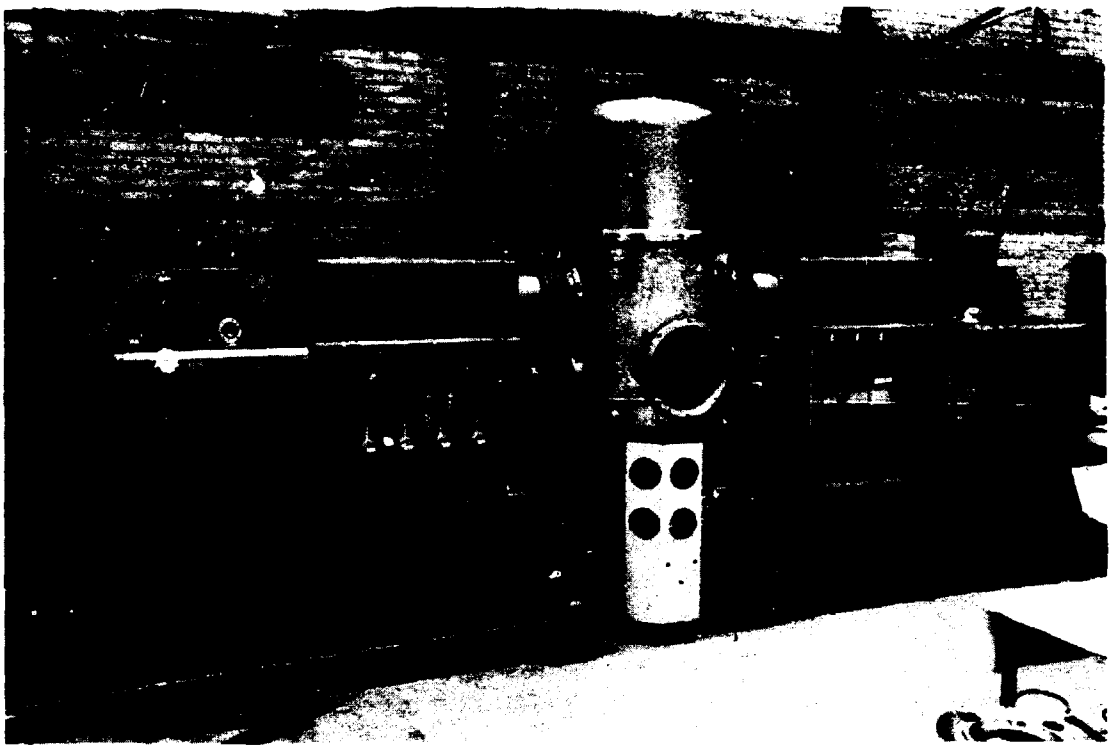

Fig. 2. Cryogenerators and joint box.

2.2. The Supercritical System

As mentioned in 2.1 the system is supercritical, i.e. the hydrogen pressure - 15 bars - is above the critical pressure, which is about 13 bars.

In a temperature-entropy chart for normal hydrogen, it may be seen that hydrogen at 15 bars will always be in a single phase. As the temperature range during operation will be 22 - 30°K, and the pressure is the above-mentioned 15 bars, the density will be 58 - 70 g/l, which is above the density of liquid hydrogen in the same temperature range.

The supercritical system offers a great advantage over other systems, because the density of the hydrogen may be changed simply by changing the cryogenerator temperature, which can be done by means of heaters. Thus the cold-neutron gain may be optimized by adjusting the effective hydrogen thickness.

All cold-neutron sources with hydrogen moderators built until now have been based on the use of liquid hydrogen. A supercritical system has been proposed in the design study of the cold source for the Harwell High-Flux Beam Reactor. In that study the system was proposed to operate in the

temperature range 33 - 38°K, which would give a reduced hydrogen density compared with the liquid-hydrogen density. This reduction was intentional and based on geometrical considerations.

2.3. Safety Philosophy

Hydrogen alone is completely harmless, and a hazard only occurs when oxygen is present too. The hydrogen/oxygen hazard may occur in two ways; firstly, if some source of ignition is present, the elements combine exothermically to form water, and secondly, if oxygen from air is irradiated at cryogenic temperatures, ozone and, if nitrogen is present too, possibly oxides and ozonides of nitrogen may form, decompose explosively, and initiate a hydrogen/oxygen reaction.

The basic principle for safety of the cold-neutron source in the DR 3 is to preclude any possibility that air may enter either the hydrogen system or regions of the equipment containing hydrogen, especially at cryogenic temperatures and in fields of high radiation.

For the cold-neutron source in the DR 3 all hydrogen equipment inside the reactor shell is contained within a high-vacuum system which is surrounded by a third containment filled with helium. The helium is always at a small positive pressure, so that a leak in the helium blanket can be detected. By adopting this triple-containment philosophy the above-mentioned basic principle for safety is fulfilled, and it is ensured that in the event of a leak in the vacuum casing, only helium can enter the vacuum system.

3. DESIGN SOLUTIONS

During the designing of the cold-neutron source for the DR 3 many special problems arose because of the low temperature and the demand for low leak rates as well as the complexity of the triple containment system.

As an example of one of the components the joint box may be mentioned. The complexity of the joint box is caused by the numerous purposes it serves. In the joint box the hydrogen and the helium heat exchangers of the cryogenerators are connected to the transfer lines leading to the moderator chamber and the neutron filters respectively, through fans and cryovalves. All these cold pipes and components are connected in the vacuum chamber of the joint box and are thus fully vacuum insulated. In the joint box the vacuum systems of the transfer lines are separated from the vacuum in the joint box and the cryogenerators for ease of maintenance and leak detection.

The vacuum chamber is totally surrounded by a helium blanket which also contains the vacuum instrumentation and two sputter-ion pumps. The demands of the triple containment philosophy have thereby been fulfilled.

The maximum leak rate of the vacuum system in the joint box is 1×10^{-6} Torrs l/s, which corresponds to an inleakage of 1 Ncm^3 per 9 days into the volume of 500 litres.

It was necessary to design the above-mentioned cryovalve specially for the triple containment system to achieve low leak and heat leak rates.

The moderator chamber design was studied from stress and flow distribution considerations simultaneously, as they are mutually dependent. The stresses were calculated by means of a computer program and checked on models with strain gauges. The flow distribution was studied in a perspex chamber with a flow of water and polystyrene particles. In the final design of the chamber the flow follows a vortex spiral.

The heat input to the hydrogen system, which mainly comes from the thermal radiation and the nuclear heating in-pile, was calculated on the basis of the system design. With this heat input the hydrogen temperature was found from the cooling power - temperature chart of the cryogenerators to be approximately $22^{o}K$.

4. COMPARISON OF SOME COLD-NEUTRON SOURCES

A comparison of the cold-neutron source for the DR 3 with those at Harwell (DIDO), Saclay (EL-3), Karlsruhe (FR-2), Jülich (FRJ-2), and Grenoble (RHF) based upon data from the literature is shown in table 1.

The DR 3 cold-neutron source is different from the other cold sources in two essential points. First, the beam hole is tangential to the core, and the cold source therefore provides two beams of cold neutrons. Second, the use of supercritical hydrogen permits adjustment of the effective hydrogen thickness as mentioned in 2.2.

REFERENCES

1) J. Als-Nielsen and J. Leth, Hvad er "kolde" neutroner? Reactor Engineering Department IR No. 168 (1969). Risø Internal Report No. 1327.

2) D.G. Pearce, Cold Neutrons. Sci. J. 3 (1967) 55-60.

3) F. Spath, E. Karb, and H. Oehme, Sicherheitsbericht für die kalte Neutronenquelle am FR2. KFK - 818 (1968) 90 pp.

4) C. Doose, H. Stiller, and A. Tholen, The Cold Source at the FRJ-2 Reactor. ICEC-3, Berlin (1970).

5) P. Ageron, J. Verdier, and R. Ewald, Die kalte Neutronenquelle für den Hochflussreaktor in Grenoble. Atomwirtschaft-Atomtechnik 16 (1971) 125-129.

Table 1

Comparison of some cold-neutron sources

Reactor	Reactor power MW	Thermal flux at the source $n/cm^2\ s$	Moderator	Moderator thickness mm	Moderator volume cm^2	Nuclear heating in Moderator W/g	Nuclear heating in Material W/g	Heat removed W
DR 3	10	7×10^{13}	H_2 supercr.	60	570	1.3	0.3	620
DIDO	15	4×10^{13}	H_2 liq.	30	200	0.75	0.2	42
EL-3	17.5	5×10^{13}	H_2+D_2 liq.	74	500	1.04	0.11	45
FR-2	43	4.9×10^{13}	H_2 liq.	45	250	0.91	0.18	50
FRJ-2	15	8.9×10^{13}	H_2+D_2 liq.	55	850	2.5	0.7	1000
RHF	60	7×10^{14}	D_2 liq.	380	25000	1.47	0.6	7000

Development of Nuclear Heat Calorimeters and Dose Separation of Nuclear Heat Components

by

Karsten Haack
DR 3

Abstract

Experimenters' demand for information about the nuclear heating in their samples and rigs in the reactor necessitated development of two types of calorimeters: (1) An adiabatic type (25 mm o. d.) with a sensitivity range of 1 - 500 mW/g for measurements in experimental facilities outside the core in the reflectors and (2) an isothermal rod type (6. 5 mm o. d.) with a sensitivity range of 0. 1 - 5 W/g for measurements in the fuel elements. A description of the calibration and measurement methods is given, and some characteristic results are shown. The dose separation comprises the calculations of the heat contributions from thermal and fast-neutron flux reactions in the calorimeter sample and structure.

1. INTRODUCTION

A fraction of the energy released by fission in a reactor is not deposited in the fuel elements, but appears as a heat source elsewhere. This fraction comprises mainly the following contributions:

(a)	Fission neutrons	3.1%
(b)	Instantaneous γ-release	3. %
(c)	Decay γ-radiation	2.6%
(d)	Decay β-radiation	2.6%
(e)	Neutrinos	5.6%

The neutrinos are not attenuated within the reactor core. The decay β-radiation is absorbed in the nearest vicinity of the fuel plates and will rarely appear in the experimental facilities; but the remaining contributions (a), (b), and (c) will produce considerable heat here, and it is therefore necessary that the experimenter knows the size of these contributions in order to establish sufficient cooling and thus obtain the desired temperature conditions in his rig.

The rig will be heated not only by this primary radiation, but also by secondary radiation, produced by neutron reactions in the rig materials.

Under the assumption that the primary radiation is not essentially attenuated by the presence of a rig, it becomes mainly a function of the fuel element position in the core. The energy deposition by the primary radiation is consequently called the "Position Dose Rate" (PDR).

The secondary radiation depends on the physical and geometrical characteristics of the rig materials, and consequently the energy deposition from this radiation is called the "Material Dose Rate" (MDR).

The total of the energy deposition from the primary and the secondary radiation (PDR + MDR) is the true dose rate, denoted the "Nuclear Heat" (NH).

As the properties of the materials in a rig and the neutron flux conditions are usually well known, the MDR can be calculated. But it is difficult to calculate the PDR in the very complex system of a research reactor core; better accuracy is obtained by measurements.

The instruments that may be used for such measurements are:

- ionization chambers
- physical or chemical dosimeters
- calorimeters.

The calorimeter resembles a rig design most closely, and therefore this instrument is usually chosen for the measurement of nuclear heat.

2. CHOICE OF CALORIMETER TYPES

The classic adiabatic calorimeter cannot be used directly, because the necessary insulation against heat exchange with the surroundings needs more space than is usually available in an experimental tube of a research reactor. The adiabatic conditions are established by surrounding the sample with a heat sheath, which is kept at the sample temperature by means of a heater on the sheath controlled by the difference signal from two thermocouples, one on the sample and one on the sheath. Between the sample and the sheath is an evacuated gas gap, see fig. 1.

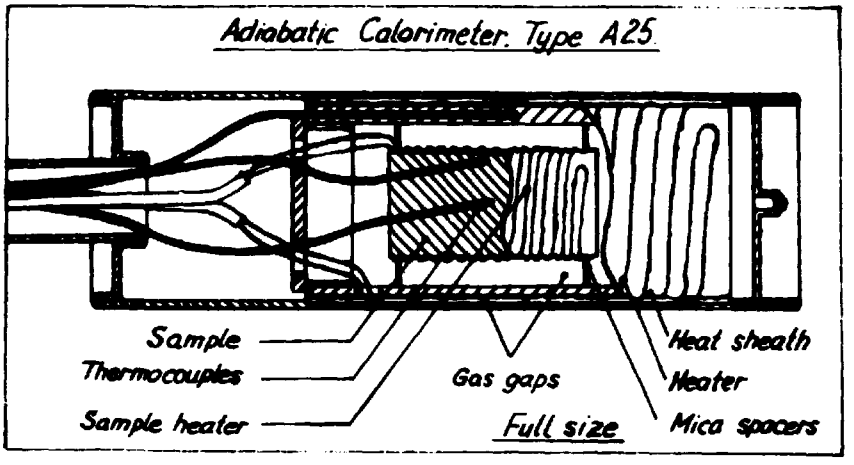

Fig. 1.

The heat deposition, q watts per gram, gives a temperature increase rate dT/dt according to the equation:

$$q = c \frac{dT}{dt} \text{ cal/g·s} = 4.1868\, c \frac{dT}{dt} \text{ W/g} , \qquad (1)$$

where c and T are the specific heat and the temperature of the sample. The dT/dt is measured graphically on the sample thermocouple recorder paper.

An adiabatic calorimeter as sketched here is suitable for measurements in the range 0.01-0.5 W/g and has been used in the experimental holes out-

side the core of the DR 3.

Inside the core, values of nuclear heat up to 2 W/g are seen, so a less sensitive type had to be used here. Furthermore this type should be smaller, as the access to the fuel elements is through 8 mm tubes. It was decided to choose an isothermal rod calorimeter type, see fig. 2.

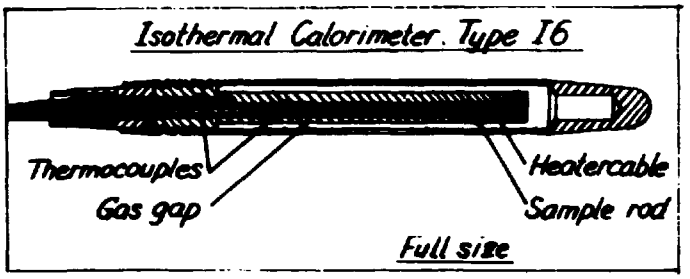

Fig. 2.

The principle of measurement appears from the following consideration: The heat balance in an infinitesimal piece of the rod-shaped sample is (see fig. 3):

$$Q_u = Q_\gamma + Q_i \quad . \tag{2}$$

If the specific heat conduction of the rod is K W/·c cm, its cross section A cm^2, and its specific weight V g/cm^3, and if the nuclear heat is q W/g, (2) can be written:

$$-KA \frac{d(T_{x+dx})}{dx} = q\,VAdx - KA \frac{d(T_x)}{dx} \quad .$$

Expansion of the left side according to the Taylor formula and exclusion of terms of order higher than 2 give the differential equation:

$$-K \frac{d^2(T_x)}{dx^2} = q\,Vdx \tag{3}$$

with the solution

$$T_o - T_x = \frac{x^2 V}{2K} q \quad , \tag{4}$$

which shows that the nuclear heat can be found by measuring the difference in temperature between the ends of the rod.

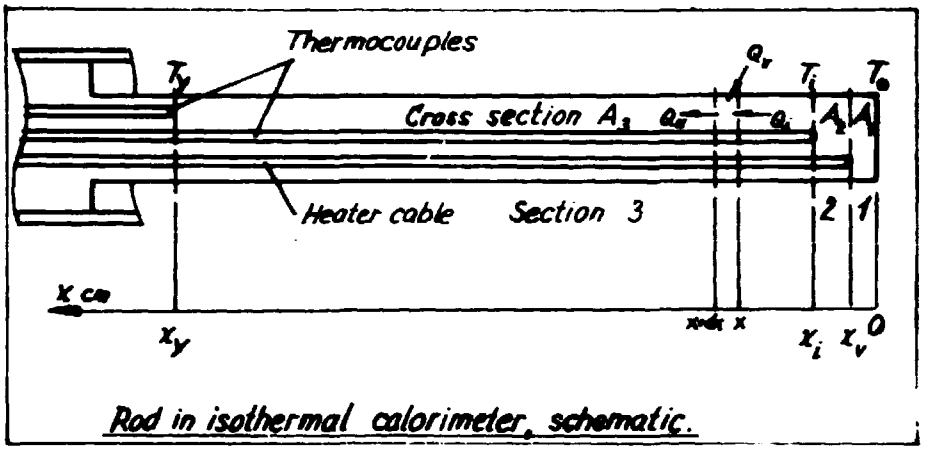

Rod in isothermal calorimeter, schematic.

Fig. 3.

3. CALIBRATIONS

The sample in the adiabatic calorimeter has a built-in electrical heater for the purpose of calibration, i.e. measuring of c in eq. (1). This value is the weighted mean value of the sample construction parts, (sample material, thermocouples, heater, cement, and suspensions):

$$c = \frac{\sum_{i=1}^{n} m_i c_i}{\sum_{i=1}^{n} m_i} , \qquad (5)$$

where m_i and c_i are the mass and the specific heat of the i'th of the n sample parts.

The calibration could be performed in the same way as an in-pile measurement, but as the sheath would be heated by the heater alone, and the heater is not uniformly suspended over all parts of the sheath, considerable temperature gradients would occur in the sheath, and the mean sample/sheath difference temperature could no longer be considered to be zero.

A better calibration is obtained by recording a small temperature transient with the sheath heater control disconnected. The transient is initiated by a small current through the sample heater which raises the sample temperature a few ^{o}C (see fig. 4). The current is switched off before equilibrium is attained, and then the cooling period is recorded. The gas gap heat conduction K_g $W/^{o}C$ can be considered constant during the transient. The heat balance is:

$$ri^2 - K_g \Delta T = C \frac{dT}{dt} \quad , \tag{6}$$

where the sample heat capacity $C = c \cdot M_p$, and M_p is the sample mass.

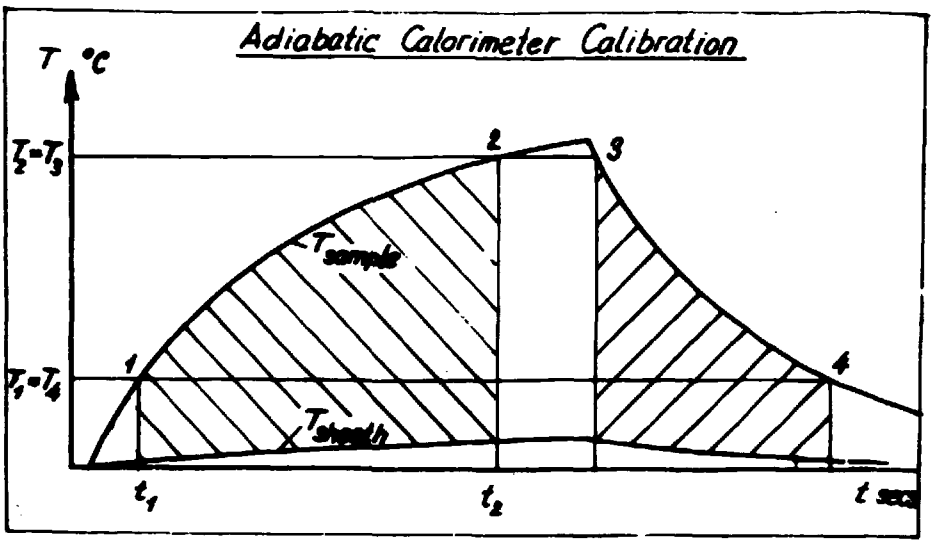

Fig. 4.

If four states during the transient are chosen, 1 and 2 at increasing, 3 and 4 at decreasing temperatures, (see fig. 4) so that

$$T_2 - T_1 = T_3 - T_4 \quad , \tag{7}$$

integration of eq. (6) will give

$$\int_1^2 ri^2 dt - \int_1^2 K_g \Delta T dt = \int_1^2 C dT \tag{8}$$

and

$$-\int_3^4 K_g \Delta T dt = \int_3^4 C dT \qquad (9)$$

with the solutions:

$$ri^2(t_2-t_1) - K_g I_{1-2} = C(T_2-T_1) \qquad (10)$$

and

$$-K_g I_{3-4} = C(T_4-T_3) \quad , \qquad (11)$$

where the integrals

$$I_{1-2} = \int_1^2 \Delta T dt$$

and

$$I_{3-4} = \int_3^4 \Delta T dt$$

can be found by graphical integration of the recorded transient. Eqs. (10) and (11) are now solved with respect to the desired value:

$$C = \frac{I_{3-4}}{I_{1-2} + I_{3-4}} \cdot \frac{t_2 - t_1}{T_2 - T_1} \cdot ri^2 \text{ joules/}^{o}C \quad , \qquad (12)$$

and, furthermore, the gas gap heat conduction can be calculated:

$$K_g = \frac{t_2 - t_1}{I_{1-2} + I_{3-4}} \cdot ri^2 \text{ W/}^{o}C \quad . \qquad (13)$$

The calibration of the isothermal rod calorimeter is performed by means of a built-in heater cable which is shown in fig. 2. This cable and the longest thermocouple cable together give a considerable contribution to the in-pile heating of the rod. The cable contributions can be allowed for by means of the proportion of their masses to the rod mass, as the mass-γ-absorption coefficient at the most frequent γ-energies in the reactor, 1-3 MeV, is the same for the elements in the cables and in the rod. But it causes different in-pile heating in rod sections 1, 2, and 3. In the

following calculations the in-pile heating will be denoted $k_1 q$, $k_2 q$, and $k_3 q$ where k_1, k_2, and k_3 are constants calculated for the respective rod sections. Furthermore the rod heat conduction is different in the three sections. The heat conduction along the cables is negligible.

Finally the cables do not extend right to the free end of the rod, and this makes the rim conditions more complicated for the solution of differential equation (3).

Because of the objections mentioned here it is necessary to reconsider the deduction of eq. (4). If the rim values for a rod section from $x = a$ to $x = b$ ($b > a$, see fig. 3) are

$$(T_a,\ Z_a = \left(\frac{dT}{dx}\right)_a) \text{ and } (T_b,\ Z_b = \left(\frac{dT}{dx}\right)_b) \ ,$$

$(T_b,\ Z_b)$ can be found by solution of the differential equation by use of the known rim values $(T_a,\ Z_a)$:

$$T_b = T_a - (x_b - x_a)^2 \frac{qV}{2K} + (x_b - x_a) Z_a \tag{14}$$

$$Z_b = -\sqrt{\frac{2qV}{K}(T_a - T_b) + Z_a^2} \ . \tag{15}$$

The discontinuity of Z at the section borders can, by a heat balance consideration, be found to be

$$Z_{(x+dx)} = \frac{A_{(x-dx)}}{A_{(x+dx)}} Z_{(x-dx)} \ . \tag{16}$$

If eqs. (14), (15), and (16) are used successively on the three rod sections, an expression of the ΔT to be measured in-pile is deduced:

$$\Delta T_m = T_{im} - T_{ym} = \frac{V_q k_3}{2K} (x_y - x_i)^2 - \frac{A_2}{A_3} (x_y - x_i) Z_{i2} \ , \tag{17}$$

where

$$Z_{i2} = -\frac{V_q}{K} \sqrt{k_2((x_i - x_v)^2 k_2 + 2(x_i - x_v) \frac{A_1}{A_2} k_1 x_v) + (\frac{A_1}{A_2} k_1 x_v)^2} \ . \tag{18}$$

Accordingly for the out-of-pile calibration

$$\Delta T_c = T_{ic} - T_{yc} = \frac{ri^2}{2A_3K}(x_y - x_i)(x_y - 2x_v + x_i) \quad . \tag{19}$$

If $\Delta T_m = \Delta T_c$, q can be found by means of eqs. (17), (18), and (19):

$$q = \frac{rk_c}{A_3V} i^2 \tag{20}$$

where

$$k_c = \frac{x_y - 2x_v + x_i}{(x_y - x_i)k_3 + 2\frac{A_2}{A_3}\sqrt{k_2((x_i - x_v)^2 k_2 + 2(x_i - x_v)x_v\frac{A_1}{A_2}k_1) + (\frac{A_1}{A_2}k_1 x_v)^2}} \quad . \tag{21}$$

A correction k_r for the increase of the heater resistance r at the higher heater wire temperatures during the calibration is introduced in each set of calibration values.

By plotting of ΔT_c versus $k_r ri^2$ a straight line appears from which the calibration factor f_c can be found:

$$f_c = \frac{d(\Delta T_c)}{d(k_r ri^2)} \quad . \tag{22}$$

Thus the nuclear heat can be calculated from a ΔT_m:

$$q = \frac{k_c}{A_3 V f_c}\Delta T_m = f_s \Delta T_m \ \ W/g \tag{23}$$

where f_s is the calorimeter sensitivity. A characteristic value of f_s is that of calorimeter I6/9: $f_s = 0.122$ W/g·°C.

4. MEASUREMENTS

Measurements by means of the adiabatic calorimeter were carried out by (1) rapid insertion of the calorimeter to the measurement position, (2) adjustment of the ΔT control device, and (3) recording of the sample temperature until the measurement was stopped at 250°C. The nuclear

heat was calculated by means of eq. (1).

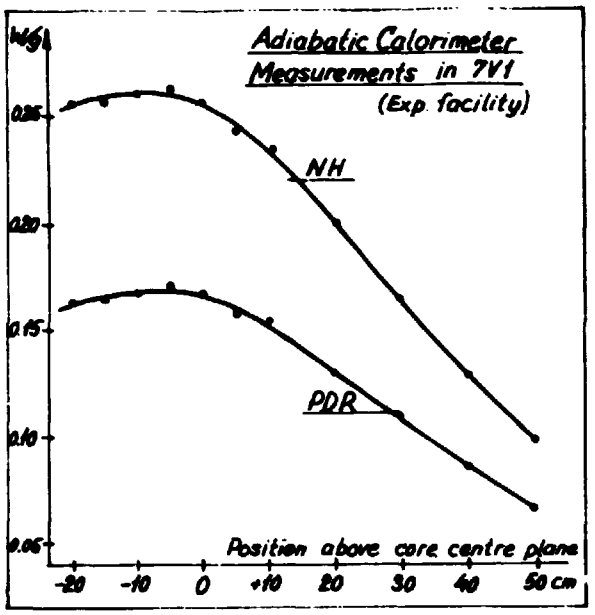

Fig. 5.

The isothermal calorimeter was kept in a measurement position until equilibrium - ΔT was attained after about eight minutes. Then it was automatically moved to a new position 10 cm higher up in the fuel element by means of a gear plug on top of the fuel element. Each vertical scan of a fuel element consisted of eight measurement points. All fuel elements that were not used for experiments were scanned at the beginning and at the end of most of reactor runs 108 - 128.

Typical nuclear heat scans with the two calorimeter types are shown in figs. 5 and 6. The figures also show the position dose rates PDR = NH - MDR obtained by means of the calculations given in chapter 5.

Figure 7 shows NH and PDR versus the distance from the vertical core centre line.

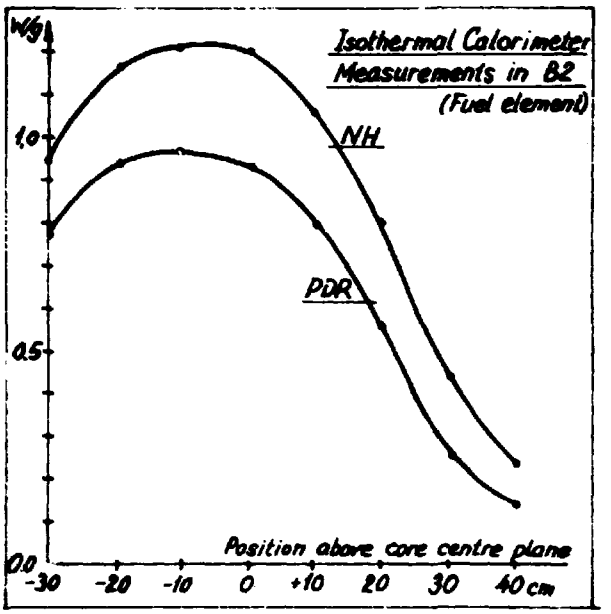
W/g
Isothermal Calorimeter
Measurements in B2
(Fuel element)
NH
PDR
1.0
0.5
0.0
Position above core centre plane
-30
-20
-10
0
+10
20
30
40 cm

Fig. 6.

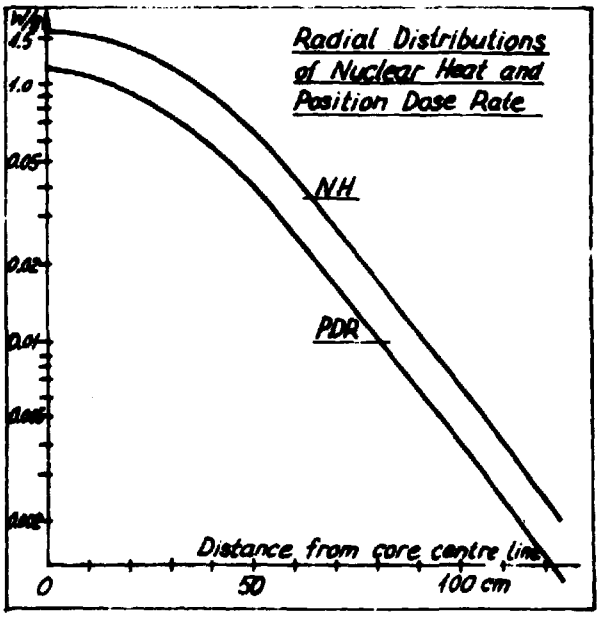
W/l
Radial Distributions
of Nuclear Heat and
Position Dose Rate
NH
PDR
1.5
1.0
0.05
0.01
0
50
100 cm

Fig. 7.

5. DOSE SEPARATION

The reactions contributing significantly to the heating of the calorimeter sample by secondary radiation are:

(A) Thermal-neutron capture in the structure

(B) Thermal-neutron capture in the sample

(C) Decay of nuclei formed in the structure

(D) Decay of nuclei formed in the sample

(E) Fast-neutron elastic scattering in the sample

(F) Fast-neutron inelastic scattering in the sample

Formulas for calculation of these contributions will be deduced below.

(A). The release of binding energy from thermal-neutron capture in the structure elements gives a total γ-source strength of

$$S_i = N \frac{M_{qi}}{A_i} \sigma_{ai} \varphi_{th} E_{bi} \quad \text{MeV/s} \quad , \tag{24}$$

where N is the Avogadro number $0.602 \cdot 10^{24}$,

M_{qi} is the mass of isotope "i" in the "q"'th structure part in grams,

σ_{ai} is the thermal-neutron absorption cross section in barns,

φ_{th} is the thermal-neutron flux (Westcott) in $n/cm^2 s$,

E_{bi} is the binding energy in MeV released by thermal-neutron capture in isotope "i".

The fraction of S_i that hits the sample is denoted $G_q S_i$. G_q is calculated for some symmetrical geometries in ref. [1]. With a linear energy absorption coefficient of the sample μ_{eai} cm^{-1} referring to the level of the binding energy of isotope "i", and a sample mass M_p grams, the total energy deposition rate in the sample from the Q structure elements consisting of I isotopes can be written:

$$\Delta W_{CSt} = \frac{1}{M_p} \sum_{q=1}^{Q} \sum_{i=1}^{I} (G_q S_i \mu_{eai}) \quad \text{MeV/s} \cdot \text{g} \quad . \tag{25}$$

By rearranging and transforming from MeV/S to watts we obtain:

$$\Delta W_{CSt} = 9.65 \cdot 10^{-14} \frac{\varphi_{th}}{M_p} \sum_{q=1}^{Q} \sum_{i=1}^{I} \left(G_q \frac{M_{qi}\sigma_{ai}}{A_i} E_{bi}\mu_{eai}\right) \text{ W/g} \quad . \tag{26}$$

(B). The thermal-neutron capture in the sample itself deposits a binding energy heat in the sample which can be found from similar considerations:

$$\Delta W_{CSp} = 9.65 \cdot 10^{-14} \frac{\varphi_{th}}{M_p} \sum_{i=1}^{I} \left(\frac{M_i \sigma_{ai}}{A_i} E_{bi} X_i\right) \text{ W/g} \quad , \tag{27}$$

where X_i is the fraction of the released energy that is absorbed in the sample itself. X_i has been calculated for different geometries by Case et al. [2].

(C). Only the most common modes of decay: γ and β^- will be considered here.

If the i'th isotope decays in K modes, and if photons from the k'th mode are expelled with a probability N_k, the total heat in the sample from γ-decay in the structure can be summed as:

$$\Delta W_{DSt\gamma} = 9.65 \cdot 10^{-14} \frac{\varphi_{th}}{M_p} \sum_{q=1}^{Q} \sum_{i=1}^{I} \left(G_q \frac{M_{qi}\sigma_{ai}}{A_i} \sum_{k=1}^{K} (N_k E_k \mu_{eak})\right) \text{ W/g} \tag{28}$$

in the equilibrium state of the decay.

The β^--particles are expelled with energies that have a continuous frequency distribution so that the spectrum is split up into a number of intervals $\Delta_1, \Delta_2, \ldots, \Delta_j, \ldots, \Delta_J$. If the mean values of energy and frequency in interval Δ_j are E_j and N_j respectively, and the probability that β^--particles in this energy interval penetrate the structure layers is δ_{Sj}, the total heat deposition in the sample due to β^--decay in the structure elements can be written:

$$\Delta W_{DSt\beta^-} = 9.65 \cdot 10^{-14} \frac{\varphi_{th}}{M_p} \sum_{q=1}^{Q} \sum_{i=1}^{I} \left(G_q \frac{M_{qi}\sigma_{ai}}{A_i} \sum_{k=1}^{K} \left(N_k \sum_{j=1}^{J} (N_j \Delta_j E_j \delta_{Sj})\right)\right) \text{ W/g} \quad . \tag{29}$$

The deduction of the β^--energy frequency distribution and the calculation of the penetration probability δ_{Sj} are given in Risø Report No. 119 [1] for aluminium.

(D). With a sample of aluminium the major contribution to the MPD is that of β^--decay in the sample. In spite of the short range of the β^--particles (5.1 mm of 2.83 MeV β^- in Al), it is necessary to take into account those β^--particles that escape through the sample surface. If this fraction is called d, the heating from γ- and β^--decay in the sample is given by:

$$\Delta W_{DSp\gamma} = 9.65 \cdot 10^{-14} \frac{\varphi_{th}}{M_p} \sum_{i=1}^{I} \left(\frac{M_i \sigma_{ai}}{A_i} \sum_{k=1}^{K} (N_k E_k X_k) \right) \text{ W/g} \quad (30)$$

$$\Delta W_{DSp\beta^-} = 9.65 \cdot 10^{-4} \frac{\varphi_{th}}{M_p} \sum_{i=1}^{I} \left(\frac{M_i \sigma_{ai}}{A_i} \sum_{k=1}^{K} ((1-d)N_k \sum_{j=1}^{J} (N_j \Delta_j E_j)) \right) \text{ W/g} \quad (31)$$

The fraction d can be calculated by means of the computer code BETA-TAB [4].

(E). Neutrons with energy E suffering elastic collisions with nuclei with mass number A lose (acc. to (3)) on an average the energy:

$$dE = \frac{E}{2} \left(1 - \frac{(A-1)^2}{(A+1)^2} \right) = \frac{2E}{(A+1)^2} \quad . \quad (32)$$

The total energy deposition in the sample from a fast-neutron flux with energy spectrum $\varphi(E)$ is consequently:

$$\Delta W_{Sc.el} = \frac{N}{A} \cdot \frac{2A}{(A+1)^2} \int_{E_1}^{E_2} \varphi(E) \sigma_{sc.el}(E) dE \quad \text{MeV/sg} \quad , \quad (33)$$

where $\sigma_{sc.el}(E)$ is the scattering cross section in barns at the energy E.

Commonly the neutron spectrum is expressed in lethargy units defined by [3]:

$$u \equiv \ln \frac{E_o}{E} \quad . \quad (34)$$

The reference energy is set to E_o = 10 MeV, and eq. (33) is transformed to lethargy units:

$$\Delta W_{sc.el} = -19.32 \cdot 10^{-14} \frac{1}{(1+A)^2} \int_o^{u_1} \varphi(u)\, \sigma_{sc.el}(u)\, du \quad W/g \quad . \qquad (35)$$

(F). Neutrons with energies above the inelastic scattering thresholds of the sample elements may suffer inelastic collisions accompanied by release of particles as photons, protons, deuterons, alphas, or other neutrons. The energy deposited in the sample is the difference between the energy of the entering neutron and that of the particle leaving the sample. The probability that an expelled particle will be absorbed in the sample is denoted X(u). Thus the total energy deposition in the sample from inelastic scattering is

$$\Delta W_{scinel} = 9.65 \cdot 10^{-14} \cdot \frac{1}{A} \int_o^{u_1} \varphi(u)\, \sigma_{scinel}(u)\, X(u)\, du \quad W/g \quad . \qquad (36)$$

The contributions (A)-(F) to the MDR from thermal and fast fluxes have been calculated as outlined above in terms of a flux of 10^{14} n/cm^{2}s. The detailed calculations are shown in Risø Report No. 119 [1].

The results are given in the table below.

Material dose rates (MDR) at a neutron flux of 10^{14} n/cm^{2}s

Reaction	Calorimeter	
	adiabatic mW/g	isothermal mW/g
Thermal-neutron capture in the structure	14.5	9.9
Thermal-neutron capture in the sample	22.1	18.3
β^--decay in the structure	9.5	17.4
γ -decay in the structure	3.8	2.6
β^--decay in the sample	94.6	91.3
γ -decay in the sample	6.1	2.5
Total from thermal-neutron flux	150.6	142.0
Elastic scattering	178	340
Inelastic scattering	~ 0	26
Total from fast-neutron flux	178	366

REFERENCES

1) K. Haack, Nuclear Heat Measurements at DR-3. Risø Report No. 119 (1972). In preparation.

2) A. K. Dickson, Nuclear Heating of Non-Fissile Materials by Thermal Neutron Reactions. TRG - Report.- 322 (D) (1962). 16 pp.

3) S. Glasstone and M. C. Edlund, The Elements of Nuclear Reactor Theory. (Van Nostrand Co., New York, 1957) 416 pp.

4) K. Haack, Computer Code P-400: BETATAB. Risø-M-938 (1969). 11 pp. Internal Report.

Pellet Stack Shortening and Cladding Elongation of Irradiated UO_2-Zr Fuel Pins

by

F. List, Reactor Engineering Department

and

P. Knudsen, Metallurgy Department

Abstract

Six UO_2-Zr fuel pins irradiated to a burn-up of 5,600 MWD/te UO_2 showed pellet stack shortenings of 5 to $8 \cdot 10^{-3}$ and pin elongations of 7 to $9 \cdot 10^{-4}$. A theoretical estimate, based on fuel - clad mechanical interaction and ratchetting, was made in an attempt to account for the length changes. The estimate for the pellet stack shortening agrees well with the observed values. The calculated pin elongation is lower than the measured values, probably because primary creep of Zr was neglected in the calculation.

1. INTRODUCTION

Six fuel pins with UO_2 pellets clad in zircaloy-2 were irradiated in a boiling-water reactor to an average burn-up of 5,600 MWD/te UO_2. Comparison of pre- and post-irradiation measurements showed that the pellet stacks had shortened, and the total pin lengths had increased. We present the experimental results and a theoretical estimate to account for the dimensional changes.

2. DESIGN

The zircaloy-2 (Zr-2) cladding had an inner diameter of 12.85 mm and an 0.6 mm wall thickness. The cylindrical, 5%-enriched UO_2 pellets were ground to a diameter of approx. 12.6 mm and had a sintered density of 10.4 g/cm^3. The pellet stacks were 1671 mm long including a 13 mm natural pellet at each end, and the total pin length was 1818 mm. Additional pin design data are included in table 1 in section 4.

The pellets were held in place inside the fuel pin by a helical Inconel X-750 spring in the fission gas plenum at the upper pin end, the axial spring force on the upper pellet being 8 kp. The six fuel pins were suspended from a common top grid and spaced laterally with Inconel 600 springs.

3. IRRADIATION

The complete fuel assembly (designated IFA 162) was irradiated in the OECD Halden Boiling-Water Reactor. The coolant was boiling D_2O at 34 ata pressure, corresponding to a boiling point of 240°C.

The average assembly burn-up was 5,600 MWD/te UO_2 as integrated from the power detectors; the total time at power was 220 days, and the average heat load was 330 W/cm. The axial form factor was about 1.3, with the highest heat load at the middle of the assembly. During the irradiation period the reactor was shut down to zero power 55 times.

4. POST-IRRADIATION EXAMINATION

Comparison of pre- and post-irradiation measurements indicated that the pins had increased in length as shown in table 1.

X-radiographs of the plenum ends showed that the helical springs were fractured except in pin M11-1; however, it is not known at what stage of

the irradiation these fractures occurred. The radiographs also revealed plenum length increases in the range of 9 to 14 mm. This was verified for two of the pins by cutting off the end plug and measuring the distance to the pellet stack with the depth gauge of a caliper. Since the pins had elongated by 1.6 mm or less, the pellet stacks had obviously shortened. Gamma scan recordings were used for a more direct measurement of pellet stack length after irradiation. The decreases in stack length thus obtained are given in table 1.

Table 1

Dimensional changes related to design parameters

Pin number	Pellet		Gap (diam.) mm	Pin elongation mm	Pellet stack shortening mm
	H/D (a)	End shape			
M8-2	1	Dished (b)	0.19	1.5	8
M77-2	1	Dished (b)	0.20	1.3	9
M48-2	1.5	Dished (b)	0.24	1.4	13
M37-2	1.5	Dished (b)	0.23	1.4	11
M29-2	1	Flat	0.28	1.5	12
M11-1	1	Flat	0.28	1.6	13

(a) H/D = height to diameter ratio.

(b) Spherical, both ends, 0.35 mm deep, 1.0 mm "shoulder".

5. THEORETICAL ESTIMATE OF DIMENSIONAL CHANGES

An interesting feature of this experiment is that the pellet stacks had shortened by 8 to 13 mm during irradiation. To account for this, it is assumed that pellets lock firmly with the cladding at a certain local heat load owing to differential thermal expansion and friction forces[1]. During further power increase the cladding will be stretched and the pellets compressed, and both will creep axially. When the reactor is at zero power, the combined forces of gravity and plenum spring may be able to relocate the pellets; during the following irradiation period the stack length is then further reduced and the pin length increased as a result of renewed creep.

For a theoretical estimate of these dimensional changes, expressions for in-pile creep of UO_2 and zircaloy are obtained as follows. At the heat loads in question, the temperatures at the inner rim of the dishing "shoulder" is well below 1000°C, thus thermal creep of UO_2 can be neglected, and the strain rate, $\dot{\varepsilon}_U$, due to irradiation-induced creep can be written (see for instance ref. 2):

$$\dot{\varepsilon}_U = A \cdot R \cdot \sigma ,$$

where A is of the order of $2.8 \cdot 10^{-10}$ $(h^{-1}) \cdot (g\ U/W) \cdot (cm^2/kp)$ (ref. 3), and R is the heat load in W/g.

The in-pile creep behaviour of zirconium alloys is rather complex (e.g. ref. 4). An expression has been derived from experimental results compiled in[5], giving in-pile creep strain of Zr-2 as a function of time, temperature, fast flux, and stress. The axial cladding stress resulting from the pellet - clad interaction is about 550 kp/cm^2 (see below); with an average cladding temperature of 265°C and a fast flux of about $4 \cdot 10^{13}$ $n/cm^2 s$, the expression for creep strain can be simplified in the stress range of interest to give an approximate creep rate of $\dot{\varepsilon}_Z = B \cdot \sigma$, where $B = 1.5 \cdot 10^{-10}$ (h^{-1}) (cm^2/kp).

At the beginning of a period at power, the pellet - clad interaction results in an elastic compression of the lower half of the pellet stack by:

$$a = \frac{E_Z \cdot F_Z}{E_U \cdot F_U + E_Z \cdot F_Z} \cdot \Delta L_o ,$$

and the cladding is stretched similarly by

$$b = \frac{E_U \cdot F_U}{E_U \cdot F_U + E_Z \cdot F_Z} \cdot \Delta L_o ,$$

ΔL_o is the difference in length between the lower half of the cladding and the pellet stack if no mechanical interaction existed, i. e.

$$\Delta L_o = \frac{L}{2} \cdot \alpha_U \cdot \frac{\Delta t_U}{\Delta Q} (Q - Q_1),$$

where

L = rod length

α_U = thermal expansion coefficient of UO_2

t_U = UO_2 temperature at dishing edge

Q = average heat load

Q_1 = average heat load when pellets at the middle of the rod lock with the cladding

E = Young's modulus

F = cross sectional area

U, Z = subscripts referring to UO_2 and Zr-2 respectively.

After a time increment of Δt, this difference has decreased owing to creep and is now

$$\Delta L_1 = \Delta L_o - \frac{E_U \cdot F_U}{E_U \cdot F_U + E_Z \cdot F_Z} \cdot \Delta L_o \cdot B \cdot E_Z \cdot \Delta t$$

$$- \frac{E_Z \cdot F_Z}{E_U \cdot F_U + E_Z \cdot F_Z} \cdot \Delta L_o \cdot A \cdot R \cdot E_U \cdot \Delta t$$

or

$$\Delta L_1 = \Delta L_o (1 - C \cdot \Delta t - D \cdot \Delta t) .$$

If the period at power is equal to $n \cdot \Delta t$, then the length difference at the end of this period is

$$\Delta L_n = \Delta L_o (1 - C \cdot \Delta t - D \cdot \Delta t)^n .$$

The sum of the corresponding pellet creep strain, ε_U, and cladding creep strain, ε_Z, is

$$\varepsilon_U + \varepsilon_Z = \Delta L_o - \Delta L_n = \Delta L_o (1 - (1 - C \cdot \Delta t - D \cdot \Delta t)^n) ,$$

or $$\varepsilon_U = \frac{D}{C+D} \cdot \Delta L_o (1 - (1 - C \cdot \Delta t - D \cdot \Delta t)^n)$$

and

$$\varepsilon_Z = \frac{C}{C+D} \cdot \Delta L_o \left(1 - (1 - C \cdot \Delta t - D \cdot \Delta t)^n\right).$$

A rough calculation shows that the upper half of the pellet stack will shorten by about half as much as the lower half. For simplicity, the irradiation time is divided into 55 periods of four days at constant power (Q = 330 W/cm), with relocation of pellets in between, and it is assumed that the axial forces in the dished UO_2 pellets are taken up by an outer 2-mm thick zone of the pellet. Thus the total calculated creep shortening of the whole pellet stack will be $1.5 \cdot 55 \cdot \varepsilon_U$; similarly the cladding creep elongation (i.e. pin elongation) becomes $1.5 \cdot 55 \cdot \varepsilon_Z$.

On the basis of the limited experience available[1] it is assumed that the pellet - clad locking occurs at a local heat load of 300 W/cm. With the above fuel pin design and irradiation conditions, the average axial cladding stress, σ_Z, can then be calculated:

$$\sigma_Z = \frac{2b}{L} \cdot E_Z = 550 \text{ kp/cm}^2 .$$

This stress level is in fair agreement with values obtained experimentally in other irradiations[6]. The dimensional changes can then be calculated and compared with the experimental results as shown in table 2.

Table 2

Comparison of calculated and observed dimensional changes

	Calculated	Observed
Pellet stack shortening, mm	10	8 - 13
Pin elongation, mm	0.5	1.3 - 1.6

6. DISCUSSION OF RESULTS

The agreement between calculated and observed pellet stack shortening is good. Experimentally, an increase in pellet length seems to lead to a more pronounced stack shortening, see table 1. This is probably related to the larger end distortions of longer pellets[7], although it is difficult to draw firm conclusions in the present case because the gap was varied at

the same time.

Flat pellet ends appear to give about the same stack shortening as dished ends, as would be expected from the "in-pile dishing" mechanism suggested previously[1]. Again, the interpretation may be incomplete because the gap was also varied.

The calculated pin elongation is smaller than the observed values. This is, at least partly, a consequence of neglecting of primary Zr-creep (for the sake of simplicity). Estimation of the constant B is another point of uncertainty, as can be seen from the scatter of the experimental results compiled in ref. 5.

Other assumptions and simplifications made in the above calculations may be additional sources of uncertainty. Thus the average heat load varied between the irradiation periods and had values up to about 450 W/cm; further, the length of individual irradiation periods varied from 0.5 to 25 days. The assumed local heat load of 300 W/cm required for pellet - clad locking is not very well established, since it has been obtained from the early irradiation history of a small number of fuel pins only[1]. Finally, the pellet - clad ratchetting at power reductions may have been different for different pins, since it is not known when the plenum spring fractures occurred.

ACKNOWLEDGEMENT

This investigation was performed as part of the Danish fuel development programme. The authors gratefully acknowledge professor T. Bjerge's stimulating interest in and support of this work.

Similarly, the authors are grateful to many staff members of the Danish AEC for discussions and assistance in the experimental work.

REFERENCES

1) G. Kjaerheim and E. Rolstad, In-Core Study of the Mechanical Interaction between Fuel and Cladding. Nucl. Appl. Tech. 7 (1969) 347-360.

2) J.B. Ainscough, Some Limiting Aspects of UO_2 Performance. TRG - Report - 1937 (S) (1970) 19 pp.

3) J.B. Ainscough, UKAEA, personal communication.

4) F.A. Nichols, On the Mechanisms of Irradiation Creep in Zirconium-Base Alloys. J. Nucl. Mater. 37 (1970) 59-70.

5) B. Watkins and D.S. Wood, The Significance of Irradiation-Induced Creep on Reactor Performance of a Zircaloy-2 Pressure Tube. In: Applications-related Phenomena in Zirconium and its Alloys. Symposium, Philadelphia, Pa., 5-7 November 1968 (ASTM Special Technical Publication, 458). (American Society for Testing and Materials, Philadelphia, Pa., 1969) 226-240.

6) E. Rolstad, Halden Project, personal communication.

7) J. Veeder, Thermo-Elastic Expansion of Finite Cylinders. AECL - 2260 (1967) 11 pp.

Dispersion-Strengthened Zirconium Products for Water-Cooled Reactors

by

E. Adolph and N. Hansen
Metallurgy Department

Abstract

To improve the strength of zirconium alloys at high temperatures a powder metallurgy process was developed for manufacture of zircaloy-2 dispersion strengthened with yttria (Y_2O_3). This work was carried out in collaboration with the UKAEA, Springfields.

Alloys with up to 10 volume per cent of yttria were produced in a high-purity argon atmosphere to insure a very low impurity content in the final material. The alloys were tensile-tested and creep-tested in the range room temperature to 600°C, and corrosion-tested in steam at 400°C. Furthermore a number of alloys were exposed to neutron irradiation before testing.

This development resulted in dispersion-strengthened alloys with good thermal and irradiation stability, twice the strength of zircaloy-2, and a corrosion resistance comparable to that of zircaloy-2.

INTRODUCTION

Few metallurgical procedures are available to increase the high-temperature strength of a metal. One is to introduce a very large number of small, hard particles into the metal, and this hardening, due to finely dispersed particles, is termed dispersion strengthening. This strengthening principle was demonstrated with the development in the late forties of sintered aluminium products or SAP. This material was a candidate for core components in organic cooled reactors, and was in 1958 selected for that purpose for the Risø Reactor Project DOR (an organic cooled, heavy-water-moderated reactor). A large development and testing programme was launched at Risø, and results from this programme together with work done at other laboratories in Europe, USA, and Canada showed in 1965 - 1966 that SAP could be used with confidence in the organic reactor. At that time, there was no incentive in Denmark to proceed along the organic reactor line, but as equipment and expertise in the field of dispersion strengthening was at hand, and as the interest in the use of dispersion-strengthened products for nuclear as well as non-nuclear components was increasing, it was decided at Risø to continue this line of research. In the mid-sixties the Danish reactor programme was shifted towards water-cooled reactors, and a programme was initiated together with the United Kingdom Atomic Energy Authority (UKAEA) to develop a dispersion-strengthened zirconium product for use as core material in such reactors. The object of this programme was to develop a material with greatly improved strength properties compared with zircaloy-2, without impairing the corrosion resistance in water and steam. The development carried out in the period 1966 - 1971 resulted in alloys with twice the strength of zircaloy-2 and about the same corrosion resistance. These alloys, composed of zircaloy-2 and yttrium oxide as the dispersoid, are described in the following.

SELECTION OF ALLOY SYSTEM

The main demands on the zirconium matrix alloy are good corrosion resistance in water and steam environments and satisfactory strength. The main demands on the dispersoid are small tendency to agglomerate in the fabrication and operating environments, and a reasonably small neutron cross section to ensure good neutron economy. On the basis of these demands zircaloy-2 was selected as the matrix metal and yttrium oxide as the dispersoid.

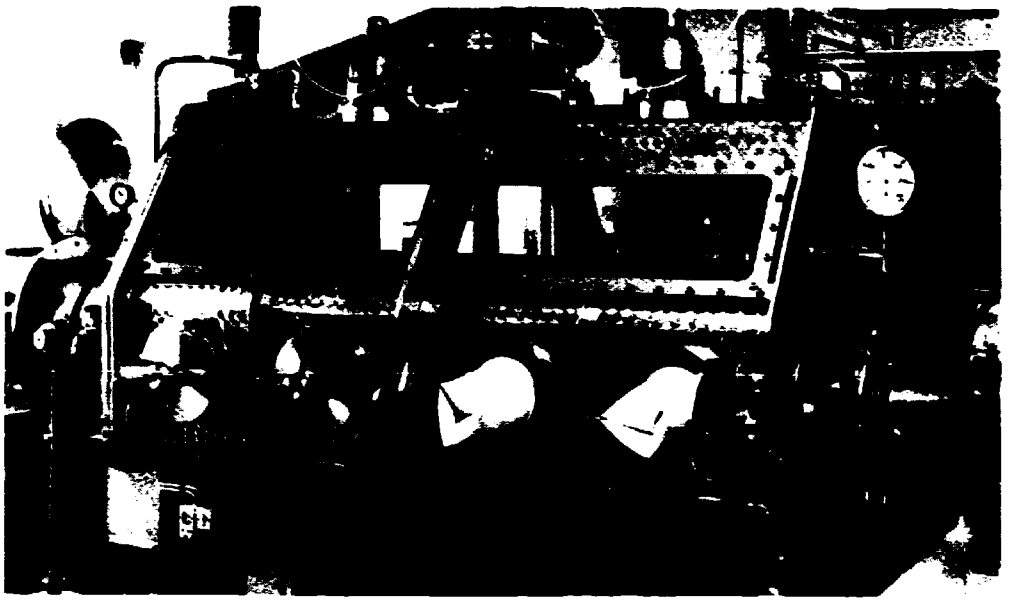

Fig. 1. Stainless-steel glove box for handling of powder materials.

FABRICATION OF ALLOYS

The introduction of small yttria particles into zirconium alloys in best achieved by powder metallurgy techniques. In order to eliminate the pick-up of gaseous impurities which degrade the properties of zirconium alloys (i. e. oxygen, nitrogen, and hydrogen), the materials are handled in an inert atmosphere of purified argon.

For this purpose a stainless-steel glove box and argon purification and analysis systems were constructed, fig. 1. The concentrations of oxygen, nitrogen, and water vapour measured in the circulating argon atmosphere of the glove box were 5, 20, and 1 ppm by weight respectively. The basic production process is shown schematically in fig. 2. The hydride of zircaloy-2 that is very friable was chosen as the starting material. For the production of zircaloy-2 + yttria alloys, rods of conventionally produced zircaloy-2 were completely hydrided at an overpressure of hydrogen at an elevated temperature. The hydride was milled in a rotating ball mill to a suitable particle size with yttria which had been pre-milled in alcohol to a size distribution shown in fig. 3(a). In general the yttria particles were rounded in shape with a small surface area. About 80% of the yttria has a diameter of less than 500 Å. The milling was carried out under argon, and

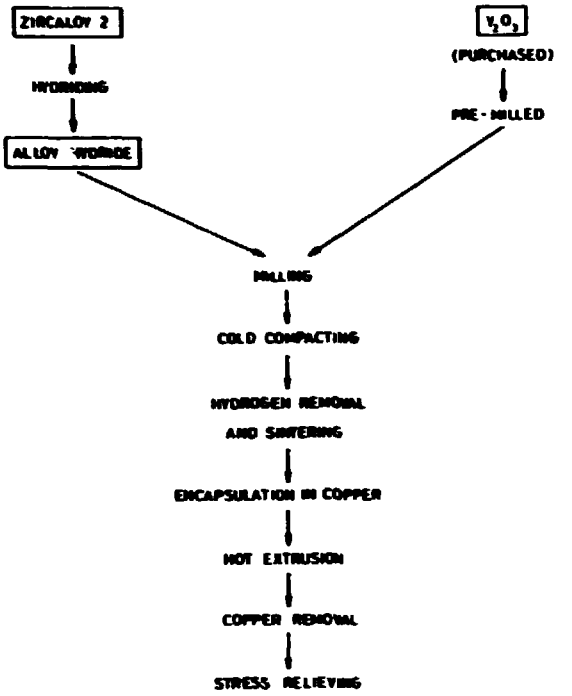

Fig. 2. Schematic flow sheet of the production route.

the milled powder mixture was then cold-compacted into pellets before being sintered to about 85% theoretical density. After sintering, the pellets were clad in copper under vacuum and hot-extruded into fully dense rod material, then stress-relieved for 10 hours at 600°C. The materials were analysed for dissolved gas content, and the results were in the region 100 - 150 ppm for nitrogen, 10 - 30 ppm for hydrogen, and 2000 - 4000 ppm for oxygen.

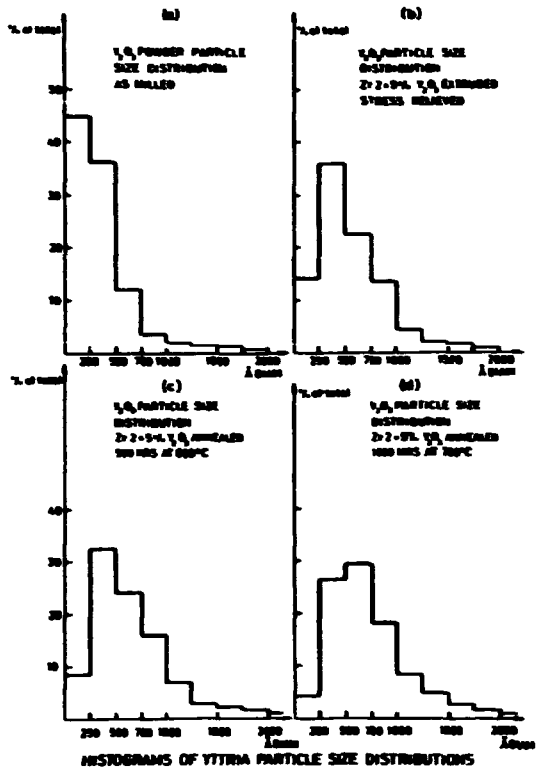

Fig. 3. Yttria particle size distribution.

METALLOGRAPHY OF EXTRUDED AND STRESS-RELIEVED ALLOYS

Fig. 4 shows the microstructure of an alloy with 5 volume per cent (v/o) yttria with a grain size of about 1.5 μm. Powder-produced zircaloy material with no yttria shows a grain size of more than 4 μm, illustrating the effectiveness of yttria in restricting grain growth in the sintering and extrusion processes.

The particle size distribution histograms in fig. 3(a) and (b) show that the average particle diameter increases during the manufacturing process. The coarsening of the yttria particles probably occurs during the sintering process. The mean particle diameter of yttria in the extruded and stress-relived products is approximately 600 Å. On the assumption that the particles form a simple cubic array, the surface to surface spacing can be calculated[1)] to be about 1500 Å. This is a satisfactorily low figure for obtaining a good contribution to the overall strength from the dispersed particles.

Fig. 4. Electron micrograph x10,000, extruded and stress-relieved zircaloy-2 + 5 v/o yttria.

THERMAL STABILITY OF DISPERSION-STRENGTHENED ALLOYS

Samples of zircaloy-2 + 5 v/o yttria were heat-treated at 600 and 700°C for up to 1000 hours. After treatment the materials were examined for grain growth and particle stability.

No noticeable grain growth was observed after heat treatment for 1000 hours at 700°C. The yttria particle size distribution was measured in samples of a zircaloy-2 + 5 v/o yttria alloy heat-treated for 500 hours at 600°C and 1000 hours at 700°C in the manner previously described. The histograms of the particle size distribution are shown in figs. 3(c) and (d). It is apparent that the particles have not coarsened significantly after 500 hours at 600°C. After 1000 hours at 700°C it is evident that the size distribution had changed slightly, and the mean particle diameter had increased to 750 Å.

From these experiments it can be concluded that the yttria particles will be reasonably stable during fabrication not involving temperatures above 800°C for fairly short periods of time, and at reactor operation temperatures it is suggested that the particles would be completely stable.

TENSILE PROPERTIES OF UNIRRADIATED ALLOYS

The tensile properties of the alloys with 0, 5, and 10 v/o yttria were established by vacuum testing.

Fig. 5 shows that the 0.2% proof stress at 350°C (max. operation temperature for a zirconium material in water-cooled reactors) of the zircaloy-2 + 5 v/o yttria alloys was increased by approx. 75%, and that of the 10 v/o yttria alloy by approx. 150% compared with similar alloys without yttria particles.

The increase in ultimate tensile stress at temperatures up to 500°C with increasing yttria additions was found to be linear up to 10 v/o yttria.

In fig. 6 the ultimate tensile stress up to 600°C of zircaloy-2 alloys containing 5 and 10 v/o yttria is compared with materials currently considered for pressure tubing in water-cooled reactors, namely zircaloy-2 in the 30% cold-worked (CW) condition and zirconium $2\frac{1}{2}$% Nb in the 20% cold-worked condition and in the heat-treated (HT) condition. The ultimate tensile stresses in the longitudinal direction of autoclaved pressure tubing material were averaged from published results[2, 3, 4]. The dispersion-strengthened alloys are significantly stronger than the cold-worked zircaloy-2 alloy. Although the ductility of the zircaloy-2 + 5 v/o yttria alloy is lower than that of cold-worked zircaloy-2 at room temperature, the ductilities at 300°C are nominally in the same range 15-20%[2, 4]. The dispersion-strengthened alloys are stronger than the cold-worked zirconium $2\frac{1}{2}$% Nb alloy, but the ultimate tensile strength of zirconium $2\frac{1}{2}$% Nb in the heat-treated condition closely approximates that of the 10 v/o yttria alloy and also has a superior ductility of about 20% at 300°C compared with about 10% for 10 v/o yttria alloys.

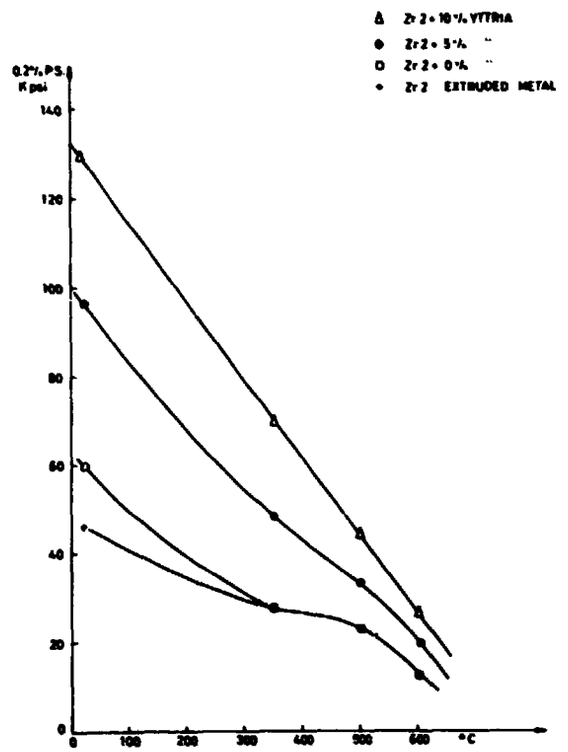

Fig. 5. 0.2% proof stress vs. temperature; zircaloy-2 + yttria alloys.

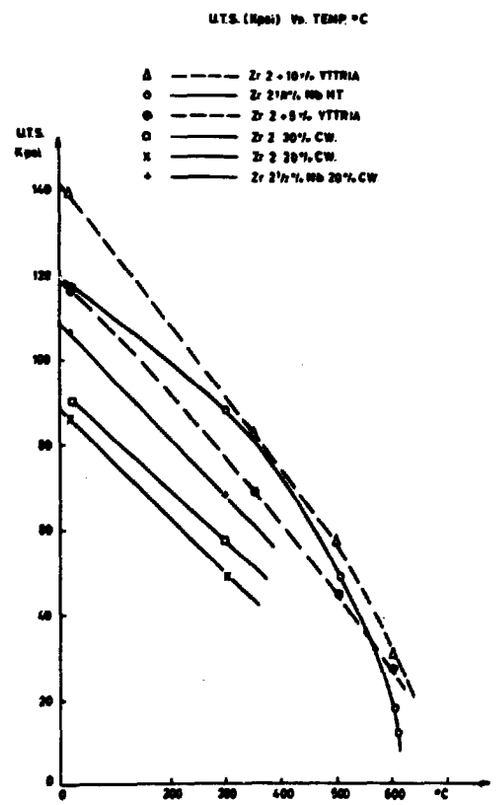

Fig. 6. Ultimate tensile strength vs. temperature.

TENSILE PROPERTIES OF IRRADIATED ALLOYS

Neutron irradiated has a substantial effect on the tensile characteristics of metals in much the same way as cold work. To gain some elementary knowledge of the effects of irradiation on the tensile properties of zircaloy-2 + yttria alloys, cylindrical tensile specimens were irradiated in the Danish reactor DR 3. The specimens were held in a rig where the temperature was kept at $285 \pm 15^{\circ}C$ by controlling the flow of the helium atmosphere around the specimens. The total irradiation time was 2800 hours, and the neutron dose received was 9.2×10^{20} n/cm^2 thermal and 2.3×10^{20} n/cm^2 fast, E $>$ 1 MeV.

Tensile tests on the irradiated specimens were performed in argon at 250 and 350°C. The tensile data obtained from these specimens are shown in table 1.

Table 1

Tensile Properties of Irradiated Alloys

	250°C						350°C					
	0.2 PS (Kpsi) unirr.	irr.	UTS (Kpsi) unirr.	irr.	Elong. (%)[x] unirr.	irr.	0.2% PS (Kpsi) unirr.	irr.	UTS (Kpsi) unirr.	irr.	Elong. (%)[x] unirr.	irr.
Commercial Zr-2 Annealed	32.5	58.5	49.5	61.5	25	5	27.8	46.3	41.0	49.0	28	5
Zr-2 + 0 v/o Yttria	35.0	65.0	55.1	71.1	24	6	28.0	58.6	45.1	60.1	28	5
Zr-2 + 5 v/o Yttria	61.7	94.7	78.2	103.2	15	4	48.0	74.6	68.9	87.9	20	5
Zr-2 + 10 v/o Yttria	88.5	105.5	100.2	115.2	7	3	69.7	85.7	82.8	102.8	10	4

[x] Gauge length 10 diameters.

The tensile properties of the irradiated alloys followed the generally observed trend for irradiated zircaloy-2, i. e. the proportional limit, 0.2% proof stress, and the ultimate tensile stress were all increased, and the elongation was reduced. The lower increases observed at 350°C probably reflect the partial recovery of irradiation damage at the higher testing temperatures.

An interesting effect of irradiation on work-hardening characteristics was observed and is illustrated in fig. 7. The alloys without yttria cease to work-harden, and the stress drops after very low plastic strains of the order of 0.25%. The alloys containing yttria continue to work-harden up to at least 0.6 - 1.0% plastic strain. The increase in tensile strengths is also clearly demonstrated.

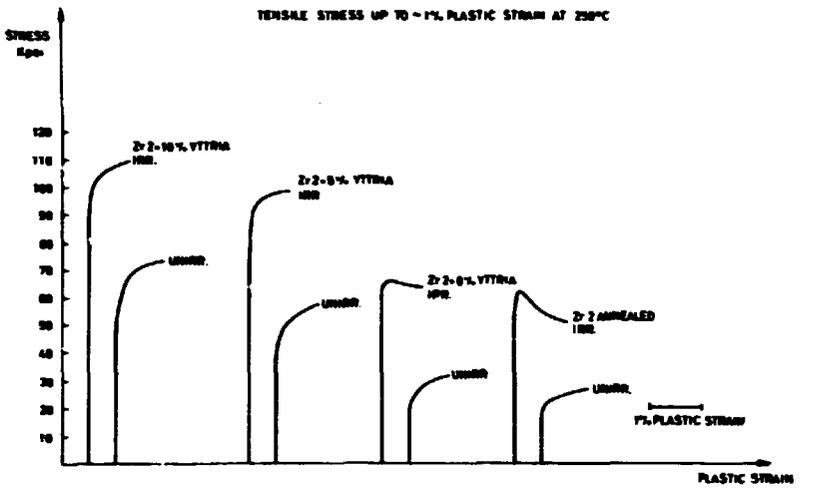

Fig. 7. Stress vs. plastic strain at 250°C in irradiated and unirradiated zircaloy-2 alloys.

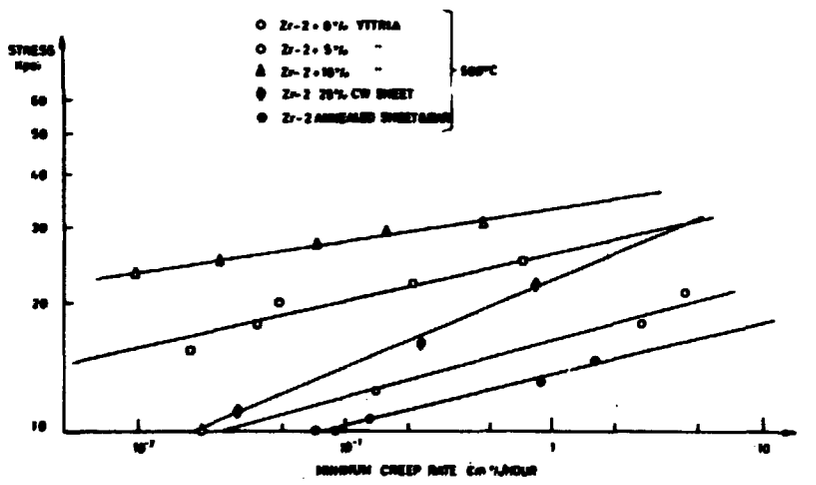

Fig. 8. Minimum creep rate vs. stress; 500°C.

CREEP RUPTURE PROPERTIES

Creep tests were carried out in vacuum on cylindrical specimens machined from extruded and stress-relieved rods.

The minimum creep rate was measured, and fig. 8 shows as an example the stress dependence of the minimum creep rate for zircaloy-2 alloys. The addition of yttria particles to zircaloy-2 significantly improves the creep resistance, and on comparison of the minimum creep rates obtained for yttria-containing alloys with those from cold-worked zircaloy-2 at 500°C[5], it is seen that much lower creep rates are exhibited by the dispersion-strengthened alloys.

The rupture lives of dispersion-strengthened alloys measured at 350-400 and 500°C proved superior both to cold-worked zircaloy-2 and to zirconium $2\frac{1}{2}$%Nb alloys, see figs. 9 and 10.

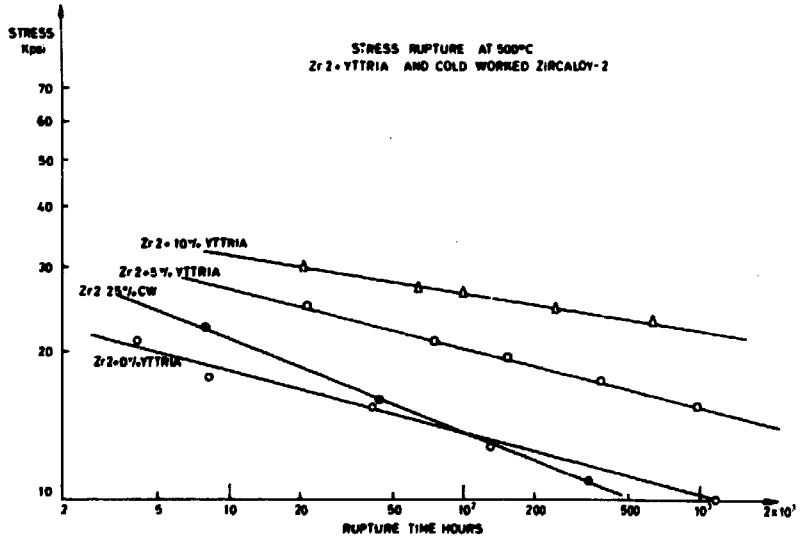

Fig. 9. Stress rupture at 500°C; zircaloy-2 + yttria and cold-worked zircaloy-2.

In fig. 10 the rupture lives of zirconium $2\frac{1}{2}$% Nb alloys (heat-treated) are compared with those of the dispersion-strengthened alloys at 450 - 500°C, and here the $2\frac{1}{2}$% Nb alloys show a much steeper slope than the dispersion-strengthened alloys, which indicates greater stability of the latter.

Contrary to many other dispersion-strengthened alloys zircaloy-2 + yttria alloys show excellent creep elongations, e. g. for a 10 v/o alloy the rupture elongation is about 30% at 500°C.

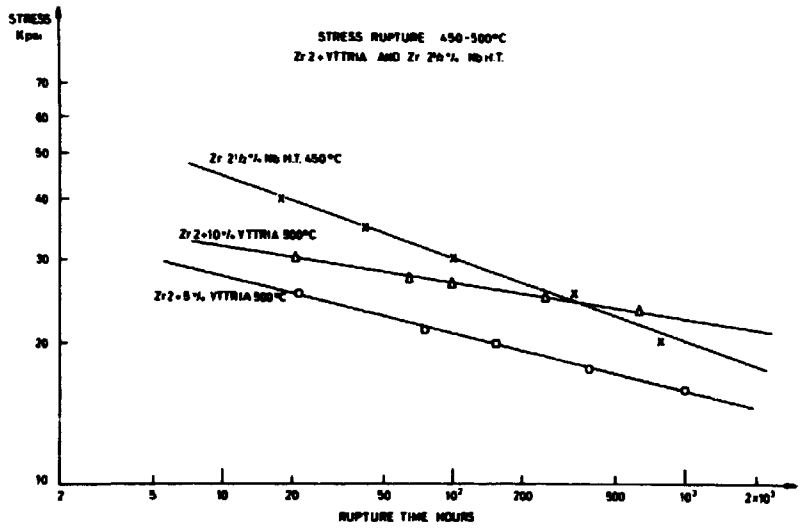

Fig. 10. Stress rupture at 450-500°C; zircaloy-2 + yttria and zirconium $2\frac{1}{2}$% Nb (heat-treated).

CORROSION

Specimens of dispersion-strengthened alloys containing 0, 5, and 10 v/o yttria together with commercial zircaloy-2 were subjected to corrosion testing in steam at 400°C and a pressure of seven atmospheres. The results of the test are shown in fig. 11. There were no substantial variations in the results obtained from powder-produced zircaloy-2 + 0 v/o yttria and from a conventional zircaloy-2 rod, and the results have been combined in one curve. Specimens from two batches of zircaloy-2 + 5 v/o yttria exhibit weight gains close to that of zircaloy-2. Specimens from the remaining batches showed poor corrosion resistance with a wide scatter in experimental results. The two batches of zircaloy-2 + 5 v/o yttria that showed good corrosion resistance also exhibited a black, adherent oxide film after corrosion testing, similar to that of commercial zircaloy-2. The surface

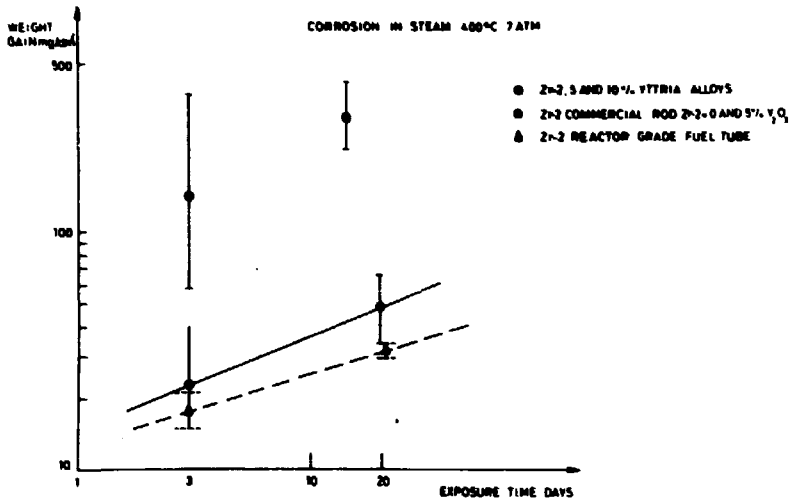

Fig. 11. Corrosion in steam - weight gain vs. exposure time.

of alloys from the other batches showed a black oxide film with white spots or stringers, and in the 10 v/o yttria-containing alloys a white oxide layer was formed. Comparisons between batches of zircaloy-2 + 5 v/o yttria alloys that exhibited widely varying responses to corrosion testing failed to reveal any obvious differences in the alloys which could be responsible for the variation in corrosion behaviour. It is possible that the concentration of dissolved oxygen and the solution of small amounts of yttrium metal varied from alloy to alloy, but such differences are difficult to measure accurately.

DISCUSSION AND CONCLUSIONS

The methods used to produce alloys of zircaloy-2 containing particles of yttria yield a material with a small-grained, continuous metal matrix and a uniform dispersion of small yttria particles.

The addition of the fine particles of yttria to a zircaloy-2 matrix results in significant increases in the 0.2% proof stress and the ultimate tensile stress. The increases are effective between room temperature and 600°C and continue to improve with the addition of yttria up to at least 10 v/o. The ultimate tensile strength in the region 300 - 350°C shows a marked superiority of the yttria-containing alloys over cold-worked zircaloy-2 and cold-worked zirconium $2\frac{1}{2}$% Nb alloy.

The lower creep rates, longer rupture lives, and good creep rupture ductilities obtained with the dispersion-strengthened zircaloy-2 + yttria alloys show that they have a clear advantage over cold-worked zircaloy-2. At temperatures of about 300 - 350°C the 10 v/o yttria alloy would compare to the stress rupture properties of zirconium $2\frac{1}{2}$% Nb alloy, but the yttria-containing alloys are shown to have better rupture lives at higher temperatures, i. e. 400 - 500°C. When irradiated at 280°C zircaloy-2 alloys containing yttria particles show a continuation in work hardening to greater plastic strains than alloys without yttria, which would be a beneficial property in fuel cladding.

Although corrosion testing in steam of zircaloy-2 alloys containing particles of yttria showed widely scattered results, the fact that some alloys containing yttria gave weight gains close to those normally observed for zircaloy-2, show that it would be possible to produce corrosion-resistant alloys containing dispersed particles of yttria. Thermodynamic consideration[6] of the stability of yttria in zirconium indicates that approximately 3000 - 4000 ppm oxygen is required in solution at 700°C for yttria to remain completely stable. Thus it is likely that the probable hypostoichiometry of yttria in zirconium with initially less than the equilibrium amount of oxygen needed for stability, combined with a small concentration of yttrium (also reported as increasing corrosion[7]), produce a reduced resistance to corrosion in steam. The above arguments are supported by preliminary experiments where the addition of oxygen to alloys which have high weight gains after exposure to steam results in a marked decrease in weight gains after corrosion testing.

The mechanical properties (strength, strain hardening, and ductility) before and after irradiation for yttria dispersion-strengthened zircaloy-2 alloys, indicate that the alloys might be considered for further development for use in nuclear components, provided the corrosion resistance can be improved.

ACKNOWLEDGEMENTS

The authors would like to acknowledge the contributions that E. Hindle, J.C. Balling Jensen, J. Kjøller, D. Marsh, D. Parsons, and E. Tolksdorf made to this work.

REFERENCES

1) N. Hansen, Dispersion Strengthening of Aluminium - Aluminium-Oxide Products. Acta Met. 18 (1970) 137-145.

2) J.K. Dawson, R.C. Asher, B. Watkins, J. Boulton, and J.N. Wanklyn, The Properties of Zirconium Alloys for Use in Water-Cooled Reactors. In: Proceedings of the 3rd International Conference on the Peaceful Uses of Atomic Energy, Geneva, 31 August - 9 September 1964, 9 (United Nations, New York, 1965) 461-467.

3) J. Winton, R.A. Murgatroyd, B. Watkins, and R.W. Nichols, The Strength of Zr-$2\frac{1}{2}$% Nb Alloy in the Annealed and Cold Work Condition. Trans. Japan. Inst. Met. 9, suppl. (1968) 630-636.

4) B. Watkins and R.E. Cockaday, The Development of Zirconium Alloy Pressure Tubes for the Winfrith Heath Steam-Generating Heavy-Water Reactor. TRG - Report - 998 (c) (1965) 18 pp.

5) F.R. Shober, J.A. Van Echo, L.L. Marsh, and J.R. Keeler, The Mechanical Properties of Zirconium and Zircaloy-2. BMI - 1168 (1957) 50 pp.

6) J. Rezek and B.G. Childs, Structure and Properties of Yttria-Zirconium Dispersions. J. Nucl. Mater. 26 (1968) 285-299.

7) H.H. Klepfer, Zirconium Alloys for Steam Service. A Preliminary Study. GEAP - 3462 (1960) 63 pp.

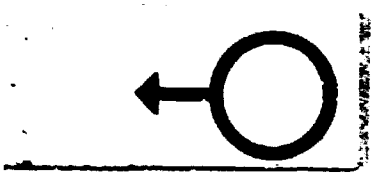

Experiments on Data Presentation to Process Operators in Diagnostic Tasks

by

Jens Rasmussen and L. P. Goodstein
Electronics Department

Abstract

Safety and reliability considerations in modern power plants have prompted our interest in man as an information receiver - especially in diagnostic tasks where the growing complexity of process plants and hence the amount of data involved make it imperative to give the staff proper support. The great flexibility and capacity of the process computer for data reduction and presentation and for storing information on plant structure and functions give the system designer great freedom in the layout of information display for the staff, but the problem for the designer is how to make proper use of this freedom to support the operators efficiently. This is especially important in connection with unique, high-risk, and generally improbable abnormalities in plant functioning.

Operator tasks and mental models and the need for matching the encoded information about the plant to these models are treated. Mention is made of scant information available to the designer and the difficulty involved in performing experiments in a realistic environment. Results from the use of verbalization techniques in an electronics maintenance shop in order to gain insight in the structure of mental procedures are described, and the paper concludes with a discussion of experimental work in display coding and formatting being carried out at the DR 2 reactor.

1. INTRODUCTION

Safety and reliability considerations in modern power plants prompted our interest in man as an information receiver in diagnostic tasks. Although power plants are amply protected by automatic safety systems, we found that there are critical periods during which plant safety to a considerable degree depends directly upon supervision and protection by the operating staff. Examples are initial plant start-up, re-start following major repair or modifications, etc. After such periods the plant may be left in an unsafe condition, not covered by the automatic protection system.

When abnormal plant conditions are detected during these phases, the staff has a diagnostic task which is, in fact, a very complicated data processing job, and it becomes increasingly important to give the staff proper support in view of the growing complexity of process plants and hence the amount of data involved in the task.

The great flexibility and capacity of the process computer for data reduction and presentation and for storing information on plant structure and functions give the system designer great freedom in his layout of information display for the operating staff, but the problem for the designer is how to make proper use of this freedom to support the operators efficiently.

2. OPERATOR TASKS AND MENTAL MODELS

The process plant operator works in a symbolic world. His task is to select relevant data from the multitude of data presented to him, to decode the information, and to transform it into a set of manipulations appropriate to the current plant condition.

During this task he needs not only the relevant set of data, but also a decoding and transformation model as well as a data handling procedure. Therefore it is important that the encoding of the data presented - i. e. the display formats or layouts - fits the operator's decoding models or allows him to form models and procedures well within his mental and perceptual capacity. The mental models and procedures of the operator are in some way modelling system information which describes plant responses and/or plant structure and internal functioning.

The problem of the designer is that the system information used by the operator is not only that supplied by the designer in the form of manuals, instructions, and education of the operator, but is also to a high degree extracted from the system itself by the operator as he acquires his extensive

operating experience. The basic difference is that system information used by the designer is related to internal system functioning, while the information forming the operator's experience is related to the external responses of the system.

One major experience from our studies and discussions with designers and operators has been the great discrepancy between the actual procedures or transformation models used by the operators and the imagining of these procedures by the designers at their writing desks.

For example, we find data presentation by digital indicators or alphanumeric listings on CRT's, as commonly found in computer-controlled display systems, a bad substitute for conventional operator consoles in many operating conditions. In the latter case, the operator normally does not read the instruments, but merely judges the position of the pointers. In addition, the geographical distribution of meters and indicators relates data to plant structure, and properly arranged groups of meter readings are viewed as patterns.

The problem of the display designer is further complicated by the fact that the conceptual transformation models and procedures used by the operator will be different under the different working conditions.

In frequent, recurrent tasks, the operator may be expected to work from "the expression on the face" of the system; that is, to apply subconscious procedures based upon recognition or experience. Ilis data handling may be likened to high-capacity parallel processing in his "peripheral system" (as in car driving), whereas, in infrequent or unique diagnostic situations, he will have to place his attention inside the system and relate his procedures to the internal functioning of the system by careful and sequential data handling in his slow, low-capacity, conscious "central processor".

If the coding and formatting of the data sets presented to the operator are to fit his procedures and models, they will have to vary greatly in the different operating situations. No one would expect the same coding of data to be appropriate for the ordinary driver's control panel in a car and for advanced diagnostic instrumentation in a test station for cars. Yet the operator's console in most process plants has to fit both types of needs. As mentioned above, the nature of the system information used by the operator to relate plant response to his manipulations is related to the frequency of the events and may have elements of subconscious training, experience from previous cases, instructions and station orders worked out by designers for infrequent but foreseen events, and - in extreme cases of unforeseen and generally improbable situations - his actions must be based on

familiarity with plant anatomy and its physical functioning.

In our context of plant safety, we have a special interest in diagnostic procedures during events implying high risks - which, in well-designed plants, are those of very low frequency - i. e. the generally improbable, unique events. While the great adaptability of man will very often reduce the importance of a proper layout of displays in recurrent and familiar tasks, the coding and formatting of displays may be very important in connection with the unique, high-risk events. Very little information is available to a display designer about mental models and procedures used by system operators in real-life environments, and we therefore have an experimental programme to supply us with such information.

3. MAN AS INFORMATION RECEIVER

We found that a reasonable way to gain insight into the structure of the mental procedures used by the operator was to ask him to verbalize his thinking.

Owing to the low frequency of events calling for real diagnostic procedures and the stress laid upon the operators when paced by the dynamics of a plant, it is difficult to perform experiments in an actual control room environment.

We therefore found it convenient to carry out preliminary experiments in an electronic maintenance shop in order to test out methods for recording and analysing verbalized records and to have an indication of the more basic features of man in a realistic diagnostic task.

Of course, detailed results from such experiments are not directly applicable to the control room environment, but some of the more general results may be helpful in display coding and for future experiments in the control room. This will be discussed later.

For the experiments we selected electronic systems with fairly complex displays, which permitted a rather close localization of the fault by rational deduction from the information available from the external response of the system. These systems included TV-receivers, oscilloscopes, and multi-channel analysers.

The procedures found will not be discussed here; a review[1,2] is published elsewhere, and some conclusions relevant to the present discussion will be presented here instead.

When a diagnostic task is not characterized by mere recognition of the faulty system response, the search for the fault is a multiple task.

The man has to collect data sequentially and control the route of search; he has to maintain or establish an overall conceptual model of the system and the interconnections of its subsystems. He has to identify the proper sources of the data needed amongst the many sources of data available. To judge the data, he has to establish a conceptual model of the related equipment at a more detailed level, and, finally, he has to keep track of his overall plan for the diagnosis.

In our studies we found - as could be expected - that difficulties in one of the subtasks may impair the performance in the other tasks greatly, and from this we drew two conclusions:

One is that great care should be taken when generalizing from clear-cut laboratory experiments with special equipment which strips all secondary or seemingly trivial activities from the main diagnostic task.

The other is that when using computer-controlled displays, not only the data should be presented to the operator as is done in alphanumeric listings or digital indicators, but the data should in some way be related to plant anatomy in order to support the operator's conceptual models. In conventional control rooms this is to some extent done by proper geographical layout of meters, indicators, and alarm panels.

Although response data in our experiments were clearly available to and observed by the man, making it possible to locate the fault by a rational deductive analysis of the data and the relationships between them, the actual search procedure was normally based upon rapid streams of simple good/bad judgements made on the data individually.

Considering the difficulty of keeping track of the different subtasks, this seems quite reasonable since the procedures used do not call for high short-term memory capacity. This may also be an important feature of the corresponding procedures followed in stressed control room operations. It seems to be convenient for the man to map the system by means of good/bad judgements. However, when information has been treated in these judgements, only the result - good or bad - seems to be remembered, and the original information is discarded and not later recalled for further control of the search.

Again, it is to be expected that presentation of accurate information in digital form will not in many circumstances be of great help to the operator. He should rather be given data in analogue form including reference to normal data in some sort of graphic, symbolic display.

We found that a general rule controlling the search procedures seems to be that as soon as information is perceived which refers to a procedure

of search normally found to be successful, attention is switched to this procedure, even though information is also clearly available showing either that the procedure will be inefficient in the actual case, or indicating the possible existence of a short-cut method, if the situation is more carefully considered.

As discussed by Bartlett[3], there seems to be a point of no return in the operator's attention to data. As soon as a familiar routine is found to be waiting ahead, this prevents further use of the information in the data currently treated.

To us this indicates that data should be presented or be available to the operator in clearly formatted sets or patterns related to relevant systems and operating conditions, to force the operator to include all pertinent information in his initial hypothesis rather than in the form of information in alphanumeric listings calling for sequential reading during which the operator's attention may switch to a familiar procedure involving an inadequate subset of data.

In our studies, as in other published experiments[4], operators have demonstrated a marked tendency to hang on to procedures they have normally found successful and, when in trouble, they have tried to repeat these procedures more carefully instead of returning to the original information at the starting point and considering it with a more open mind.

This may be an important point to consider in plant environments since poor data presentation may cause the operator to spend too much effort in considering familiar procedures related to familiar subsets of the data presented.

This tendency may be countered if automatic data and alarm analysis by a computer are used to classify plant conditions, group data in relevant sets, select and edit display formats, and relate data to plant structure.

The general diagnostic procedures found in our experiments may seem inefficient if the man is supposed to minimize the number of decisions necessary in order to be rational, informationally speaking. If, however, he is supposed to minimize the time generally needed to identify the system condition by use of procedures based upon operating experience and well within his limits for short-term memory and inference, the procedures are highly efficient, except in very infrequent cases.

The influence from man's objectives and from the cognitive strain upon his choice of procedure has been treated thoroughly in the experiments on concept formation by Bruner et al.[5].

4. EXPERIMENTAL WORK ON DISPLAYS

As mentioned earlier, very little information is available to process plant designers about the functioning of the human operator in the control room. As a step towards increasing the available information, a computer-controlled instrumentation was developed and is running "on-line" at the DR 2. This instrumentation includes a control console with an advanced display facility for conducting experiments in display coding and formatting and interactive data retrieval (see fig. 1).

The console forms the basic man - machine interface of the digital instrumentation system. It will be used by both engineering and operational personnel under all conditions of reactor operation in an environment which could be said to approach the "industrial". It should be stressed that the console performs only a display function; basic reactor monitoring and control are carried on from the existing control room.

The control console is equipped with several types of display equipment. The most prominent and important is the cathode-ray-tube (CRT) display which comprises three tubes - two large conventional ones and one small storage tube. These are driven from two display processors with associated character generators. The computer can communicate with each display processor and cause any desired pattern of lines, curves, dots, and characters to be generated on the CRT's. By splitting the screen of the two large tubes into a right and a left half via programming, a total of five different pictures can be maintained simultaneously. In addition, there are two digital displays, a status display, four keyboards, and a light pen. However, the point is not the quantity of equipment, but the uses to which it can be put to satisfy the various needs for information coded in an effective manner for the tasks at hand. The digital displays and the five selectable CRT pictures are meant to serve as a compressed and integrated substitute for the large panorama of displays, controllers, meters, and recorders found in present-day control rooms.

The strategy intended for use here is that of using the various CRT pictures as a supplement to the normal alarm system to give the operator the information he needs to formulate his diagnosis. Whereas, at present, his survey consists in running his eye over many square feet of control room panels, the operator substitutes, in our system, a sequence of "picture select" and "examine" operations. In a conventional plant he gets his detailed information by walking over to a particular meter or recorder;

with the control console the operator can use the light pen or keyboards to get the same information.

It is appropriate to say here that our first efforts in display formatting were directed at retaining commonly used data types and symbols - such as the equivalent of meter pointers and faces, mimic panels, text, etc. - and using them within the framework of the CRT display. A later step, based on experience and further experimental work, might be to broaden the spectrum of symbolics for better matching to the operator's peripheral system.

5. OPERATION

If a process status change is detected, several things occur automatically:

A bell sounds, and the appropriate status display window - pinpointing the affected reactor sub-system - blinks to indicate whether a new alarm has been detected, or whether a previous alarm has become normal again.

In addition, the detected status change and the time are listed automatically in text form on one of the CRT half sectors. The original presentation is lost until the operator acknowledges the change.

Multiple status changes will appear on the CRT in order of detected occurrence, and each will give rise to an appropriate indication on the status display. No kind of pre-processing of alarms is performed at the present time.

On the basis of this initial information - i. e. affected reactor sub-system(s) and channel numbers within the sub-system - the operator can now seek further information from the display system. By use of either of two "CRT Display Select" keyboards, he can build on the four CRT sectors the set of process status information he feels is best suited to the existing situation.

Figures 2 to 4 illustrate several of the CRT display formats used at the present time. A short description is included with each figure. In general, they are analogue in form to permit quick comparison of actual multi-parameter-process information to be made with a reference pattern existing in the operator's mind for the particular sub-system. Rather than accuracy, capability of inspiring a quickly grasped appreciation of the actual situation is required.

The light pen can then be used in several ways to request further information via the analogue presentation. For example, by pointing first to the dot inside any desired variable-indicating diamond, box, arrowhead, cross, etc., and then to one of the light dots on the screen, an updated digital value for the selected channel will be displayed.

The operator can also request "trend" information for any two (at one time) of the displayed process variables on any one of several time scales by means of similar light pen and keyboard operations. These curves, which can give valuable insight into plant behaviour up to the present moment, will appear automatically on the other half of the "requesting" screen. Use of the light pen on a "trend" curve will permit the recovery in digital form of any desired point on the curve. This can be useful in, for example, post-incident analyses.

In this way, the operator has easy access to detailed data through the selected sub-system analogue display, but he is actually forced to examine a significant part of the process behaviour before gaining this access. He is thus somewhat more restricted in the automatic reflex type of reaction he can make which, for example, might limit his attention to a minimum set of probably inappropriate variables or instruments when a true emergency arises.

The light pen can also be used to change alarm limits. Most analogue process variables have associated high and/or low alarm references which are used by the computer programme to check the status. Some of these references are fixed by the designer, and others can be adjusted to match operating conditions. This can be especially useful during commissioning or repair. Alarm limits are displayed as short horizontal line segments. If the light pen is pointed at the desired limit, two extra lines appear automatically, one above and one below the existing line, corresponding to a $\pm$ 5 to 10% spread. The limit line segment will then blink. Moving the light pen up or down results in the set of added bound-lines following. When the desired value is reached, the "GO" key is pressed, the new alarm value is accepted (various criteria can be employed here) and inserted in the appropriate lists in store, and the display is adjusted to show the limit in its new position without the two extra bounds.

Although the present system capability is limited to display and process information retrieval, there is no technical reason for not employing the light pen (or some similar device) to take any ultimate control action that may be required.

In conclusion, a few words about the future programme. The operating staff of the DR 2 will soon begin to use the control console to follow start-ups and shut-downs of the reactor. We are very interested in obtaining their comments on and criticism of the operation of the system. It will also be possible to use the computer to measure quantitatively the operators' utilization of the various console features under the various reactor operating conditions.

The department is also about to acquire an off-line interactive display terminal which, among other things, can be used for investigating more restricted problem areas which arise from the experimental work. For example, future work will deal with a more fitting format for alarm presentation which we feel should tie the alarm situation more closely to the anatomy of the plant, a feature which alphanumeric text listings do not offer.

REFERENCES

1) Jens Rasmussen, Man as Information Receiver in Diagnostic Tasks. In: Conference on Displays, Loughborough, 7 - 10 September 1971. (IEE Conference Publication No. 80), (Institution of Electrical Engineers, London, 1971) 271-282.

2) Jens Rasmussen and Aage Jensen, A Study of Mental Procedures in Electronic Trouble Shooting. To be published.

3) Frederic Bartlett, Thinking. An Experimental and Social Study. (Unwin University Books, London, 1958) 203 pp.

4) Abraham S. Luchins, Mechanization in Problem Solving. Psychological Monographs 54 No. 6 (1942) 95 pp.

5) Jerome S. Bruner, J.J. Goodnow, and G.A. Austrin, A Study of Thinking. (John Wiley, New York, 1967) 330 pp.

6) L.P. Goodstein, Operator Communications in Modern Process Plants. In: Conference on Displays, Loughborough 7-10 September 1971 (IEEE Conference Publication No. 80) (Institution of Electrical Engineers, London, 1971) 149-153.

Fig. 1. Control Console.

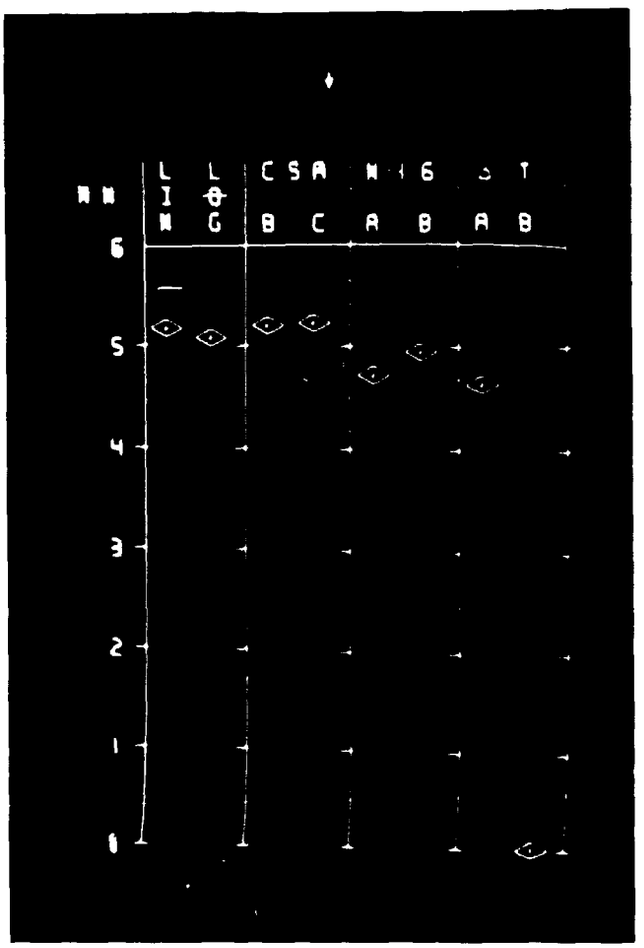

Fig. 2. Reactor power at "full power". Channels corresponding to three different methods of measuring power are displayed simultaneously. A typical analogue survey presentation.

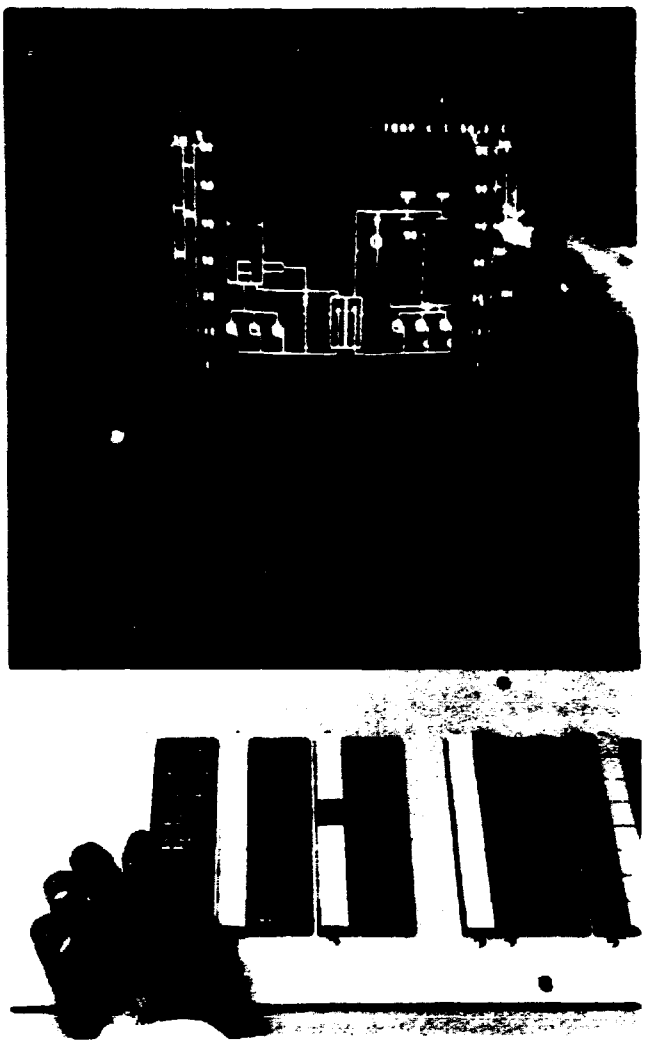

Fig. 3. Reactor sooling system. Quantitative data on temperatures, flows and water level are combined with a symbolic representation of the reactor core, cooling pumps, heat exchanger, cooling tower, and blowers. On/off status of pumps plus cooling fan speeds are included. A portion of the "display select" keyboard and the light pen can also be seen.

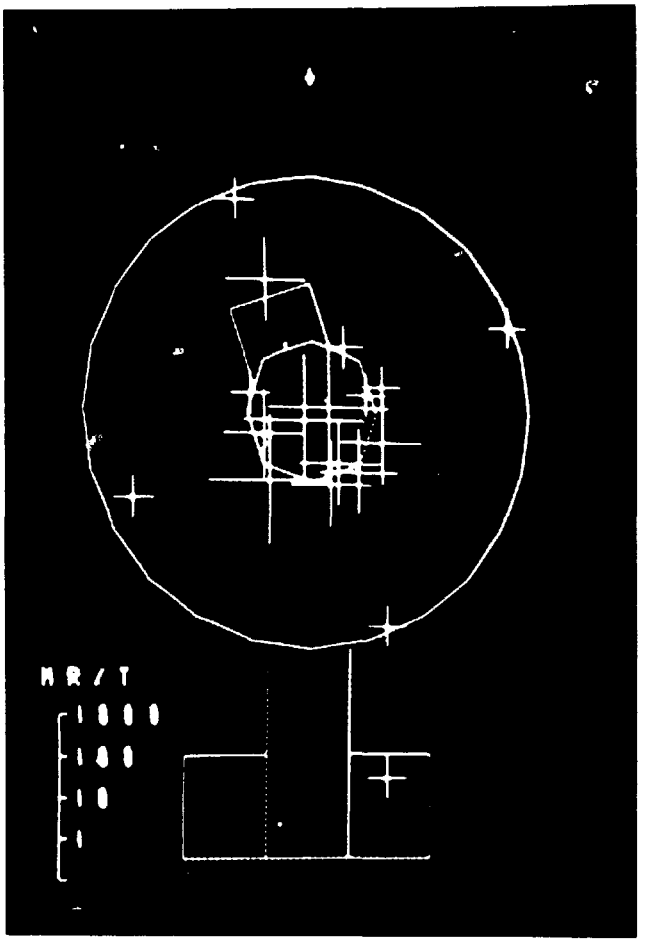

Fig. 4. A symbolic representation of the DR 2 reactor hall and cellar with a radiation detector located at the centre of each cross whose length is proportional to the radiation intensity measured at the detector. The included scale allows a rough quantification to be made.

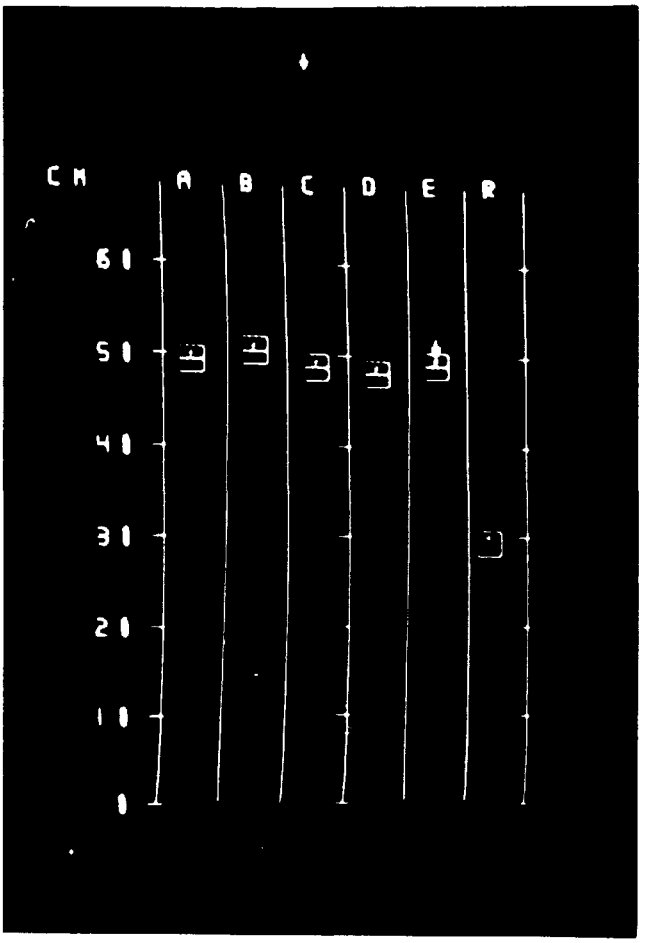

Fig. 5. Survey of the reactor control rods. Each rod has a magnet (upper rectangle) which holds the rod (lower rectangle). Movement of the rods is indicated approximately by the arrows.

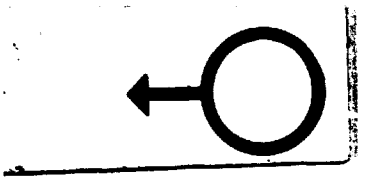

Analysis of Metallic Ores by Radioisotope--Excited X-ray Fluorescence

by

L. Løvborg and H. Kunzendorf

Electronics Department

Abstract

The principles and techniques of X-ray fluorescence analysis using radioisotope excitation sources and energy-dispersive methods of X-ray detection are explained. The performance of the measurement method for the determination of metal contents in metallic ores is illustrated by examples, which include the use of portable equipment and semiconductor-detector X-ray spectrometers.

1. INTRODUCTION

X-ray fluorescence analysis (XFA) is a technique for multi-element analysis of a variety of materials. The method is based on the fact that each element has a characteristic spectrum of fluorescent X-radiation which can be excited by means of a suitably chosen source of ionizing radiation. The equipment used in ordinary XFA comprises an X-ray tube and a wavelength-dispersive X-ray spectrometer (Bragg spectrometer). Because the operation of an X-ray tube presupposes a supply of high-voltage power and cooling water, and because a Bragg spectrometer is a fairly delicate and complex device, ordinary XFA can only be used under well-equipped laboratory conditions.

The need in the mineral exploration and exploitation field for a method permitting assessment of metallic ores in the rigid environment presented by an exploration area or a mine resulted in 1965 in the development of a portable, rugged X-ray fluorescence analyser[1]. In this and similar instruments, which are now commercially available, the X-ray tube and its ancillary units have been substituted by a small-sized, radioactive source, and energy-dispersive techniques are used for the measurement of the characteristic K X-rays emitted by the metals sought after. Radioisotope XFA carried out with portable equipment is basically a single-element method of analysis, as the equipment must be adjusted to register a narrow range of X-ray energies. The limit of detection which can be obtained with portable XFA instruments is of the order of 0.1% metal content[2].

Another kind of radioisotope XFA, whose applicability to the mining industry seems promising, is based on energy-dispersive X-ray spectrometry using lithium-drifted semiconductor detectors. The good energy-resolution which can be obtained with such detectors (less than 0.5 keV), makes it possible to design XFA systems for multi-element analysis of rocks and ores. At present such systems can be used for the determination of most metals with $Z > 15$, and they permit metal contents in the tens of ppm region to be detected[3].

In this paper the authors wish to outline the techniques of radioisotope XFA with a view to its application to the analysis of metal content in ores. We shall illustrate the performance of the techniques by giving examples from our studies in connection with mineral exploration in Greenland.

2. PRINCIPLES AND TECHNIQUES

2.1. X-Ray Fluorescence

X-ray fluorescence can be produced by means of ionizing radiation whose energy exceeds the binding energy of a K electron belonging to an atom of the element of interest. An atom from which a K electron has been ejected is only stable for about 10^{-15} s, after which the missing electron in the K shell is replaced by an electron from one of the other electron shells. Most likely, an L electron is transferred to the K shell, leaving a hole in the L shell. This hole is in turn occupied by a subsequent electron transition to the L shell, e.g. from the M shell. This sequence of events continues until the atom is left in a stable condition, the possible electron transitions being governed by the selection rules: $\Delta l = \pm 1$, and $\Delta J = 0$ or ± 1.

The energy released by the sequence of electron transitions is either emitted in the form of X-rays (X-ray fluorescence) or used for the ejection of outer orbital electrons (Auger effect), the fraction of produced X-radiation (the fluorescence yield ω) being an increasing function of the atomic number Z.

2.2. XFA

The K X-rays resulting from electron transitions to the K shell are the ones mainly used for the determination of elemental abundances by XFA. The fact that the energy of the predominant K_α X-rays (the radiation emitted as a result of L-K transitions) approximately varies as Z^2 (Moseley's law) makes it relatively easy to identify and assay an element from a measurement of the energy and intensity of its characteristic fluorescent K_α X-radiation.

Certain difficulties arise, however, in XFA of materials which are composed of many elements, e.g. rocks and ores. Firstly, the K_α X-rays from the element(s) of interest may be more or less obscured by fluorescent or scattered X-rays introduced by the other elements in the sample material. Secondly, the degree of absorption of the K_α X-rays in the sample material depends in a complex manner on the physical form and the chemical composition of the sample. These error sources (inter-element and heterogeneity effects) can be reduced or eliminated by the use of special sample preparation methods or by means of sophisticated computational correction methods. Neither of these techniques are consistent with the aim of radioisotope XFA,

the justification of which lies in its wide adaptability and ease of operation. Instead, one generally prefers to make use of calibration curves which pertain to the particular material under investigation, e.g. a specific ore type in pulverized or solid form.

2.3. Radioisotope Sources

The fluorescent K X-radiation of an element is most efficiently excited by means of electromagnetic radiation, the energy of which just exceeds the K-electron binding energy. As it is of great importance to reduce to a minimum the amount of backscattered radiation from the sample material, an excitation source which emits mono-energetic photons is generally preferred. Only a very limited number of sufficiently long-lived radioisotopes emit abundant, low-energy photon radiation. The five sources most commonly used for the production of radioisotope-excited X-ray fluorescence are given in table 1.

Table 1

Commonly used radioisotope sources for the excitation of fluorescent K X-radiation in ore metals

Radio-isotope	Half-life (years)	Decay mode	Typical source strength (mCi)	Energy (keV) and kind of radiation used	Usable for the determination of
^{55}Fe	2.7	E.C.	5	5.9 Mn K_α X 6.4 Mn K_β X	Ti, V, Cr
^{238}Pu	86.4	α	30	13.5, 15.4, 17.2 U L X	Fe, Co, Ni Cu, Zn
^{109}Cd	1.3	E.C.	3	22.1 Ag K_α X 25 Ag K_β X	Zr, Nb, Mo
^{241}Am	458	α	10	59.6 γ	Ag, Sn, Sb rare earths
^{57}Co	0.7	E.C.	1	122, 136 γ	W, Pt, Au Hg, Pb

The excitation efficiency which can be obtained by means of the radioisotope sources given in the table strongly depends on the difference between the source energy and the energy of the K absorption edge of the metal whose K X-rays are to be excited. For instance, the 17.5 keV K_α X-rays of Mo are very efficiently excited with the 22 keV Ag K_α X-rays following the decay $^{109}Cd \xrightarrow{E.C.} {}^{109}Ag$, while the 25 keV K_α X-rays of Sn are poorly excited with the 60 keV γ-rays following the decay $^{241}Am \xrightarrow{\alpha} {}^{237}Np$. Nevertheless, the five radioisotopes mentioned in table 1 suffice for the determination of most ore metals by radioisotope XFA.

2.4. Portable Instruments

In a portable XFA instrument the K_α X-rays of the metal searched for are isolated from other possibly excited X-rays by means of a pair of balanced X-ray filters.

An X-ray filter consists of a thin layer of material having a high abundance of a particular element with K absorption-edge energy E_K. The effect of the filter is described by the equation

$$T(E) = \exp[-\mu(E)\rho t],$$

where T(E) is the relative transmission of the filter for X-rays with energy E, and where $\mu(E)$, ρ, and t are the mass-absorption coefficient, the density, and the thickness of the filter material. Owing to the abrupt change in $\mu(E)$ for $E = E_K$, a distinct filter action is obtained for X-rays whose energies fall on either side of E_K. Fig. 1 shows the variation of $\mu(E)$ for Y and Zr across the respective K absorption-edge energies (17.0 and 18.0 keV). The interval delineated by these energies encompasses the K_α X-ray energy of Mo (17.4 keV). A passband for the isolation of Mo K_α X-rays can therefore be realized if the thicknesses of the Zr and Y filters are adjusted so that their relative transmissions are made equal outside the passband.

The configuration of the excitation source, filter pair, and X-ray detector normally used is shown in fig. 2(a). To facilitate operation under field conditions, these components are usually contained in a probe unit in which the filter pair is pivotally mounted in a spring-loaded tray so that the two filters can be quickly interchanged. The counting of X-rays is carried out by means of a rugged, battery-operated scaler unit in which the result of a counting appears in the form of luminous figures. Portable XFA instruments, which weigh less than ten kg and are adaptable to field analysis of a variety of ore metals, are commercially available.

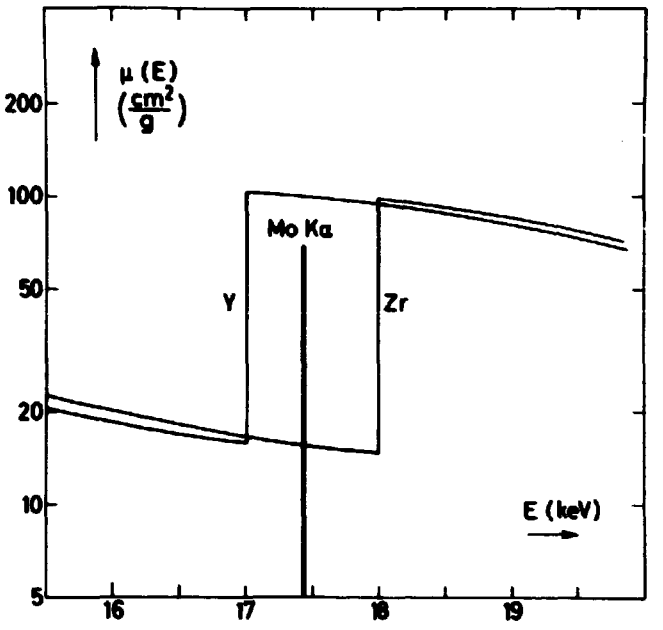

Fig. 1. Mass-absorption coefficient versus X-ray energy for Y and Zr. The figure explains how a balanced filter can be constructed for the isolation of Mo K_α X-rays.

In order to determine a given metal, the appropriate excitation source and filter pair must be installed in the probe unit, and an optimum setting of the single-channel analyser in the scaler unit must be found. An ore assessment comprises two successive countings, each typically lasting ten seconds, one using the filter with the highest E_K energy, the other using the other filter. Since the difference between the two counting results is a (linear) measure of the metal content in the ore sample, this content can be determined from a suitably constructed calibration curve.

2.5. X-Ray Spectrometers

The configuration of an energy-dispersive X-ray spectrometer system is indicated in fig. 2(b). The basic element of the system is a Si(Li) or Ge(Li) X-ray detector a few mm thick and cooled to a temperature of about -190°C by means of a cryostat and a supply of liquid nitrogen. The weak signals given off by the detector are amplified in a charge-sensitive, low-noise preamplifier and then fed to a multichannel analyser with a core

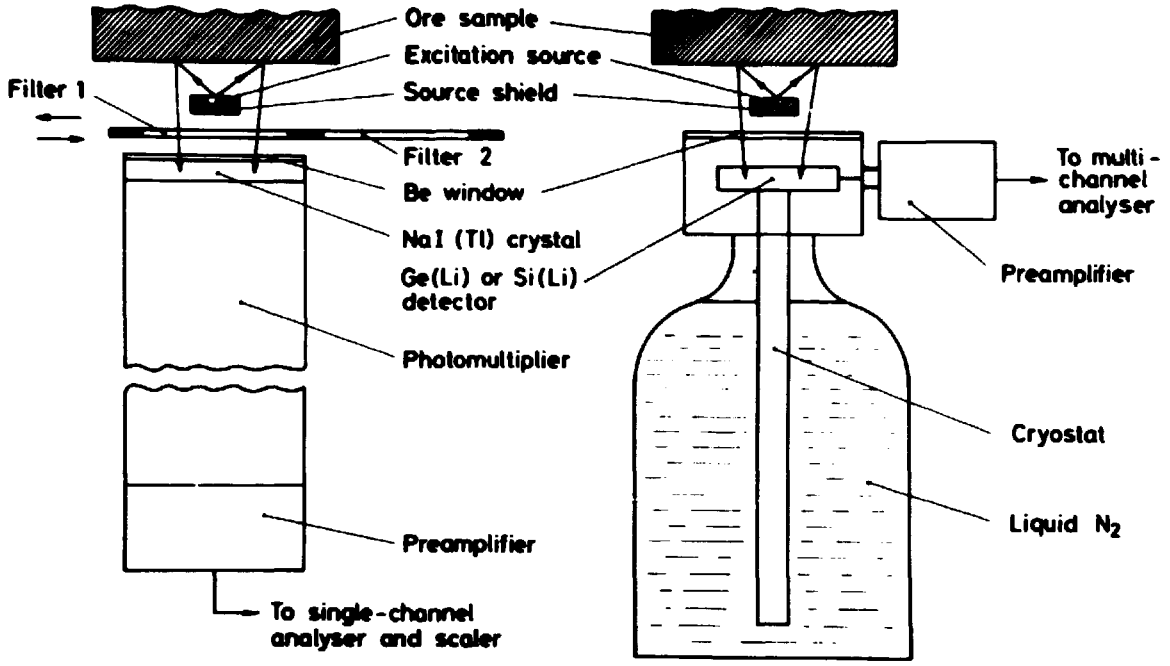

Fig. 2. Schematic diagram showing the principle of metallic-ore analysis by means of portable instruments (a) and X-ray spectrometers (b).

memory of at least 512 words. The applicability of the system to elemental analysis by XFA is based on the fact that the spectrum recorded with the multichannel analyser is a close reproduction of the energy spectrum of the fluorescent X-radiation excited in the sample.

Fig. 3 shows the spectrum of a powdered rock specimen containing 0.56% Zr and 0.07% Nb. The spectrum was recorded by means of a Si(Li) detector 3 mm thick and with a diameter of 6 mm, and having an energy resolution of 260 eV in the detection of 6 keV X-rays. The K_α and K_β X-rays of Zr and Nb are readily distinguished in the spectrum. Furthermore, the fact that the K_α X-rays of Rb and Y are also detected reveals the presence of these elements in the sample.

The determination of metal contents from a measured X-ray spectrum can be made by the solution of a system of linear equations which relate the metal contents to the count rates in energy intervals centred at the K_α peaks

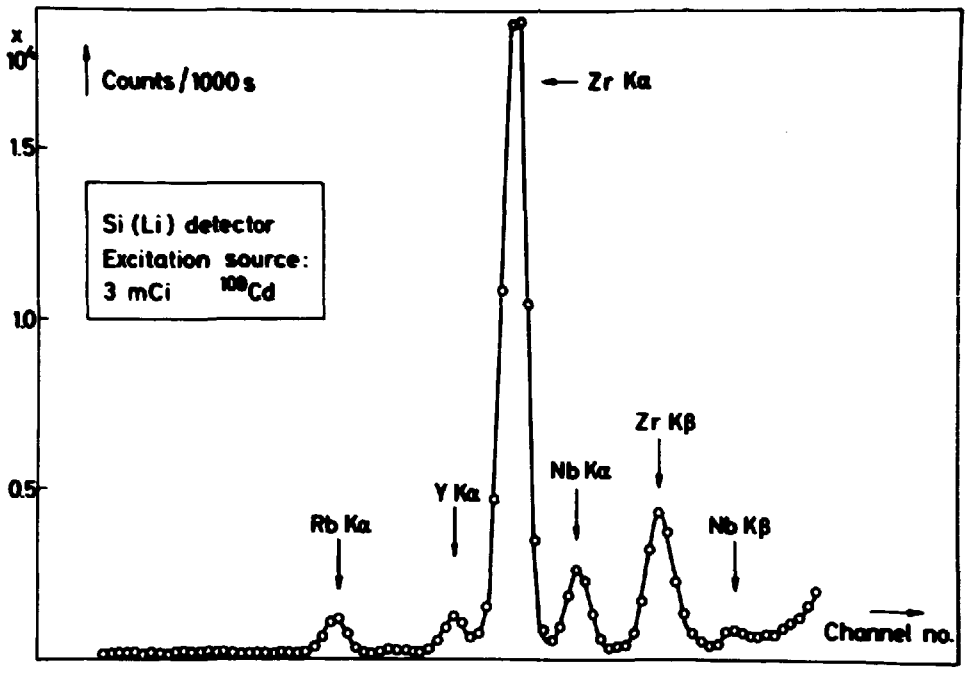

Fig. 3. The X-ray energy spectrum of a pulverized rock specimen containing 0.56% Zr and 0.07% Nb. The spectrum was recorded by means of a multichannel analyser with a core memory of 1024 words.

of the metals. Or one can make use of the least-squares method to fit the spectra of a series of carefully selected standard samples to the spectrum of the unknown sample. In both cases one must consider the possible error sources mentioned in subsection 2.2. Most conveniently, the processing of the X-ray spectra is done on a digital computer which may form part of the multichannel analyser itself.

3. APPLICATIONS

The authors began their studies of radioisotope XFA in 1968 with a view to using this technique in prospecting for metalliferous ores in Greenland. The investigations summarized here comprise

a) An evaluation of detection limits in the analysis of powdered metallic ores by portable XFA equipment.

b) The application of portable XFA equipment for the direct analysis of exposed rock surfaces.

c) The use of a Si(Li) X-ray spectrometer for the determination of low contents of various ore metals.

Most of the results and conclusions given have been reported in greater detail in the literature cited in references[4 to 7].

3.1. Analysis of Powdered Ores

Samples of eight different metallic ores, most of which derived from Greenland, were crushed and finely ground. Powdered samples showing a sufficiently great variation in their respective metal contents were not further treated, whereas samples having a limited range of metal contents were used for the preparation of new samples containing various amounts of powdered, non-metalliferous material. The added material either consisted of granite ($\overline{Z} \simeq 10$) or gabbro ($\overline{Z} \simeq 12$), depending on which of these two rock types most closely fitted the natural host rock of the ore. About 50 g of each sample was poured into a sample container, the bottom of which consisted of a thin melinex film, and the sample was placed on the top of the measuring head of an Ekco Mineral Analyser. By means of a suitable excitation source (table 1) and filter pair (table 2), the difference count rate from each sample was measured three times. Before each of the two last measurements the sample was poured out of the sample container and back again.

A detection limit for each of the nine measured metals was estimated on the assumption that the average difference count rate is a linear function of the metal content if the latter is sufficiently low. Fig. 4 shows the corresponding regression line for Mo and its 95% confidence limits. In connection with the use of the regression line, we understand by "detection limit" the minimum content of Mo that must be present in a sample to ensure that there is only 2.5% probability for not detecting any Mo in the sample. Combining the calculated variances of the calibration constants a and b with the variance of the difference count rate y, one is able to assign 95% confidence limits $x \pm \Delta x(y)$ to any estimated Mo content $x = (y-a)/b$. The detection limit x_d is given by the condition $x_d = \Delta x$, and it can therefore be determined graphically as indicated in fig. 4.

The estimated detection limit for Mo, 0.03%, is low enough to make the instrument used practically applicable, as the economic cut-off limit in the mining of Mo ore is typically 0.1%. A lower detection limit could have been obtained if more samples with very low contents of Mo had been used for calibration of the instrument. The use of a better balanced filter

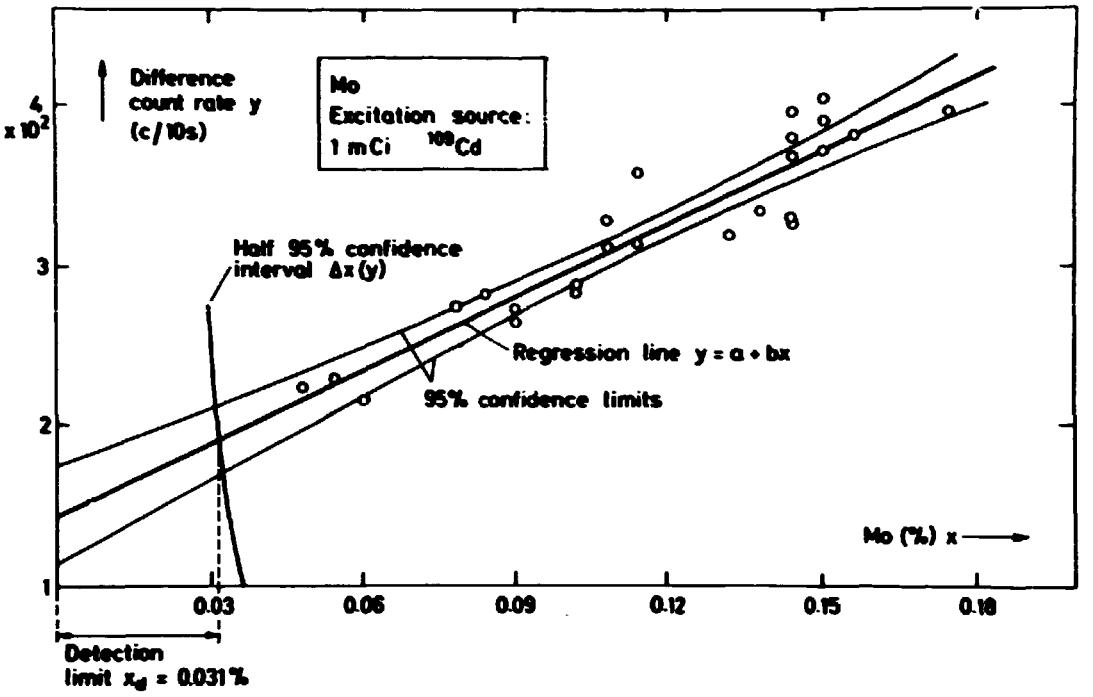

Fig. 4. Evaluation of the detection limit in the analysis of pulverized samples of Mo ore by means of portable XFA equipment. The detection limit is given by the condition $x - \Delta x = 0$ where Δx is the half 95% confidence interval for x when y is known.

pair (one yielding a lower zero count rate a) would also result in an improved detection limit.

The detection limit determined for the other eight measured metals can be found in table 2 (La + Ce is considered as one metal). The table may serve as a guide to the performance of portable XFA equipment, but we emphasize that the actual detection limit of such equipment depends both on the composition of the particular ore type to be assayed and the calibration procedure used.

Table 2

Determination of detection limits in the assessment of powdered ore samples by means of portable XFA equipment

Metal	Ore mineral	Added material	Filter pair	% average metal content in samples	Detection limit (%metal content)
Cr	Chromite	Gabbro	Ti/V	4.2	0.2
Ni	Rammelsbergite	Gabbro	Fe/Co	0.45	0.06
Cu	Bornite	Granite	Co/Ni	1.5	0.15
Zn	Sphalerite	Granite	Ni/Cu	1.2	0.15
Zr	Eudialyte	None	Rb/Sr	1.8	0.2
Nb	Eudialyte	None	Sr/Y	0.2	0.07
Mo	Molybdenite	None	Y/Zr	0.1	0.03
La+Ce	Monazite	Granite	I/Cs	0.2	0.02
Pb	Galena	Granite	Ir/Re	0.9	0.10

3.2. Analysis of Exposed Rock Surfaces

The study comprised measurements with a portable XFA instrument on outcrops of vein and disseminated types of mineralization in southwest Greenland. The metals searched for were Zr, Nb, and Ce+ La. The measurements were made at five to ten cm intervals across the contacts between different rock types, while the measurement locations were spaced by one or two m on uniform rock formations. The micro relief of the rocks examined was of the order of a few tenths of a centimetre. Chip samples and hand specimens of material from the traverse lines were collected for later assay by conventional methods of analysis.

Detection limits of 0.45% Zr, 0.15% Nb, and 0.2% La+ Ce were evaluated by application of regression analysis to the experimental data as described in subsection 3.1. As might be expected, these values are greater than the detection limits which were found when the same metals were measured in powdered ore samples (table 2). However, the fact that the portable

XFA instrument responded so well to the metal contents of exposed rock surfaces encourages one to believe that satisfactory on-the-outcrop assessment of ore grade can be made at least in some kinds of metallic-ore deposits.

3.3. Tracing Ore Metals in Rock Samples

Seven standard rock powder-samples obtained from the U.S. Geological Survey were measured for 400 s each with an XFA system, incorporating a one-mCi ^{109}Cd excitation source, a Si(Li) detector 3 mm thick and with a diameter of 6 mm, and a 1024-channel multichannel analyser. The resulting X-ray spectra were processed by summation over six energy intervals covering the K_α X-ray energies of the elements Rb (Z = 37) to Mo (Z = 42). Using the fact that the count rate in the energy interval containing the K_α peak of element Z also contained the K_β peak of element Z - 2, a system of linear equations were set up whose solution furnished six count rates, each being proportional to the sample content of the respective element.

The elements searched for comprised the ore metals Zr, Nb, and Mo, the contents of which averaged 230, 16, and 3 ppm respectively. The spectrometer system was not sensitive enough to detect Nb and Mo at these concentration levels. For Zr a detection limit of 65 ppm was determined, which may be compared with the detection limit of 2000 ppm Zr found when a portable XFA instrument was tested, another sample series being used (table 2). Generally speaking, we estimate that an X-ray spectrometer is of one to two orders of magnitude more sensitive than a portable XFA instrument.

4. CONCLUSION

Radioisotope X-ray fluorescence analysis lends itself well to the assessment of ore grade at various stages in the exploration and exploitation of metallic-ore deposits. Portable XFA equipment is very valuable for rapid, non-destructive analysis of ore samples and outcrops or cut faces of ore-bearing rock, as the obtainable detection limit is lower than the economic cut-off grade of most metallic ores. Energy-dispersive X-ray spectrometers, though somewhat complex to operate, are suitable for tracing small quantities of ore metals in rock specimens. Instruments like these may therefore prove useful in prospecting for metallic ores.

5. ACKNOWLEDGEMENTS

The authors wish to thank their colleagues at the Geological Survey of Greenland and the Institute of Petrology of the Copenhagen University for their co-operation in our studies of radioisotope XFA. We are in particular indebted to Harold Wollenberg of the Lawrence Berkeley Laboratory, who participated in most of the investigations summarized here.

REFERENCES

1) S.H.U. Bowie, A.G. Darnley, and J.R. Rhodes, Portable Radioisotope X-Ray Fluorescence Analyser. Trans. Inst. Mining Met. 74 (1965) 365-379.

2) M.J. Gallagher, Portable X-ray Spectrometers for Rapid Ore Analysis. In: Proceedings of the 9th Commonwealth Mining and Metallurgical Congress, London, May 1969, 2 (Institution of Mining and Metallurgy, London, 1970) 691-729.

3) C.G. Clayton, Applications of Radioisotope X-Ray Fluorescence Analysis in Geological Assay, Mining and Mineral Processing. In: Nuclear Techniques and Mineral Resources. Proceedings of a Symposium, Buenos Aires, 5-9 November 1968 (IAEA, Vienna, 1969) 293-324).

4) H. Kunzendorf, L. Løvborg, and H. Wollenberg, Assay of Powdered Metallic Ores by Means of a Portable X-Ray Fluorescence Analyser. Risø Report No. 251 (1972) 29 pp.

5) H. Wollenberg, H. Kunzendorf, and J. Rose-Hansen, Evaluation of Niobium, Zirconium, and Lanthanum plus Cerium by Isotope-Excited X-Ray Fluorescence Measurements on the Outcrop in the Ilímaussaq Intrusion, South Greenland. Econ. Geol. 66 (1971). In press.

6) H. Bohse, C.K. Brooks, and H. Kunzendorf, Field Observations on the Kakortokites of the Ilímaussaq Intrusion, South Greenland, Including Mapping and Portable X-Ray Fluorescence Analysis for Zirconium and Niobium. Rapp. Grønlands Geol. Unders. No. 38 (1971) 43 pp.

7) H. Kunzendorf, An Instrumental Procedure to Determine Fe, Rb, Sr, Y, Zr, Nb, and Mo in Rock Powders by Si(Li) X-Ray Spectrometry. J. Radioanal. Chem. (1971). In press.

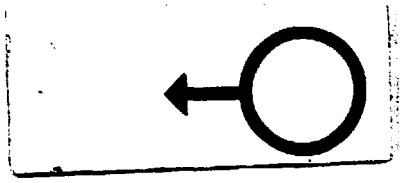

On the Volume Measured by Subsurface Neutron Moisture Gauges

by

P.L. Ølgaard
Technical University of Denmark

and

V. Haahr
Agricultural Research Department

Abstract

The volume measured by subsurface neutron moisture gauges is of considerable importance for the practical application of these gauges, both with respect to the determination of the proper calibration drum size and to an evalution of the resolution of the gauge with depth.

Results from two series of investigations are reported. The first of these deals with the effect of the drum size on the calibration curve obtained, and is a combined experimental and theoretical investigation. It demonstrates that unless the diameter and the height of the calibration drums are around 80 to 100 cm or larger, important errors may be introduced.

The second series is an attempt to estimate the size of the sphere of importance of a gauge in an inhomogeneous, infinite medium, and is based on calculations only. It indicates that the radius of the sphere of importance of a typical Danish soil is 30 to 40 cm at 5 moisture volume per cent and around 20 cm at 30 moisture volume per cent.

1. INTRODUCTION

When a subsurface neutron moisture gauge is used to measure the water content of soils or similar media, the probe of the gauge, which contains a fast-neutron source and a slow-neutron detector, is lowered into the medium through an access tube to the point of interest. Here the count rate of the neutron is measured, and from this result the moisture content can be determined by use of proper calibration curves. However, it is inherent in the method that the result obtained is not the moisture content of a point of the medium, but some sort of average moisture content of a certain volume around the probe. The reason is that the fast source-neutrons must undergo a number of collisions in the medium before they are slowed down and can be detected by the neutron detector. During the slowing-down process the neutrons will move around in a certain volume of the medium which is roughly a sphere with the probe at the centre. The measured count rate is therefore dependent on the properties of the whole volume of the sphere, primarily its water content. Consequently the measured moisture content is some sort of an average value for the sphere.

This feature of the neutron moisture gauge has its advantage in that the results obtained are not sensitive to small inhomogeneities of the medium, e.g. stones. It does, on the other hand, also limit the resolution of the gauge with depth, and this characteristic is important when stratified media are considered. The resolution with depth is important not only because it influences the accuracy of the moisture profile (moisture content versus depth) measured, but also because it affects the optimum distance between adjacent measuring points.

The fact that a neutron moisture gauge measures the moisture content of a volume, not of a point, is also of importance for calibration measurements in finite drums. If the results of such measurements are to be of relevance for field measurements in large media, the volume of the drum must be large enough to contain the volume measured by the gauge in an infinite medium. If the drum is significantly smaller, important errors will be introduced owing to neutron leakage from the drum and the correspondingly lower count rate.

It is therefore of considerable interest to calculate the size of the volume measured by subsurface neutron moisture gauges. Several methods for making such estimates have been proposed.

In 1956 van Bavel et al.[1] introduced the concept of the sphere of influence, which was defined as the sphere around the source which contains

95 per cent of all thermal neutrons, and a formula for calculating the radius of this sphere was also given.

This concept and in particular the radius formula was criticized by Ølgaard [2], who introduced instead the sphere of importance, defined as the sphere around the source which, if all medium material outside the sphere is removed, will yield a neutron flux at the source that is 95 per cent of the flux obtained if the medium is infinite. In [2] a formula for determining the radius of the sphere of importance is also given.

However, Zuber and Cameron [3] raised some justified objections to this definition, and in a panel convened by the IAEA a modified definition was agreed upon: the sphere of importance for subsurface probes is the sphere around the source which, if all material outside the sphere is removed, will yield a count rate that is a stated fraction of the count rate obtained in an infinite medium. Further a fraction value of at least 0.99 was recommended for investigations of calibration drum dimensions [4]. The reason for choosing the figure of 0.99 is that the statistical uncertainty of measured count rates is often about one per cent.

This definition is very useful in connection with the determination of calibration drum dimensions. However, when it comes to probe resolution with depth, it is of more dubious value, and other approaches have to be considered.

In this paper the results of two series of investigations are reported. The first series deals with the volume measured by the probe in relation to calibration drum dimensions, the second with the volume measured in the case of large media with varying composition and is thus relevant to the resolution with depth.

2. INVESTIGATIONS OF THE VOLUME MEASURED BY A SUBSURFACE GAUGE RELEVANT FOR CALIBRATION DRUM DIMENSIONS

Van Bavel et al. [5] have demonstrated experimentally that the size of the calibration drum is of great importance for the calibration curves obtained from measurements in such drums, Unfortunately no information was given in [5] concerning the composition of the soil used. Since we intended to perform both theoretical and experimental investigations and to compare the results obtained from these two approaches, it was found necessary to carry out new measurements with a soil of known composition, i.e. a soil for which calculations could also be executed.

2.1. Experimental Investigations

The measurements were made with a Nuclear Chicago subsurface probe (model P-19) connected to a Danish-produced scaler, BASC.

The soil used was Risø subsurface soil, which is a sandy clay loam. The chemical composition of this soil has been reported earlier [6].

Four calibration drums of different sizes were used during the investigations (see fig. 1). The drums were made of 2 mm iron plate. The individual drum diameters were equal to the heights and were 90 cm (570 litres), 55 cm (129 litres), 40 cm (49 litres), and 30 cm (20 litres) respectively.

Fig. 1. The four calibration drums used in the measurements. The probe shield containing the P-19 probe is situated on top of one of the access tubes. At the bottom the BASC scaler is seen.

Before the soil was filled into the drums, its moisture content was adjusted to the desired value either by wetting or by drying and by subsequent thorough mixing. A gravimetric determination was made of the water concentration of the soil material. The calibration drums were filled gradually with 5-cm thick soil layers and packed to a dry-soil density of around 1.4 g/cm^3. The density and the calculated water volume per cent were checked after the neutron measurement by volumetric sampling at the centre of the

drums. All moisture contents above 30 volume per cent were obtained by supplying water to the soil surface in the drums until free water drained out through holes in the bottom. After the draining had stopped, the measurements were made. This procedure resulted in a slight reduction of the soil volume due to subsidence.

The gauge readings were taken with the neutron source at the centre of the drums. To eliminate the influence of the sourroundings, the two smaller drums were placed at a distance of at least 50 cm from the floor and the walls. The paraffin probe shield was in all drums placed on top of a one-metre long aluminium access tube. The outher diameter of the tube was 44.5 mm.

2.2. Theoretical Investigations

The theoretical investigations were performed by use of the computer program MOPS-III [7], which has been developed from the MOPS-II-C program[8]. Both of the programs are based on three-group diffusion theory and deal with point-source, line-detector geometry. However, MOPS-III includes a number of features which are not found in MOPS-II-C, and of these the following should be mentioned since they are used in these investigations.

While MOPS-II-C can be used for subsurface probes in infinite, homogeneous media only, MOPS-III can also treat a probe situated in a finite, spherical, and homigeneous medium with the neutron source positioned at the centre of the sphere.

The use of MOPS-II-C is limited to the calculation of calibration curves. However, MOPS-III can also perform a direct comparison between experimental and theoretical count rates for a medium of a given, dry composition. When the program operates in this mode, sets of experimentally determined values of water volume per cent, dry-medium density, count rate and medium radius are read into the computer which then calculates the corresponding theoretical count rates and compares them with the experimental values. In addition MOPS-III computes the sum for all experimental points of the square of the difference between the theoretical and the corresponding experimental count rate. This feature allows a least-square fit to be performed rather easily.

Often the chemical composition of the medium of interest is not known very accurately. This gives rise to uncertainty in the calculation of the value of the macroscopic absorption cross section of the dry medium, Σ_a.

However, since Σ_a is for practical purposes the only unknown, it can be used as a fitting parameter [9]. Such a fitting can be performed with MOPS-III by use of Σ_a/ρ_{dry} as the the parameter; ρ_{dry} is the dry-medium density.

Since the calibration drums used in the measurements were all cylindrical, and since MOPS-III can only consider spherical media, a convention had to be established to convert the dimensions of a cylinder into the radius of the equivalent sphere. It is obvious that this radius must be larger than that of the largest sphere that, with the source at the drum centre, can be inscribed in the soil medium. It is equally obvious that the radius must be smaller than that of the sphere that has the same volume as the soil cylinder. Rather arbitrarily we chose to calculate the equivalent radius as the mean value of these two radii.

As pointed out in subsection 2.1., the soil used in the experimental investigations is Risø soil. However, the soil sample used in the present investigations was not quite identical to that used in the investigations of [6]. Further the soil sample used in the present investigations had been stored outdoors for fairly long period after excavation, and even though it was covered with plastic foil during this storage period, it was probably exposed to a certain amount of wash-out, whereby important neutron absorbers may have been removed. Thus the Σ_a calculated from the composition given in [6] is likely to be too high. Such a tendency is as a matter of fact already found in fig. 4 of [6]. Since the main purpose of the investigations was to determine the effect of the medium size on the count rate obtained, it was found reasonable to adjust the Σ_a/ρ_{dry}-value used in all calculations in such a way that the best possible agreement between the measured and the calculated count rates was obtained for the drum with the 90 cm diameter. The adjustment was made by use of a least-square fit, and the necessary reduction in Σ_a/ρ_{dry} amounted to 24 per cent.

2.3. Comparison between Experimental and Theoretical Results

The results of the measurements of subsection 2.1. and the corresponding calculations are given in fig. 2.

The experimental count rates for the drum with a diameter of 90 cm agree well with the calculated count rates. This is hardly surprising since by variation of Σ_a/ρ_{dry} the theoretical results for this drum have been fitted, as discussed in subsection 2.2., to the experimental ones so as to obtain the best possible agreement. However, the experimental count rates for the 55 cm diameter drum also agree quite well with the calculated values.

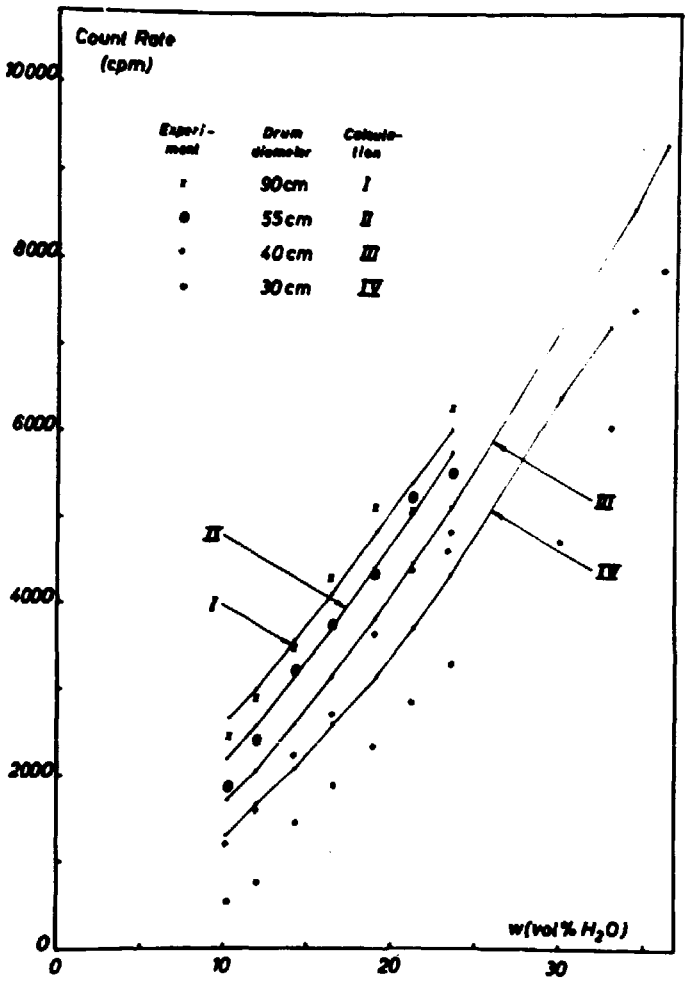

Fig. 2. Comparison between measured and calculated count rates obtained with different calibration drum sizes. The soil used is Riss subsurface soil with reduced Σ_a/ρ_{dry} value. Note that the calculated count rates for a given drum size do not lie on a smooth curve owing to variations in dry-soil density.

For the smaller drum diameters (40 and 30 cm) there are significant disagreements, and the measured values are consistently lower than the calculated ones. The smaller the drum, the larger the disagreement.

This disagreement may at least partially be explained by the following effect. In the theory used it is assumed that the perturbation caused by the insertion into the medium of the access tube and the probe is independent of the medium composition and can consequently be corrected for by proper normalization[2]. This assumption seems to be quite reasonable as long as large media are considered. However, in small media or drums insertion

of the access tube will cause a larger fractional reduction of the soil volume than in large drums. This effect, which will cause increased neutron leakage and consequently lower count rates, has not been taken into account in the theoretical calculations. The tendency of the discrepancy was consequently to be expected.

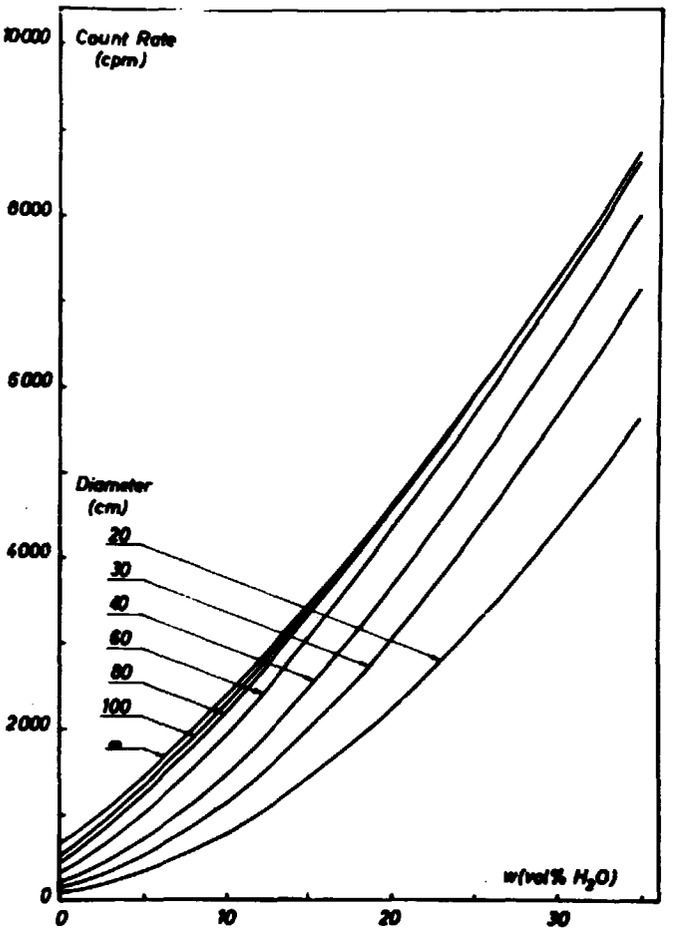

Fig. 3. Calculated calibration curves for spherical soil media with varying diameter. Riso soil, no correction of Σ_a/ρ_{dry}. Dry-soil density equal to 1.4 g/cm^3. P-19 probe.

In fig. 3 the calculated calibration curves for spherical media with varying diameter and constant dry-medium density are shown. Since the theoretical model seems to give acceptable results for large media, the following conclusions can be made based on fig. 3. A medium with a diameter of 100 cm should be equivalent to an infinite medium down to a water volume per cent of around 10 (error in count rate less than 3 per cent), while a medium

with a diameter of 60 cm gives count rates in the moisture range of 10 to 20 volume per cent, which is 18 to 6 per cent lower than those obtained in an infinite medium.

In conclusion the following points should be made:

While it is understandable that many calibration measurements are performed in rather small drums (e. g. with a diameter of 60 cm) in order to limit the amount of soil which has to be handled, the use of such drums introduces significant errors in the calibration curves if these curves are used in connection with measurements in large media. A reasonable compromise for the drum dimension should be a diameter of 80 to 100 cm, somewhat dependent on the moisture range of interest, and a height roughly equal to the drum diameter.

While the MOPS-III-program can calculate calibration curves for infinite and large media fairly accurately, the theory used in the program does not seem to be satisfactory when the medium dimensions correspond to "diameters" of around 40 to 50 cm and below.

3. INVESTIGATIONS OF THE VOLUME MEASURED BY A SUBSURFACE GAUGE RELEVANT FOR RESOLUTION WITH DEPTH

As discussed in the introduction it is of considerable practical importance to assess the resolution of a subsurface probe with depth, partly to get an idea of how accurately a moisture profile can be measured, partly to determine the distance between adjacent measuring points.

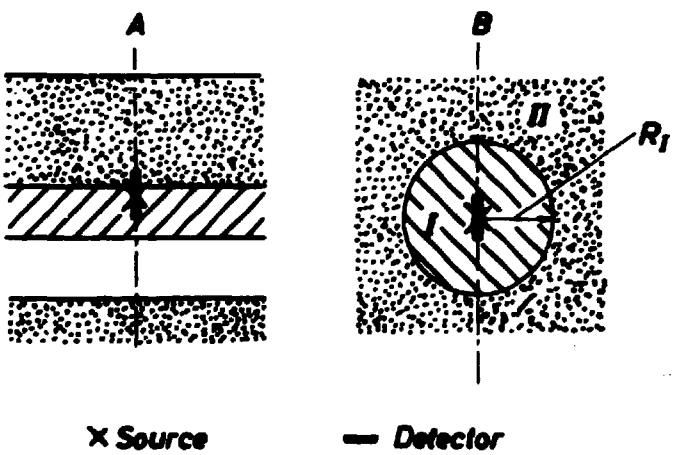

Fig. 4. Geometries relevant to investigations of resolution with depth of subsurface moisture probes.

Since field investigations usually involve measurements in stratified media, a program which can treat a case as outlined in fig. 4 A is desirable if the resolution with depth is to be investigated theoretically. The thickness of the layers and their composition as well as the position and type of the probe should be variables. Such a program is unfortunately not available at present. However, another program, SOFIE-III [10], can provide some information on the problem, and this program was used in the investigations discussed in this section.

SOFIE-III is based on the arrangement shown in fig. 4 B. For a fixed composition of the outer zone (II) and a varying moisture content of the inner (I), the program calculates the radius of the inner zone, R_I, for which the ratio between the count rate of the detector and the count rate that would be obtained if the inner zone extended to infinity is equal to a given input value. This value was in all cases considered equal to 0.99. Also, in all cases considered, the data of the probe were identical to those used in section 2, and the dry composition of zones I and II was that of Risø soil (ref. 6, no correction of Σ_a), while the dry-soil density was 1.40 g/cm^3 in both zones.

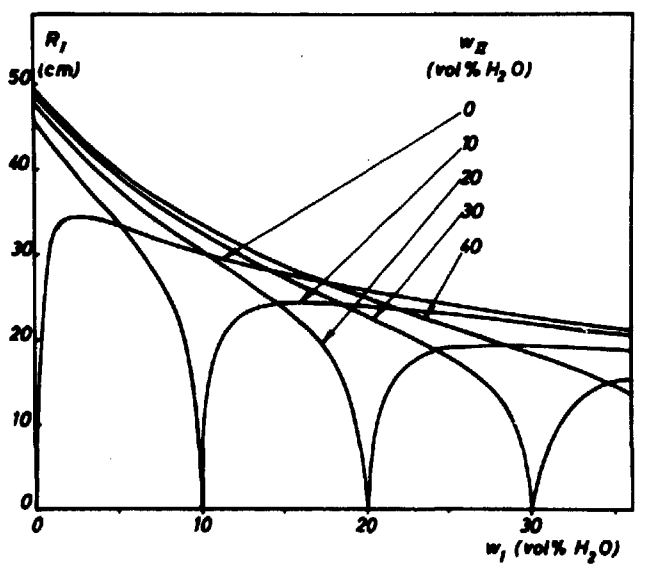

Fig. 5. Radius of the sphere of importance as a function of water content of the inner zone, w_I. The water content of the outer zone, w_{II}, is 0, 10, 20, 30, and 40 volume per cent respectively. Risø soil without Σ_a correction in both zones, ρ_{dry} = 1.4 g/cm^3. P-19 probe.

Fig. 5 gives the results of five SOFIE calculations in which the moisture content of the outer zone, w_{II}, was 0, 10, 20, 30, and 40 volume per cent respectively. The general trend of the curves is the following. At very low values of moisture content in the inner zone, w_I, the R_I value is rather large, but as the moisture content increases, the value of R_I decreases owing to better slowing-down of the neutrons. As w_I approaches the value of w_{II}, R_I approaches zero, since the difference between the two media vanishes. As the moisture content of the inner zone exceeds that of the outer, R_I rises steeply and goes through a maximum. With further increase in w_I, the R_I value decreases slowly owing to better neutron slowing-down.

It is important to note in fig. 5 that except for the regions where $w_I \simeq w_{II}$, the curves obtained for R_I as a function of w_I are relatively insensitive to the value of w_{II}. If we neglect the region where $w_{II} \simeq w_I$ and R_I is consequently small, the curves will all lie inside the hatched area of fig. 6.

Thus the hatched area of fig. 6 gives roughly the radius of the sphere of importance as a function of the moisture content of the zone around the probe. This "curve" is valid only when the inner zone is surrounded not by vacuum, but by a medium with properties not too different from those of the inner medium.

The SOFIE-III program also allows the calculation of the radius of the sphere of importance as defined in [4]. With a fraction value of 0.99 the curve given in fig. 6 is obtained. It is seen that the radius of the sphere of importance in the case of vacuum outside the sphere is roughly twice as large as in the case of a material medium outside the sphere.

The relation between R_I and w_I given by the hatched area of fig. 6 will of course depend on the chemical composition and density of both the inner and the outer media, but unless very large deviations exist between these two media, the effect of composition and density is probably not very important. Further the idea behind a concept such as the sphere of importance is only to give an estimate of the sphere of importance, not an exact value.

Hence it may be concluded that at a moisture volume per cent of 5 the radius of the sphere of importance of a subsurface gauge well below the surface is 33 - 40 cm, while at a volume per cent of 30 is 16 - 23 cm.

Another important conclusion which can be obtained from these investigations is that it is better to surround the samples with a material not too different from that of the sample than to have just air around the sample if the calibration curve measurements have to be made on too small sample sizes. A similar approach has been used by Couchat [11], and it is the same

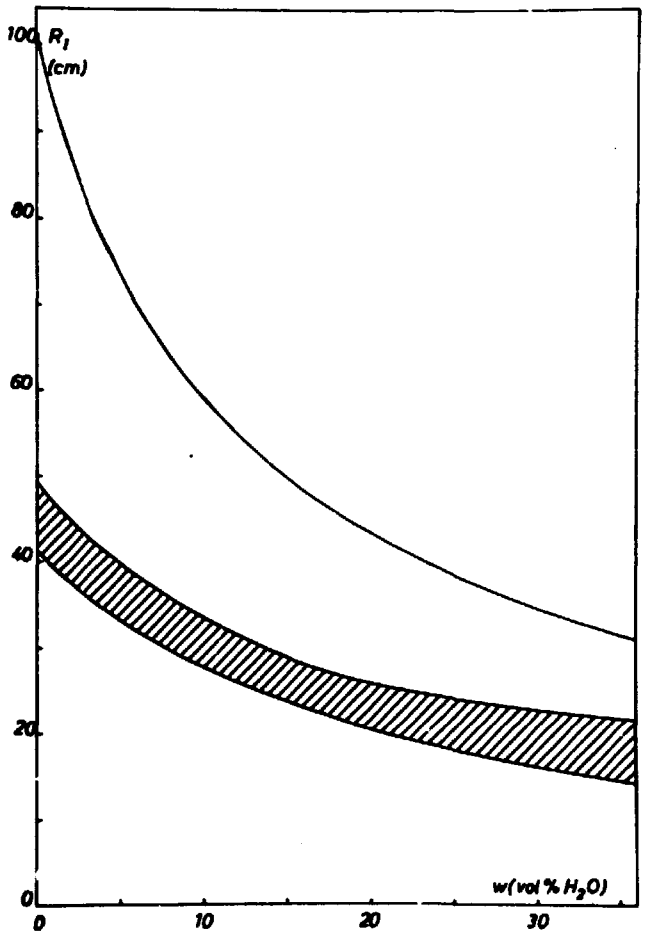

Fig. 6. Radius of the sphere of importance as a function of the water content of the spherical zone around the source. For the upper curve the medium outside the sphere is vacuum. For the lower, hatched "curve" the medium outside has varying water content (0 to 40 vol. per cent). Riss soil, ρ_{dry} = 1.4 g/cm^3. P-19 probe.

principle which is sometimes used in measurements near the soil surface, if material is placed at the surface around the access tube. It is well known that this procedure allows measurements closer to the surface than would be possible if no material had been placed there.

4. ACKNOWLEDGEMENT

It is a pleasure to acknowledge the interest which Professor T. Bjerge has always shown in the co-operation between the Agricultural Research and the Reactor Physics Departments in the field of neutron moisture gauges;

the present paper is a result of this co-operation.

We would also like to acknowledge the assistance of the Computer Group in the execution of the numerical calculations and that of Mr. B. Skovsgaard in performing the laboratory work involved in the measurements.

REFERENCES

1) C. H. M. van Bavel, Newton Underwood, and R. W. Swanson, Soil Moisture Measurements by Neutron Moderation. Soil Sci. 82 (1956) 29-41.

2) P. L. Ølgaard, On the Theory of the Neutronic Method for Measuring the Water Content in Soil. Risø Report No. 97 (1965) 44 pp.

3) A. Zuber and J. F. Cameron, Neutron Soil Moisture Gauges. At. Energy Rev. 4 No. 4 (1966) 143-164.

4) Appendix of ref. No. 3, 164-167.

5) C. H. M. van Bavel, D. R. Nielsen, and J. M. Davidson, Calibration and Characteristics of Two Neutron Moisture Probes. Soil Sci. Soc. Amer., Proc. 25 (1961) 329-334.

6) V. Haahr and P. L. Ølgaard, Comparative Experimental and Theoretical Investigations of the Neutronic Method for Measuring the Water Content in Soil. In: Isotopes and Radiation in Soil-Plant Nutrition Studies. Proceedings of a Symposium, Ankara, 28 June - 2 July 1965. (IAEA, Vienna, a965) 129-146.

7) P. L. Ølgaard, Description of the MOPS-III Programme. Risø-M-1450. To be published.

8) P. L. Ølgaard, Description of the MOPS-II-C Programme. Risø-M-481 (1966) 18 pp.

9) P. L. Ølgaard, Use of Theoretical Models for Neutron Moisture Gauge Calibration and Design. In: Nuclear Techniques and Mineral Resources. Proceedings of a Symposium, Buenos Aires, 5-9 November 1968. (IAEA, Vienna, 1969) 65-78.

10) P. L. Ølgaard, Description of the SOFIE-III Programme No. P-405. Risø-M-637 (1967) 52 pp. Internal Report.

11) P. Couchat, CEN, Cadarache, France, private communication.

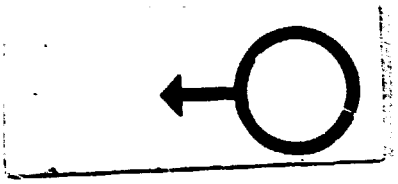

On the Relevance of Absorbed-Dose Standardization and International Dose Intercomparisons with Respect to the Use of Pulsed Electron Accelerators*

by

Niels W. Holm

Accelerator Department

Abstract

The increasing use of high-energy photon and electron sources in radiation therapy and in radiation processing has caused the international and national standards laboratories to devote much effort to providing for absorbed-dose standardization services for these sources. The purpose of the present paper is to draw attention to the serious influence on the radiation effect of a given absorbed dose at the extreme dose rates obtained from pulsed electron accelerators and to suggest alternative means of standardization.

---

* also presented at the Joint IAEA/WHO Panel on National and International Radiation-Dose Intercomparisons. Vienna, 13 - 17 December 1971.

1. INTRODUCTION

The need for national and international radiation-dose intercomparisons is being justified partly by the growing use in medicine and industry of high-energy photon and electron beams. While exposure standards are well established in international and national laboratories (see e. g. ICRU handbook 10 b), absorbed-dose standards are only at the introduction and testing stages at these laboratories. As long as absorbed-dose calibration facilities are not available, intercomparison services are being offered on the basis of the Fricke dosimeter (IAEA[1], NBS[2], and NPL[3]) and the TLD systems (IAEA[4]).

While previous intercomparison activities centred primarily upon radiotherapy sources, such as ^{60}Co and X-ray equipment with a limited range of radiation energies and absorbed-dose rates, the long-term objective of absorbed-dose standardization seems to be much wider in the sense that radiation protection as well as radiation therapy and industrial irradiation are being included in the planning of future activities in the standardization field[5]. This implies that absorbed-dose ranges of perhaps 9 - 10 orders of magnitude and absorbed-dose-rate ranges of perhaps 10 - 15 orders of magnitude are to be covered.

The purpose of the present paper is to discuss the relevance and usefulness of pursuing this ambitious objective. Factors influencing the effects of a radiation treatment are discussed, and some experimental data are used to illustrate the influence on the absorbed-dose-response function of a particularly important parameter, the absorbed-dose rate. Some other means of intercomparing radiation treatments are suggested.

2. FACTORS INFLUENCING THE EFFECTS OF A RADIATION TREATMENT

The ideal situation for a radiation user is one where he can base his treatment on a firm correlation between a radiation effect and a radiation-absorbed dose.

It is well known, however, that a number of factors may influence the effect of a given radiation-absorbed dose. Environmental parameters, such as temperature and the presence - or absence - of atmospheric air or other gases, influence many radiolytic reactions significantly. If the subject to be irradiated is a biological tissue or a microorganism, we know that e. g. the metabolic state may influence the resulting effect. In the practical situation, however, it is usually possible either to standardize the environmental con-

ditions and the condition of the subject, or to establish appropriate weighting factors to account for changes in response caused by changes in these parameters. Also the characteristics of the radiation field enter the picture. Radiation biologists have long ago recognized the need for applying RBE-factors according to the effect of differences in radiation type and LET on the biological response. While the use of such RBE-factors is essential in the application of, e.g., neutrons, protons, alfa particles or mixed fields, they may quite safely be dispensed with for electrons and photons at radiation energies in the 1 - 10 MeV range, where the influence of the above-mentioned parameters is insignificant. Small differences in effects are noticeable, however, already when we go down in energy to 250 kV X-rays, where, e.g., the radiolytic yield of the Fricke dosimeter is decreased by a few per cent.

On this basis, it may be concluded that the absorbed dose does remain a convenient and useful subject of standardization and intercomparison measurements for photon and electron irradiation equipment of modest and comparable output, i.e. ^{60}Co and conventional X-ray therapy units and low-power betatrons. The situation is, in the opinion of the author, quite different, when we extend the absorbed-dose standardization and the activity of international dose intercomparisons to include also modern pulsed irradiation sources, such as electron linear accelerators, field emission devices, etc., at least when the electrons are being used without conversion into X-rays. While such dose intercomparison activities may be of great value for basic research work, they do not seem to be particularly useful for practical radiation applications at the present stage. The main reason is the dominating - and hitherto insufficiently investigated - influence on the radiation effect of a given absorbed dose at the extreme dose rates available from pulsed accelerators.

A number of examples are compiled in the following section in order to substantiate this opinion.

3. PRACTICAL EXAMPLES OF ABSORBED-DOSE-RATE EFFECTS

Most of the examples given in this section have been selected from experiments carried out by various research groups at Risø. Irradiations were performed at the sources operated by the Accelerator Department, which means that the absorbed-dose dosimetry related to the various experiments was carried out by the same staff. Any possible error in absorbed-dose measurements is therefore likely to be systematic and would

tend to cancel out in comparative absorbed-dose-rate-effect determinations.

3.1. Absorbed-Dose-Rate Effects Observed at ^{60}Co Sources

In polymerization reactions initiated with ^{60}Co-gamma rays, it is well established that the rate of polymerization is inversely proportional to the square root of the absorbed-dose rate at rates less than approx. 10^4 rads/h (see e.g., Chapiro[6]). Also other chain reactions show absorbed-dose-rate dependence.

For living systems, such as microorganisms or biological tissues, no gross effects have been observed at the absorbed-dose rates usually applied for therapy or industrial processing.

An example may be given of a somewhat peculiar absorbed-dose-rate effect in aqueous solutions of a simple organic compound, oxalic acid. The use of oxalic acid for chemical dosimetry was suggested in 1955 by Draganić[7]. Holm et al.[8] observed that the decomposition yield of oxalic acid decreased continuously with increasing absorbed dose approximately following first-order kinetics, and Draganić suggested[9] that the absorbed dose could be conveniently calculated from the following equation

$$D = a \cdot c_o \cdot \log \frac{c_o}{c}$$

where D is the absorbed dose, a is a calibration constant, and c_o and c are the concentrations in molecules per ml of oxalic acid before and after irradiation respectively. Based on data from this and other laboratories, experimentally determined a-values were calculated and compared (see table 1). The author was involved in the absorbed-dose calibrations at the Natick ^{60}Co plant[10] and at the Risø ^{60}Co facility[11].

Calorimeters of quite similar design were used for absorbed-dose calibrations. The Natick plant was operated in a batch mode with a constant dose rate, while the Risø facility operates in a continuous mode, so that the absorbed-dose rate varies throughout the irradiation period.

As is apparent from table 1, the difference between the lowest (37.0) and the largest (49.2) a-values obtained at Risø and Natick respectively amounts to more than 30%, this being far beyond the limits of experimental error. This phenomenon may be explained on a radiation chemical basis, when the mode of delivering the absorbed dose is taken into account (see fig.1). The decomposition of oxalic acid proceeds over several stages. Among the first products formed are dihydroxytartaric acid and glyoxylic acid[12], which

Table 1

(Data from Holm and Draganić, Atompraxis, 14, Heft 11/12, 1968)

Laboratory	Oxalic-acid concentration (mM)	a-value
Vinča (Yugoslavia)	50 to 600	41.5
Risø (Denmark)	50	37.0
	100	38.2
	200	39.1
Natick (USA)	50	49.2
	100	44.1
NAEC (USA)	100	45.6
	300	47.4
Dow Chem. Comp. (USA)	50	40.5
BNL (USA)	100	43.0
Rez (Czechoslovakia)	50	46.7
Zagreb (Yugoslavia)	100	43.0
	250	42.8

react further in slow condensation reactions. When the irradiation time is of the same order of magnitude - or less - than the "lifetime" of dihydroxy-tartaric acid and glyoxylic acid in the solution, these products will react to a greater extent with the primary radicals than with the oxalic acid, thus decreasing the decomposition rate and increasing the a-value.

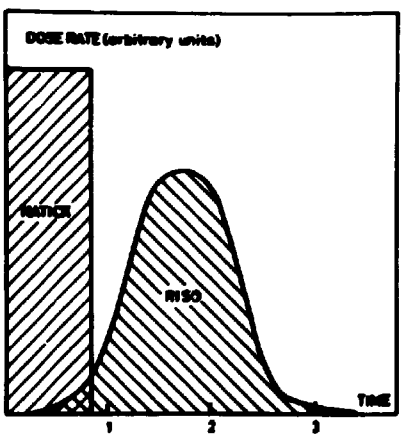

Fig. 1. Dose rate vs. irradiation time for delivering same total absorbed dose at Natick and at Risø ^{60}Co plants.

The absorbed-dose-rate effect reported here is probably far from being unique; similar combinations of reaction-rate constants are likely to be found in many other aqueous organic or biological systems. That this example seems to be the only one so far reported is probably because of the fact that a system investigated for its dosimetric properties attracts very close scrutiny and very accurate analysis when such unexpected discrepancies crop up.

3.2. Absorbed-Dose-Rate Effects Observed by Comparison of ^{60}Co Irradiation and Pulsed Electron Linear Accelerator Irradiation

While absorbed-dose-rate effects in aqueous and biological systems are only seldom reported within the absorbed-dose-rate ranges obtained at ^{60}Co plants, there are many examples of such effects when we compare ^{60}Co-gamma irradiation with electron linear accelerator irradiation. In aqueous systems, radical-radical recombination reactions compete very well with radical-solute reactions at high absorbed-dose rates and we observe in most systems a significant change in radiation yields. The G-value for the Fricke dosimeter remains constant at 15.6 from ^{60}Co absorbed-dose rates up to (linear accelerator) about 10^3 rads per 1 μs pulse (peak absorbed-dose rate ~10^9 rads/s) and decreases by 15% to approx. 13.2 at 10^4 rads per 1 μs pulse (~10^{10} rads/s) and 45% to approx. 8.6 at 10^5 rads per 1 μs pulse (~10^{11} rads/s)[13].

Systematic differences in the responses of polymer systems at the two types of sources are not fully investigated, but the practical experience gained at Risø from radiation sterilization of disposable medical supplies made from plastic shows that radiation degradable polymers tolerate two to five times higher absorbed doses at the high absorbed-dose rates obtained from a 10 MeV - 5 kW electron linear accelerator than they do at the low dose rates obtained in a 10,000 Ci ^{60}Co facility.

For biological systems an interesting example is available. The influence of the absorbed-dose rate was investigated on a vegetative bacterium, Str. faecium, strain $A_2$1, and on a sporeforming bacterium, B. sphaericus, strain C_IA. The two strains are used in the form of dried standard test pieces produced at the Accelerator Dept., Risø, for comparing the microbiological efficiency of radiation sterilization plants in IAEA member countries[14]. Very careful investigations at the Risø sources disclosed that a given inactivation factor for Str. faecium, strain $A_2$1, requires a 15-20% lower absorbed dose at the ^{60}Co plant than at the electron linear accelerator. In the case of the B. sphaericus, strain C_IA, no differences in acti-

vating efficiency of the two sources could be detected under exactly identical irradiation conditions. No proven explanation is offered for this observation. It may be suggested that the higher water content of the vegetative organism leads to chemical recombination reactions similar to those occurring in aqueous solutions at high absorbed-dose rates. The example must be considered relevant also outside the world of microorganisms; other biological systems are likely to behave in similar ways.

3.3. Absorbed-Dose-Rate Effects Observed by Comparison of a 400 keV ICT Electron Accelerator and a 10 MeV Pulsed Electron Linear Accelerator

The absorbed-dose rate from an electron accelerator is determined by the beam-current intensity, which can be varied in a number of ways, e.g., by changing the load current, or by focusing, defocusing, scattering or scanning the electron beam. Accurate measurements of the size and shape of the beam spot, the intensity distribution within the spot, scanning effects, etc., are therefore necessary in order to determine the absorbed-dose rate and absorbed-dose-rate distribution. Unfortunately, such measurements are difficult or even impossible to execute with DC-machines, such as the 400 keV-50 mA ICT electron accelerator at Risø. For window protection, the electron beam must be xy-scanned and single "pulses" or single scan sweeps cannot be provided for. The absorbed-dose rate must therefore be estimated in an empirical and rather crude way.

For pulsed machines, such as electron linear accelerators and field emission devices, other problems arise. How do we define the absorbed-dose rate? According to ICRU (report 11, 1968) the absorbed-dose rate is the quotient of ΔD by Δt, where ΔD is the increment in absorbed dose in time Δt, and the special unit may be any quotient of the rad or its multiple or submultiple by a suitable unit of time (rad/s, mrad/h, etc.). The following example based on a chemical polymerization process may indicate that this definition alone is not very helpful for correlating data obtained from different electron accelerators.

The Chemistry Department at Risø is presently involved in a research programme concerning curing of surface coatings by means of electron-beam irradiation. Pending the installation of a low-energy accelerator, some experiments were made at the electron linear accelerator. The preliminary results from these experiments as well as from later experiments performed at the ICT accelerator are shown in fig. 2.

The special unit for absorbed-dose rate at the linear accelerator is

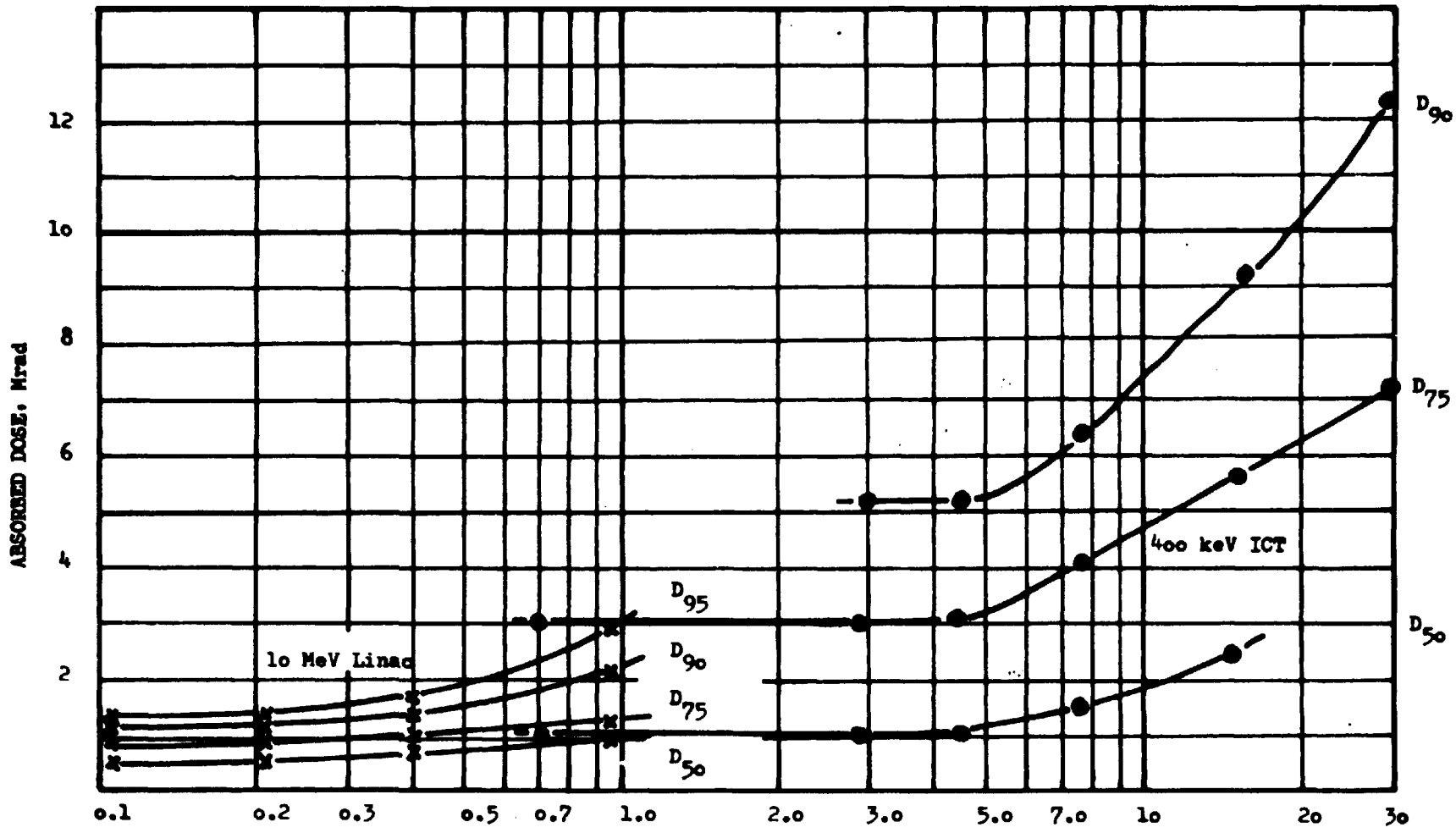

Fig. 2. Radiation doses necessary for different degrees of conversion as function of absorbed-dose rate at 10 MeV electron linear accelerator (7 μs pulses) and at 400 keV electron accelerator. Data from ref. 15.

chosen to be Mrad/s, i. e. the absorbed dose delivered over a time period of one second. The two sets of curves in fig. 2 are not very consistent when considered together. The special unit for absorbed-dose rate at the linear accelerator could also be chosen to be Mrad/μs. In that case the absorbed-dose rate would be zero during most of the time of irradiation and approx. 500 times higher than is the average absorbed-dose rate in Mrad/s, whenever a 7 μs pulse is delivered (pulse repetition rate was 300 pps). Replotting the linear accelerator data according to such a "peak" absorbed-dose rate evidently makes matters even worse. Not even a gross error in the determination of the absorbed doses or the absorbed-dose rates provides a reasonable explanation. It seems that it is difficult to define and interpret the absorbed-dose rate in terms of its impact on radiation effects from different types of accelerators.

3.4. Absorbed-Dose-Rate Effects at the "Same" Absorbed-Dose Rate

Radiation chemists have already for some years found it necessary to give their absorbed-dose-rate data in terms of rad/pulse, and more recently they have acknowledged that even the length of the pulse needs specification in order to provide adequate means for comparing experimental data.

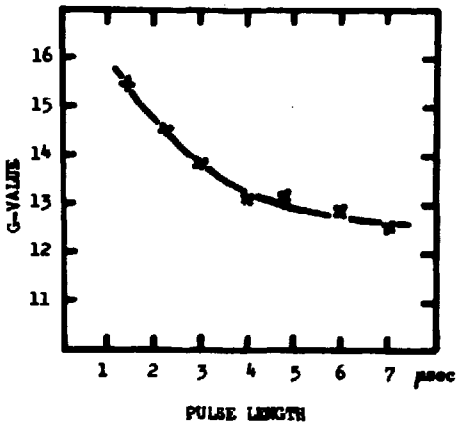

Fig. 3. G-value of the Fricke dosimeter as function of pulse length for constant pulse current. Pulse repetition rate = 18.75 pps. Total dose approx. 20 krads. Data from ref. 16.

Fig. 3 illustrates this problem on the basis of the standard Fricke dosimeter. The experiments were carried out by Sehested in 1965[16] at the 10 MeV linear accelerator at Risø. According to the ICRU $\frac{"\Delta D"}{\Delta t}$ definition, the absorbed-dose rates are the same for all the pulse lengths (the current intensity being constant during the pulse), and yet an absorbed-dose-rate effect of some 20% is observed.

This absorbed-dose-rate effect for the "same" absorbed-dose rate is not unique as may be seen from fig. 4, which is based on recent paint curing

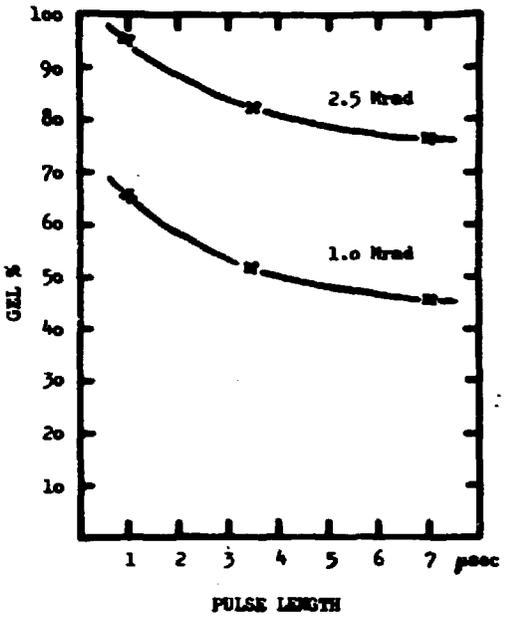

Fig. 4. Gel % as function of pulse length for constant pulse current. Pulse repetition rate = 300 pps. Same polymer systems as in fig. 2. Data from ref. 17.

work by Batsberg Pedersen and Singer[17]. Irradiations were also in this case carried out at the 10 MeV linear accelerator at Risø and more sophisticated absorbed-dose-monitoring equipment was used than that available for Sehested in 1965[16]. The message, however, is precisely the same. The absorbed-dose-rate effect for the "same" absorbed-dose rate is of the same order of magnitude, although it is obtained for an entirely different chemical system and in a different experimental set-up.

4. CONCLUSIONS AND SUGGESTIONS

Based on the different examples given above, the author is convinced that the absorbed-dose-rate effects observed are real and not artefacts. Additional examples from the literature could easily have been included, but it was felt important that most - if possible all - of the experiments presented were based on one and the same source of absorbed-dose calibration. All irradiation facilities at Risø have been calibrated by calorimetry and all secondary dosemeters used have been calibrated against a calorimeter under the conditions of practical use.

It has been demonstrated that substantial absorbed-dose-rate effects take place 1) within the limited - and low - range of absorbed-dose rates available at ^{60}Co plants; 2) from "^{60}Co absorbed-dose rates" to "linear accelerator absorbed-dose rates"; 3) from one type of electron accelerator to another; and 4) at the "same" absorbed-dose rate for pulsed electron accelerators. In all cases, absorbed-dose-rate effects of some 20% or even more have been experienced.

While such effects may be of minor significance for the practical use of ^{60}Co sources and X-ray equipment, they seem to be of general importance for electron accelerators. For such machines, the use of absorbed-dose-rate weighting factors seems to be necessary for predicting radiation effects on the basis of radiation-absorbed dose, and for comparing radiation effects at different machines. Such weighting factors will have to be determined for each type of accelerator, possibly even for the individual accelerator set-up and mode of operation. An absorbed-dose intercomparison alone thus becomes somewhat meaningless for the practical application. What is the purpose of being able to deliver a given absorbed dose with an accuracy of say $\pm$ 2%, if the radiation effect cannot be predicted within 20% owing to unknown absorbed-dose-rate influence?

It would seem to be much easier and perhaps more appropriate to standardize and intercompare the product of absorbed dose and the absorbed-dose-rate weighting factor, or to go even a step further and standardize on a relevant radiation effect.

Such a philosophy has indeed been adopted in radiation sterilization of medical products according to IAEA's Recommended Code of Practice. "Effects"-dosimetry (or in other words control on the desired effect of the integrated process) is a long-term tradition in hospital sterilization, where autoclaves are tested by means of microbiological standard test pieces. Once such an "effects"-standardization has taken place and the effect has been correlated to the process parameters (in radiation sterilization, to the machine parameters or to the absorbed-dose calibration), a physical or chemical process monitor may be used in the daily routine (in radiation sterilization, an appropriate secondary dosemeter). The Accelerator Department at Risø has coordinated efficiency-intercomparison testings through IAEA over the past few years. Fig. 5 (see next page) gives an example of dose-response curves for B. sphaericus, strain C_1A, test pieces irradiated at two ^{60}Co plants[14]. Also test pieces of Str. faecium, strain $A_2$1, are included in the efficiency testings. As might be expected, no absorbed-dose-rate effects are seen in this comparison testing. In other testings, where

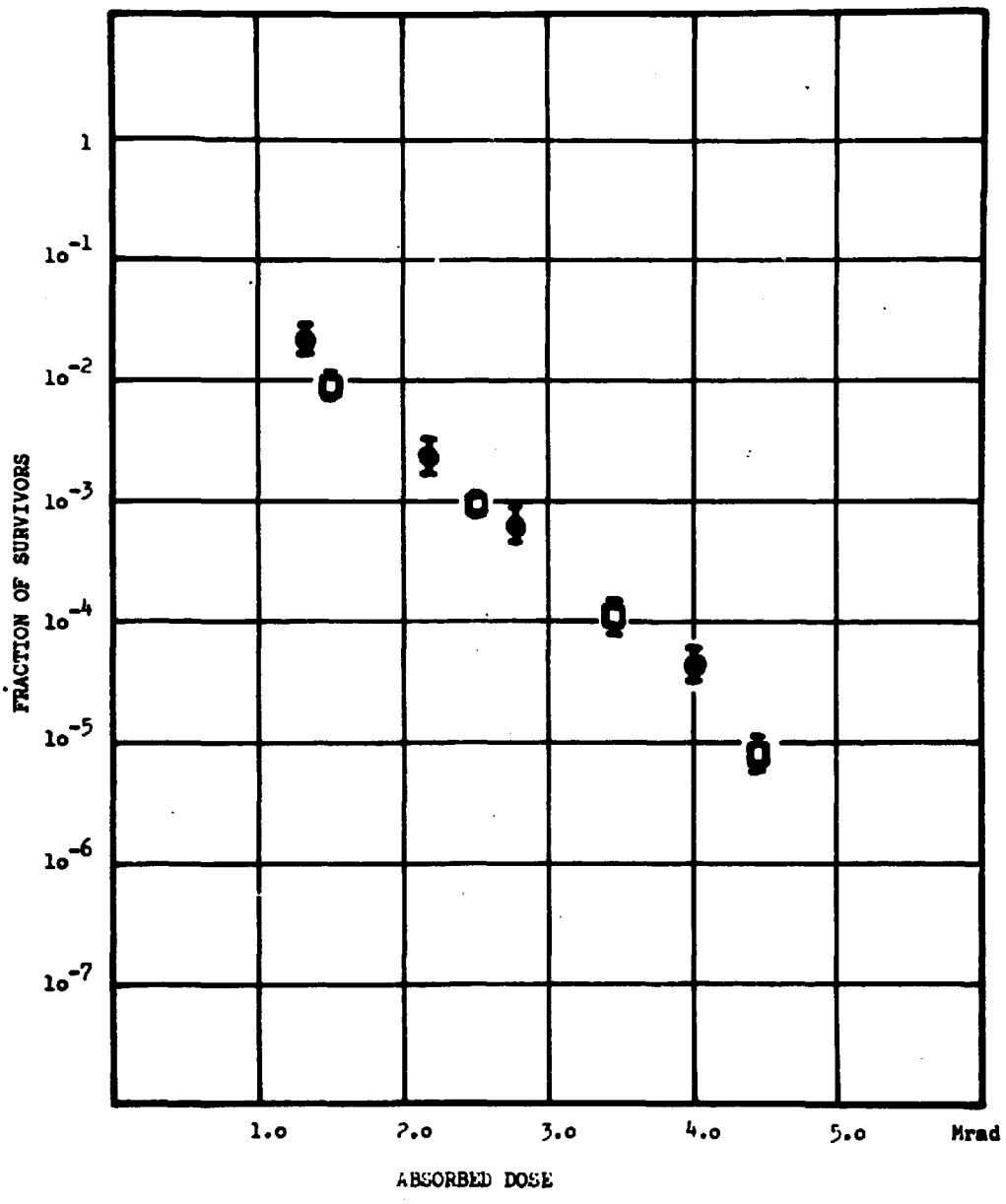

Fig. 5. Typical counting data from intercomparison test with B. sphaericus, strain C_1A, based on local dosimetry data[14]. □ data from Risø ^{60}Co plant. ● data from foreign ^{60}Co plant.

the efficiency of an electron accelerator plant has been compared with that of a ^{60}Co plant, differences of up to 20% have been found for test pieces of Str. faecium, strain $A_2 1$.

We therefore propose that the idea of standardizing and intercomparing on the basis of an effect relevant to the purpose of the radiation treatment rather than by means of absorbed dose be also considered for other types of radiation treatments.

Microbiological test pieces may not be considered very relevant with regard to absorbed-dose range and with regard to the purpose of the treatment in connection with radiation therapy. It seems possible, however, to suggest systems also for such a "process". Berry and Andrews[18] have investigated the dose-response function of various mammalian cells. Fig. 6 shows the inactivating effect of X-ray irradiation on P-388 leukemia cells. The absorbed-dose range as well as the type of tissue appear to be relevant for the purpose of radiotherapy.

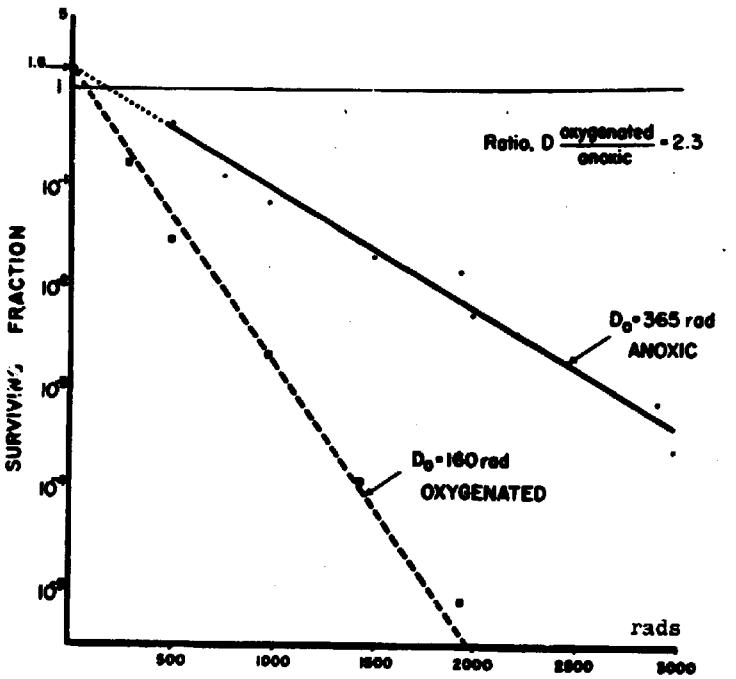

Fig. 6. Dose-response curves for Leukemia-P-388 cells. 3 MeV X-rays. By courtesy of Berry and Andrews[18].

The implementation of the suggestions given here would open the doors of the standards laboratories for bacteriologists, radiobiologists, radiation chemists, and possible specialists from other branches of science. However, this might be considered a positive development, since there is surely no reason why the facilities of standards laboratories should be reserved "for physicists only".

ACKNOWLEDGEMENT

In the course of the compilation of the examples presented in this paper, my colleagues K. Sehested and C. Emborg of the Accelerator Department, Risø, K. Singer of the Chemistry Department, Risø, E. A. Christensen of the Control Department, Statens Seruminstitut, and W. Batsberg Pedersen of the Scandinavian Paint and Printing Ink Research Institute were very helpful in making raw experimental data available to me. Their help in this matter as well as the discussions with them concerning the significance of their data are greatly appreciated.

REFERENCES

1) J. Nagl, Status Report PL-394/5. Working paper given at the Joint IAEA/WHO Panel on Absolute Determination of Radiation Dose and Absorbed Dose Standards, Research Establishment Risø, 25-29 May 1970.

2) R. Loevinger, Current Status of Dosimetry Calibrations at NBS. Working paper given at the Joint IAEA/WHO Panel on Absolute Determination of Radiation Dose and Absorbed Dose Standards, Research Establishment Risø, 25-29 May 1970.

3) W. A. Jennings, Status Report PL-394/4. Working paper given at the Joint IAEA/WHO Panel on Absolute Determination of Radiation Dose and Absorbed Dose Standards, Research Establishment Risø, 25-29 May 1970.

4) V. Balamutov, H. H. Eisenlohr, W. L. Moos, and J. Nagl, Status Report PL-394/7. Working paper given at the Joint IAEA/WHO Panel on Absolute Determination of Radiation Dose and Absorbed Dose Standards, Research Establishment Risø, 25-29 May 1970.

5) Report of the Joint IAEA/WHO Panel on Absolute Determination of Radiation Dose and Absorbed Dose Standards, Research Establishment Risø, 25-29 May 1970. (IAEA, Vienna, 1970).

6) A. Chapiro, Radiation Chemistry of Polymeric Systems, (High Polymers, 15). (Interscience, New York, 1962) 712 pp.

7) I. G. Draganić, Action des rayonnements ionisants sur les solutions aqueuses d'acide oxalique. J. Chim. Phys. 52 (1955) 595-598.

8) N. W. Holm, E. Bjergbakke, K. Sehested, and I. G. Draganić, An Investigation of the Oxalic-Acid System for Co-60 Dosimetry. Risø Report No. 111 (1967) 38 pp.

9) I. G. Draganić, Recent Work on the Use of Oxalic Acid in Aqueous Solutions or in Solid State, for Chemical Dosimetry in Multi-Megarad Region. In: Proceedings of the 2nd Tihany Symposium on Radiation Chemistry, Budapest, 15-19 May 1966. Edited by Janos Dobo and Peter Hedvig. (Akadediai Kiado, Budapest, 1967) 139-147.

10) N. W. Holm and W. B. Alexander, Absolute Dose Measurements on a Megacurie Co-60 Source by Means of Calorimetry. Research Report. (U.S. Army Natick Laboratories, Natick, Mass., 1964) 63 pp.

11) A. Brynjólfsson and N. W. Holm, Calorimetric Measurements of Y-Rays and Calibration of Ferrous Sulphate Radiation Dosimeters. In: Metrology of Radionuclides. Proceedings of a Symposium, Vienna, 14-16 October 1959. (IAEA, Vienna, 1960) 419-425.

12) V. Marković, K. Sehested, and E. Bjergbakke, Radiolysis of O_2-Free Aqueous Oxalic Acid Solutions at pH 1 to 3. Int. J. Radiat. Phys. Chem. In press.

13) K. Sehested, E. Bjergbakke, C. Lang-Rasmussen, and H. Fricke, Reactions of H_2O_3 in the Pulse-Irradiated Fe(II)-O_2 System. J. Chem. Phys. 51 (1969) 3159-66.

14) C. Emborg, E. A. Christensen, W. H. Eriksen, and N. W. Holm, Control of the Microbiological Efficiency of Radiation Sterilization Plants by Means of B. sphaericus, Strain C_1A and Str. faecium, Strain $A_2$1. Progress Report No. 7, IAEA Research Contract No. 973 RB (1971).

15) W. Batsberg Pedersen and K. Singer, Electron-Beam Curing of Organic Surface Coatings. Dose-Rate Effects on the Rate of Polymerization of Prepolymer Monomer Mixtures. In: 3rd Tihany Symposium on Radiation Chemistry, Balatonfüred, 10-15 May 1971. In press.

16) K. Sehested, Accelerator Department, Risø, unpublished work, 1965.

17) W. Batsberg Pedersen and K. Singer, Chemistry Department, Risø, unpublished work, 1971.

18) R. J. Berry and J. R. Andrews, Quantitative Relationships between Radiation Dose and the Reproductive Capacity of Tumour Cells in a Mammalian System in Vivo. Radiology 77 (1961) 824-830.

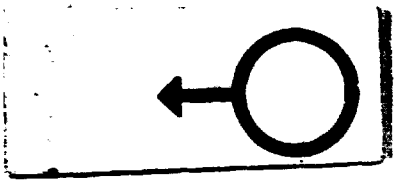

Use of a System for Repeated Blood Volume Determinations Using HSA-^{131}I with Constant Uncertainty

by

M. Faber, J. Bojsen, J. Brøckner, H. Funch-Rosenberg, and Th. Müller

The Finsen Laboratory and The Surgical Department
The Finsen Institute, Copenhagen, Denmark

Abstract

A system for repeated blood volume determinations without increasing uncertainty is reported. It is based on single injection doses of HSA-^{131}I prepared in a series of correctly spaced, increasing radioactivity together with an instrument with direct read-out, programmed to give both final results and standard deviation. The results from 26 duplicate volume determinations on patients in a steady state are presented. The mean coefficient of variation calculated from the duplicate determinations under these conditions is not significantly different from the mean coefficient of variation in a single determination.

INTRODUCTION

Determination of the circulating blood volume by a radioisotope technique is commonly used in the pre- and post-operative control in connection with major surgery.

The value of the determination, however, depends upon the possibility of detecting variations in blood volume within relatively short time intervals and with an uncertainty in the difference between two determinations smaller than the smallest variation that calls for treatment.

Several semiautomatic instruments are available for this determination[2, 8, 4, 13]. They measure the four necessary variables: Blood sample before injection, full syringe, emptied syringe, and blood sample after injection, but present only the final calculation of the blood volume in litres, without correction for individual haematocrit.

The radioactive test solution can be bought in only two sizes, and furthermore the instruments offer no possibility of determining the residual amount of activity before injection.

The uncertainty on the single blood volume determination will according to classical isotope physics increase with any increase in residual radioactivity in the blood from previous determinations. The semiautomatic instruments offer no possibility of detecting or avoiding this increase in uncertainty when unknown test solutions are used.

The present paper will discuss the results of a series of studies on phantoms and on patients in a steady state, with a system where these drawbacks have been taken into consideration.

MATERIALS AND METHODS

The instrument used is described in detail elsewhere[3]. The injections[6] are delivered from tubules, which are prepared weekly at our isotope laboratory[10]. Five dose sizes of HSA-^{131}I are prepared with an approximate doubling from dose to dose, the lowest dose being 2.3 µCi and the highest 25 µCi according to a scheme where after a week of decay all doses will correspond to the dose one number lower in the dose sequence.

Human serum albumin labelled with ^{131}I from The Radiochemical Centre, Amersham, was used. They state that: "At least 95% (usually above 98%) of the activity is protein bound" and "less than 5% globulin and no denatured albumin are present".

Gel chromatography of the diluted preparation after one week's storage in tubules showed that 91% of the ^{131}I-activity was situated at a place similar to that of monomer albumin, 7% was present at the place of the dimer form, and the last 2% was found as tailing from the point of application to that of the dimer albumin.

The radioactive tracer was injected through a catheter placed in a central vein[9] or, where this was not possible, into a peripheral vein; in both cases the injection was followed by flushing with glucose water. The blood samples were drawn from this catheter or cannula without, or with the smallest possible, stasis.

The blood samples were collected in test tubes treated with saponine to obtain haemolysis, in order to avoid changes in measuring geometry by the settling of the red cells[10]. The steps in the determination are outlined in fig. 1.

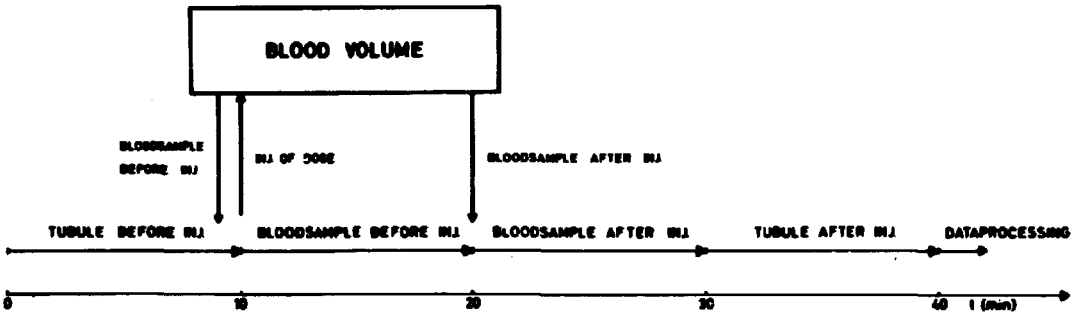

Fig. 1. Scheme for one blood volume determination.

After five subsequent blood volume determinations, the whole-body radiation dose received by the patient is 0.2 rads[11], which is approximately twice the amount of radiation received from a single chest X-ray. The radiation dose to the thyroid is calculated to be below 2.5 rads if the uptake is blocked by 250 mg NaI given perorally prior to the study[11].

RESULTS

Theoretical Results

A theoretical experiment with calculated count rates in a computer program showed that by using the same ^{131}I dose in five determinations the coefficient of variation increases from 1.3% on the first determination

to 3.1% on the fifth, whereas a doubling of the amount of ^{131}I-HSA from measurement to measurement would result in a decrease in the coefficient of variation from 1.3% on the first to about 1.0% on the fifth determination[10], the decrease being caused by better counting statistics.

In vitro Results

The system was tested on three known water phantoms. It was found that a doubling of the dose from one measurement to the next through five determinations on each of three volumes resulted in a coefficient of variation between 1.3 and 1.8% increasing with volume and decreasing with dose size.

In vivo Results

The results from 26 duplicate blood volume determinations are presented in table 1. The patients were in steady state as far as blood volume is concerned, and furthermore the second measurement was performed within $2\frac{1}{2}$ hours after the first one. Columns A and B show the volumes and the uncertainties.

The coefficient of variation was calculated from the uncertainties on the single determination with the following formula:

$$\frac{2 \cdot s(BV_v) \cdot 100}{(A + B)} \%,$$

and is shown in column D. The coefficient of variation was calculated from the duplicate determinations alone according to the following formula:

$$\frac{(|A - B|) \cdot 2 \cdot 100}{\sqrt{2} \cdot (A + B)} \%,$$

and is shown in column E.

The mean value of the "technical" coefficient of variation containing counting uncertainties and geometrical factors (column D) is $1.3\% \pm 0.04\%$ (mean value $\pm$ standard error of mean), while the mean coefficient of variation on the total measuring procedure (column E) is $1.7\% \pm 0.2\%$. The figures in the two columns, D and E, which are presumed to be normal distributed, were tested by Student's t-test and were found not to be significantly different ($0.1 < P < 0.2$).

Table 1

The results from 26 duplicate blood volume determinations

Pt. No.	1st determination		2nd determination		C. Time between the two determinations (h m)	D. The coefficient of variation (%)	E. The coefficient of variation (%)
	BV_V(litres)	$\pm 2 \cdot s(BV_V)$(litres)	BV_V(litres)	$\pm 2 \cdot s(BV_V)$(litres)			
1	4.3	0.11	4.5	0.12	1 00	1.4	3.1
2	5.5	0.16	5.3	0.14	1 30	1.5	2.6
3	3.9	0.08	3.9	0.09	1 15	1.2	0
4	6.2	0.18	5.9	0.16	0 45	1.5	3.4
5	6.8	0.15	6.9	0.17	1 00	1.2	0.9
6	6.2	0.17	6.2	0.17	1 00	1.4	0
7	4.3	0.10	4.1	0.08	0 45	1.2	3.3
8	4.6	0.06	4.7	0.09	1 00	1.0	1.4
9	5.0	0.14	4.9	0.11	1 00	1.4	1.4
10	4.4	0.07	4.5	0.09	1 30	1.0	1.5
11	5.7	0.16	5.6	0.15	1 00	1.4	1.2
12	5.6	0.09	5.3	0.10	1 00	0.9	3.8
13	5.1	0.14	5.2	0.14	1 15	1.4	1.3
14	5.1	0.14	5.0	0.13	1 00	1.4	1.3
15	5.8	0.19	5.7	0.16	1 00	1.7	1.2
16	4.3	0.10	4.4	0.10	1 00	1.1	1.5
17	4.1	0.11	4.1	0.10	1 15	1.3	0
18	3.8	0.09	4.0	0.09	1 00	1.2	3.6
19	4.3	0.12	4.1	0.10	1 00	1.4	3.3
20	5.0	0.14	5.0	0.13	1 00	1.4	0
21	6.0	0.19	5.9	0.17	1 00	1.6	1.1
22	7.0	0.13	6.9	0.14	2 00	1.0	0.9
23	4.8	0.12	4.6	0.10	1 30	1.3	2.9
24	4.8	0.18	5.0	0.11	1 15	1.16	2.8
25	4.1	0.12	4.0	0.10	2 30	1.5	1.6
26	5.6	0.11	5.6	0.13	1 30	1.2	0

DISCUSSION

The automatic calculation of physical uncertainty is important for the clinical evaluation of the result, and as failures in the procedure will mostly result in an alteration of the "normal" uncertainty, these failures may be detected.

The good agreement within the duplicate determinations was primarily a result of the use of increasing doses. The following points may, however, also have been of influence: (1) the injection technique prevented retention of the tracer at the point of injection, (2) the sample technique prevented differences in haematocrit caused by stasis, (3) the HSA-^{131}I used on a patient was from the same batch, so that differences caused by different amounts of unbound iodine were avoided. Degradated HSA-^{131}I may cause errors in the blood volume determination. This denaturation can be estimated by gel chromatography. About 30% of the 7% dimer albumin present in a preparation of HSA-^{131}I can be regarded as being denatured[12] and may rapidly leave the blood. Freeman[5] has found 75% of heat-denatured albumin in perfused rat liver between 8 and 15 min after injection.

As the time between injection of the tracer and the withdrawal of the sample was only 10 minutes, the passage of native albumin to the extravascular compartment is probably negligible. Andersen[1] has found the 24-hour passage to the extravascular compartment of HSA-^{131}I to be 39%. He has drawn attention to the fact that this elimination rate is determined after the initial mixing period so that nothing is known about the passage during this period. However, if it is assumed that the passage follows a single exponential during the mixing period as is found to be the case after complete mixing, the elimination in 15 minutes is approximately 0.5%. The 2% free iodine can be regarded as having been completely cleared from the blood during this period of time. Accordingly, the amount of injected radioactivity remaining intravenously must be at least 96% (91% native serum albumin + 70% of the 7% dimer serum albumin). The measured blood volume will be too high, but not by more than 5%. Since the clinical interest is that of the difference between two subsequent determinations, this maximum error of 5%, which is the same in both determinations, is not important.

The system has proved to yield satisfactory results in clinical use.

ACKNOWLEDGEMENT

The authors wish to thank Jette Lise Hansen, Knud Jørgensen, and Poul Buus for their excellent technical assistance.

REFERENCES

1) Andersen, S.B. and Gabuzda, T.G., Simultaneous Determination of Plasma Volume with T-1824 and ^{131}I-labelled Autologous and Homologous Paraprotein. Clin. Sci. 26 (1964) 41-45.

2) Aust, J.B., Chou, S.N., Marvin, J.F., Brackney, E.L., and Moore, G.E., A Rapid Method for Clinical Total Blood Volume Determination Using Radioactive Iodinated Human Serum Albumin (RIHSA). Proc. Soc. Exp. Biol. Med. 77 (1951) 514-518.

3) Bojsen, J., Funch-Rosenberg, H., and Müller, Th., The Construction of an Instrument for More Accurate, Repeated Blood Volume Determinations Using HSA-^{131}I. Int. J. Appl. Radiat. Isotop. 21 (1970) 691-695.

4) Fields, T., Kaplan, E., and Terril, M., A Simplified Technique for Blood Volume Determinations Using I^{131}HSA. J. Lab. Clin. Med. 43 (1954) 332-334.

5) Freeman, T., The Biological Behaviour of Normal and Denatured Human Plasma Albumin. Clin. Chim. Acta 4 (1959) 788-792.

6) Funch-Rosenberg, H. and Müller, Th., Die Tubule als Einzeldosisbehälter für Radioisotopen. Dansk Tidsskr. Farm. 43 (1969) 75-79.

7) Gregersen, M.I. and Rawson, R.A., Blood Volume. Physiol. Rev. 39 (1959) 307-342.

8) Hlad, C.J. and Tanz, R., An Analysis of Technical Errors in Radioalbumin Blood Volume Methods and Presentation of a Modified Method. J. Lab. Clin. Med. 52 (1958) 289-298.

9) Ladegaard-Pedersen, H.J. and Engell, H.C., Blood Volume Determination Using One Catheter Located in a Central Vein. Acta Chir. Scand. 135 (1969) 105-108.

10) Müller, Th., Funch-Rosenberg, H., and Bojsen, J., Successive Blood Volume Determinations with Human Serum Albumin-^{131}I without Increasing Uncertainty. A Solution of Dose and Dosage Problems. Dansk Tidsskr. Farm. 43 (1969) 181-187.

11) Statens Strålskyddsinstitut, Stråldoser från radioaktiva ämnen i medicinskt bruk (1969).

12) Wallevik, K., The Finsen Laboratory, The Finsen Institute, private communication.

13) Williams, J. A. and Fine, J., Measurement of Blood Volume with a New Apparatus. New Engl. J. Med. 264 (1961) 842-848.

A Thermodynamic Flow Meter

by

N. E. Kaiser

Section for Experimental Technology

Abstract

A flow transducer for use in extracorporeal blood loops was developed. The transducer works on the principle of a cooling fin. The flow is determined from measurement of two temperatures in the fin. The transducer was tested with water, and the test results are in good agreement with calculations.

A prototype flow transducer has been developed for use in extracorporeal blood loops such as artificial kidneys and blood irradiation units.

The transducer is very simple. In order not to harm the blood, the wetted surface of the transducer has no corners or sharp edges. There are no blind loops, no change in flow area, and no heating. The necessary electronic equipment is very small and fairly inexpensive.

The transducer works on the basic principle of a cooling fin between two heat sources of the same temperature T_o above the surroundings (fig. 1).

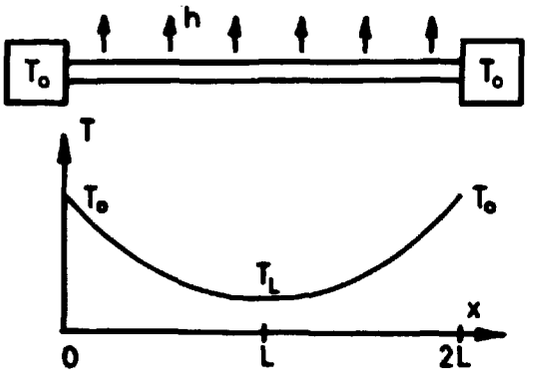

Fig.1.

In a straight cooling fin of length 2L, made of a material with thermal conductivity k, with a constant cross section A, and cooled along the perimeter P with a heat transfer coefficient h, the temperature distribution along the fin T_x can be expressed as

$$T_x = T_o \cdot (\exp(m(2L - x)) + \exp(m \cdot x))/(1 + \exp(m \cdot 2L)),$$

where $m = \sqrt{(h \cdot P)/(k \cdot A)}$.

In particular, we get the temperature in the middle (x = L)

$$T_L = T_o/\cosh(\sqrt{(h \cdot P)/(k \cdot A)} \cdot L).$$

Note, that this equation does not contain the amount of heat transferred from the fin to the coolant.

With the dimensionless groups, Reynolds', Prandtl's, and Nusselt's numbers defined as $Re = c \cdot d \cdot \rho/\mu$, $Pr = \mu \cdot C_p/k$, and $Nu = h \cdot d/k$, the heat transfer coefficient h can be determined from the equations

$$Nu = 3.65 + 0.0668(Re \cdot Pr \cdot d/L)/(1 + 0.045(Re \cdot Pr \cdot d/L)^{2/3})$$

and

$$Nu = 0.116(Re^{2/3} - 125)Pr^{1/3} \cdot (1 + (d/L)^{2/3})$$

valid in the laminar and turbulent flow regimes respectively.

Combining the above equations we get

$$T_o/T_L = f(\text{flow, geometry, fin material data, fluid data}).$$

With a fixed geometry and known material and fluid data the temperature ratio is a function of flow alone.

In the transducer the fin is curved into the shape of a circular ring, and the heat is transferred from the inner surface by the flow through the ring. In order not to harm the blood, the ring is not heated, but cooled (with air of room temperature). This gives the same heat transfer equations, but with temperatures of opposite sign.

The prototype transducer is shown in fig. 2. It contains two constantan rings cast in araldite resin, making a smooth tube. The two rings are connected with a small constantan wire. The left-hand ring is the real transducer and can be cooled through a small copper rod. The right-hand ring

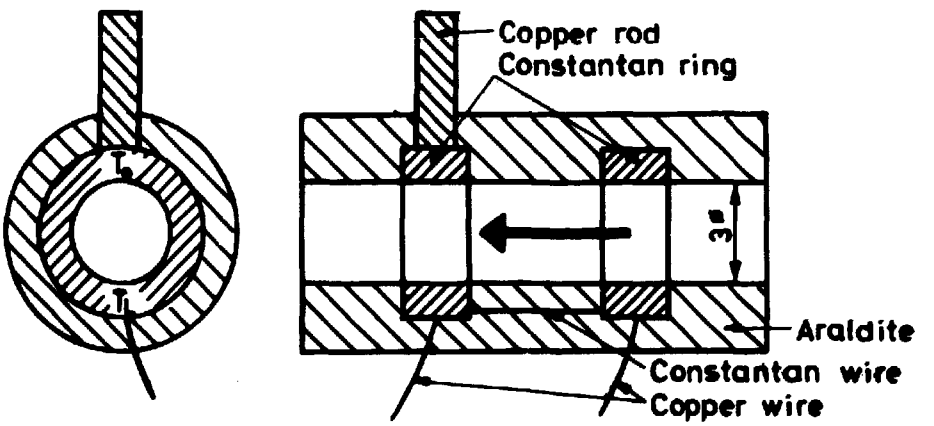

Fig.2.

is used as reference junction for the temperature measurements. Constantan was chosen because of a suitable thermal conductivity and a high thermoelectric force against copper so that it can be used directly as one of the leads in a thermocouple.

With the data for the prototype transducer, the theoretical values of the temperature ratios as functions of flow were calculated with water and human blood as fluids.

The calculations were carried out with two models.

In the first the formula for the straight fin is used directly (one-dimensional heat conduction) with a mean length of the ring and a "cooled" perimeter reduced to the mean length, but without taking into account the heat conduction in the araldite resin.

In the other model a two-dimensional model of the actual circular geometry is used, and heat conduction in the araldite is included. Two versions of this model were used, one without and one with heat loss to the surroundings. The calculations on the two-dimensional model were made with the B-6500 computer.

The results of the calculations are shown in the diagrams in figures 3, 4, and 5. Figure 3 shows the heat transfer coefficient h as a function of the Reynolds number Re with blood and water as fluids. Figure 4 shows the temperature ratio T_o/T_L as a function of the heat transfer coefficient h. In the actual range of h there is remarkably good agreement between the very simple one-dimensional model and the most complicated (and thus the most realistic) model. In figure 5, figures 3 and 4 are combined to give the temperature ratio as a function of the flow represented by the Reynolds number.

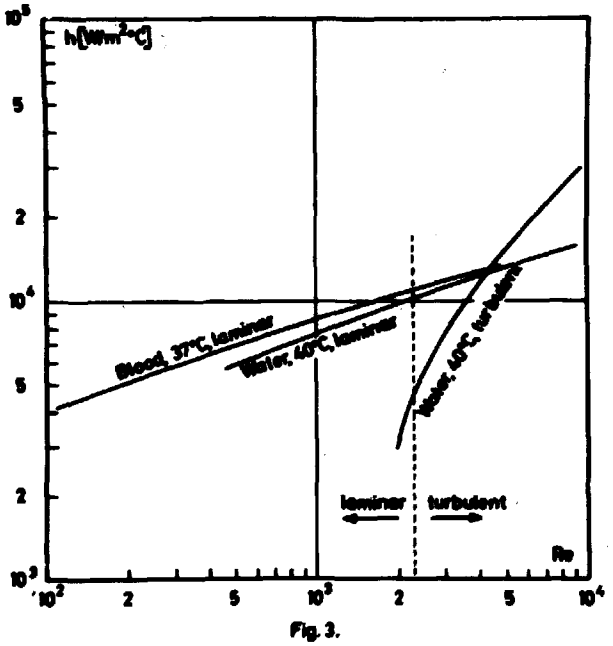

Fig. 3.

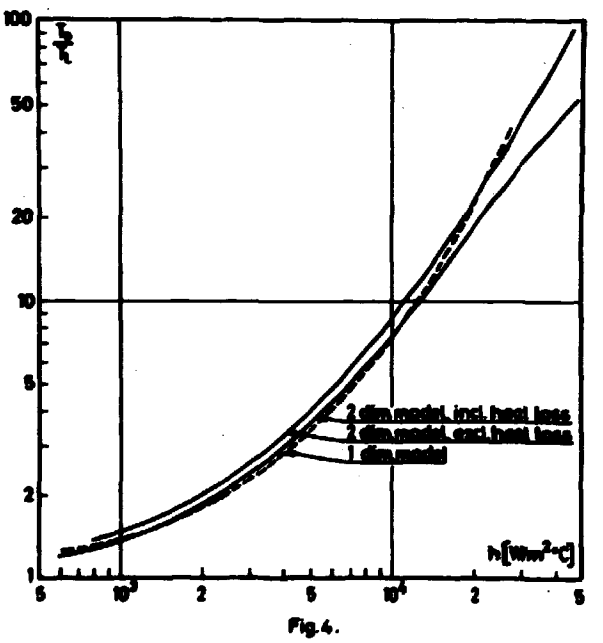

Fig.4.

Nomenclature:

A	area	P	wetted perimeter
c	velocity	Pr	Prandtl's number
C_p	specific heat	Re	Reynolds' number
d	diameter	T	temperature
h	heat transfer coefficient	x	length coordinate
k	thermal conductivity	μ	dynamic viscosity
L	length	ρ	dens y
Nu	Nusselt's number		

REFERENCES

P. S. Andersen, The Finite Element Method Employed for the Calculation of Stationary and Nonstationary Temperature Fields. Risø-M-2012 (1968) 22 pp.

P. S. Andersen, A Computer Programme for the Solution of

$$\frac{\partial}{\partial x}\left(k_x \frac{\partial \Phi}{\partial x}\right) + \frac{\partial}{\partial y}\left(k_y \frac{\partial \Phi}{\partial y}\right) + q''' - c \frac{\partial \Phi}{\partial t} = 0$$

by the Finite Element Method. Risø-M-2013 (1968) 23 pp.

M. Jacob, Heat Transfer 1 .(Wiley, New York, 1958).

W. H. McAdams, Heat Transmission, 3rd edition. (McGraw-Hill, New York, 1954) 532 pp.

Konrad Diem (editor), Scientific Tables. Documenta Geigy, 6th edition. (J. R. Geigy S. A., Basel, 1962) 778 pp.

VDI-Wärmeatlas. Berechnungsblätter für den Wärmeübergang. (VDI-Verlag, Düsseldorf, 1963). Loose leaves.

Simultaneous Determination of Arsenic, Manganese and Selenium in Biological Materials by Neutron Activation Analysis

by

K. Heydorn and E. Damsgaard
Isotope Division

Abstract

A new method was developed for the simultaneous determination of arsenic, manganese, and selenium in biological material by thermal-neutron activation analysis.

The use of Se-81m as indicator for selenium permitted a reduction of activation time to 1 hour for a one-gram sample, and a possible loss of volatile compounds during irradiation was avoided.

No pre-treatment of the sample is required, and the radiochemical separation scheme is based on simple chemical operations, completed in less than 3 hours.

A systematic experimental investigation of the performance characteristics of the method was carried out, including studies of the accuracy of the results.

The actual precision achieved in routine application of the method in the analytical laboratory was in good agreement with the calculated precision, and the results are therefore well suited for statistical evaluation of differences at the ppb level in samples of biological tissue.

INTRODUCTION

The possible development of abnormal trace element concentrations in uraemic patients undergoing regular peritoneal dialysis has been suggested as a factor in the evolution of uraemic polyneuropathy[1].

The observation by Brune et al.[2] that uraemic patients show elevated concentrations of arsenic in blood, focused attention on this element, and the unique metabolic antagonism between arsenic and selenium[3] made the simultaneous determination of both these elements desirable. Manganese was included because the concentrations of manganese appear to be regulated by a homeostatic mechanism which does not depend on excretion through the kidneys[4].

Reliable measurement of possible deviations from normal levels of these elements in human tissue requires analytical techniques capable of determining concentrations at the ppb-level with good precision and accuracy.

Manganese can be determined in small biological samples with sufficient sensitivity by the catalytic oxidation of leucomalachite green with periodate[5], while selenium can be determined by fluorometry of the 2, 3-diaminonaphthalene complex[6]. For arsenic colorimetric measurement of the reaction of arsine with silver diethyldithiocarbamate[7] is satisfactory for larger samples only, while small samples require the use of neutron activation analysis[8].

Either of the three elements can be determined by neutron activation analysis. Selenium may be determined instrumentally after intense irradiation and several weeks' decay by the measurement of Se-75 with a Ge(Li)-detector[9], or, in dialyzed samples, after a very short irradiation followed by the measurement of Se-77m with a scintillation detector[10]; comparable sensitivity is achieved by β-counting of Se-81 after rapid radiochemical separation[11], while the highest sensitivity and precision is reached by combining radiochemical separation with the measurement of Se-75[12]. Attempts to utilize Se-79m[13] or Se-81m[14] have so far been unsuccessful for achieving a satisfactory limit of detection. Neither arsenic nor manganese have been determined in biological samples with satisfactory precision by purely instrumental analysis, but only relatively simple radiochemical separations are needed before measurement of As-76[15] or Mn-56[16].

A combined determination of all three elements is possible with the automatic group separation system developed by Samsahl[17], but it requires

the use of special apparatus not available in most laboratories.

An analytical procedure employing standard laboratory equipment was therefore developed for the simultaneous determination of arsenic, manganese, and selenium in biological material by neutron activation analysis.

METHOD OF ANALYSIS

The absence of reagent blanks characteristic of activation analysis is limited to the post-irradiation treatment of the sample, and operations before irradiation should be restricted to the bare minimum necessary for sampling; radiochemical separation thus becomes necessary for all three elements.

Irradiation

Intense reactor irradiation of biological samples leads to radiolysis of the sample material and is often accompanied by a temperature rise, both of which may result in volatilization of elements such as arsenic and selenium. Mild irradiation conditions are thus preferable together with irradiation times at the minimum needed for satisfactory sensitivity.

The pneumatic tube system of the Danish reactor DR 2 offers a thermal neutron flux of 7×10^{12} neutrons/cm^2/s, and the energy absorption in biological tissue from the accompanying fast neutrons and γ-irradiation is about 5 Mrads/h, corresponding to a maximum decomposition loss of well below 0.5% per hour of irradiation.

Experimental sensitivities reported by Yule[18] show that, for an irradiation time of one hour, Se-81m is the most sensitive indicator for selenium, apart from Se-77m which leaves no time for chemical separation. Counting yields observed for As-76 and Mn-56 produce satisfactory sensitivities for arsenic and manganese as compared with selenium.

It was found that satisfactory precision for all three elements in biological material could be achieved with a one-hour irradiation in the pneumatic tube system by choosing a sample size of about one gram. The surface temperature of the sample during irradiation did not exceed 42°C, and the total activity at the end of irradiation was less than 2 mCi. No special precautions were therefore called for in the transfer and handling of the irradiated sample.

Radiochemical Separation

Incorporation of separation procedures for manganese and selenium into an existing method for the separation of arsenic[15] led to a simple method for the combined separation of all three elements.

Selenium was precipitated with ascorbic acid immediately after decomposition of the sample and before the cupferron scavenging. Manganese can be determined after the precipitation of arsenic with thioacetamide by the removal of sodium with hydrated antimony pentoxide[16].

Further purification of selenium by dissolution and extraction into methyl isobutyl ketone[19] proved necessary, whereas no separation of manganese was required - except for samples of blood serum.

The separation procedure is shown schematically in fig. 1; it is completed within 3 hours after the end of irradiation.

Detection and Measurement

Satisfactory sensitivity required counting in well-type NaI(Tl) scintillation detectors for up to 80 minutes, and for Se-81m an additional counting period of the same length some hours later was needed to eliminate the influence of Se-75 and other long-lived activities.

Counting times were small compared with the half-lives of Mn-56 and As-76, but for Se-81m the counting time exceeded one half-life, and a correction was necessary for decay during the counting period.

Counting data from the multi-channel analyzers were produced on punched paper tape and processed via a teletype terminal in a GE 265 time-sharing computer system.

Peak areas were calculated from a smoothed spectrum generated by a five-point polynomial convolution of the counting data with the technique described by Savitzky and Golay[20]. Peak boundaries for both sample and comparator were decided by the method of Yule[21], except that the sign changes of the first derivative were determined from a third degree polynomial convolution of the smoothed sample spectrum.

All samples and comparators were counted in half-dram polyethylene vials as 1.0 ml solutions, so as to eliminate differences in counting geometry.

Chemical Yield

Determination of chemical yield by re-irradiation has several advantages over other methods of yield determination. No transfer from the counting

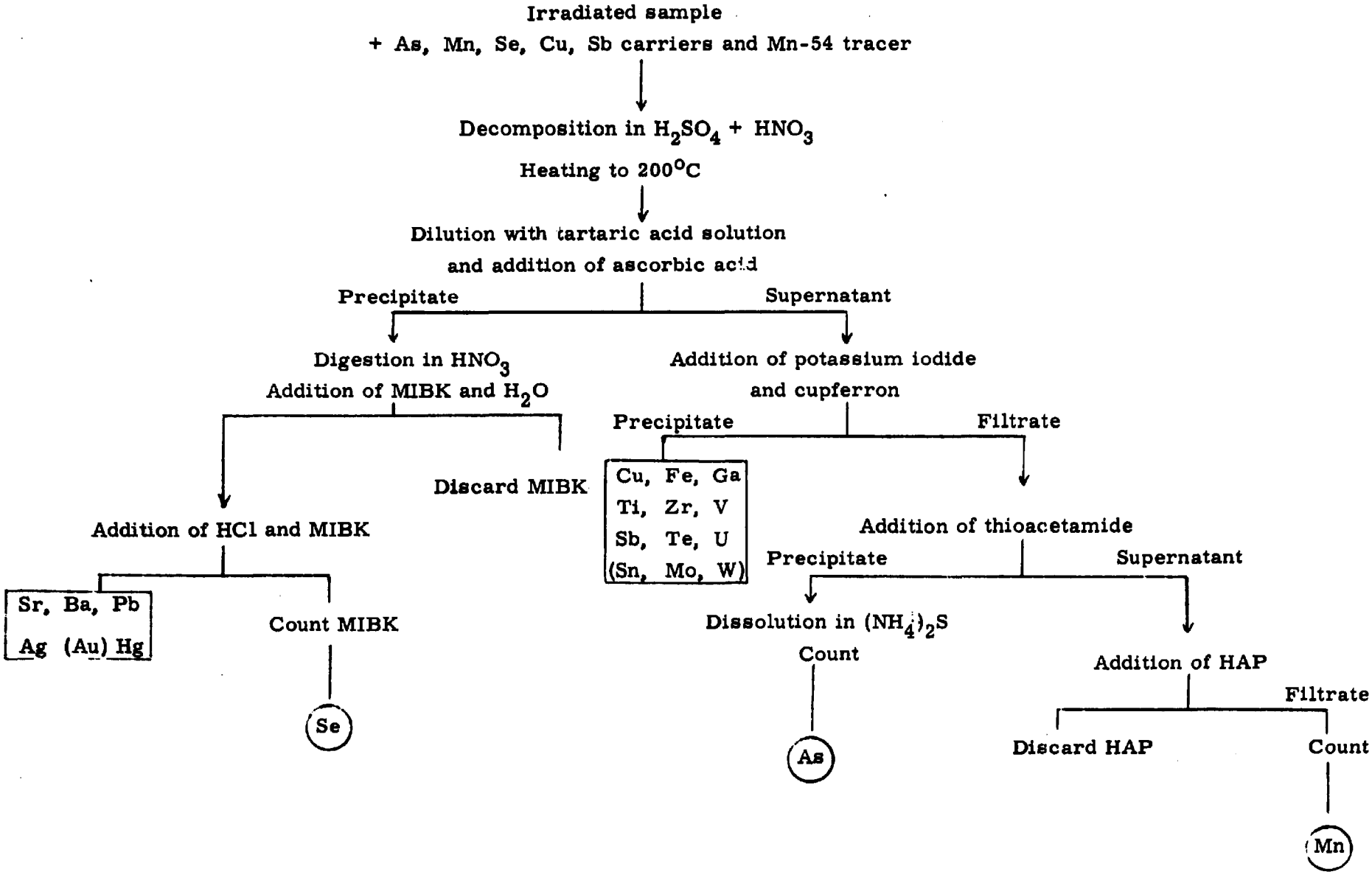
Irradiated sample
+ As, Mn, Se, Cu, Sb carriers and Mn-54 tracer
Decomposition in H_2SO_4 + HNO_3
Heating to 200°C
Dilution with tartaric acid solution
and addition of ascorbic acid
Precipitate
Supernatant
Digestion in HNO_3
Addition of MIBK and H_2O
Addition of potassium iodide
and cupferron
Precipitate
Filtrate
Discard MIBK
Cu, Fe, Ga
Ti, Zr, V
Sb, Te, U
(Sn, Mo, W)
Addition of HCl and MIBK
Addition of thioacetamide
Precipitate
Supernatant
Sr, Ba, Pb
Ag (Au) Hg
Count MIBK
Dissolution in $(NH_4)_2S$
Count
Addition of HAP
Filtrate
Discard HAP
Count
Se
As
Mn

vial takes place, and when identical indicators are used for both analysis and yield, differences in self-absorption between sample and comparator are automatically compensated for.

In addition, positional differences in neutron flux during the simultaneous irradiation of sample and comparator may be neutralized, and the influence of interfering elements may be reduced[15].

The yield of selenium was determined by re-irradiation for 10 seconds and counting under exactly the same conditions as in the analytical determination of Se-81m. The arsenic yield was measured after 10 minutes' re-irradiation in a γ-ionization chamber for the determination of As-76[22].

The manganese yield was determined as the recovery of Mn-54 tracer added to the manganese carrier, by counting the sample after the decay of Mn-56. The practically identical γ-energies at 0.84 MeV give the same compensation for differences in self-absorption as that achieved by re-irradiation.

Procedure

Apparatus

Danish reactor DR 2 operating at 5 MW with pneumatic tube system extending into a thermal neutron fluence of 7×10^{12} n/cm^2/s.

Nuclear Data multi-channel pulse height analyzers with Harshaw 3"x3" and 2" x 1 3/4" well-type NaI(Tl) scintillation detectors.

Vibron Electrometer connected to Solartron Digital Voltmeter with National Physical Laboratory ionization chamber.

Reagents

Sulphuric acid 97-98%
Nitric acid 100%
Hydrochloric acid 37%
Methyl isobutyl ketone (MIBK)
Thioacetamide
Hydrated antimony pentoxide (HAP), Carlo Erba
Ascorbic acid
Ammonium sulphate solution 50% w/v
Ammonium sulphide solution 40%, Riedel-de Haën
Tartaric acid, 1% w/v
Potassium iodide, 15% w/v
Cupferron, 6% w/v solution prepared weekly

Except where otherwise indicated, all reagents are Merck p. a.

Carriers

Se-carrier, 10 mg/ml as Se(IV) in aqueous solution
As-carrier, 10 mg/ml as As(III) in 0.15 M ammoniacal solution
Mn-carrier, 10 mg/ml as Mn(II) in 4 M nitric acid, containing 2 μCi/ml of Mn-54
Cu-carrier, 10 mg/ml as Cu(II) in aqueous solution
Sb-carrier, 10 mg/ml as Sb(III) in 1 M citric acid and 0.25 M oxalic acid solution

Carrier solutions are stable systems that can be stored in rubber-stoppered glass bottles for long periods of time. Accurately prepared carrier solutions, whose concentrations have been verified by chemical analysis, are used for the preparation of comparator standards by dilution with redistilled water.

Comparator Standards

Se-comparator, 50 μg Se/ml
As-comparator, 0.5 μg As/ml
Mn-comparator, 0.2 μg Mn/ml

Comparator solutions are stored in screwcap polyethylene bottles, and the changes in concentration were found to be about 1% per month for Mn and significantly less for As and Se.

Irradiation

Samples of about 1 gram are weighed into half-dram polyvials * and stored in a deep freezer until activation.

Comparator standards of about 1.2 ml of Se, As, and Mn are transferred to half-dram polyvials.

All polyvials are heat-sealed and placed in a polyethylenebag which is also heat-sealed, and subsequently transported in a polyethylene rabbit to the irradiation position, where neutron activation takes place for 1 hour.

Decomposition

In a 50 ml beaker 2 ml of Cu-carrier, 0.1 ml of Sb-carrier, and 100 μl of Mn-carrier are dried at 110°C. After cooling 500 μl of Se-carrier and 100 μl of As-carrier are added, followed by 2.5 ml of sulphuric acid.

Identical volumes of Se-, As-, and Mn-carrier are transferred to separate half-dram polyvials, and diluted to 1.0 ml; the vials are heat-sealed and set aside for yield determination.

The irradiated sample is transferred to the beaker, taking care to moisten all sample material with the sulphuric acid carrier mixture. The beaker is placed on a hot plate at 130°C, and nitric acid is added dropwise to prevent charring, while the plate temperature is slowly raised to 250°C. After complete destruction of organic matter, heating is continued until fumes of sulphuric acid evolve.

Separation of Selenium

After cooling, the solution is poured slowly into a 40 ml centrifuge tube containing 5 ml of tartaric acid solution, and 10 ml of water are added.

Selenium is now precipitated by addition of 0.5 g ascorbic acid, followed by stirring for at least 3 minutes. After centrifugation the supernatant is transferred to another centrifuge tube for subsequent separation of arsenic.

---

* Olympic Plastics Corporation, Los Angeles

The selenium precipitate is washed twice with water and dissolved in 15 drops of nitric acid. Addition of 0.5 ml MIBK is followed by up to 10 drops of water to bring about the separation of two layers. After centrifugation the MIBK layer is discarded, 2.0 ml of hydrochloric acid with 1.1 ml of MIBK are added, and selenium is extracted by stirring for 1 minute.

After centrifugation the aqueous layer is discarded, and the MIBK phase is washed 3 times by stirring with 3 x 2 ml of ammonium sulphate solution.

Finally, the MIBK is transferred to a half-dram polyvial which is then heat-sealed and ready for counting.

Counting of Selenium-81m

A comparator standard is made by transferring 1000 µl of the irradiated Se-comparator to a half-dram polyvial.

The selenium sample is counted for 80 minutes live time beginning 90 minutes after pile-out in a 2" x 1 3/4" well-type scintillation detector at a gain of 3.3 keV/channel. The comparator standard is then counted for 4 minutes under the same conditions.

Both sample and comparator are recounted under identical conditions 2 hours later.

Yield of Selenium

The separated selenium sample and the Se-carrier sample set aside for yield determination are irradiated together in the reactor for 10 seconds.

About 3 hours after pile-out each sample is counted for 4 minutes under the same conditions as above.

The chemical yields of selenium averaged 75%.

Calculation of Result

Selenium is determined from the 103 keV peak area of the difference spectrum between the first and the second counting, correction being made for deviations in decay and counting time between sample and comparator.

With decay corrections referring to the midpoint of the counting period, a factor of 0.96 must be applied to the results from the 80 minute countings.

The chemical yield is calculated in the same way from the direct spectra of the re-irradiated sample and carrier.

The selenium content, corrected for chemical yield, is converted into nanograms.

Separation of Arsenic

To the supernatant from the selenium precipitation are added 4.0 ml of potassium iodide and 2.5 ml of cupferron solution under vigorous stirring. Stirring is continued for 3 minutes, and after at least 1 hour the slurry is filtered through a dense filter*. About 100 mg of thioacetamide are added to the filtrate, and arsenic is precipitated as the sulphide by gentle heating on a water bath. After centrifugation the supernatant is transferred to another centrifuge tube for subsequent separation of manganese.

The precipitate is washed 3 times with water, dissolved in 1.0 ml of ammonium sulphide solution, and finally transferred to a half-dram polyvial which is then heat-sealed and ready for counting.

Counting of Arsenic-76

A comparator standard is made by transferring 1000 µl of the irradiated As-comparator to a half-dram polyvial.

* Schleicher and Schüll, type 602 eh

The arsenic sample is counted for 80 minutes live time 24 hours after pile-out in a 3" x 3" well-type scintillation detector at a gain of 6.7 keV/channel. The comparator standard is counted for 8 minutes under the same conditions.

Yield of Arsenic

The separated arsenic sample and the As-carrier sample set aside for yield determination are irradiated together in the reactor for 10 minutes.

About 24 hours after pile-out the samples are measured in the NPL ionization chamber with a polarizing voltage of 90 V, the voltage drop across a 100 GΩ resistor being read 3 times with 20 seconds' interval for each sample.

The chemical yields of arsenic averaged 85%.

Calculation of Result

Arsenic is determined from the 559 keV peak areas of sample and comparator corrected for differences in decay and counting time. The chemical yield is determined directly as the ratio between the average ionization chamber readings of the re-irradiated sample and carrier.

The arsenic content, corrected for chemical yield, is converted into nanograms.

Separation of Manganese

To the supernatant from the arsenic sulphide precipitation is added 0.5 g of HAP, and the mixture is stirred for 5 minutes. After centrifugation 1.0 ml is transferred to a half-dram polyvial, which is then closed and ready for counting.

Counting of Manganese-56

A comparator standard is made by transferring 1000 µl of the irradiated Mn-comparator to a half-dram polyvial.

The manganese sample is counted for 40 minutes live time no later than 5 hours after pile-out with a 3" x 3" scintillation detector at a gain of 6.7 keV/channel. The comparator standard is counted for 4 minutes under the same conditions.

Counting of Manganese-54

The separated manganese sample and the Mn-54 carrier sample set aside for yield determination are counted not earlier than 24 hours after pile-out under the same conditions as above.

Calculation of Result

Manganese is determined from the 847 keV peak area of the difference spectrum between the first and the second counting of the sample corrected for deviations from the comparator in decay and counting time.

The chemical yield is calculated in the same way from the 835 keV peak of the sample and carrier and should always be close to 4%.

The manganese content, corrected for chemical yield, is converted into nanograms.

ANALYTICAL EVALUATION

While neutron activation analysis shares with other analytical methods a number of possible errors such as interference from other elements, an investigation of its performance-characteristics[23] must include parameters of its own, whereas others, such as range, may be excluded.

A sharp distinction between random and non-random errors is not always relevant, because a proper design of analytical procedure permits cancellation of systematic errors so that their effect is randomized and may influence the precision, but not the accuracy, of the analytical results.

In the present method re-irradiation yield determinations of arsenic and selenium result in cancellation of errors from differences in self-absorption and irradiation position between sample and comparator, and may with optimum carrier composition[15] even result in randomization of interference from other elements.

Besides on interference from other elements, the accuracy of the method depends on complete exchange of activated nuclides with their respective carriers, and on the absence of a blank value.

The precision of the analytical results is affected by counting statistics and by random variations in neutron fluence between sample and comparator.

Interference

Interference from other elements is expressed as the ratio between a quantity of a particular element and the corresponding error of the analytical result.

Interference in activation analysis is therefore the product of a separation factor[24] S and an effective value f of the interfering element irradiated and counted as a sample and calculated by reference to a comparator standard of the element to be determined.

The experimental determination of a separation factor is carried out in two steps: measurement of a decontamination factor D, followed by determination of chemical yield y, where $D \times y = 1/S$.

The decontamination factor was determined by adding 10-100 μCi of a radioactive tracer of the highest possible specific activity of the interfering element to an unirradiated sample which was then processed according to the specified procedure. The ratio between the added activity and the activity of the separated sample is D.

The chemical yields of arsenic and selenium were determined by re-irradiation, while a fixed yield of 4% was assumed for manganese.

The effective value was determined by irradiating an aqueous sample of the interfering element for 1 hour along with comparator standards. A known quantity m of the irradiated interfering element was transferred to a half-dram polyvial and diluted to 1.0 ml with water; this sample was counted along with a comparator standard according to the specified counting procedure, and calculations were made to produce the apparent quantity of the element to be determined m^*. The effective value f is the ratio m^*/m, and may be negative.

The interference can now be expressed as f x S µg of As, Mn, Se error per µg of interfering element present, or its reciprocal D x y/f expressing the concentration of interfering element not to be exceeded to keep the error in the determination of As, Mn, and Se below 1 ppb.

The choice of interfering elements selected for investigation was made on the basis of expected effective values > 0.01 or comparatively poor separation factors. Experimentally determined interferences for the elements arsenic, selenium, and manganese, are listed in tables 1-3.

Carrier Exchange

Complete isotopic exchange between activated nuclides and carrier is usually brought about by quantitative oxidation or reduction to a common ionic species. Thus all forms of As are oxidized to As(V) during the nitric-sulphuric acid decomposition, and all Mn is reduced to Mn(II) by the addition of ascorbic acid. However, Se(IV) is partly oxidized to Se(VI) by nitric acid, and Se(VI) is not reduced by ascorbic acid; the accuracy of the selenium analysis therefore depends on the complete exchange between Se(IV) and Se(VI).

This was checked by adding 0.5 µCi Se-75 as selenate(VI) to an unirradiated sample, which was then processed according to the specified procedure; the separated selenium sample was counted, and the chemical yield determined by re-irradiation. The recovery of Se-75 and the chemical yield agreed well within counting statistics, proving that complete exchange between Se(IV) and Se(VI) had taken place during sample decomposition.

Blank

The blank value was determined by analysis of redistilled water according to the specified procedure; while no arsenic or selenium could be detected, small quantities of Mn were invariably observed.

The polyethylene vials used for irradiation contain about 20 ppb of Mn,

and it was found that up to 10% could be released to the water during irradiation, thereby giving rise to a manganese blank.

The limited contact between a tissue sample and the container wall makes a tissue blank value lower than that of water, and it is assumed to be < 3 ppb.

PRECISION AND ACCURACY

Calculated Precision

Random variations in neutron fluence between samples and comparator standards were determined by simultaneous irradiation of several comparators, and the standard deviation of the neutron fluence was found to be 2.5%.

The ratio between sample and comparator therefore has a standard deviation of 3.5%, which represents the limiting precision for single determinations of manganese. For arsenic and selenium, where a single determination requires 2 irradiations, the limiting precision corresponds to a standard deviation of 5%.

The precision expected from counting statistics is calculated from counting data on the assumption that the covariances between channels are zero[25], and its contribution is included in the calculated total standard deviation of a single determination.

Measured Precision

Experimental determination of precision was made by repeated analysis of biological materials covering the range of interest. Observed and calculated weighted average standard deviations are given in table 4, and they show satisfactory agreement.

The calculated standard deviation of a single determination is therefore a reasonable estimate of the actual precision of the result.

Limit of Detection

The a priori detection limit according to Currie[26] with errors of the first and the second kinds both equal to 5%, is 3.29 times the standard deviation of a blank.

The detection limit is here based on the standard deviation from counting statistics only, using the lowest results among the samples analysed. The resulting limits are given in table 2, but the ultimate limit of detection may be slightly lower.

For manganese the limit of detection is determined by the concentration of sodium in the sample, but the ultimate detection limit is estimated at 10 - 20 ppb.

Accuracy

With a manganese blank of less than 3 ppb, all three elements have blank values well below the detection limit for actual samples, and no detectable bias in the results can be expected.

Interferences from other elements at the levels expected in biological tissue are below the detection limit for all the elements investigated, and the significance of observed differences between analytical results can safely be tested on the basis of calculated standard deviations.

In the absence of suitable reference material of biological tissue, dried plant material was chosen for analysis, and results for kale and orchard leaves are presented in table 5.

The concentrations of arsenic and manganese far exceed those encountered in biological tissue, and reduction of sample weight yields poor precision of selenium results. The agreement with published values for kale is entirely satisfactory, while the results for As in orchard leaves are not consistent with the preliminary value given by National Bureau of Standards.

CONCLUSION

Simultaneous determination of arsenic, manganese, and selenium at the ppb level in biological tissue can be carried out by neutron activation followed by radiochemical separation.

No treatment of the sample material before activation is required so that contamination of the sample is avoided, and only moderate irradiation is employed so the loss of volatile elements is negligible.

The radiochemical separation is based on simple chemical operations and requires no precise control; its robustness makes it a reliable routine method in the analytical laboratory.

Conventional photo-peak integration was shown to yield accurate results with satisfactory precision for biological tissue.

Good agreement between experimental and calculated precision makes the results directly amenable to statistical evaluation.

ACKNOWLEDGEMENT

This work was initiated under the directorship of Professor T. Bjerge, whose invaluable support of a proposal by Professor M. Faber to study medical applications of neutron activation analysis is gratefully acknowledged.

The medical aspects of the present work are covered by experts at the Copenhagen Municipal Hospital, to whom we extend our sincere thanks for continuing inspiration and fruitful co-operation.

REFERENCES

1) P. Christoffersen, E. Damsgaard, K. Heydorn, N.A. Larsen, B. Nielsen, and H. Pakkenberg, Concentrations of Arsenic, Manganese, and Selenium in Peripheral Nervous Tissue of Patients with Uremia and a Control Group. Proc. Eur. Dialysis Transplant Ass. 6 (1969) 198.

2) D. Brune, K. Samsahl, and P.O. Wester, A Comparison between the Amounts of As, Au, Br, Cu, Fe, Mo, Se, and Zn in Normal and Uraemic Human Whole Blood by Means of Neutron Activation Analysis. Clin. Chim. Acta 13 (1966) 285-291.

3) O.A. Levander and L.C. Argrett, Effects of Arsenic, Mercury, Thallium, and Lead on Selenium Metabolism in Rats. Toxicol. Appl. Pharmacol. 14 (1969) 308-314.

4) G.C. Cotzias and P.S. Papavasiliou, Primordial Homeostasis in a Mammal as Shown by the Control of Manganese. Nature 201 (1964) 828-829.

5) A.A. Fernandez, C. Sobel, and S.L. Jacobs, Sensitive Method for the Determination of Submicrogram Quantities of Manganese and Its Application to Human Serum. Anal. Chem. 35 (1963) 1721-24.

6) J.H. Watkinson, Fluorometric Determination of Selenium in Biological Material with 2,3-Diaminonaphtalene. Anal. Chem. 38 (1966) 92-97.

7) J. Bäumler, J.I. Obersteg, and R. Shafer, Determination of the Level of Arsenic in Human Bodies (Population of Basle). Deut. Z. Gericht. Med. 64 (1968) 56-61.

8) K. Heydorn, Environmental Variation of Arsenic Levels in Human Blood Determined by Neutron Activation Analysis. Clin. Chim. Acta 28 (1970) 349-357.

9) B. Maziere, D. Comar, and C. Kellershohn, Dosage, par radioactivation neutronique, du selenium dans les milieux biologiques. Bull. Soc. Chim. Fr. (1970) 3767-71.

10) R.C. Dickson and R.H. Tomlinson, Instrumental Radioactivation Analysis of Selenium in Biological Materials. Int. J. Appl. Radiat. Isotop. 18 (1967) 153-159.

11) H.J.M. Bowen and P.A. Cawse, The Determination of Selenium in Biological Material by Radioactivation. Analyst 88 (1963) 721-726.

12) E. Steinnes, Determination of Traces of Selenium in Biological Tissue by Neutron Activation. Int. J. Appl. Radiat. Isotop. 18 (1967) 731-734.

13) R. Kuroda, Activation Analysis of Selenium Using the 3.9-Min Se-79m Isomer. TID 17272 (1962) 68-69.

14) W.H. Strain, C.G. Rob, W.J. Pories, R.C. Childers, M.F. Thompson, J.A. Hennesen, and F.M. Graber, Element Inbalances of atherosclerotic aortas. In: Modern Trends in Activation Analysis. Proceedings of the 1968 International Conference, Gaithersburg, Md., 7-11 October 1968. Edited by J.R. DeVoe and P.D. LaFleur. (National Bureau of Standards, Special Publications, 312) 1 (USGPO, Washington, 1969) 128-133.

15) K. Heydorn, Improvement of Accuracy by Multiple Carrier Addition Followed by Reirradiation Yield Determination in a Simple Method for the Determination of Arsenic in Biological Material. In: Nuclear Activation Techniques in the Life Sciences. Proceedings of a Symposium, Amsterdam, 8-12 May 1967. (Vienna, IAEA, 1967) 179-188.

16) F. Girardi and E. Sabbioni, Selective Removal of Radio-Sodium from Neutron-Activated Materials by Retention of Hydrated Antimony Pentoxide. J. Radioanal. Chem. 1 (1968) 169-178.

17) K. Samsahl, P.O. Wester, and O. Landström, An Automatic Group Separation System for the Simultaneous Determination of a Great Number of Elements in Biological Material. Recovery and Reproducibility Studies. Anal. Chem. 40 (1968) 181-187.

18) H.P. Yule, Experimental Reactor Thermal-Neutron Activation Analysis Sensitivities. Anal. Chem. 37 (1965) 129-132.

19) H. Goto, Y. Kakita, and T. Furukawa, Methyl Isobutyl Ketone Extraction and Determination of Metallic Salts. I. Extraction of Iron, Antimony, Tin, Arsenic, Selenium, Tellurium, and Germanium from Solutions Containing Hydrochloric and (or) Other Acids. Nippon Kagaku Zasshi 79 (1958) 1513-20.

20) A. Savitzky and M. J. E. Golay, Smoothing and Differentiation of Data by Simplified Least Squares Procedures. Anal. Chem. 36 (1964) 1627-39.

21) H. P. Yule, Data Convolution and Peak Location, Peak Area, and Peak Energy Measurements in Scintillation Spectrometry. Anal. Chem. 38 (1966) 103-105.

22) K. Heydorn, Use of the National Physical Laboratory Ionization Chamber Type 1383 A in Neutron Activation Analysis. J. Radioanal. Chem. 10 (1972).

23) A. L. Wilson, The Performance-Characteristics of Analytical Methods. Talanta 17 (1970) 21-44.

24) L. Erdey, L. Pólos, and R. A. Chalmers, Development and Publication of New Gravimetric Methods of Analysis. Talanta 17 (1970) 1143-55.

25) N. D. Eckhoff, A Study of the Variance-Covariance Matrix for Gamma-Ray Spectra. Nucl. Instrum. Methods 68 (1969) 93-102.

26) L. A. Currie, Limits for Qualitative Detection and Quantitative Determination. Anal. Chem. 40 (1968) 586-593.

Table 1

Experimentally determined interferences in arsenic analysis

Interfering element	Radioactive tracer	Activity μCi	Mass μg	Separation factor S	Effective value f	ppm of element ~± 1 ppb of As
Cu	Cu-64	300	*	2.3×10^{-5}	0.29	150
Br	Br-80m	100	3	1.1×10^{-3}	0.09	10
Sb	Sb-122	1	*	5.3×10^{-3}	0.72	0.25
W	W-187	20	0.1	7.2×10^{-3}	-0.29	0.5

*Irradiated carrier

Table 2

Experimentally determined interferences in manganese analysis

Interfering element	Radioactive tracer	Activity μCi	Mass μg	Separation factor S	Effective value f	ppm of element ~ ± 1 ppb of Mn
Na	Na-24	*		1.0×10^{-2}	1.6×10^{-4}	600
K	K-42	*		1	0.2×10^{-5}	500
Ga	Ga-72	200	7	5.8×10^{-3}	5.8×10^{-4}	300
Br	Br-80m	100	3	1.2×10^{-1}	2.0×10^{-3}	4

* Irradiated sample

Table 3

Experimentally determined interferences in selenium analysis

Interfering element	Radioactive tracer	Activity μ Ci	Mass μg	Separation factor S	Effective value f	ppm of element ~ ± 1 ppb of Se
Cl	Cl -38	*		2.0×10^{-5}	-0.01	5000
Br	Br -80m	100	3	5.6×10^{-4}	-0.01	> 40
Mo	Mo-99	60	12	2.1×10^{-5}	0.05	800
Ba	Ba -140	90	< 0.1	0.9×10^{-5}	0.16	>300
Dy	Dy -165	5000	5	3.7×10^{-7}	1200	2
Au	Au -198	0.7	0.001	1.9×10^{-1}	-0.53	0.01
Hg	Hg-203	0.8	0.2	1.4×10^{-2}	0.11	0.6

* irradiated sample

Table 4

Precision of analysis of biological samples

Element determined	Number of results	Number of materials	Range ppb	Average standard deviation experimental	Average standard deviation calculated	Detection limit ppb
As	30	11	4-20	0.6	0.5	1
Mn	24	9	30-300	5	9	*
Se	27	9	70-500	9	10	20

* Determined by the sodium content of the sample

Table 5

Analytical results for plant reference material

Material	Number of samples	Weight mg	This work			Recommended values			Reference
			ppm As	ppm Mn	ppm Se	ppm As	ppm Mn	ppm Se	
Kale	4	500	0.114 ± 0.003	14.6 ± 0.3	0.132 ± 0.008	0.14	14.9	0.15	a
Orchard leaves	4	500	8.7 ± 0.2	87.1 ± 1.6	0.088 ± 0.007	14	100	0.08	b

a) H. J. M. Bowen, Standard Materials and Intercomparisons. Advan. Activ. Anal. 1 (1969) 101-113.

b) Provisional Certificate of Analysis. In: National Bureau of Standards, Reference Material 1571 (1971).

Direct Contamination of Barley with ^{7}Be, ^{22}Na, ^{115}Cd, ^{125}Sb, ^{134}Cs, and ^{133}Ba

by

A. Aarkrog

Health Physics Department

Abstract

Radionuclides of Be, Na, Cd, Sb, Cs, and Ba were applied as a spray to barley plants at six different stages of development.

Initial retention (IR), distribution between grain, husks, and straw, field loss (FL), and the normalized specific activity (NSA) of the different nuclides were determined.

The percentage IR was approximately equal to the age of the plants in days at the time of contamination. Sb, Na, and especially Cs were translocated to the grain from other parts of the plants. This was not the case with Be, Ba, and Cd. FL followed a two-exponential decay for all nuclides except Na. The field loss coefficients were 0.08 - 0.21 $days^{-1}$ in the first part of the growth period and 0.03 - 0.04 $days^{-1}$ in the second part. Cd showed the lowest FL, Sb the highest. NSA varied from approx. 2 $m^2 \cdot day \cdot kg^{-1}$ (Be and Ba) to 7.4 (Cs). The direct contamination of barley grain from Cd in precipitation was estimated.

INTRODUCTION

Contamination of the human food chain with radioactive as well as conventional pollutants primarily takes place as direct contamination, i. e. adsorption of the debris on the aerial parts of the crops, often followed by absorption.

We have earlier[1,2] studied the uptake, translocation, and loss in cereals, especially in barley, of radionuclides representing long- and medium-lived fall-out nuclides (Sr, Cs, Ce, Mn) as well as corrosion products (Co, Cr, Fe, Zn) from nuclear reactors. Furthermore we have looked at some conventional contaminants from the heavy-metal group (Pb and Hg).

The purpose of the present study was to obtain further information on the behaviour in cereals of contaminants applied directly to the surface of the crops during the growth period. The risk of contamination of our environment with conventional as well as radioactive pollutants justifies such studies.

This time we selected three representatives of common fission and activation products (^{133}Ba, ^{125}Sb, and ^{134}Cs), two cosmic-ray-produced nuclides (^{7}Be, ^{22}Na), which also occur in nuclear weapon debris[3,4], and finally cadmium (^{115}Cd), which is a conventional pollutant of increasing importance[5].

Owing to the consumption of whole-grain products (rye bread), cereals are main donors of radioisotopes and presumably also of some conventional pollutants in the Danish diet. From our measurements of fall-out nuclides[6], we know that, although differences exist between the levels found in the various grain species, barley is a reasonable average representative of the four species of grain found in Denmark. As barley is furthermore easy to grow in small experimental plots where it gives satisfactory and homogeneous yields, we used this species in our recent experiments.

EXPERIMENTAL METHODS

The study was carried out in the same area and according to the same principles as used previously[1,2]. The experimental field was divided into forty plots made up of ten rows and four columns. The plots were numbered in succession. To minimize cross-contamination between experiments, they were arranged systematically, as shown in table 1, according to increasing degree of contamination.

Table 1

Experimental data

Experiment	Plot Nos.	Spraying date	Height of plants in cm	Dry-matter weight of herbage in a plot: grammes ± 1 SE at spraying	Remarks
I	1-6	25 May	17	6.8 ± 0.6	
II	8-13	6 June	41	24.2 ± 0.2	
III	15-20	17 June	64	56.6 ± 3.1	
IV	22-27	30 June	85	106.3 ± 12.0	Start of ear emergence
V	28-33	14 July	91	148.8 ± 0.6	The ears fully emerged
VI	35-40	28 July	87	133.5 ± 19	

The grain was seeded on 20 April 1971, it germinated on 6 May, and was harvested on 20 Aug. 1971. The average weight of the mature plants in a plot was 154 ± 2 g (1 SE). 48.6% was grain, 6.9% husks, and 44.5% straw on a dry-weight basis. The number of plants in a plot was 46 ± (1 SE). The spraying solution contained on 1 May 1971: 0.2 mCi ^{7}Be, 2 μCi ^{22}Na, 1.6 mCi ^{115}Cd, 6 μCi ^{125}Sb, 2 μCi ^{134}Cs, and 3 μCi ^{133}Ba per 10 ml solution with 25 ppm carrier as the nitrate. The plots with even numbers were cut 24 hours after spraying and used for determination of the initial retention of the crops. Plots Nos. 7, 14, 21, and 34 were sprayed with distilled water and used as background samples for the neighbouring experiments.

As the rather small area of a plot (1/8 m^2) introduces a risk of edge effects, we placed the circular experimental plot in the middle of a larger, square plot (1 x 1 m^2) where we also grew barley. Before the spraying we placed a plastic ring around the experimental plot. The ring was kept in the plot until harvest so we could identify the treated plants from the untreated.

Each circular plot was sprayed with 10 ml spraying solution and then with 10 ml distilled water. Before the measurement the plant material was dried at 80°C for 24 hours and divided into grain, husks, and straw in a glove box. The radioactivity was determined on a 30 cm^3 Ge(Li) detector connected to a 1024-channel Hewlett Packard analyser and a H. P. -9100 B calculator. We used the following photo peaks: ^{133}Ba:276 keV, ^{125}Sb:427 keV, ^{7}Be:477 keV, ^{134}Cs:796 keV, ^{115}Cd:935 keV, and ^{22}Na:1275 keV.

RESULTS AND DISCUSSION

Initial Retention: IR

IR is the ratio between the activity found in the herbage from a plot and the amount of activity dosed. As there was no significant difference between the IR's of the different nuclides, we used the mean and found

$$IR\,\% = 55\ g \cdot cm^{-1},$$

where g is the dry weight of the herbage in a plot and cm the average height of the plants, i. e. g cm^{-1} is an expression for the surface of the crops.

In 1970[2] we found

$$IR\,\% = 22\ g \cdot cm^{-1}.$$

The retention in 1971 was thus two or three times greater than in 1970 for the same g · cm^{-1} value. However, if the age of the plants was considered, the IR for 1971 was for the same age only a little higher than that found in 1970. We got for 1970 and 1971:

$$IR\,\% = 1.05\ days,$$

where days is the period from germination to contamination (cf. fig. 1)

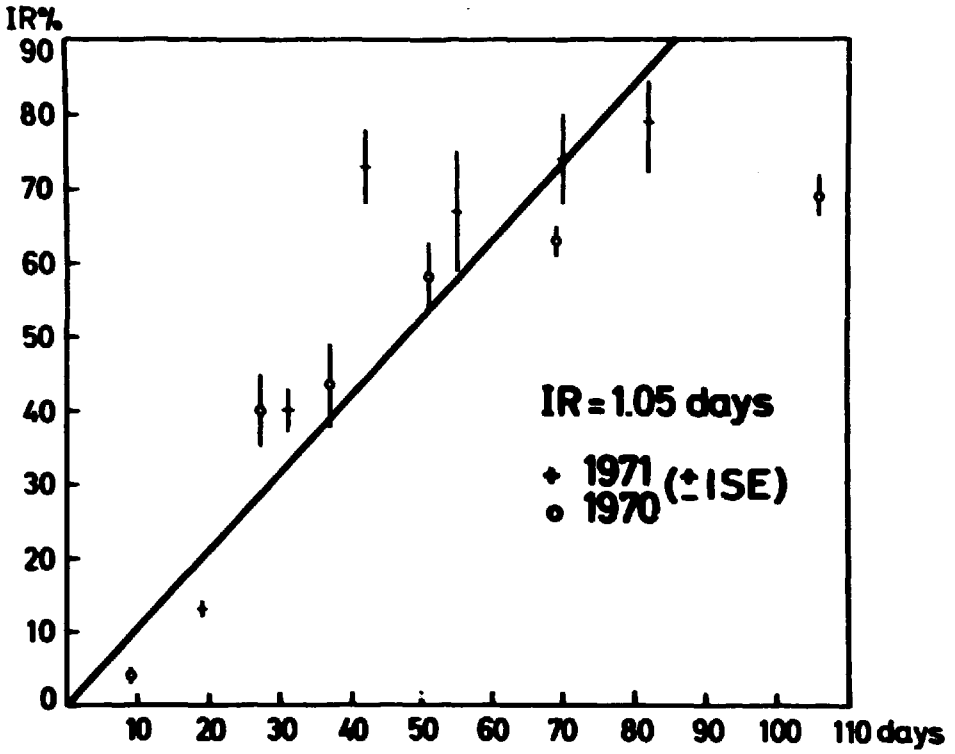

Fig. 1. Initial retention (IR) as a function of time in days from germination to contamination.

Thus we must conclude that the IR is not solely dependent on the $g \cdot cm^{-1}$ figure. The stage of development plays a more important role. This is perhaps not surprising when we remember that the morphology of the barley plants changes markedly during the growth period. When the crops are approx. two months old, the ears appear, which alters the shape of the surface and with it the ability of interception and retention of particles. Later, when the crops ripen, the nature of the surface changes from fresh and soft to withered and dry, and this might also influence the IR.

Table 2

Per cent of activity in the 10 ml spraying solution dosed on a plot and retained in mature, grain, husks, and straw (corrected for radioactive decay)

Plant part	Nuclide	Exp. I	Exp. II	Exp. III	Exp. IV	Exp. V	Exp. VI	Exp. I'
Grain	Ba	0.001	0.004±0.002	0.015±0.001	0.12±0.01	0.78±0.12	4.3±1.4	0.0001
	Sb	0.002±0.001	0.09±0.02	0.59±0.04	1.0±0.2	5.2±0.7	7.5±2.1	0.0002
	Be	0.0009	0.0065±0.0005	0.042±0.004	0.13±0.01	0.55±0.10	2.7±0.9	-
	Cs	0.064±0.013	0.89±0.18	3.0±0.4	5.5±0.6	8.9±1.5	9.1±2.6	0.0008
	Cd	0.025±0.007	0.07±0.01	0.37±0.10	0.42±0.06	1.8±0.2	3.8±1.2	0.0006±0.0003
	Na	0.17±0.02	0.18±0.01	0.40±0.03	1.8±0.2	5.3±0.8	7.0±2.3	0.02±0.01
Husks	Ba	0.0004±0.00002	0.008±0.004	0.038±0.007	0.37±0.08	1.2±0.1	7.4±1.9	0.003
	Sb	-	0.06±0.01	0.38±0.06	0.71±0.15	1.1±0.2	7.1±1.6	0.0015±0.001
	Be	-	0.01±0.007	0.06±0.01	0.48±0.07	2.0±0.5	9.7±2.3	0.003
	Cs	0.008±0.002	0.10±0.03	0.4±0.1	0.80±0.14	1.2±0.2	3.7±0.9	0.002
	Cd	0.003	0.01±0.01	0.09±0.02	0.41±0.06	1.9±0.3	8.4±1.8	0.003
	Na	0.05±0.01	0.045±0.007	0.11±0.02	0.48±0.06	1.3±0.1	2.8±0.8	0.009±0.003
Straw	Ba	0.10±0.03	3.4±0.5	8.6±1.0	16.4±1.6	10.2±1.1	31±2	0.007±0.0006
	Sb	0.050±0.006	2.1±0.3	5.2±0.9	10.1±1.3	2.8±0.6	21.5±1.5	0.005±0.001
	Be	0.03±0.03	3.6±0.7	11±2	18±2	9.6±1.6	32±2	0.003±0.0004
	Cs	0.11±0.02	1.7±0.4	3.4±0.9	6.1±1.2	4.5±1.0	18±3	0.005±0.003
	Cd	0.18±0.04	3.5±0.6	11±2	16.5±2	11.4±1.2	34±2	0.004
	Na	3.4±0.3	3.4±0.2	4.4±1.0	6.0±1.2	3.4±0.8	7.8±0.9	0.23±0.07

The error term is the SE of the mean of triplicates. All samples were corrected for the background activity found in the nearest background plot (cf. table 1). Exp. I' was the regenerated plants in the even-numbered plots in exp. I. The yields in the regenerated plots were one order of magnitude lower than those of the other mature plants; we did not try to correct for this.

Distribution in Mature Crops

Table 2 shows the grain levels (as per cent of the activity dosed on a plot, corrected for decay). Regression analysis of the single nuclides yielded the equations:

$$\% \text{ Be} = 0.0025\ e^{0.11t} \quad (1)$$

$$\% \text{ Ba} = 0.0015\ e^{0.125t} \quad (2)$$

$$\% \text{ Cd} = 0.031\ e^{0.079t} \quad (3a) \text{ or } \% \text{ Cd} = 0.0565t - 0.62 \quad (3b)$$

$$\% \text{ Na} = 0.12t - 1.10 \quad (4a) \text{ or } \% \text{ Na} = 0.12\ e^{0.067t} \quad (4b)$$

$$\% \text{ Sb} = 0.13t - 1.61 \quad (5)$$

$$\% \text{ Cs} = 0.16t - 0.33 \quad (6)$$

where t is the time in days since the first spraying (exp. I).

Be and Ba followed exponential equations, while Sb and Cs were better described by linear expressions. Cd and Na took up intermediate positions. All equations showed significant ($P > 99\%$) or probably significant ($P > 95\%$) linear regression, and the deviations from regression were in no cases significant.

To examine the distribution of the six nuclides within the plant we further analysed husks and straw (cf. table 2). To simplify the interpretation of the data we used three ratios: Ba/Be, Sb/Cd, and Na/Cs and carried out analysis of variance (anova) of the natural logarithms of the three ratios. Our hypothesis was that there was no significant difference between the levels of two nuclides in a ratio, and that they showed variation neither between plant parts (grain, husks, and straw) nor between experiments (II, III---VI). We omitted exp. I in the anovas because this experiment was atypical partly on account of a significant root uptake of some of the nuclides (see below) and partly because the levels were so low that the error on the measurement was higher than in the other experiments.

The anovas showed that the interactions between plant parts and experiments for the three ratios were highly significant ($P > 99.5\%$). Hence we must reject the hypothesis and conclude that the two nuclides in a ratio did not behave in a similar way in the plants. Fig. 2 shows how the ratios varied.

Ba/Be. Ba migrated more easily to the grain than Be when the crops were contaminated after emergence of the ears. Husks contained less Ba than Be. In straw there was no significant difference between Ba and Be.

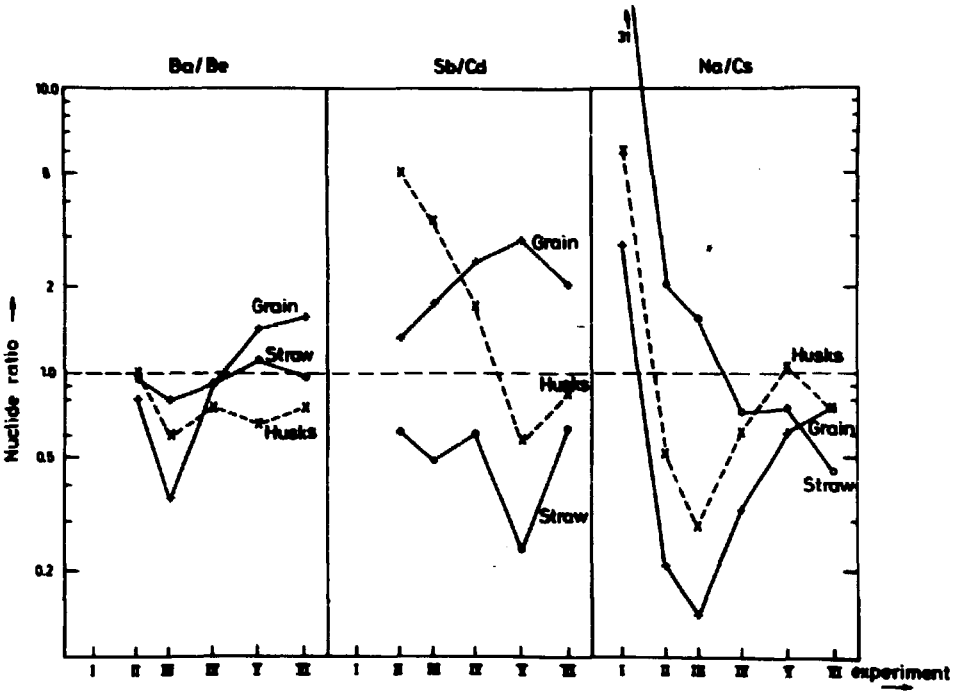

Fig. 2. Ba/Be, Sb/Cd, and Na/Cs ratios in mature grain, husks, and straw in the six experiments.

Sb/Cd. Compared with Cd, Sb is translocated to a greater extent to the grain from other parts of the plant. Thus grain contained more, straw less, Sb than Cd. In husks we found more Sb than Cd in the plots sprayed at an early stage of the development (exp. II-IV), while the opposite was the case for the last experiments (V and VI).

Na/Cs. Husks and especially grain contained significantly more Cs than Na because Cs was translocated to a greater extent than Na to the grain (and husks). In straw the Na/Cs ratio decreased with time. This was partly due to the above-mentioned preferential translocation of Cs, partly to the root uptake of Na from the soil, which played an important role especially in the first experiment (cf. below).

Indirect Contamination

In experiment I the barley was allowed to regenerate on the three plots used for initial samples. The regenerated plants were harvested along with the other samples.

The activity levels in these samples were used for an estimate of the root (or stem base) uptake of the plants in experiment I (cf. table 2). How-

ever, the yields differed by one order of magnitude between the regenerated plants and the other mature plants. It was therefore difficult to get an exact estimation of the soil uptake in the not-regenerated plants. From table 2 we estimate the soil uptake to be significant in exp. I for the Ba, Sb, Be, and Na levels, while Cs and Cd primarily came from direct contamination. In the other experiments the direct contamination was the dominating factor for all nuclides.

Field Loss: FL

In 1970 we found that FL, i. e. the removal of radioactivity from the plants by processes other than radioactive decay, could be described by two exponential equations. This was also the case in the present study. In the first part of the growth period the loss rate was rather fast, and in most cases the half-life was less than a week. In the last part of the growth period, where the growth rate of the plants is slower, the field loss rate was also slower, corresponding to a half-life of approx. three weeks. This difference in FL was as discussed earlier[2] attributed to differences in growth rate and morphology at the spraying time.

As shown in 1970[2] FL could also be expressed by a linear equation. In the calculation of the regression equations shown in fig. 3 we omitted exp. V because eleven days after the fifth spraying there was a storm (24 mm of rain), which we suspected had removed a comparatively large part of the freshly deposited activity. The equations in fig. 3 are only valid for the period covered by the experiments.

In the mature total plants we found for all experiments more Cd than Cs and Ba, and more Ba than Sb. As the IR was the same for all nuclides, we concluded that $FL_{Sb} > FL_{Ba} > FL_{Cd}$ and $FL_{Cs} > FL_{Cd}$.

As regards Na it was not possible to ascertain a linear field loss equation. Fig. 3 shows that the FL for Na was approx. 90% in exp. II, III, and IV, while it was only 70% in exp. I and approx. 80% in exp. VI. The rather low FL% in exp. I was attributed to the root uptake of Na, which increased the Na levels in the mature plants from this exp., especially in straw, as compared with the other nuclides (cf. also fig. 2).

Generally the field loss in this study was greater than in the 1970 experiment. We ascribe this to the greater wash-off of activity from the plants this year, where the amount of precipitation during the growth season was 153 mm against 86 mm in 1970.

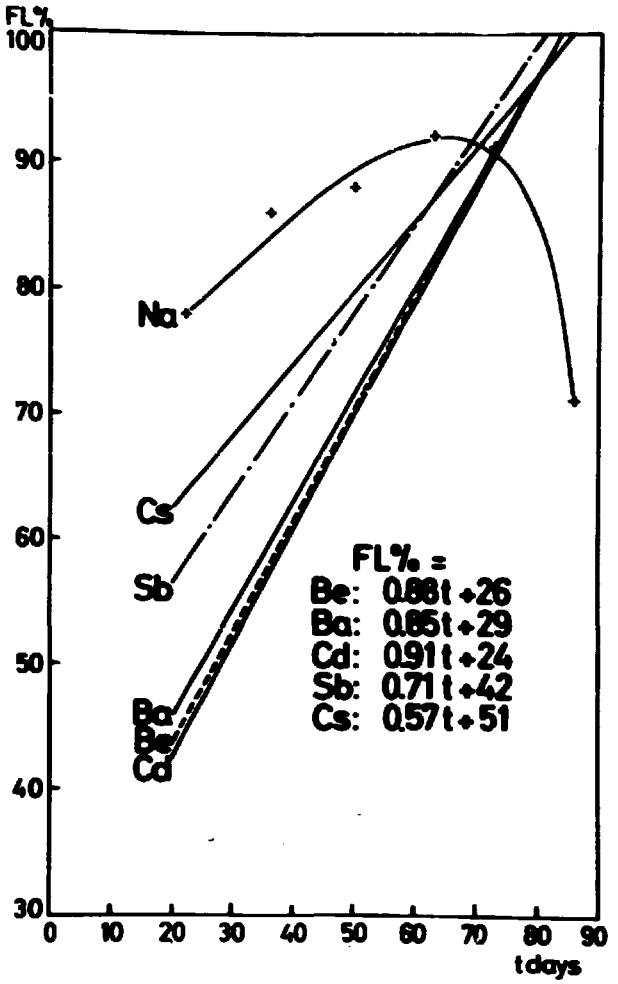

Fig. 3. Field loss (FL) as a function of days of weather exposure, i.e. the time from the day of spraying until harvest.

Contamination Model

The normalized specific activity: N.S.A. is, according to Chamberlain[7], the ratio

$$\frac{\text{Activity kg}^{-1}\text{ dry weight of crop}}{\text{Activity deposited day}^{-1}\text{ m}^{-2}\text{ of ground}}$$

We have for barley grain for nuclide (i)

$$NSA_{(i)} = \left[\int_{-19}^{64} f(x_i)dx + (q_{16} + 5)2^{-1} \cdot 23\right] 0.6 \cdot 10^{-2},$$

where $f(x_i)$ is per cent of activity in mature grain as given by equations (1)-(6); q_{i6}: the activity level (in per cent) in the grain from exp. VI; 0.6: kg grain per m^2; 19, 64, and 23: the intervals in days from germination to exp. I, from exp. I to VI, and from exp. VI to harvest respectively; 5: the mean level in grain for all nuclides, when the crops are sprayed just before harvest[1,2]. We calculated the following NSA values for barley grain: Cs:7.4, Na:4.7, Sb:4.1, Cd:2.9, Ba:2.3, and Be:1.9.

From fall-out measurements in Denmark[6] in the period 1962-68 we found the NSA for ^{137}Cs in barley grain to be equal to 7.5, which is in accordance with the experimentally found value given above for ^{134}Cs. We will therefore consider the present experiment applicable to natural conditions also as regards the other nuclides.

Cadmium in Grain

It might be of special interest to calculate the Cd level in grain from the environmental contamination with this nuclide. We have no information on precipitation levels of Cd in Denmark, but if we use American data[8] from precipitation collected in New York in 1970, the daily mean fall-out rate is 10 $\mu g\ m^{-2}\ day^{-1}$. Hence the Cd concentration in barley grain becomes: $2.9 \cdot 10\ \mu g\ kg^{-1} = 0.03$ mg Cd kg^{-1}; this is close to the lower level found in two barley samples from Germany analysed by Kropf et al.[9] in 1968. They found 0.04 and 0.23 mg Cd kg^{-1}. However, the levels are hardly exclusively due to direct contamination, as Schroeder and Balassa[10] have shown that Cd is also taken up by crops from superphosphate in soil.

For occupational exposure to Cd in air a maximum air concentration value of 0.1 mg m^{-3} has been adopted[5]. From studies of wash-out ratios for ^{90}Sr and lead[8] we estimated the corresponding concentration in precipitation to be 50 mg Cd l^{-1}. For a mean precipitation rate of 2 mm per day in the growth period, the fall-out rate becomes 100 mg Cd $m^{-2}\ day^{-1}$ and the corresponding grain level 300 mg Cd kg^{-1}. In the Japanese case of endemic Cd poisoning near Toyama City the rice contained 0.4 - 3.4 mg Cd kg^{-1}[5].

An air concentration of 0.1 mg Cd m^{-3} is thus not safe when the contamination of cereals is also considered.

CONCLUSION

The initial retention (IR) in growing barley was related to the age rather than to the surface figure: g cm^{-1} of the plants. The IR in % was nearly equal to the age in days of the crops at spraying.

If the plants were contaminated throughout the growth season Ba, Be, and Cd followed nearly the same pattern, and approx. 5% of the activity was in the grain, 85% in the straw, and the remainder in the husks. Sb, Na, and Cs were translocated to the grain and showed 20, 30, and 40% respectively in the grain and 65-50% in the straw.

The field loss rate for Be, Ba, and Cd corresponded to 3-6 days' half-life in the first part of the growth period and approx. 25 days in the last part. Cs and Sb decayed with a half-life of 5-8 days in the first, but 18 days in the last part of the growth period; $FL_{Sb} > FL_{Ba} > FL_{Cd}$ and $FL_{Cs} > FL_{Cd}$. Na was atypical owing to a significant root uptake in the first experiments. As compared with last year's study the field loss rate this year was nearly two times faster, undoubtedly because the amount of precipitation (and thus the wash-off) this time was nearly a factor of two higher than last year.

The study indicated that in the case of a fall-out rate of 10 µg Cd m^{-2} day^{-1} during the growth period, we would expect 0.03 mg Cd kg^{-1} barley grain from direct contamination.

ACKNOWLEDGEMENT

This study demanded a joint effort by many of Risø's departments. The Isotope Laboratory delivered the isotopes, which to some extent were produced at the DR 3. The Agricultural Research Department placed the experimental field at our disposal, assisted with the planning, sowed the grain, and treated the crops with pesticides. The Maintenance Division assisted with the fencing and covering of the area. GIER in the Reactor Physics Department was used for the statistical calculations of the results. The Waste Treatment Plant took care of the considerable volumes of waste. The Health Physics Department performed the spraying, harvesting, threshing, and measuring of the samples together with the health physics survey during the experiment. The Ge-detector used was also constructed in that department. This flexible and effective interdepartmental work is an example of the spirit of co-operation fostered at Risø by Professor T. Bjerge.

REFERENCES

1) A. Aarkrog, on the Direct Contamination of Rye, Barley, Wheat, and Oats with ^{85}Sr, ^{134}Cs, ^{54}Mn, and ^{141}Ce. Radiat. Bot. 9 (1969) 357-366.

2) A. Aarkrog and J. Lippert, Direct Contamination of Barley with ^{51}Cr, ^{59}Fe, ^{58}Co, ^{65}Zn, ^{203}Hg, and ^{210}Pb. Radiat. Bot. 11 (1971) 463-472.

3) J. F. Bleichrodt and E. R. van Abkoude, Artificial Beryllium 7 in the Lower Stratosphere. J. Geophys. Res. 68 (1963) 4629-31.

4) R. W. Perkins, J. M. Nielsen, and C. W. Thomas, Air Concentrations of Twelve Radionuclides from 1962 through mid-1964. Science 146 (1964) 762-764.

5) R. Nilsson, Aspects on the Toxicity of Cadmium and Its Compounds. (Natural Science Research Council, Stockholm, 1970).

6) A. Aarkrog, Prediction Models for Strontium-90 and Caesium-137 Levels in the Human Food Chain. Health Phys. 20 (1971) 287-311.

7) A. C. Chamberlain, Interception and Retention of Radioactive Aerosols by Vegetation. Atmos. Environ. 4 (1970) 57-78.

8) Edward P. Hardy, Fallout Program. Quarterly Summary Report, December 1, 1970 - March 1, 1971. HASL- 242 (1971) 1-99.

9) R. Kropf und M. Geldmacher-v. Mallinckrodt, Der Cadmiumgehalt von Nährungsmitteln und die tägliche Cadmiumaufnahme. Arch. Hyg. Bakteriol. 152 (1968) 218-224.

10) H. A. Schroeder and J. J. Balassa, Cadmium: Uptake by Vegetables from Superphosphate in Soil. Science 140 (1963) 819-820.

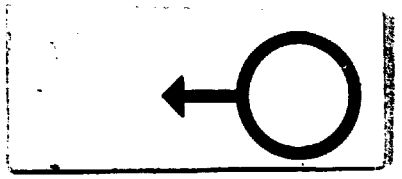

Effects of Nitrogen Nutrition on the Uptake, Distribution, and Chemical Binding of Strontium and Calcium in Oat Plants

by

Arna J. Andersen

Agricultural Research Department

Abstract

The uptake of added radioactive Sr and Ca increased almost linearly with increasing supply of NH_4NO_3 to the soil. The $^{85}Sr/^{45}Ca$ ratio varied between plant parts, being lower in leaves, glumes, pales and grain than in stems and flower stalks. This indicates that discrimination against ^{85}Sr relative to ^{45}Ca occurs during transfer of the two ions from the conducting system. The compounds of stronger chemical bindings contained more ^{85}Sr than ^{45}Ca. This may explain some of the discrimination against ^{85}Sr during the transport of the two ions within the plants, but it cannot account for the very low $^{85}Sr/^{45}Ca$ ratio obtained in grain with high N supply. An active N-dependent discriminatory mechanism is assumed to regulate the transfer of Sr and Ca to oat grain.

INTRODUCTION

The occurrence and behaviour of Sr in the biosphere have acquired increasing interest since the advent of its long-lived radioactive isotopes which are products of nuclear fission. Small quantities of native Sr are widely distributed in soils, plants and animals, where its abundance is usually compared to that of the homologous element Ca. The extent to which Sr can substitute for Ca in plant nutrition and the possibility of Sr toxicity to plants have been the main purpose of the "pre-atomic age" studies on the behaviour of Sr in the soil-plant system.

Early investigations by Haselhoff (1893) indicated that Sr substitutes for Ca in plants, and Scharrer and Schropp (1937) reported a slightly stimulating effect by partly replacing Ca with Sr, while Walsh (1945) found that Sr could largely replace Ca in the vegetative growth but not in the formation of grain in cereals. Symptoms of Sr injury in wheat were described by Hurd-Karrer (1937), who found that the toxicity depended on the Sr/Ca ratio in the rooting medium. The Sr/Ca ratio in plants was found by Collander (1941) to be almost equal to that in the nutrient solution.

During the last two decades numerous experiments have been carried out in order to evaluate various factors affecting the uptake and translocation of radioactive Sr relative to that of Ca in plants. It is generally recognized that accumulation of Sr and Ca by plants occurs through quite similar processes. Nevertheless, some discrimination between the two ions may occur both during uptake and translocation within the plants (Russel, 1963). Discrimination against Sr relative to Ca in translocation has been shown to be due to greater retention of Sr in roots and stems, and consequently the Sr/Ca ratio in leaves and seeds may be less than in roots and the external rooting medium.

Plant nutrient supply may change the relative availability of Sr and Ca in soils and also the relative rate of translocation within the plants (Andersen 1971). It was shown that increasing supply of nitrogen (N) decreased the Sr/Ca ratio in grain relative to that in straw. The objectives of the present study were to further elucidate the extent to which N affects the uptake and distribution of Sr and Ca in different parts of oat plants and to investigate a possible effect of N on the chemical bindings of Sr and Ca in the vegetative part of the oat plants at flowering time, when translocation to the grain is supposed to take place.

EXPERIMENTAL METHODS

The growth conditions were essentially the same as previously described (Andersen 1971). Increasing amounts of NH_4NO_3 and 5 μ Ci of ^{85}Sr and ^{45}Ca per kg of soil were mixed into a sandy loam soil taken from the experimental field at Risø. The isotopes were added in a solution of Sr-$CaCl_2$ with a specific activity of 6 mCi ^{85}Sr/mg Sr and 0.25 mCi ^{45}Ca/mg Ca. The soil contained about 2 micro-equivalent (μeq) Sr per milli-equivalent (meq) Ca. Thirty-five seeds of oats (Avena sativa, variety "Stål") were sown per pot which were then placed in a randomized block design and daily watered with deionized water to 70% of the waterholding capacity. After germination the seedlings were thinned out to 28 plants per pot, and at flowering time 3 plants per pot were harvested. The remaining 25 plants per pot were harvested at maturity.

Samples of mature straw and grain were taken for the determination of the ^{85}Sr and ^{45}Ca contents. Five main shoots from different N treatments were used to investigate the ^{85}Sr and ^{45}Ca contents in different parts of the plants. Straw (stem + leaves) from flowering plants was used to investigate the chemical bindings of ^{85}Sr and ^{45}Ca in the vegetative part of the growing plants.

The method used for investigating the chemical bindings of Sr and Ca was the procedure described by Schilling (1960) but in a slightly modified form. One gram of plant powder was successively extracted with water, 0.5 N $NaNO_3$ and 1.0 N acetic acid. The chemical bindings of Sr and Ca extracted by this technique are assumed to be: free Sr and Ca in the water soluble fraction; exchangeable ions in the $NaNO_3$ extract; and phosphate and carbonate complexes extracted by the acetic acid, while the residue contained the insoluble oxalate and metabolically fixed Sr and Ca.

Radioactivity of plant samples and extracting solutions were determined by use of standard procedures. The ^{85}Sr was determined by γ-spectrometry with a well-type scintillation crystal and the ^{45}Ca was measured with an end-window flowcounter. Appropriate corrections for self-absorption and activity decay were made.

RESULTS AND DISCUSSION

Yield and Uptake of ^{85}Sr and ^{45}Ca

The effects of increasing supply of NH_4NO_3 on the yield and the uptake

of ^{85}Sr and ^{45}Ca are presented in fig. 1. Maximum yield was obtained by

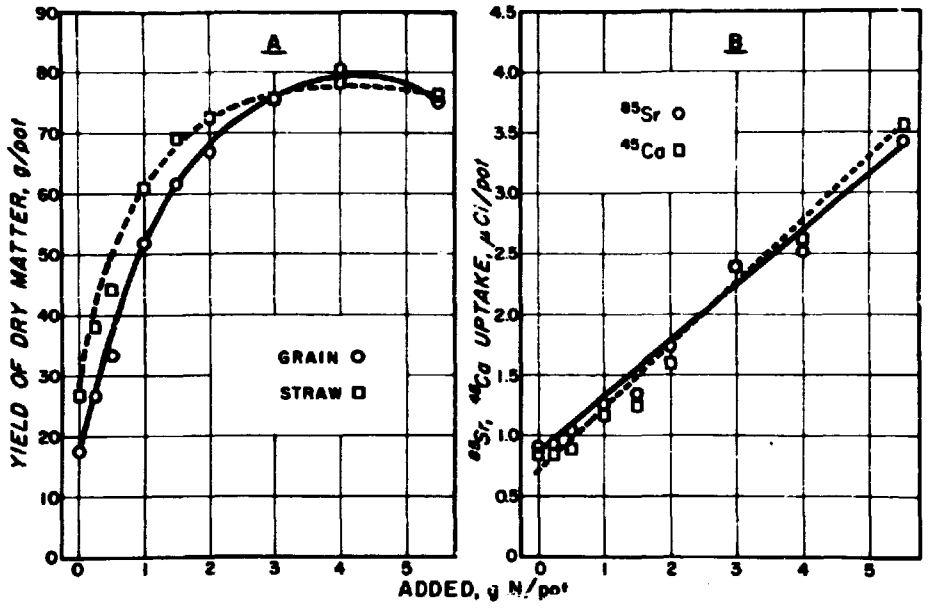

Fig. 1. Relationships between nitrogen supply and yield of dry matter (A) and total uptake of ^{85}Sr and ^{45}Ca (B).

adding 4 g N per pot; increase of the N supply to 5.5 g depressed the yield. The uptake of ^{85}Sr and ^{45}Ca increased almost linearly with the N supply, whereas the shapes of the curves relating the N supply to the concentrations of ^{85}Sr and ^{45}Ca (fig. 2) consisted of a declining part followed by an increasing

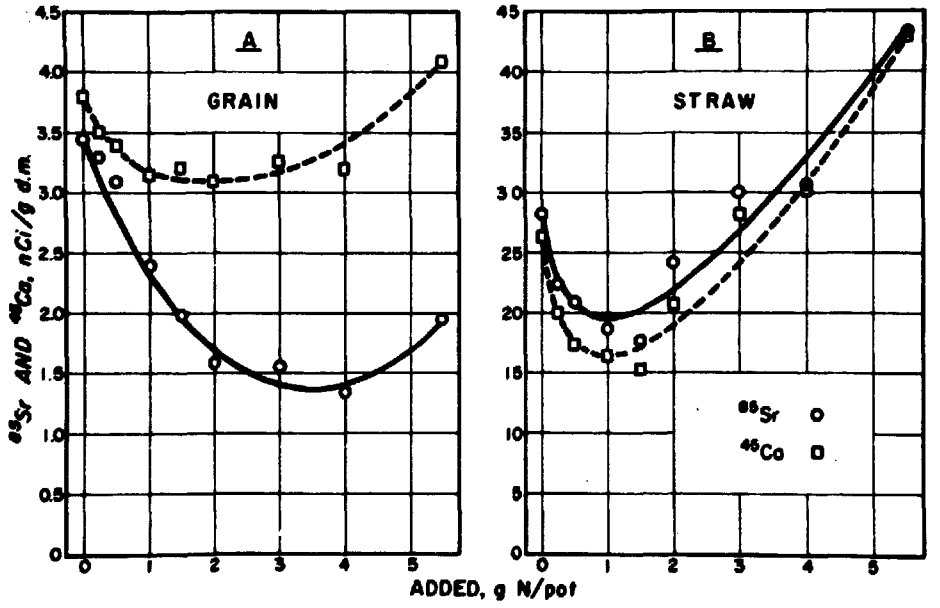

Fig. 2. Relationships between nitrogen supply and concentrations of ^{85}Sr and ^{45}Ca in grain (A) and straw (B). Note that the (A) ordinate is expanded tenfold compared with the (B) ordinate.

section. Small additions of N increased the yield of dry matter more than the uptake of ^{85}Sr and ^{45}Ca, and as a consequence the concentration of the two ions decreased. Large N supplies cause the reverse to happen. A comparison between fig. 1A and fig. 2B reveals that the decrease in the ^{85}Sr and ^{45}Ca concentrations coincides with the very steep rise in dry matter production. This is in accordance with the general observations of the relationship between yield and concentration of a plant nutrient present in sufficient amount in the growth medium (Steenbjerg and Jacobsen, 1963). However, the concentration of ^{85}Sr in grain continued to decrease until the maximum yield was obtained by the addition of 4 g N per pot.

The concentration of ^{85}Sr in straw was slightly higher than that of ^{45}Ca (fig. 2B), whereas the opposite was found in grain (fig. 2A), which indicates that discrimination against ^{85}Sr occurred during the translocation of the two ions from straw to grain. This discrimination against ^{85}Sr was apparently influenced by N since the $^{85}Sr/^{45}Ca$ ratio decreased relatively more in grain than it did in straw (fig. 3).

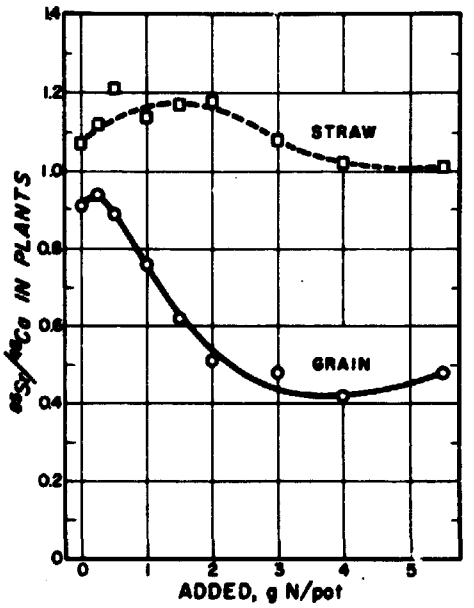

Fig. 3. Relationships between nitrogen supply and the $^{85}Sr/^{45}Ca$ ratio in grain and straw.

The N supply increased the uptake of ^{45}Ca more than that of ^{85}Sr (fig. 1B). Similar effects have been observed in water culture (Andersen, 1972), and this fact may indicate that N nutrition affects the ability of oat roots to discriminate between Sr and Ca.

Distribution of ^{85}Sr and ^{45}Ca in Different Plant Parts

The concentration of ^{45}Ca was 5 - 10 times higher in straw than in grain (fig. 2), and the difference between the concentrations of ^{85}Sr in straw and grain became even greater because the concentration in grain continued to decrease with the N supply up to 4 g per pot. The ^{85}Sr and ^{45}Ca concentrations were measured in twelve separate plant parts sampled from each of two N treatments. Samples of stems, leaves, flower stalks, glumes, pales and grain were obtained by cutting the plants into fractions as indicated in table 1. The concentrations of both ions varied considerably between different plant parts. The highest concentrations were found in leaves, flower stalks, and glumes. The older leaves contained more ^{85}Sr and ^{45}Ca than the younger (top) leaves. This trend was opposite to that in stems, where the concentration increased from the base to the top sections and flower stalks. Increase of the N supplies caused the ^{85}Sr and ^{45}Ca concentrations in all plant parts to rise except in the grain and pales.

Table 1

Effects of nitrogen nutrition on the concentrations of ^{85}Sr and ^{45}Ca and on the $^{85}Sr/^{45}Ca$ ratios in different parts of oat plants. Radioactivity expressed as nCi per g of dry plant material

Plant parts	Nitrogen supply, g N per pot					
	1 5	3.0	1.5	3.0	1.5	3.0
	^{85}Sr		^{45}Ca		$^{85}Sr/^{45}Ca$	
Grain	1.5	0.86	1.7	1.6	0.88	0.54
Pales	3.5	2.6	7.4	6.9	0.47	0.38
Glumes	17.8	22.0	33.0	45.6	0.54	0.48
Flower stalk	26.8	35.5	16.4	22.4	1.63	1.58
x) 1 Leaf	16.2	28.7	24.5	44.9	0.66	0.64
2 Leaf	22.3	35.6	31.6	49.7	0.71	0.72
3 Leaf	28.5	40.5	35.2	48.7	0.81	0.83
4 Leaf	39.0	44.7	47.5	55.6	0.82	0.80
x) 1. Stem internode	18.3	18.2	7.1	8.6	2.6	2.1
2. Stem internode	12.1	16.6	4.8	8.6	2.5	1.9
3. Stem internode	7.3	11.4	3.4	7.0	2.1	1.6
4. Stem internode	5.3	9.1	2.9	4.0	1.8	2.3

x) Numbered from the top.

The $^{85}Sr/^{45}Ca$ ratios (table 1) vary between plant parts being higher than one in stem sections and flower stalks and lower than one in leaves, glumes, pales, and grain. The ratio in stem sections increased from base to top, which may be explained as a result of a continued preferential transport of ^{45}Ca to leaves. This will necessarily result in a relative increase of ^{85}Sr in stems. The discrimination between ^{85}Sr and ^{45}Ca during transport from stems to leaves was apparently not influenced by the N nutrition since the $^{85}Sr/^{45}Ca$ ratio did not change in leaves by the increase of the N supply. During translocation of the two ions to glumes, pales, and grain the N supply seems to increase the discrimination against ^{85}Sr since the $^{85}Sr/^{45}Ca$ ratios decreased.

Chemical Bindings of ^{85}Sr and ^{45}Ca

Increase of the N supplies increased all the chemical fractions of ^{85}Sr and ^{45}Ca determined in oat straw sampled at the flowering stage (fig. 4).

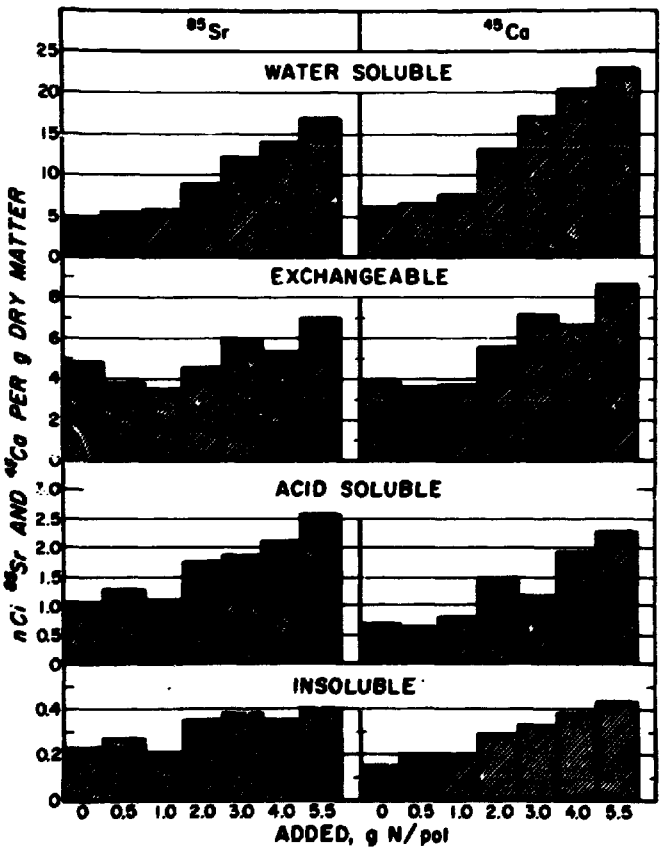

Fig. 4. Chemical bindings of ^{85}Sr and ^{45}Ca in straw (stem + leaves) of flowering oat plants grown in pot experiment with increasing supply of nitrogen. Note the scale differences.

Less ^{85}Sr than ^{45}Ca occurred in the water soluble form, while the opposite was found in the acid soluble and in the undissolved residue, and almost equal amounts of the two ions were found in the exchangeable fractions. The ^{85}Sr content in acid soluble plus insoluble form varied between 11% and 15% while the content of ^{45}Ca in these fractions amounted to only 6% to 9% of the total amount present in the straw.

The differential chemical bindings of ^{85}Sr and ^{45}Ca can be evaluated from the $^{85}Sr/^{45}Ca$ ratios shown in table 2. The data demonstrate the preferential accumulation of ^{85}Sr in compounds of stronger chemical bindings. This is in good agreement with the result obtained by Ringoet and de Zeeuw (1968) for oats at the flowering stage. Since the ions translocated may be assumed primarily to occur in water soluble form, the low $^{85}Sr/^{45}Ca$ ratios in this fraction may explain some of the discrimination against ^{85}Sr relative to ^{45}Ca, which occurs during transfer of the two ions to grain. The $^{85}Sr/^{45}Ca$ ratio of all the chemical fractions decreased with increasing N supply, which accords with the results obtained for mature plants (fig. 3). The ratio in mature grain (fig. 3) decreased appreciably more by the N supply than did the ratio in the water soluble fraction (table 2). This may indicate the presence of an N-dependent discriminatory mechanism which selectively transfers Ca in preference of Sr to the grain.

Table 2

Effects of nitrogen nutrition on the $^{85}Sr/^{45}Ca$ ratios in fractions of different chemical bindings in straw of oats sampled at flowering time

Added g N/pot	Water soluble	Exchangeable	Acid soluble	Insoluble
0	0.81	1.25	1.5	1.5
0.5	0.82	1.05	2.0	1.4
1.0	0.76	0.96	1.4	1.1
2.0	0.69	0.83	1.2	1.2
3.0	0.72	0.83	1.6	1.2
4.0	0.69	0.80	1.1	0.9
5.5	0.74	0.81	1.1	0.9
S.E.	± 0.04	± 0.07	± 0.09	± 0.3

SUMMARY AND CONCLUSION

Increasing supply of NH_4NO_3 to oats grown in a pot experiment increased the uptake of added ^{85}Sr and ^{45}Ca almost linearly. The uptake of ^{45}Ca was stimulated more by the N supply than was the uptake of ^{85}Sr, and consequently the $^{85}Sr/^{45}Ca$ ratio in the plants decreased. The $^{85}Sr/^{45}Ca$ ratio varied between plant parts being lower in leaves, glumes, pales and grain than in stems and flower stalks. This indicates that discrimination against ^{85}Sr relative to ^{45}Ca occurs during transfer of the two ions from the conducting system. Nitrogen supply increased this discrimination against ^{85}Sr during the transfer of the two ions to the grain. Relatively more ^{45}Ca than ^{85}Sr was present in a water soluble form and consequently the compounds of stronger chemical bindings contained more ^{85}Sr than ^{45}Ca. This may cause some discrimination against ^{85}Sr during the transport of the two ions within the plants, but it cannot explain the very low $^{85}Sr/^{45}Ca$ ratio obtained in grain with increasing N supply. An active, N-dependent discriminatory mechanism apparently regulates the transfer of Sr and Ca to the grain.

REFERENCES

Andersen, A. J., Influence of Phosphorus and Nitrogen Nutrition on Uptake and Distribution of Strontium and Calcium in Oat Plants. Soil Sci. Soc. Amer., Proc. 35 (1971) 108-111.

Andersen, A. J., Influence of Nitrogen Nutrition on the Discrimination between Strontium and Calcium in Oat Plants. FAO/IAEA Symposium on the Use of Isotopes and Radiation in Research on Soil Plant Relationships including Application in Forestry, 13-17 December 1971. (IAEA, Vienna 1972) (in press).

Collander, R., Selective Absorption of Cations by Higher Plants. Plant Physiol. 16 (1941) 691-720.

Haselhoff, E., Experiments in the Substitution of Strontium for Lime in Plant Nutrition. Landwirt. Jahrb. 22 (1893) 851-867.

Hurd-Karrer, A. M., Rubidium and Strontium Toxicity to Plants Inhibited by Potassium and Calcium, respectively. J. Wash. Acad. Sci. 27 (1937) 351-353.

Ringoet, A. and de Zeeuw, D., Discrimination between Calcium and Strontium in Oat Plants. II. Relation to the Differential Chemical Binding of Both Ions. Z. Pflanzenphysiol. 59 (1968) 249-257.

Russel, R. Scott, The Extent and Consequences of the Uptake by Plants of Radioactive Nuclides. Annu. Rev. Plant Physiol. 14 (1963) 271-294.

Scharrer, K. and Schropp, W., The Effects of Strontium and Barium Ions upon the Growth of Some Plants. Bodenk. Pflanzenernaehr. 3 (1937) 369-385.

Steenbjerg, F. and Jakobsen, S. T., Plant Nutrition and Yield Curves. Soil Sci. 95 (1963) 69-88.

Walsh, T., Effect Produced on the Growth of Plants by Substitution of Strontium for Calcium in Acid Soils. Proc. Roy. Irish Acad. 50B (1945) 287-294.

Spectra of Turbulence in the Atmospheric Surface Layer

by

Niels E. Busch and Søren E. Larsen

Physics Department

Abstract

Measurements of velocity components and temperature were performed at 5.66 metres over flat and uniformly rough terrain by means of hot-wire and cold-wire techniques. Twenty-five one-hour long runs were analysed in terms of power spectra and cross spectra.

Velocity spectra are presented in the frame work of Monin-Obuchov similarity. Over the entire frequency interval, i.e. 0.001 - 200 cps, the spectra are well organized according to hydrostatic stability. The most important scale length appears to be λ_m, the wave length at which $nS_w(n)$, the logarithmic spectrum of vertical velocity, has its peak. The wave length λ_m decreases monotonically as the hydrostatic stability increases. In indifferent density stratification λ_m is 1.8 times the height of observation.

For wavelengths λ such that $\lambda/\lambda_m \lesssim 0.055$, the spectra behave according to the concept of local isotropy.

Irrespective of density stratification the ratio S_w/S_u between the vertical and the longitudinal velocity spectra is a function of $n\lambda_m/\bar{u}$ only. When plotted against $n\lambda_m/\bar{u}$, the ratio S_v/S_u exhibits two branches with one branch pertaining to stable and the other to unstable density stratification. This indicates important differences between the flows in slightly stable and slightly unstable atmospheres, the shift from the one flow structure to the other being abrupt and not gradual.

INTRODUCTION

Micrometeorological field experiments of a complexity that would have been impossible a decade ago are now feasible thanks to recent technological developments. Such programmes are now producing increasingly precise and reliable data of value to atmospheric science and to those concerned with processes, activities, and structures in the atmospheric boundary layer.

Despite the advances in measurement and analysing techniques, the experimental and theoretical difficulties connected with investigations of turbulent shear flows in density-stratified media are so formidable that it appears prudent to seek out the simplest possible, nontrivial class of such flows. Therefore the concept of stationary, horizontally homogeneous turbulence with steady, plane-parallel mean flow was developed.

This is obviously a type of flow which is impossible to realize in a strict sense - especially on a rotating earth. Nevertheless, in limited heights over terrain which is uniformly rough and flat, the idealized flows may be closely approximated by the actual flows provided that the external pressure field is weak, and that the effects of radiative and latent heat transfer can be neglected.

In the summer of 1968 the meteorology group of the Danish AEC participated in a micrometeorological experiment conducted by the Air Force Cambridge Research Laboratories (AFCRL) over the plains of southwestern Kansas (Haugen et al., 1971). The aim of this experiment was to obtain comprehensive sets of measurements of wind and temperature structure over a flat, uniform terrain so that the hypotheses associated with the idealized concepts mentioned previously could be tested experimentally.

The purpose of this paper is to present some of the results derived from an extensive analysis of twenty-five sets of measurements taken by the Risø group. Each set consists of one-hour long runs during which all three velocity components and air temperatures were measured at a height of 5.66 m above the ground and recorded by FM methods. A fuller description of the instrumentation, method of analysis, and results is soon to be published.

INSTRUMENTATION AND DATA REDUCTION

The sensor arrangement used by the Risø group in the 1968 Kansas experiment consisted of three hot wires and one cold wire for measurements of fluctuating wind velocities and temperatures respectively. All the wires were 5 μm tungsten wires with an active length of 1.25 mm. The hot wires

were operated in constant temperature mode using DISA 55D05 anemometers whose outputs were linearized before the signals were recorded. The cold-wire temperature measurements were performed with a DISA 55D01 anemometer coupled as a constant current anemometer with a very small probe current.

Two of the hot wires were arranged in an X-configuration on a fast responding, slightly subcritically damped wind vane with a distance constant of 1.4 m/cycle. If we assume that the vane turns the X-wires into the plane of the instantaneous wind, the corresponding vertical and total horizontal wind components may be determined from the linearized anemometer outputs.

The position of the vane was recorded by means of a precision potentiometer attached to the shaft of the vane. This system allows determination of all three velocity components, u, v, and w. The longitudinal component u is the component in the direction of the horizontal mean vector-wind; v and w are the lateral and vertical wind components respectively.

The sluggish response of the vane to changes of wind direction affects, to some extent, the accuracy with which rapid wind fluctuations can be measured. It can be shown that within the frequency range used in this study, the u and w components are only insignificantly modified by the vane response, whereas the v component suffers a severe frequency cut-off at frequencies of the order of or greater than the natural frequency. Thus, wave lengths of the order of, or smaller than, the distance constant are attenuated.

The third hot wire was stationary and aligned vertically. Hence it provided an independent check of the total horizontal wind as measured by means of the rotating X-wires. The cold wire was also stationary. Both stationary wires were located a few centimetres in front of and below the X-wires.

In this paper we shall discuss only results derived from the analysis of the signals from the vane-X-wire system.

The entire analysis of the recorded signals was carried out on an EAI 680 analogue computer. In principle the procedure had two stages. The first was a coordinate transformation of the measured velocities and directions into a Cartesian coordinate system with the z-axis vertically upwards and the x-axis in the direction of the mean wind, which was defined as the horizontal mean vector-wind averaged over the hour-long duration of the run. The second stage involved computation of covariances and cross-covariances, power spectra, cospectra, and quadrature spectra. The spectral analyses were performed by means of active band-pass filters according to the principles laid out by Larsen (1971).

Owing to its finite length a hot wire does not exhibit a perfect cosine response, and thus it does not measure exactly the wind component in the plane perpendicular to the wire. Particularly for wires which are slanted with respect to the mean wind direction, the deviations from the cosine response must be taken into account. In the present work we employed an adaptation of the correction method suggested by Champagne et al. (1967).

SIMILARITY THEORIES

From considerations based on the Bonssinesq approximate equations of motion and entropy, it follows that in stationary, horizontally homogeneous turbulence of the type discussed in the introduction the vertical fluxes of momentum and heat must be constant. In high Reynolds number turbulence, the molecular contributions to the fluxes can be neglected, so that the friction velocity $u_* = \sqrt{-\overline{u'w'}}$, the temperature flux $\overline{\theta'w'}$, and the buoyancy parameter g/T_o may be taken as characteristic scaling quantities. Primes denote deviations from the mean, θ is the potential temperature, g acceleration due to gravity, and T_o is the dry-adiabatic temperature profile in ^oK. Over-bars denote averaging.

The idea that certain properties of the mean flow should depend only on the height of observation and the three scaling parameters is due to Obuchov (1946), who together with Monin presented the first experimental evidence in 1954. The 1968 Kansas experiment essentially confirmed these ideas (Haugen et al., 1971, Businger et al., 1971).

Extension of the Monin - Obuchov similarity reasoning to velocity spectra leads to

$$\frac{\kappa P_\beta(\kappa)}{u_*^2} = H_\beta(\kappa z, \frac{z}{L}); \quad \beta = u, v, w, \tag{1}$$

κ being the wave number, $P_\beta(\kappa)$ the spectral energy densities, and L the Monin - Obuchov stability length

$$L = - \frac{u_*^3 T_o}{k g \overline{\theta'w'}} . \tag{2}$$

The minus sign and the von Karman constant k have been introduced in accordance with common usage.

Eq. 1 should be valid only over a restricted wave number region. At large wave numbers where the main part of the viscous dissipation takes place, the spectra must show an explicit dependence on viscosity. Unavaidable effects from nonstationarity and large-scale inhomogeneities set a lower wave number limit below which Monin - Obuchov similarity cannot be expected.

Busch and Panofsky (1968) and Busch et al. (1968) found that the vertical velocity spectra obey the Monin - Obuchov similarity theory up to a height of about 50 m, whereas considerable uncertainty exists concerning to what extent the longitudinal and lateral velocity spectra follow similarity laws (see also Fichtl and McVehil, 1970). Recent analyses based on experimental data from the 1968 Kansas experiment (Kaimal et al., 1971) show that such laws are indeed applicable over a wide wave number range, if the terrain is sufficiently homogeneous.

In any case, it is obvious that if an inertial subrange exists, and the vertical velocity spectrum obeys similarity laws, then the two remaining energy spectra must comply with the same scaling at least in this region.

On the basis of the concept of local isotropy and the assumption of incompressible flow, in conjunction with the assumption that the shape of the energy spectra is uniquely determined by the viscosity ν and the rate of kinetic energy dissipation ε, it may be shown that the one-dimensional energy spectra must have the form (see e.g. Batchelor, 1953)

$$P_\beta(\kappa) = (\nu^5 \varepsilon)^{1/4} E_\beta [\kappa (\nu^3/\varepsilon)^{1/4}] , \tag{3}$$

where E_β represents universal functions related by

$$E_w = E_v \tag{4}$$

and

$$E_w(y) = \frac{1}{2} [E_u(y) - y \frac{\partial E_u(y)}{\partial y}] . \tag{5}$$

In the inertial subrange the spectra are not explicitly controlled by viscosity, which by dimensional arguments leads to

$$P_\beta(\kappa) = a_\beta \varepsilon^{2/3} \kappa^{-5/3} , \tag{6}$$

or by application of the Monin - Obuchov scaling to

$$\frac{\kappa P_\beta(\kappa)}{u_*^2} = \frac{a_\beta}{k^{2/3}} \varphi_\varepsilon^{2/3} (\kappa z)^{-2/3}. \tag{7}$$

By virtue of the similarity assumption the nondimensional rate of dissipation

$$\varphi_\varepsilon = \frac{kz\varepsilon}{u_*^3} \tag{8}$$

is a function of the stability parameter z/L only.

By means of Taylor's hypothesis in the form

$$\kappa = \frac{n}{\bar{u}} \tag{9}$$

where n is the frequency in cycles per unit time (κ in cycles/unit length), and $\bar{u}$ is the mean wind speed, the wave number spectra may be converted into frequency spectra such that

$$\kappa P_\beta(\kappa) = n S_\beta(n). \tag{10}$$

The reduced frequency becomes

$$f = \kappa z = \frac{nz}{\bar{u}}. \tag{11}$$

All velocity spectra are defined such that

$$\int_0^\infty S_\beta(n)\, dn = \sigma_\beta^2, \tag{12}$$

σ_β^2 being the velocity variances.

DISCUSSION OF RESULTS

On the basis of the discussion above we suggest that the velocity spectra may be written

$$\frac{n S_\beta(n)}{u_*^2} = K_\beta K_2^{2/3} \varphi_\varepsilon^{2/3} g_\beta(f, \tfrac{z}{L}) F_\beta(K_2 f) \qquad \beta = u, v, w \tag{13}$$

where

K_β are universal constants

K_2 is a scaling factor which is a function of z/L only and equal to unity in neutral stratification (i. e. $z/L = 0$)

F_β integrate logarithmically to unity and give the shapes of the spectra in neutral stratification

g_β are equal to unity in neutral stratification and for reduced frequencies bigger than some critical value.

Once the functions F_β have been determined, the values of K_β can be obtained easily. The values obtained for the longitudinal and vertical spectra were (see Appendix for details)

$$K_u = 5.11 \quad \text{and} \quad K_w = 1.51 \,. \tag{14}$$

With the regions of the w-spectra over which $g_w(f, z/L)$ is supposed to be unity and with an analytical expression for F_w, machine computations provided least-square fitted values of K_2 and $\varphi_{\varepsilon w}$ for each spectrum. When the K_2-values were used on the u-spectra, a similar procedure involving an analytical expression for F_u readily gave values for $\varphi_{\varepsilon u}$.

In figs. 1 and 2

$$\frac{n\, S_\beta(n)}{K_\beta (K_2\, \varphi_{\varepsilon\beta})^{2/3}\, u_*^2} = g_\beta\left(f, \frac{z}{L}\right) F_\beta(K_2 f); \qquad \beta = u, w \tag{15}$$

are plotted against $x = K_2 f$. The twenty-five runs were divided into the five stability categories displayed in table I.

Table I

	No. of runs	$(z/L)_{min}$	$(z/L)_{max}$
Strongly unstable	5	-0.53	-0.24
Moderately unstable	5	-0.16	-0.11
Near neutral	7	-0.11	0.032
Moderately stable	5	0.040	0.13
Strongly stable	3	0.20	0.82

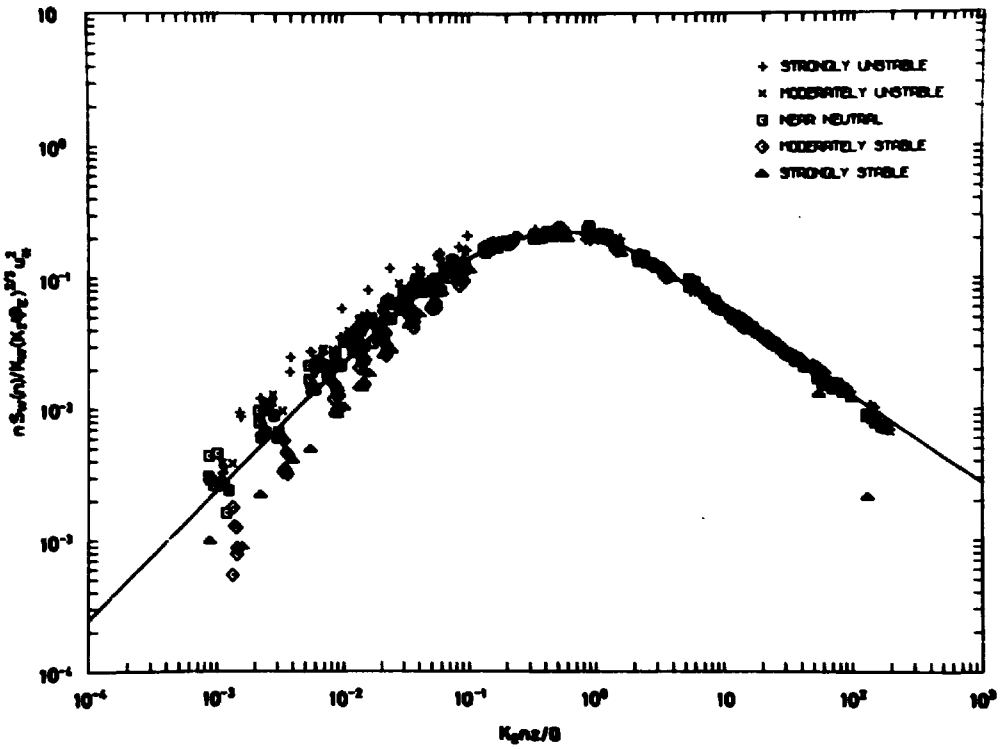

Fig. 1. The normalized w-spectra plotted against $K_2nz/\bar{u}$ and grouped in stability categories.

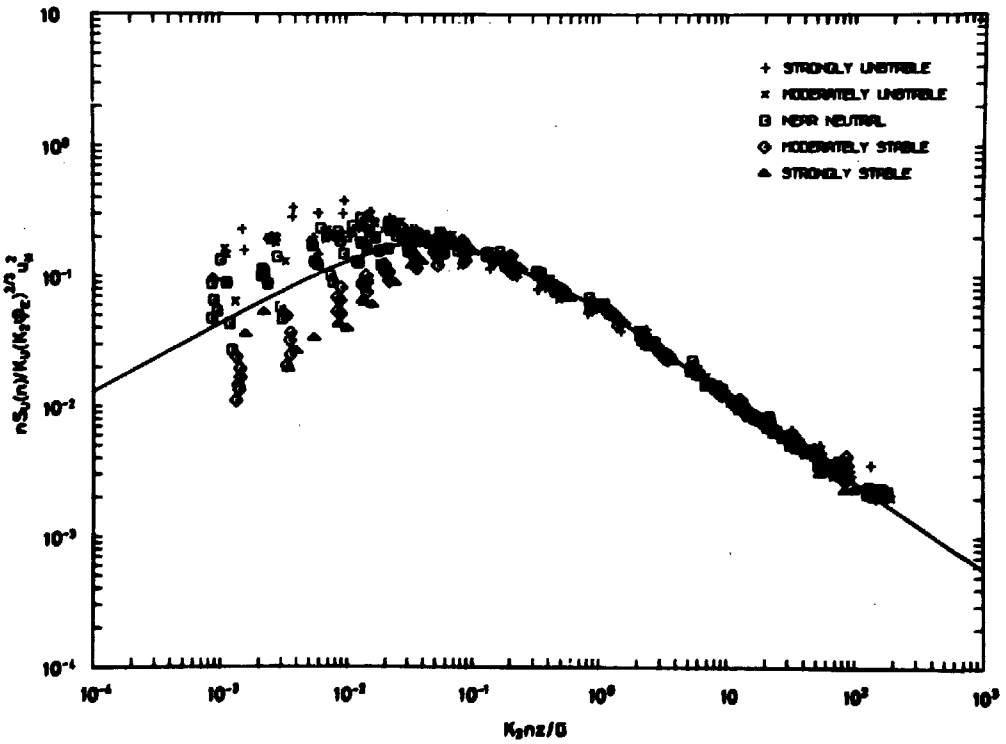

Fig. 2. The normalized u-spectra plotted against $K_2nz/\bar{u}$ and grouped in stability categories.

For $0.1 \leq x = K_2 f \leq 120$ the standard deviations around F_w and F_u are 6 and 8 per cent respectively. For $x < 0.1$ the points are systematically stratified according to thermal stability. Obviously g_w and g_u are not significantly different from unity for $x > 0.1$.

Since the peak of the logarithmic w-spectrum $nS_w(n)$ is at $x > 0.1$, one may interpret $K_2 = f_{mN}/f_m$, where f_{mN} is the location of the peak in hydrostatically neutral atmosphere, and f_m is the actual location.

Fig. 3 displays the scaling factor K_2 versus z/L. $\varphi_{\varepsilon w}$ and $\varphi_{\varepsilon u}$ are plotted against z/L in fig. 4. The empirical variation of φ_ε with stability suggested by Wyngaard and Coté (1971) is also shown.

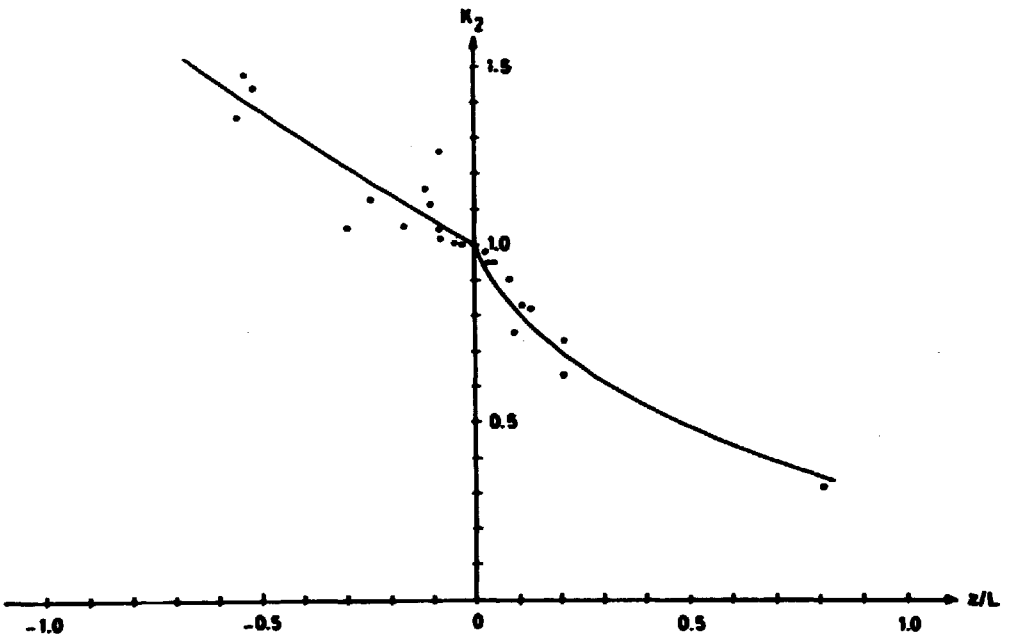

Fig. 3. The scaling factor K_2 plotted against z/L.

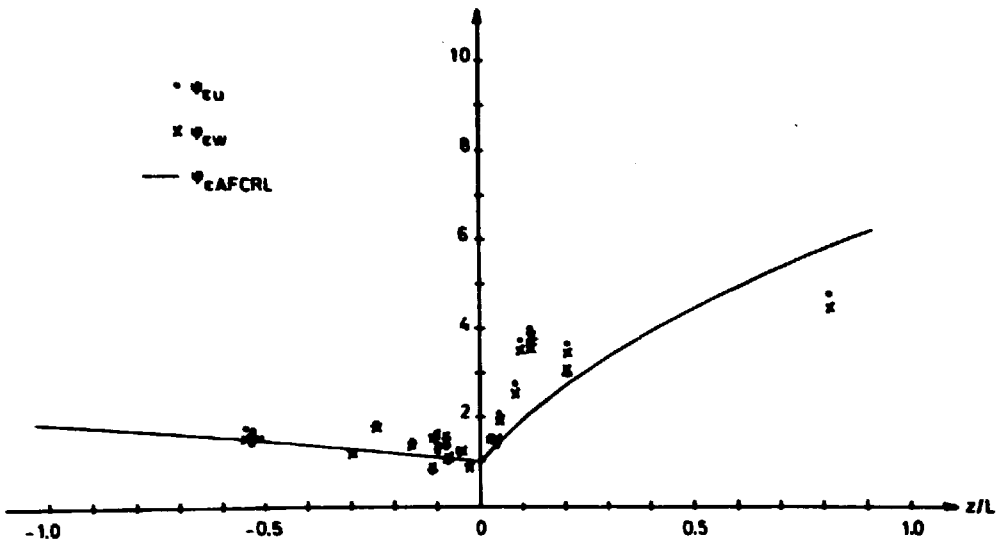

Fig. 4. $\varphi_{\varepsilon w}$ and $\varphi_{\varepsilon u}$ plotted against z/L and compared with the analytical expression proposed by AFCRL.

Vertical Velocity Spectra in Neutral Air

The neutral spectrum of the vertical velocity is described quite well by

$$\frac{n\,S_w(n)}{u_*^2} = \frac{1.95\,f/f_{mN}}{(1 + 2.04\,f/f_{mN})^{5/3}}\;G_w(f) \qquad (16)$$

with $f_{mN} \simeq 0.55$ and a corresponding maximum value of 0.33. The function $G_w(f)$ was introduced in order to eliminate a slight but systematic deviation from the simpler expression. G_w is always equal to or bigger than unity. Its maximum value occurs for $f \simeq 1.35$ and is equal to 1.16. G_w contributes approximately 5 per cent of the total energy and may be neglected for practical purposes. If it is neglected, the peak frequency is reduced to $f_{mN} \simeq 0.4$, and the expression for the vertical spectrum reads

$$\frac{n\,S_w(n)}{u_*^2} \simeq \frac{1.44\,f/f_{mN}}{(1 + 1.5\,f/f_{mN})^{5/3}} \qquad (17)$$

in agreement with the spectrum proposed by Busch et al. (1968) for spectra measured at Brookhaven National Laboratory. However, they report $f_{mN} \simeq 0.3$. Note that $K_w = (\sigma_w/u_*)^2$ for neutral stratification. Busch et al. (1970) found $(\sigma_w/u_*)^2 = 1.48$ in agreement with the value 1.51 suggested here.

The spectra compiled by Kaimal et al. (1971) and measured by means of sonic anemometers at three heights (5.66, 11.3, and 22.6) agree well with eq. 16 except for very low frequencies, where they are about 40 per cent lower. The discrepancy is probably not significant.

In the inertial subrange the spectrum has the form given by eq. 7. For $f \to 0$ the suggested form is

$$\frac{n S_w(n)}{u_*^2} = Bf. \qquad (18)$$

Table II summarizes characteristics of some vertical velocity spectra. All the results are based upon direct measurements of spectra and friction velocities.

Table II

	$\left(\frac{\sigma_w}{u_*}\right)^2$	$\frac{a_w}{k^{2/3}\varphi_\varepsilon^{2/3}}$	B	f_{mN}	$\left(\frac{nS_w(n)}{u_*^2}\right)_{max}$
1. Kaimal et al., 1971	1.51	0.391	2.1	0.56	0.38
2. Busch and Panofsky 1968	1.67	0.388	3.4	0.32	0.43
3. Busch et al., 1968	1.48	$\approx$ 0.345	$\simeq$ 5.0	$\simeq$ 0.3	$\simeq$ 0.32
4. Present study	1.51	0.394	3.5	0.55	0.33
Average $\pm$ max. deviation	1.54	0.380	3.5	0.43	0.37
	$\pm$ 0.13	$\pm$ 0.035	$\pm$ 1.5	$\pm$ 0.13	$\pm$ 0.06

For lines 2 and 3 in table II the low values for f_{mN} are almost certainly due to contamination from unstable cases used in the averaging procedure. Although some of the differences displayed in table II may be real, we believe that to a large extent they reflect experimental difficulties and differences in data reduction procedures.

Longitudinal Velocity Spectra in Neutral Air

The neutral spectrum of the longitudinal velocity is approximated well by

$$\frac{n\,S_u(n)}{u_*^2} = 0.56\,\left[\frac{f}{f_{mN}}\,(1 + 2.04\,\frac{f}{f_{mN}})\right]^{-1/3} G_u(f)\,, \qquad (19)$$

where $f_{mN} = 0.55$ is the reduced frequency at which the vertical velocity spectrum has its peak. Eq. 19 has its peak at $f_{mu} = 0.047$ with a maximum value of 0.97 (see Appendix for details).

For $f \geq 0.1$ $G_u(f)$ may be neglected for all practical purposes. In this region it is always greater than or equal to unity and smaller than 1.11, the maximum value occurring at $f \simeq 1.35$.

Table III compares characteristics of the longitudinal spectra in neutral air summarized by Kaimal et al. (1971) with those reported here. The agreement is indeed very good. For $f \geq 0.005$ the analytical expression for the neutral u-spectrum given by Kaimal et al. differs at the most by 10 per cent from eq. 19. The major difference between the two expressions is that eq. 19 implies

$$\frac{n\,S_u(n)}{u_*^2} \longrightarrow 8.49\,f^{1/2} \quad \text{as} \quad f \longrightarrow 0, \qquad (20)$$

whereas Kaimal et al. find

$$\frac{n\,S_u(n)}{u_*^2} \longrightarrow 105\,f \quad \text{as} \quad f \longrightarrow 0. \qquad (21)$$

Table III

	$\left(\frac{\sigma_u}{u_*}\right)^2$	$\frac{a_u}{k^{2/3}}\,\varphi_\varepsilon^{2/3}$	f_{mu}	$\left(\frac{n\,S_u(n)}{u_*^2}\right)_{max}$
Kaimal et al., 1971	4.72	0.305	0.06	1.01
Present study	5.11	0.295	0.047	0.97

The two asymptotes yield curves that cross at $f \simeq 0.0066$. Thus both in the w- and the u-spectra our measurements yield more energy at low frequencies than those performed by AFCRL.

Ratios of Spectra and Isotropy

Eqs. 4, 5, and 6 imply that if local isotropy is reached at the small-scale end of the spectra, and if an inertial subrange exists, then in the inertial subrange the ratios of the spectra should attain the values

$$S_w(n)/S_u(n) = 4/3 \quad \text{and} \quad S_w/S_v = 1 \,. \tag{22}$$

From eq. 13 and the Appendix it follows that the ratio between the w- and the u-spectra may be written

$$S_w(n)/S_u(n) = \frac{4}{3} \frac{(2.04\ f/f_m)^{4/3}}{(1+2.04\ f/f_m)^{4/3}} \frac{g_w(f, \frac{z}{L})}{g_u(f, \frac{z}{L})} \frac{G_w(0.55\ f/f_m)}{G_u(0.55\ f/f_m)} , \tag{23}$$

where f_m is the reduced frequency at which the logarithmic w-spectrum has its peak.

In neutral stratification $g_w \equiv g_u \equiv 1$, and hence

$$S_w(n)/S_u(n) = \frac{4}{3} \frac{(2.04\ f/f_m)^{4/3}}{(1+2.04\ f/f_m)^{4/3}} \frac{G_w(0.55\ f/f_m)}{G_u(0.55\ f/f_m)} . \tag{24}$$

For all stratifications and for $K_2 f \gtrsim 0.1$, i.e. $f/f_m \gtrsim 0.18$, we may neglect G_w/G_u. Furthermore $g_w/g_u = 1$, so

$$\frac{S_w(n)}{S_u(n)} = \frac{4}{3} \frac{(2.04\ f/f_m)^{4/3}}{(1+2.04\ f/f_m)^{4/3}} . \tag{25}$$

In figs. 5a and b the measured ratios $S_w(n)/S_u(n)$ are plotted versus $x = K_2 f = 0.55\ f/f_m$. The curve in the figures is the one given by eq. 24. To the left in figure 5a is also shown the values of $(4/3)(\varphi_{\varepsilon w}/\varphi_{\varepsilon u})^{2/3}$, i.e. the values of S_w/S_u obtained for $f \to \infty$ when the individual spectra are smoothed by least-square fits to the analytical expressions given in the Appendix.

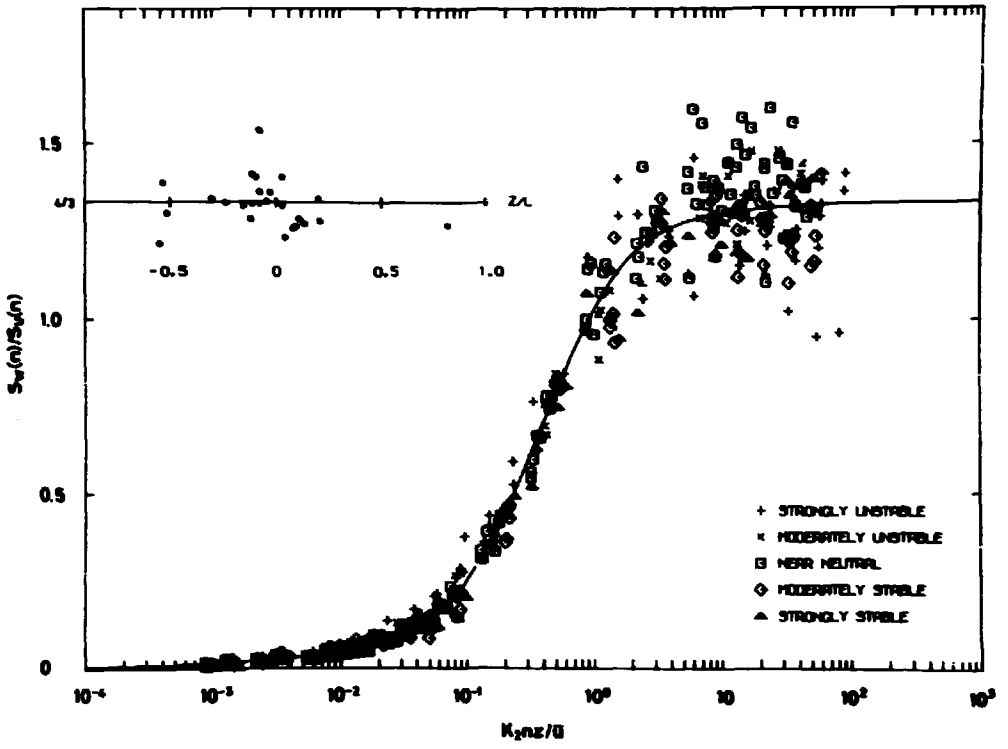

Fig. 5a. The measured ratios $S_w(n)/S_u(n)$ plotted against $K_2nz/\bar{u}$. The ratios of the smoothed spectra, $S_w(n)/S_u(n)$, in the inertial subrange are also plotted against z/L.

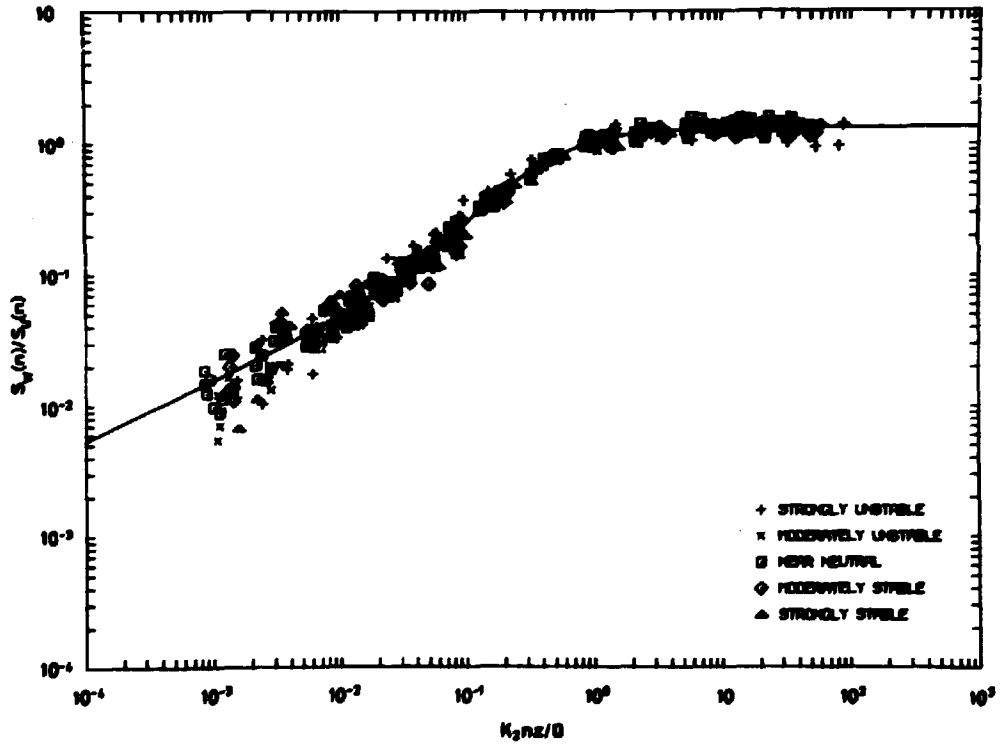

Fig. 5b. The measured ratios $S_w(n)/S_u(n)$ plotted against $K_2nz/\bar{u}$.

Fig. 6 displays the ratio $S_w(n)/S_v(n)$ plotted against $K_2 f$, and in fig. 7 the uw - cospectra are shown normalized by the variance of the vertical velocity component.

The approximate lower limit for a 4/3 ratio between $S_w(n)$ and $S_u(n)$ appears to be $K_2 f = 10$. The ratio S_w/S_v behaves in such a way that a value equal to unity is to be expected for $K_2 f = 10$. At $K_2 f = 10$ the logarithmic cospectra are going steeply towards zero and have values about two orders of magnitude smaller than their peak values. Hence we conclude that isotropy is reached for $K_2 f \geq 10$, and that an inertial subrange exists in which the spectra behave according to eqs. 4, 5, and 6.

If we assume that the upper limit for an inertial subrange is

$$x_d = K_2 f_d = K_2 \frac{z}{2\pi 10 \eta} , \tag{26}$$

where $\eta = (\nu^3/\epsilon)^{1/4}$ is the Kolmogorov scale (see e.g. Pond et al., 1966), then we may write

$$x_d \simeq 0.02 K_2 \varphi_\epsilon^{1/4} \left(\frac{z u_*}{\nu}\right)^{3/4} . \tag{27}$$

By means of eq. 27 it was found that x_d was approximately 330 in the most unstable case, 240 in a typical near-neutral case, and 30 in the most stable case. The u_* -values vary from 8 to 52 cm/s. Hence we should expect only a decade or so of inertial subrange. Over very smooth terrain or over water, in which cases u_* is small, an inertial subrange may not exist at all. This of course does not exclude the possible existence of local isotropy at high wave numbers, but it leads to difficulties concerning the proper choice of scaling parameters.

Inspection of fig. 5 reveals that the ratios $S_w(n)/S_u(n)$ are closely approximated with eq. 24 for all stabilities. There is no apparent stratification of the points according to z/L. The standard deviation of the relative deviations is 19 per cent. This result implies that the functions $g_w(f, \frac{z}{L})$ and $g_u(f, \frac{z}{L})$ must be equal throughout the frequency domain considered, and that for a fixed (f/f_m) the energy ratio is independent of z/L.

$S_w(n)/S_u(n) = 1$ for $K_2 f = 1$, and hence $f = 1/K_2$ is the reduced frequency at which the u-spectrum crosses through the w-spectrum.

The behaviour of $S_w(n)/S_v(n)$ as displayed in fig. 6 is somewhat different. For $K_2 f \geq 0.1$ the points agree fairly well. For $K_2 f \simeq 0.4$ we find $S_w/S_v = 1$, which means that the w-spectra and the v-spectra cross

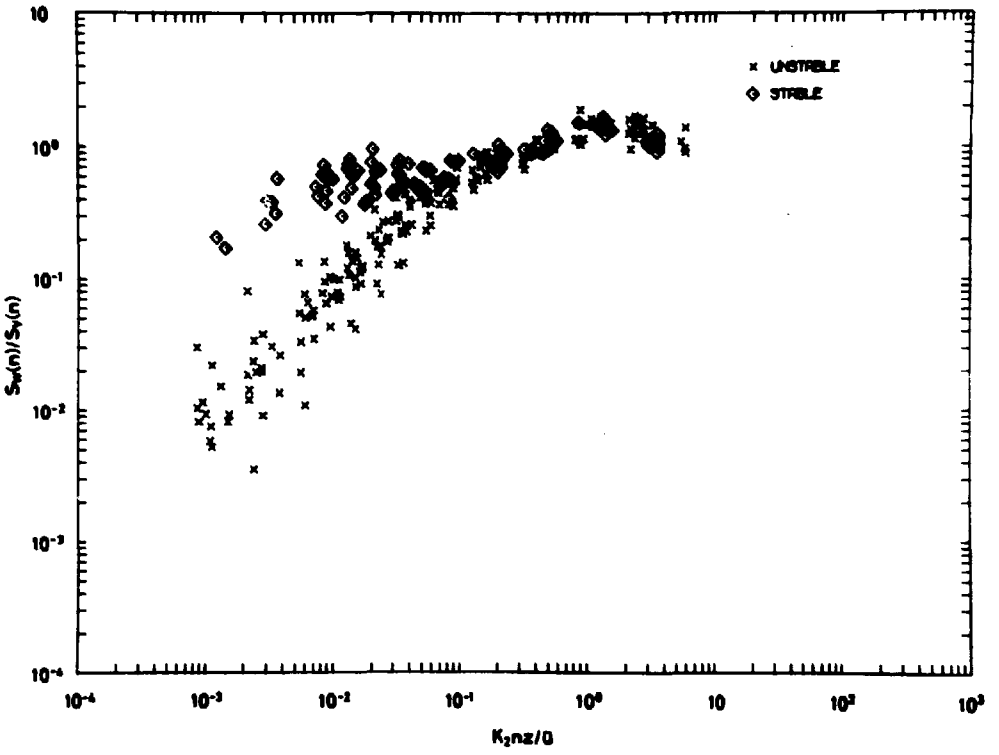

Fig. 6. The measured ratios $S_w(n)/S_v(n)$ plotted against $K_2nz/\bar{u}$.

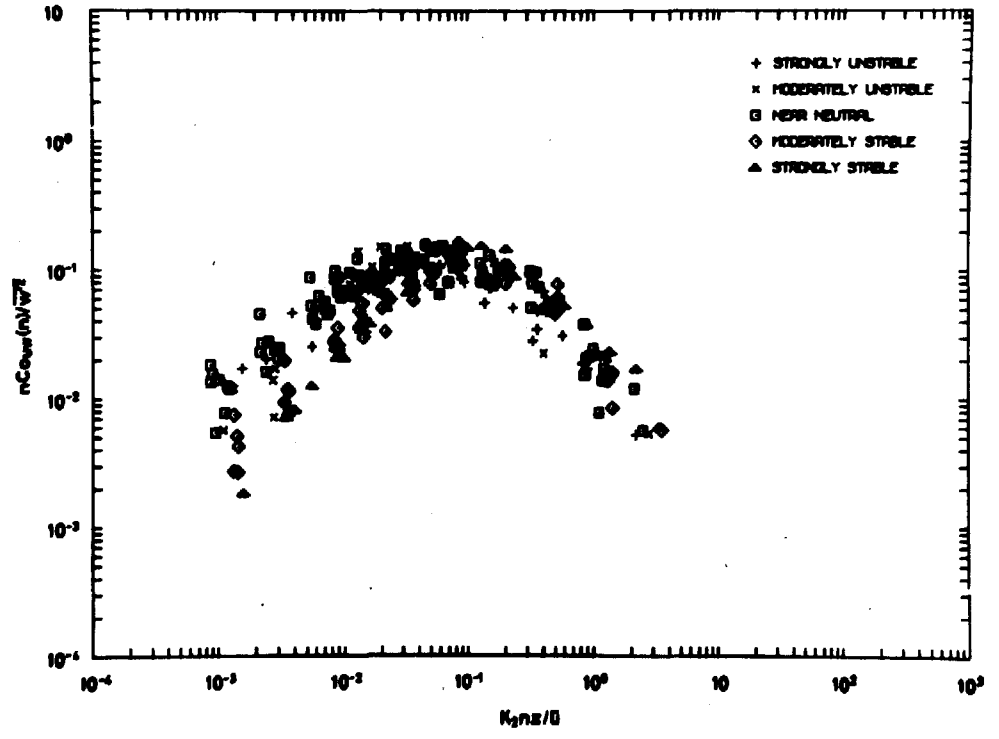

Fig. 7. $nCo_{uw}(n)$ normalized by the variance of the vertical velocity component plotted against $K_2nz/\bar{u}$.

each other at $f \simeq 0.4/K_2$ with the v-spectra approaching the w-spectra from below at higher wave numbers.

For $K_2 f < 0.1$ the points branch out with the upper branch pertaining to stable and the lower to unstable situations. This indicates a distinct difference between the flow regimes in stable and unstable stratification with an abrupt change from one to the other which is primarily observed through the behaviour of the v-spectrum.

CONCLUSIONS

Within the accuracy of measurement, the one-dimensional velocity spectra in the surface boundary layer seem to conform with the Monin - Obuchov similarity hypothesis over a wide wave number range. The most important scaling parameter appears to be λ_m, the wave length at which the logarithmic spectrum of vertical velocity has its peak. The ratio $K_2 = \lambda_m/\lambda_{mN}$ between λ_m and its value under hydrostatically neutral conditions is a monotonically decreasing function of the stability parameter z/L.

For reduced frequencies $f = \frac{nz}{\bar{u}}$ such that $K_2 f \geq 0.1$, the normalized velocity spectra can be described by

$$\frac{n\, S_\beta(n)}{u_*^2} = K_\beta (K_2 \varphi_\varepsilon)^{2/3}\, F_\beta(K_2 f); \quad \beta = u, v, w, \tag{28}$$

where the K_β are "universal" constants, and the $F_\beta(y)$ are "universal" functions describing the shapes of the spectra in neutral stratification.

For $K_2 f > 10$ local isotropy is reached. The spectra follow -5/3-laws, as they should according to Kolmogorov's hypotheses leading to the concept of an inertial subrange, and the spectral ratios have their proper values.

For $K_2 f < 0.1$ the shapes of the spectra show a marked dependence on hydrostatic stability. It is suggested that the transition from stable to unstable stratification causes an abrupt change of the low-frequency part of the flow field. In both the regimes the spectral ratios $S_w(n)/S_u(n)$ and $S_w(n)/S_v(n)$ are functions of $K_2 f$ only.

ACKNOWLEDGEMENT

Without the generous help and cooperation extended to us by the Boundary Layer Branch of the AFCRL the results presented here would have been far less interesting and the work leading to them far less pleasant.

APPENDIX

The shapes of the neutral u- and w-spectra were determined as follows. The normalized, near-neutral spectra were plotted against the reduced frequency in doubly logarithmic plots. Smooth curves were drawn to that they either separated the stable spectra from the unstable ones or were mean curves where no separation of the points according to thermal stability was obvious.

Then analytical expressions were constructed which resembled the curves as closely as possible. Hence the expressions given below fit the high-frequency part of the near-neutral spectra, separate stable from unstable spectra in the low-frequency end, and integrate logarithmically to unity.

For the vertical velocity spectrum we found

$$F_w(x) = \frac{2.36\,x}{(1 + 3.74\,x)^{5/3}}\; G_w(x), \tag{A1}$$

where

$$G_w(x) = \begin{cases} 1 & \text{for } x \leq x' = 0.2 \\ \exp\{0.11 \ln^2 \frac{x}{x'} \exp\{-0.274 \ln^2 \frac{x}{x'}\}\} & \text{for } x \geq x' = 0.2. \end{cases}$$

$F_w(x)$ has its maximum at $x = 0.55$ with $F_{wmax} = 0.22$. For $x \to \infty$ we obtain

$$F_w(x) \to A_w\, x^{-2/3} \quad \text{with} \quad A_w = 0.26. \tag{A2}$$

For the longitudinal velocity spectrum we found

$$F_u(x) = 0.0894\; [x(1 + 3.74\,x)]^{-1/3}\; G_u(x) \tag{A3}$$

where

$$G_u(x) = \begin{cases} (\frac{x}{x''})^{5/6} \exp\{1 - (\frac{x}{x''})^{5/6}\} & \text{for } x \leq x'' = 0.1 \\ 1 \quad \text{for} \quad 0.1 \leq x \leq 0.2 & \\ \exp\{0.0763 \ln^2 \frac{x}{x'} \exp\{-0.274 \ln^2 \frac{x}{x'}\}\} & \text{for } x \geq x' = 0.2 \end{cases}$$

$F_u(x)$ has its maximum at $x = 0.047$ with $F_{umax} = 0.19$. For $x \to \infty$ we obtain

$$F_u(x) \to A_u x^{-2/3} \quad \text{with} \quad A_u = 0.058. \tag{A4}$$

From eqs. 7, 13, A2, and A4 it follows that

$$K_u = \frac{a_u}{A_u k^{2/3}} = 5.11 \quad \text{and} \quad K_w = \frac{a_w}{A_w k^{2/3}} = 1.51 \tag{A5}$$

where we have used the value for the von Karman constant $k = 0.35$ found in Kansas (Businger et al., 1971). For the Kolmogorov constants we have inserted $a_u = \frac{4}{3} a_w = 0.146$ corresponding to a value $\alpha = 0.5$ for the longitudinal Kolmogorov constant when wave numbers are in radians per unit length (Kaimal et al., 1971).

REFERENCES

Batchelor, G. K., The Theory of Homogeneous Turbulence. (Cambridge University Press, Cambridge, 1956) 197 pp.

Busch, N. E. and H. A. Panofsky, Recent Spectra of Atmospheric Turbulence. Quart. J. Roy. Meteorol. Soc. 94 (1968) 132-148.

Busch, N. E., J. A. Frizzola, and I. A. Singer, The Micrometerology of the Turbulent Flow Field in the Atmospheric Surface Boundary Layer. Acta Polytech. Scand. Ph59, Copenhagen (1968) 50 pp.

Busch, N. E., R. M. Brown, and J. A. Frizzola, Vertical Velocity Variances and Reynolds Stresses at Brookhaven. J. Appl. Meteorol. 9 (1970) 583-587.

Businger, J. A., J. C. Wyngaard, Y. Izumi, and E. F. Bradley, Flux-Profile Relationships in the Atmospheric Surface Layer. J. Atmos. Sci. 28 (1971) 181-189.

Champagne, F. H., C. A. Sleicher, and O. H. Wehrmann, Turbulence Measurements with Inclined Hot Wires. J. Fluid Mech. 28 (1967) 153-182.

Fichtl, G. H. and G. E. McVehil, Longitudinal and Lateral Spectra of Turbulence in the Atmospheric Boundary Layer at the Kennedy Space Center. J. Appl. Meteorol. 9 (1970) 51-63.

Haugen, D. A., J. C. Kaimal, and E. F. Bradtley, An Experimental Study of Reynolds Stress and Heat Flux in the Atmospheric Surface Layer. Quart. J. Roy. Meteorol. Soc. 97 (1971) 168-180.

Kaimal, J. C., J. C. Wyngaard, Y. Izumi, and O. R. Coté, Spectral Characteristics of Surface Layer Turbulence (submitted to Quart. J. Roy. Meteorol. Soc.).

Larsen, S. E., Spectral Analysis Based on Analog Technique. In: Statistical Methods and Instrumentation in Geophysics. Proceedings of the NATO Advanced Study Institute in Norway, April 1971. Edited by A. G. Kjelaas. (Teknologisk Forlag, Oslo, 1971) 137-154.

Monin, A. S. and A. M. Obukhov, Basic Laws of Turbulent Mixing in the Atmosphere Near the Ground. Tr. Geofiz. Inst. Akad. Nauk SSSR No. 24 No. 151 (1954) 163-187.

Obukhov, A. M., Turbulence in an Atmosphere with Inhomogeneous Temperature. Tr. Inst. Teor. Geofiz. Akad. Nauk SSSR 1 (1946) 95-115.

Pond, S., S.D. Smith, P.F. Hamblin, and R.W. Burling, Spectra of Velocity and Temperature Fluctuations in the Atmospheric Boundary Layer over the Sea. J. Atmos. Sci. 23 (1966) 376-386.

Wyngaard, J.C. and O.R. Coté, The Budgets of Turbulent Kinetic Energy and Temperature Variance in the Atmospheric Surface Layer. J. Atmos. Sci. 28 (1971) 190-201.

Investigation of the NH_2 Radical Produced by Pulse Radiolysis of Ammonia in Aqueous Solution

by

Palle B. Pagsberg

Abstract

Hydroxyl radicals react with ammonia to form NH_2 radicals with a rate constant $k = 1.0 \times 10^8\ M^{-1}s^{-1}$. The ammonium ion is inert toward hydroxyl radicals. The NH_2 radical has a very weak absorption band at 530 nm with a band width of 200 nm and an extinction coefficient of 81 $M^{-1}cm^{-1}$. The spectral properties of the visible absorption band and the ultraviolet bands occurring simultaneously indicate that NH_2 radicals form charge transfer complexes with solvent and solute molecules. Hydrazine is formed with a maximum yield $G = 2.7$ by dimerization of NH_2 radicals, the rate constant being $2k = 4.4 \times 10^9\ M^{-1}s^{-1}$. Hydroxylamine is formed with a yield which goes through a maximum and a minimum with increasing ammonia concentration. The more important reaction at low ammonia concentrations is $NH_2 + OH \rightarrow NH_2OH$ with the rate constant $k = 9.5 \times 10^9\ M^{-1}s^{-1}$. At high ammonia concentrations $G(N_2H_4) = 2.7$ and $G(NH_2OH) = 0.7$, indicating that hydrogen peroxide is the precursor of the excess oxidation yield. It seems possible that the stoichiometric reaction $H_2O_2 + NH_3 \rightarrow NH_2OH + H_2O$ may proceed by a chain reaction with the radical NHOH as a chain carrier. The reactivity of NH_2 radicals toward H_2O_2, O_2, N_2H_4, and NH_2OH was investigated. The decay of NH_2 changed into pseudo first-order kinetics in the presence of H_2O_2 and O_2, corresponding to $k(NH_2 + H_2O_2) = 9 \times 10^7\ M^{-1}s^{-1}$ and $k(NH_2 + O_2) = 3 \times 10^8\ M^{-1}s^{-1}$, whereas the decay remained unchanged in the presence of N_2H_4 and NH_2OH.

INTRODUCTION

There is a pronounced difference between pulse radiolysis and steady-state radiolysis of ammonia in aqueous solution as far as the observable stable products are concerned. In their work on the action of X-rays on ammonia in aqueous solution Rigg, Scholes, and Weiss[1] reported the absence of oxidation products in evacuated solutions, whereas nitrite was formed in the presence of oxygen. In the present pulse radiolysis work high yields of hydrazine and hydroxylamine were found, and the kinetics of the NH_2 radical and the OH radical were studied spectrophotometrically to obtain the absolute rate constants of the reactions involved.

EXPERIMENTAL

The experimental work was started at Risø, but a major part of the pulse radiolytic investigations were performed during the author's stay at the Argonne National Laboratory. The pulse radiolysis instrumentations used at the two laboratories have been described previously[2, 3]. The dose rates applied in the present work were 1 - 10 krads/μs, and the duration of the electron pulses 0.4 - 2 μs. An optical path length of 8 cm gave optical densities of the NH_2 band of the order of 0.03, detectable with a signal to noise ratio of about 100. The total rise time of the detection system was 80 ns. The ferrocyanide system which has been investigated by Rabani and Matheson[4] was used as a convenient instant dosimeter. The dose was calculated from the absorbance of the ferricyanide band observed at the end of the electron pulse. The extinction coefficient of ferricyanide is 1000 M^{-1} cm^{-1} at 420 nm, and it was assumed that $G(Fe(CN)_6^{3-}) = G_{e^-_{aq}} + G_{OH}$ for a dosimeter consisting of 1 mM $K_4Fe(CN)_6$, 25 mM N_2O, and about 0.1 mM O_2. In this system N_2O converts e^-_{aq} into OH which in turn oxidizes ferrocyanide. The oxygen is added to remove H atoms which would otherwise react with the ferricyanide formed. The determination of the yields of hydrazine and hydroxylamine was carried out by colorimetric standard methods[5, 6]. The methods were tested on mixtures of N_2H_4 and NH_2OH which gave results identical with those of the pure standards. It was also found that the presence of 50 mM H_2O_2 did not interfere with the analysis. The analysis of NH_2OH was found to be less reliable when ammonia was added in concentrations above 10 mM. The formation of indooxine was slower, and the absorbance reading was observed to increase very slowly.

RESULTS

The fate of NH_2 radicals produced by pulse radiolysis of ammonia in aqueous solution was deduced from the radiolytic yields combined with the information obtained by kinetic spectroscopy. The reactions taking place in nitrous-oxide-saturated solutions are

$$e^-_{aq} + N_2O \rightarrow OH + OH^- \quad (1)$$

$$OH + OH \rightarrow H_2O_2 \quad (2)$$

$$OH + NH_3 \rightarrow NH_2 + H_2O \quad (3)$$

$$OH + NH_2 \rightarrow NH_2OH \quad (4)$$

$$NH_2 + NH_2 \rightarrow N_2H_4 \quad (5)$$

$$H_2O_2 + NH_2 \rightarrow NHOH + H_2O \quad (6)$$

$$NHOH + NH_3 \rightarrow NH_2OH + NH_2 \quad (7)$$

$$NHOH + C \rightarrow P \quad (8)$$

The chain reaction can be terminated by reaction (8). The competitor, C, may be a radical or a molecular species. Hydrogen atoms may participate in the reactions

$$H + NH_3 \rightarrow NH_2 + H_2 \quad (9)$$

$$H + R \rightarrow Q \quad (10).$$

R may be any of the radicals present in the solution, including H. The yield of hydrogen atoms is about ten per cent of the total radical yield. However, in the present investigation the effect of hydrogen atoms on the yields and the kinetics seemed to be of minor importance. Since the standard heat of reaction (9) is close to zero, this reaction may be very slow compared with the radical reactions (10). In addition it appears that the combination of hydrogen atoms must be much faster than any of the other reactions H + R.

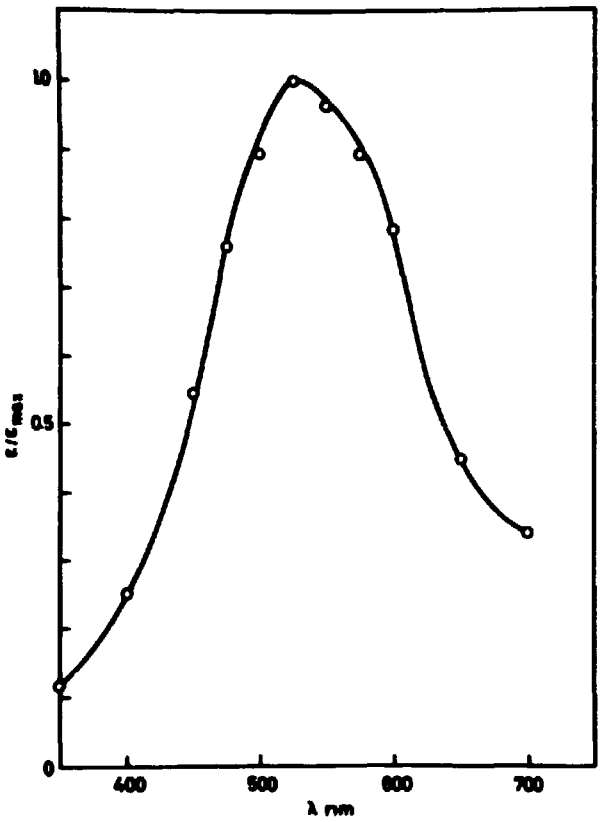

Fig. 1. Visible spectrum of the NH_2 radical in aqueous solution. ϵ_{max} = 81 ± 2 $M^{-1}cm^{-1}$.

Spectral Properties of the NH_2 Radical

The visible spectrum of NH_2 is shown in fig. 1. The assignment of this transient absorption to the NH_2 radical is supported by the following observations:

(a) The initial absorbance at 530 nm increases with increasing ammonia concentration and decreases with increasing concentration of ferrocyanide acting as an OH scavenger. This demonstrates that the precursor is the hydroxyl radical which reacts with ammonia.

(b) The absorbance decays by second-order kinetics, and the yield of hydrazine, which depends on the ammonia concentration, is proportional to the time integral of the square of the absorbance, $G(N_2H_4) \propto \int A^2 dt$. This implies that the species absorbing at 530 nm is the precursor of the hydrazine yield.

Furthermore the $^2A_1 \leftarrow {}^2B_1$ transition of NH_2 in the gas phase occurs in the same spectral region[7, 8].

The ultraviolet part of the spectrum is shown in fig. 2.

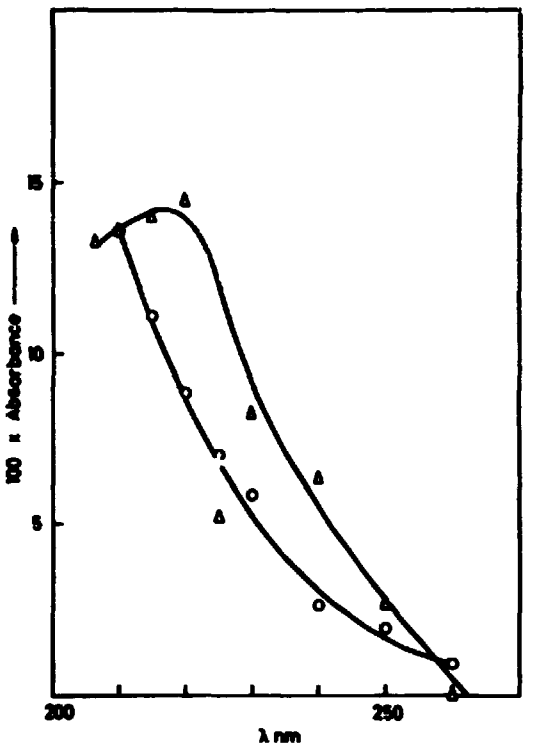

Fig. 2. Ultraviolet absorption bands at the end of the electron pulse after correction for contribution from OH radicals. Δ 25 mM NH_3, and O 250 mN NH_3.

The absorption band observed at low ammonia concentrations has a maximum at 215 nm. The band is gradually shifted toward shorter wave lengths with increasing ammonia concentration. The decay of the visible band changed into first-order kinetics in the presence of hydrogen peroxide, and the same effect was observed in the ultraviolet region. This indicates that the two absorption bands originate from the same species, viz. NH_2.

KINETICS

Determination of k_3 and $\varepsilon(NH_2)$

The hydroxyl radical has a weak absorption band at 230 nm[9, 10]. The replacement of OH by NH_2 via reaction (3) could therefore be studied by kinetic spectroscopy of both of the radical species. The evaluation of k_3

and $\varepsilon(NH_2)$ was accomplished by three different methods.

(I) The effect of ammonia concentration on the initial yield of NH_2.

Integration of the rate equation shows that the fraction of OH radicals being converted into NH_2 radicals during the electron pulse can be expressed by $G/G_{max} = 1 - \frac{1}{x}(1-\exp(-x))$, where $G_{max} = G_{OH} + G_{e^-_{aq}}$, $x = k_3[NH_3]t_p$, and t_p is the pulse duration. Combination of NH_2 radicals could be neglected when the applied dose rate was 5 krads/μs and t_p = 1 μs.

The maximum absorbance of NH_2 was derived from the asymptotic expression, $A/A_m = G/G_m \sim (1 - \frac{1}{x})$ when $x \geq 4$.

Hence A_m was obtained from a plot of absorbance versus reciprocal ammonia concentration, and the extinction coefficient could be calculated, $\varepsilon(NH_2) = \varepsilon_D \times A_m/A_D$, where $\varepsilon_D = 1000\ M^{-1}cm^{-1}$ is the extinction coefficient of the ferricyanide dosimeter, and A_D is the absorbance of the dosimeter. The rate constant was calculated from a plot of x versus ammonia concentration, $k_3 = \frac{1}{t_p}\frac{dx}{d[NH_3]}$.

(II) Kinetics of the hydroxyl radical.

The rate constant was derived from the pseudo first-order decay $k_3 = -(1/[NH_3])d\ln[OH]/dt$. Method (I) was also applied to the hydroxyl radical.

(III) Competition between ammonia and ferrocyanide.

Only the ratio $k_3/k(OH + Fe(CN)_6^{4-})$ could be determined by this method. k_3 was calculated using the value reported by Rabani and Matheson[4] $k(OH + Fe(CN)_6^{4-}) = (1.07 \pm 0.10)\ m^{-1}s^{-1}$.

The methods (I), (II), and (III) gave almost identical results

$$k_3 = (1.0 \pm 0.1) \times 10^8\ M^{-1}s^{-1}$$

$$\varepsilon(NH_2) = 81 \pm 2\ M^{-1}cm^{-1}.$$

Method (II) was applied to series of different pH. The same value of k_3 was found at pH = 8.5 and at pH = 10.0. This shows that the hydroxyl radicals react only with NH_3, whereas NH_4^+ is inert.

Determination of $k_4 = k(OH + NH_2)$

The amount of hydroxylamine formed via reaction (4) is

$$NH_2OH = k_4\int [OH][NH_2]\,dt.$$

k_4 could be calculated from this expression since both the yield and the value of the integral were available from the experimental data. Fig. 3 shows that the integral and the yield have their maxima at the same ammonia

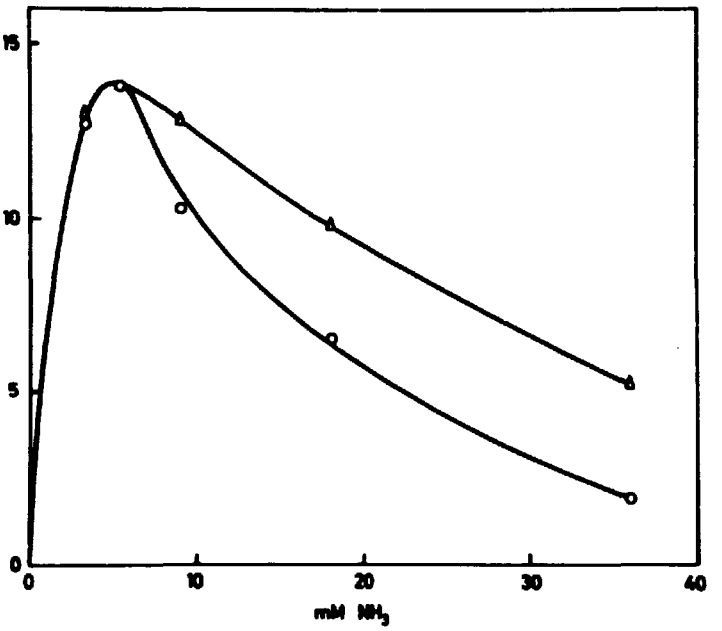

Fig. 3. Effect of ammonia concentration on the relative yield of hydroxylamine. The circels represent $(10^{12}/C_t) \int_0^{\infty}[OH][NH_2]dt$ and the triangles represent $100\ G(NH_2OH)/(G_{e^-_{aq}} + G_{OH})$. C_t is the sum of hydrated electrons and hydroxyl radicals produced during the electron pulse.

concentration. The integral vanishes at high ammonia concentrations, whereas the yield goes through a minimum and approaches the value $G(NH_2OH) = G_{H_2O_2}$ at these concentrations. k_4 was evaluated from the maximum of the two curves

$$k_4 = 9.5 \times 10^9\ M^{-1}s^{-1}.$$

Dimerization of NH_2 Radicals

Fig. 4 shows the kinetics of NH_2 radicals at three different ammonia concentrations. The time derivative, $d(1/A)/dt$, approaches a minimum value at high ammonia concentrations, and this value was identified with $k_5/\varepsilon L$, where L is the optical path length

$$k_5 = 2k(NH_2) = 4.4 \times 10^9\ M^{-1}s^{-1}.$$

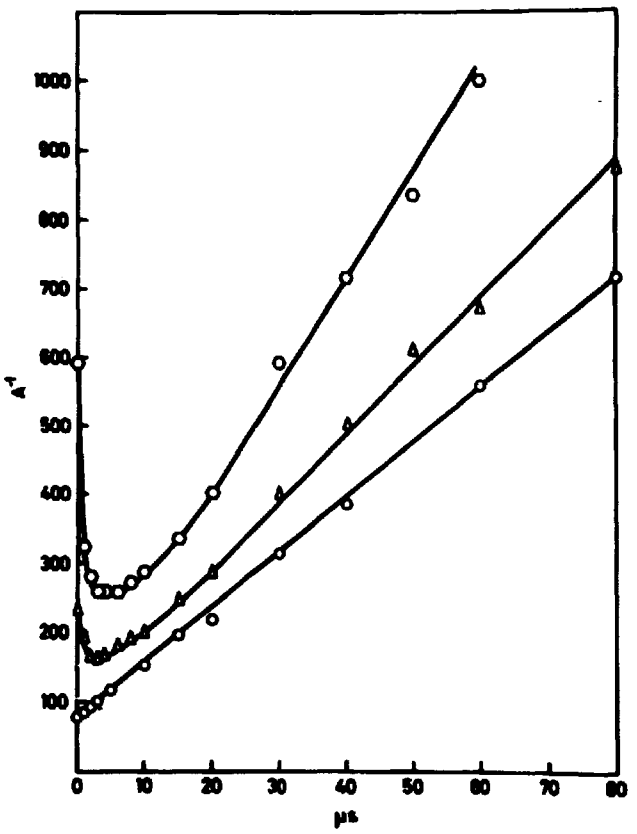

Fig. 4. Effect of ammonia concentration on the kinetics of NH_2 radicals monitored at 530 nm. ○ 2.3 mN NH_3, △ 5.3 mM NH_3, ○ 135 mM NH_3.

The yield of hydrazine increases steadily to a maximum value of $G(N_2H_4) = \frac{1}{2}(G_{OH} + G_{e^-_{aq}})$ at high ammonia concentrations.

The same value of k_5 was obtained from the expression

$$k_5/(\epsilon L)^2 = [N_2H_4]/\int A^2 dt.$$

The right-hand side of this equation remained constant irrespective of the ammonia concentration.

The Fate of Hydrogen Peroxide

The yield of hydroxylamine produced via reaction (4) vanishes at high ammonia concentrations because the half-life of reaction (3) becomes extremely short. The yield of hydroxylamine was observed to pass through a minimum and increase to a maximum value of $G(NH_2OH) = G_{H_2O_2}$ with increasing ammonia concentration. Thus it appears that hydrogen peroxide is the precursor of the excess yield of hydroxylamine, and the effect of con-

centration indicates that a reaction involving ammonia competes with other reactions. Aqueous solutions of ammonia and hydrogen perioxide are quite stable although the reaction $H_2O_2 + NH_3 \rightarrow NH_2OH + H_2O$ is exothermic by about 23 kcal/mole. A chain reaction could possibly be initiated by the reaction between NH_2 radicals and hydrogen peroxide. This reaction was investigated by kinetic spectroscopy, and the decay of NH_2 remained first order in H_2O_2 corresponding to the rate constant

$$k(NH_2 + H_2O_2) = 9 \times 10^7 \, M^{-1}s^{-1}.$$

The following reactions were considered

$$NH_2 + H_2O_2 \rightarrow NH_2OH + OH \qquad (6a)$$

$$NH_2 + H_2O_2 \rightarrow NH_3 + HO_2 \qquad (6b)$$

$$NH_2 + H_2O_2 \rightarrow H_2O + NHOH \qquad (6c)$$

On the basis of an estimate of $\Delta H_f(NHOH) = 44$ kcal/mole and the reported values of ΔH_f of the other species[11], reactions (6a), (6b), and (6c) were found to be exothermic by 2.7 kcal/mole, 12.5 kcal/mole, and 23.6 kcal/mole respectively.

A very efficient chain reaction could be established by reactions (3) and (6a). However, the steady state of NH_2 radicals anticipated by this mechanism was not observed, and $G(-H_2O_2)$ was small at high concentrations of H_2O_2, contrary to expectation. Reaction (6a) must therefore be rejected. Reactions (6b) and (6c) may be distinguished by the spectral properties of HO_2 and NHOH. The spectra of HO_2 and O_2^- have been investigated in great detail[12]. Several overlapping ultraviolet absorption bands were observed in the system $NH_2 + H_2O_2$, but no definite assignment has been possible as yet. However, reactions (6), (7), and (8) can account for the experimental observations. It has been proposed that reaction (7) can proceed in the opposite direction[13]. Since the estimated heat of reaction is close to zero, it seems plausible that the reaction may be reversible. The low value of $G(-H_2O_2)$ observed at high concentrations of H_2O_2 may be explained by assuming that H_2O_2 can terminate the chain reaction via reaction (8). Further information about the radical NHOH is being obtained in a current investigation of the reaction between hydroxyl radicals and hydroxylamine.

Reaction with Oxygen

NH_2 radicals disappear by a rapid first-order reaction in oxygen-saturated solution,

$$k(NH_2 + O_2) = 3 \times 10^8\ M^{-1}s^{-1}$$

and nitrite is formed with a yield of about one. The observation of consecutive ultraviolet absorption bands shows that the mechanism is complex. The primary product may well be the adduct, NH_2O_2, as proposed by Rigg et al.[1], but it seems necessary to carry out a more detailed analysis of the radiolytic products in order to establish a definite mechanism.

DISCUSSION

Protolysis has a remarkable effect on the stability of ammonia. Protonation of the lone pair enhances the $s \rightarrow p$ promotion character on the nitrogen atom, and the result is a large increase in bond energies, which makes the ammonium ion inert toward hydroxyl radicals, $D(H - NH_3^+)$ = 130 kcal/mole[13], $D(H - OH)$ = 116.8 kcal/mole, and $D(H - NH_2)$ = 105.4 kcal/mole[11]. A similar effect has been observed in pulse radiolysis of hydrazine[14].

The spectral properties of NH_2 radicals in aqueous solution indicate a strong interaction with solvent and solute molecules. The visible band is shifted toward shorter wave lengths relative to the gas phase transition. The ultraviolet bands are tentatively assigned to charge transfer complexes, (NH_2, H_2O) and (NH_2, NH_3). The NH_2 radical has an electron affinity of 1.21 eV[11], and the complex formed by the reaction $NH_2 + NH_3 \rightarrow N_2H_5$ may be comparable with the halogen molecular ions which can be formed by the reactions $X + X^- \rightarrow X_2^-$ and $X_2 + e_{aq}^- \rightarrow X_2^-$. A recent investigation of the reaction $N_2H_5^+ + e_{aq}^-$ has confirmed the existence of N_2H_5 as an intermediate species[14]. However, it is still an open question whether the ground state of this species is repulsive or not.

The disproportionation reaction, $2\ NH_2 \rightarrow NH + NH_3$, reported to take place in the gas phase[15] was not observed in aqueous solution. However, as NH has been reported to react very fast with water to form NH_2OH[16], this might be the reason for the absence of any detectable NH absorbance at 340 nm. The application of ethylene as a possible scavenger for NH gave an indication of formation of small amounts of aziridine. These experiments

were, however, not sufficiently conclusive to establish the presence of NH.

ACKNOWLEDGEMENT

I wish to express my appreciation to Dr. E. J. Hart for his support in this investigation which was partly performed during my stay at the Argonne National Laboratory.

I am most indebted to Mrs. Jytte Eriksen for her excellent technical assistance in analytical chemistry and evaluation of the kinetic results.

REFERENCES

1) T. Rigg, G. Scholes, and J. Weiss, Chemical Actions of Ionising Radiations in Solutions. The Action of X-Rays on Ammonia in Aqueous Solution. J. Chem. Soc. No. 580 (1952) 3034-38.

2) H. C. Christensen, G. Nilsson, P. B. Pagsberg, and S. O. Nielsen, Pulse Radiolysis Apparatus for Monitoring at 2000 Å. Rev. Sci. Instrum. 40 (1969) 786-789.

3) M. S. Matheson and L. M. Dorfman, Detection of Short-Lived Transients in Radiation Chemistry. J. Chem. Phys. 32 (1960) 1870-71.

4) J. Rabani and M. S. Matheson, The Pulse Radiolysis of Aqueous Solutions of Potassium Ferrocyanide. J. Phys. Chem. 70 (1966) 761-769.

5) T. Dambrauskas and H. H. Cornish, A Modified Spectrophotometric Method for the Determination of Hydrazine. Amer. Ind. Hyg. Ass. J. 23 (1962) 151-156.

6) D. S. Frear and R. C. Burrell, Spectrophotometric Method for Determining Hydroxylamine Reductase Activity in Higher Plants. Anal. Chem. 27 (1955) 1664-65.

7) D. A. Ramsay, The Analysis of the a-Bands of Ammonia. Mem. Soc. Roy. Sci. Liege 18 (1957) 471-479.

8) S. Gordon, W. Mulac, and P. Nangia, Pulse Radiolysis of Ammonia Gas. II. Rate of Disappearance of the $NH_2(X^2B_1)$ Radical. J. Phys. Chem. 75 (1971) 2087-93.

9) J. K. Thomas, J. Rabani, M. S. Matheson, E. J. Hart, and S. Gordon, Absorption Spectrum of the Hydroxyl Radical. J. Phys. Chem. 70 (1966) 2409-10.

10) P. B. Pagsberg, H. C. Christensen, J. Rabani, G. Nilsson, J. Fenger, and S. O. Nielsen, Far-Ultraviolet Spectra of Hydrogen and Hydroxyl Radicals from Pulse Radiolysis of Aqueous Solutions. Direct Measurement of the Rate of H + H. J. Phys. Chem. 73 (1969) 1029-38.

11) V. I. Vedeneyev et al., Bond Energies Ionization Potentials and Electron Affinities. (Edward Arnold Ltd., London, 1966) 202 pp.

12) J. Rabani and S. O. Nielsen, Absorption Spectrum and Decay Kinetics of O_2 and HO_2 in Aqueous Solutions by Pulse Radiolysis. J. Phys. Chem. 73 (1969) 3736-44.

13) V. L. Tal'roze and B. L. Frankevich, Investigation of the Ion-Molecular Elementary Act of a Radiation Chemical Process. In: All-Union Conference on the Application of Radioactive and Stable Isotopes and Radiation in the National Economy and Science. Abstracts of Papers from the Conference, Moscow, 2-5 April 1957. (Consultants Bureau, New York, 1958) 11-15.

14) P. B. Pagsberg and J. W. Sutherland, (submitted for publication).

15) J. D. Salzman and E. J. Bair, Recombination and Disproportionation of NH_2 Radicals. J. Chem. Phys. 41 (1964) 3654-55.

16) A. Treinin and E. Hayon, Spectroscopic Observation of the Azide Radical in Solution. J. Chem. Phys. 50 (1969) 538-539.

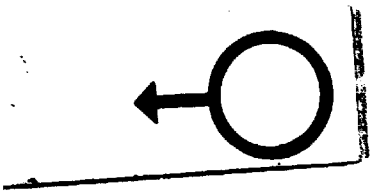

Mechanisms of Magnetic Anisotropy in Terbium

by

H. Bjerrum Møller, J. C. G. Houmann, J. Jensen,
P.-A. Lindgård, and M. Nielsen

Physics Department

and

A. R. Mackintosh

University of Copenhagen and Risø

Abstract

The magnetic field dependence of the magnon energies in Tb has been studied by inelastic neutron scattering. From the results at $q = 0$, it was confirmed that the frozen-lattice model is applicable, and the single-ion anisotropy parameters and their temperature dependences were deduced. Measurements in the c-direction at finite $\underline{q}$ revealed that the two-ion coupling between the moments is highly anisotropic.

1. INTRODUCTION

The study of the magnons in rare earth metals by inelastic neutron scattering has proved to be a rich source of information on the magnetic interactions in these materials[1]. The early studies on Tb were principally concerned with the exchange interactions between the magnetic ions, and the mechanisms through which these contributed to the stability of the different magnetic phases[2]. It was tacitly assumed that the magnetic anisotropy was due to the crystal fields in the unstrained lattice and could be written in a simple single-ion form. Later experiments on the temperature dependence[3], and particularly the magnetic field dependence[4], of the magnon energies showed, however, that this assumption is not strictly valid. Measurements on a Tb-10% Ho single crystal[4] showed unambiguously that magnetoelastic effects, due to the distortion of the lattice on magnetization, contribute to the single-ion anisotropy and actually dominate the hexagonal component. Furthermore, it was shown that the lattice strain is unable to follow the rapid precession of the moment when a magnon is excited, so that the 'frozen-lattice' model is valid.

In this paper, we present a detailed study of the dependence of the magnon energies in Tb on magnetic field. The results obtained at zero wavevector allow us to draw some further qualitative and quantitative conclusions concerning the mechanisms and magnitudes of the single-ion anisotropy. We have also extended our measurements to finite q-values in the c-direction and these give completely new, and rather unexpected, information on the anisotropic coupling between the magnetic ions. The significance of these conclusions for our present understanding of the magnetic interactions in Tb will be briefly discussed.

2. THE HAMILTONIAN

The various contributions to the spin wave Hamiltonian comprise an exchange coupling between the moments, which we allow to be anisotropic, single-ion anisotropy terms arising from crystal fields and magnetoelastic effects respectively, and a two-ion magnetoelastic coupling. In addition, we include a Zeeman term due to an external magnetic field. The total Hamiltonian then takes the form

$$H = H_x + H_{cf} + H_{me}^{I} + H_{me}^{II} - g\beta \sum_i \underline{J}_i \cdot \underline{H} . \qquad (1)$$

We use a set of Cartesian axes such that ζ is along the hexagonal axis and ξ is the easy direction of magnetization in the plane. The various contributions to the Hamiltonian in the ferromagnetic phase are then:

$$H_x = -\sum_{i>j} \left\{ J_{ij}^{aa}(J_{i\xi}J_{j\xi} + J_{i\eta}J_{j\eta}) + J_{ij}^{cc}J_{i\zeta}J_{j\zeta} \right\} \tag{2}$$

$$H_{cf} = -\sum_i \left\{ P_2 J_{i\zeta}^2 - \tfrac{1}{2}P_6^6 \left[(J_{i\xi} + iJ_{i\eta})^6 + (J_{i\xi} - iJ_{i\eta})^6 \right] \right\} \tag{3}$$

$$H_{me}^{I} = -\sum_i \left\{ \frac{cC}{J_1} \left[(J_{i\xi}^2 - J_{i\eta}^2)\, \bar{\varepsilon}_1^{\gamma} + 2 J_{i\xi}J_{i\eta}\, \bar{\varepsilon}_2^{\gamma} \right] \right. \tag{4}$$

$$\left. + \frac{cA}{J_3} \left[\tfrac{1}{2}(J_{i\xi}^4 - 6J_{i\xi}^2 J_{i\eta}^2 + J_{i\eta}^4)\, \bar{\varepsilon}_1^{\gamma} - 2J_{i\xi}J_{i\eta}(J_{i\xi}^2 - J_{i\eta}^2)\, \bar{\varepsilon}_2^{\gamma} \right] \right\}$$

$$H_{me}^{II} = -\sum_{i>j} \left\{ \sqrt{3}\, D_{ij}^{\alpha}\, \bar{\varepsilon}^{\alpha} \left[J_{i\zeta}J_{j\zeta} - \tfrac{1}{3}\, \underline{J}_i \cdot \underline{J}_j \right] \right. \tag{5}$$

$$\left. - D_{ij}^{\gamma} \left[(J_{i\xi}J_{j\xi} - J_{i\eta}J_{j\eta})\, \bar{\varepsilon}_1^{\gamma} + (J_{i\xi}J_{i\eta} + J_{i\eta}J_{j\xi})\, \bar{\varepsilon}_2^{\gamma} \right] \right\}.$$

The notation used in these expressions is explained in refs. 1 and 4. The first term of (5) has the same form as the anisotropic exchange (2), and we shall therefore include it by an appropriate redefinition of the parameters J_{ij}. Similarly the average value of the second term in (5) can be included by redefining the parameter C in (4), while a higher-order magnetoelastic term results in a similar renormalization of A in (4). For simplicity, we have neglected certain other magnetoelastic terms[8] whose effect we will briefly mention in the next section.

3. THE MAGNON DISPERSION RELATIONS

When the field is applied in the hard (η) direction, the magnetization rotates so that it makes an angle Φ with the field, given by

$$g\beta H = 12 \cos\Phi (2\cos 4\Phi + 1)(-P_6^6 J_5 + \tfrac{1}{2} c\, AC). \tag{6}$$

Above the critical field

$$g\beta H_c = 36(-P_6^6 J_5 + \tfrac{1}{2} c\,AC) \tag{7}$$

the magnetization lies in the field direction and Φ is zero. The Hamiltonian (1) may be diagonalized by the standard techniques to give the spin wave energies

$$\epsilon^2(\underline{q}) = (A_o + B_o + A_{\underline{q}} + B_{\underline{q}})(A_o - B_o + A_{\underline{q}} - B_{\underline{q}}). \tag{8}$$

Since we are interested principally in the dispersion relations in the c-direction, we will use the double-zone representation[1] for the hcp structure throughout. For $H < H_c$ in the hard direction, we find

$$(A_o + B_o) = -2JP_e + c(2C^2 + A^2) + \tfrac{1}{6} g\beta H_c(1 + 2\cos 2\Phi + 2\cos 4\Phi) - \Delta M \cos 6\Phi \tag{9}$$

$$(A_o - B_o) = 8cAC + 4c(C^2 + A^2) + \tfrac{1}{6} g\beta H_c(1 + 2\cos 2\Phi + 2\cos 4\Phi - 5\cos 6\Phi) \tag{10}$$

$$(A_{\underline{q}} + B_{\underline{q}}) = J[J^{cc}(o) - J^{cc}(\underline{q})] \tag{11}$$

$$A_{\underline{q}} - B_{\underline{q}} = J[K^{aa}(o) - K^{aa}(\underline{q})] \tag{12}$$

where we have defined

$$JP_e = J_1 P_2 + J^{cc}(o) - J^{aa}(o) \tag{13}$$

$$K^{aa}(o) - K^{aa}(\underline{q}) = J^{aa}(o) - J^{aa}(\underline{q}) - C[D(o) - D(\underline{q})] \tag{14}$$

and $J^{aa}(\underline{q})$, $J^{cc}(\underline{q})$ and $D(\underline{q})$ are the Fourier transforms of J_{ij}^{aa}, J_{ij}^{cc}, and D_{ij}^{γ} respectively.

The parameter ΔM arises from higher-order magnetoelastic effects and is defined in terms of the parameter B_ℓ^m of the crystal field[6] as

$$\Delta M = 22\,C B_6^4 J_6 - A(18 B_6^2 J_6 - 7 B_4^2 J_4). \tag{15}$$

When the applied field in the hard direction exceeds H_c, the magnon energies are given by the same expressions with $\Phi = 0$ and with the addition

of a term $g\beta(H-H_c)$ to both (9) and (10). Similarly, if the field is applied in the easy direction, $\Phi = \pi/2$ and (9) and (10) are both agumented by a term $g\beta H$.

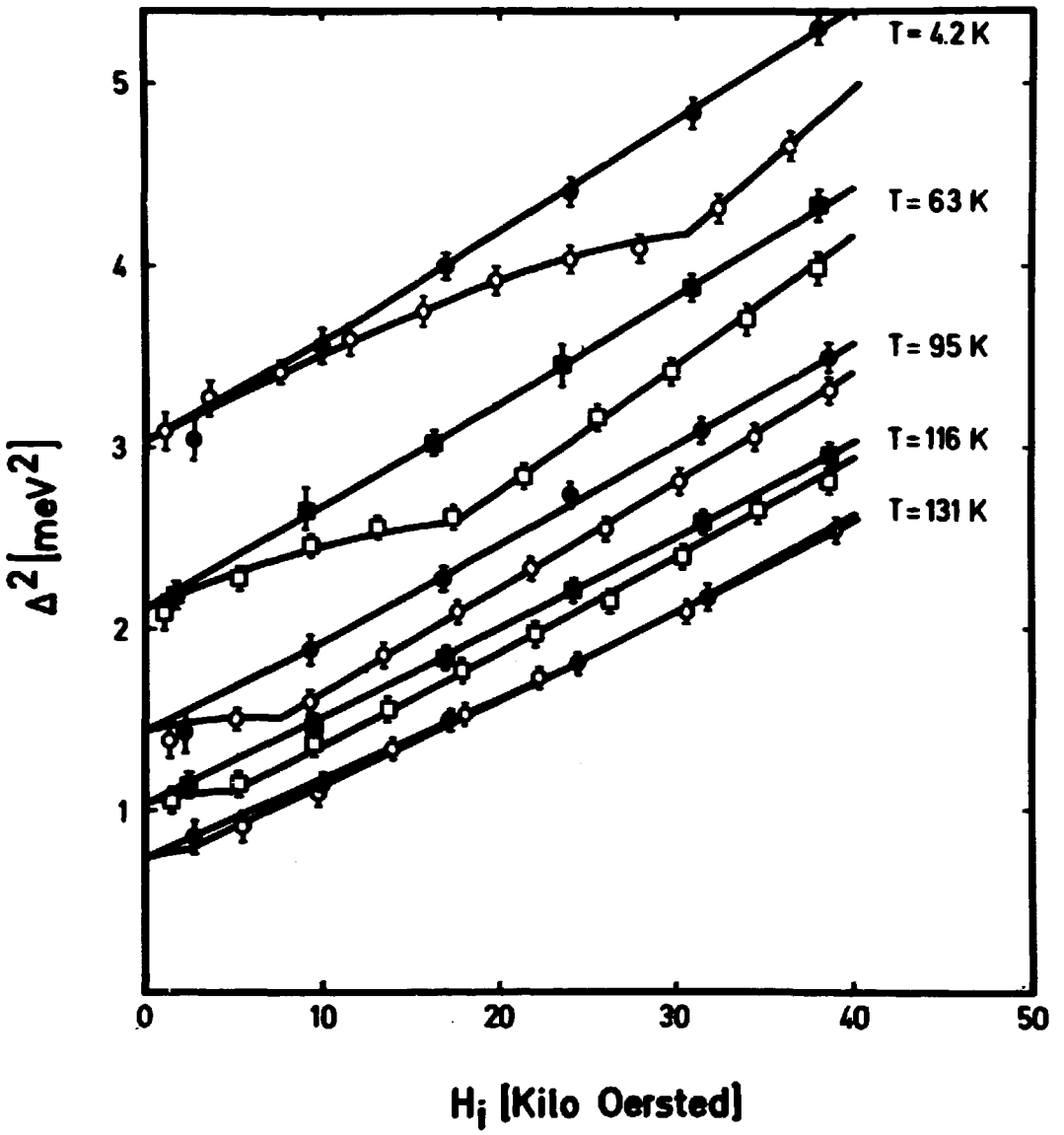

Fig. 1. The dependence of the square of the magnon energy gap on internal magnetic field in Tb. Open symbols represent results for the field in the hard direction, and closed the easy direction. The full lines are least-squares fits of the theoretical expressions given in the text to the experimental results.

4. THE SINGLE-ION ANISOTROPY

The magnon energies were measured as a function of temperature and applied magnetic field, by inelastic neutron scattering at the DR 3 reactor at Risø. The sample was a monocrystalline disc of Tb with a diameter of about 14 mm and a thickness of about 5 mm, and with the c-axis normal to the faces. An external field of up to 48 kG could be applied by means of a superconducting solenoid. A selection of the results for the magnon energy gap at q = 0 is shown in fig. 1. They are qualitatively similar to earlier

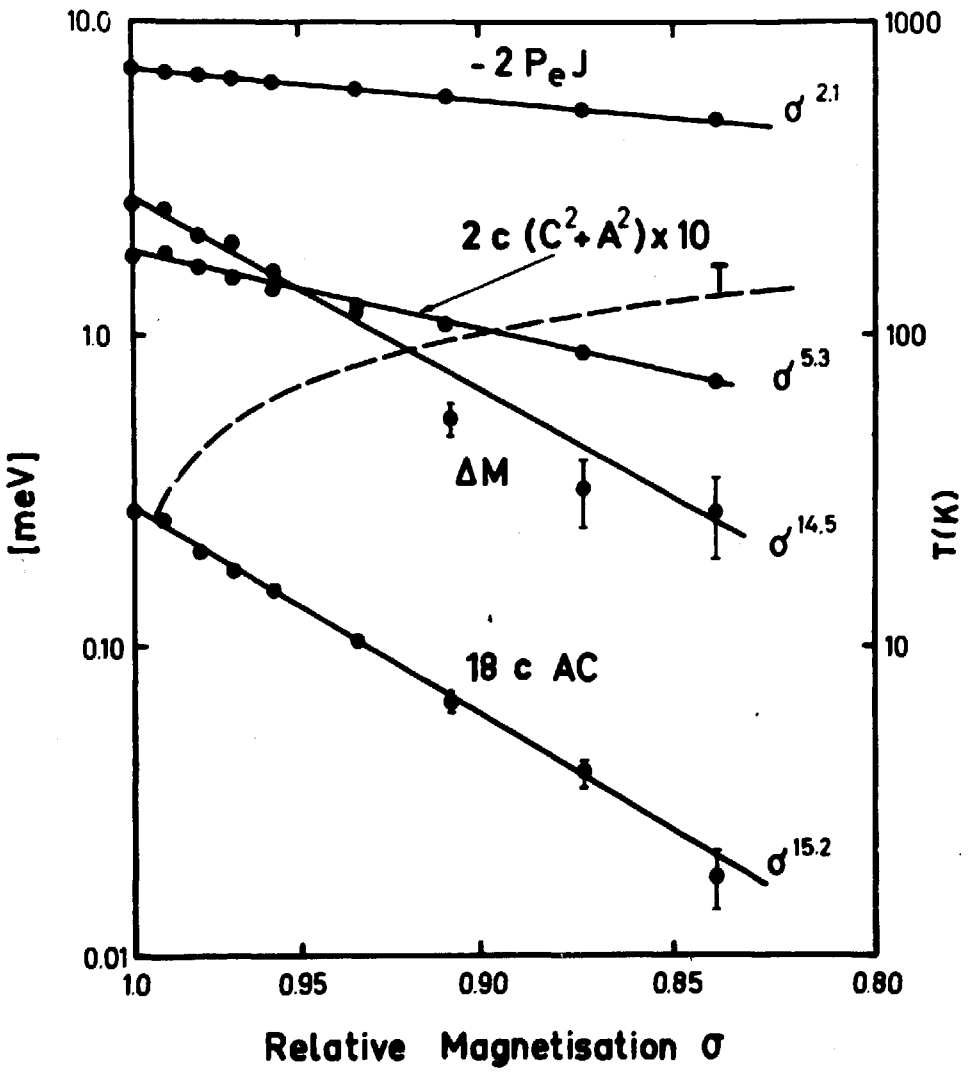

Fig. 2. The single-ion anisotropy parameters in Tb, as a function of magnetisation, deduced from the results of fig. 1 and similar measurements at different temperatures.

measurements[4] on Tb-10% Ho, but they are made with considerably greater precision, and the decreased hexagonal anisotropy in Tb results in significant quantitative changes.

The single-ion anisotropy parameters shown in fig. 2 were deduced from a least-squares fitting of the experimental results to equation (8), evaluated at $q = 0$. The necessity for including the high-order magnetoelastic parameter ΔM may be seen directly in the measurements of fig. 1, since it is responsible for the difference between the slopes of the straight lines obtained for fields applied in the easy and hard directions. It is also impossible to obtain a satisfactory fit to the experimental points for $H < H_c$ in the hard direction unless this term is included. Unfortunately, the addition of this extra parameter makes it very difficult to determine the hexagonal crystal field anisotropy $36P_6^6J_5$, which we can only characterize as small compared with 18cAC. The dependences of the anisotropy parameters on the relative magnetization σ follow quite closely the theoretical prediction of Callen and Callen[5], despite the limitations of their theory discussed by Brooks[7]. There is general agreement between the magnitudes of the anisotropy parameters deduced from our results and from macroscopic measurements[8], although there are quantitative discrepancies, especially in the magnetostriction coefficients, which deserve further study.

5. ANISOTROPIC COUPLING BETWEEN IONS

As may readily be seen from equations (8) - (12), a study of the field-dependence of the magnon energies for different q-values gives explicit information about the anisotropic coupling between moments on different sites. Differentiating (8), we find, for a field applied in the easy direction

$$a_{\underline{q}} = \frac{d\epsilon^2(\underline{q})}{dH} = 2g\beta(A_o + A_{\underline{q}}) . \tag{16}$$

As may be seen from (11) and (12), if the two-ion anisotropy vanishes, so does $B_{\underline{q}}$, in which case, from (8)

$$\frac{a_{\underline{q}}}{g\beta} = 2[\epsilon^2(\underline{q}) + B_o^2]^{1/2} . \tag{17}$$

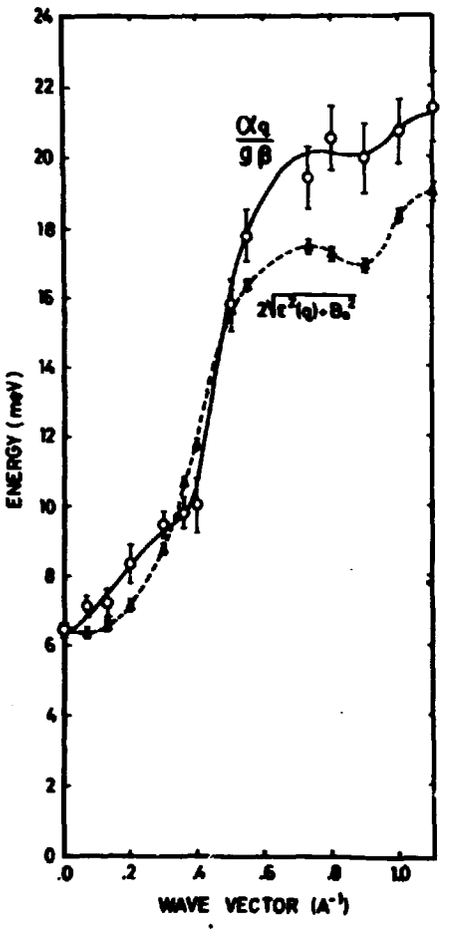

Fig. 3. A comparison between the functions $a_q/g\beta$ and $2[\epsilon^2(q) + B_o^2]^{1/2}$ for the c-direction of Tb at 4.2 K. The difference between them is a result of anisotropy in the two-ion coupling.

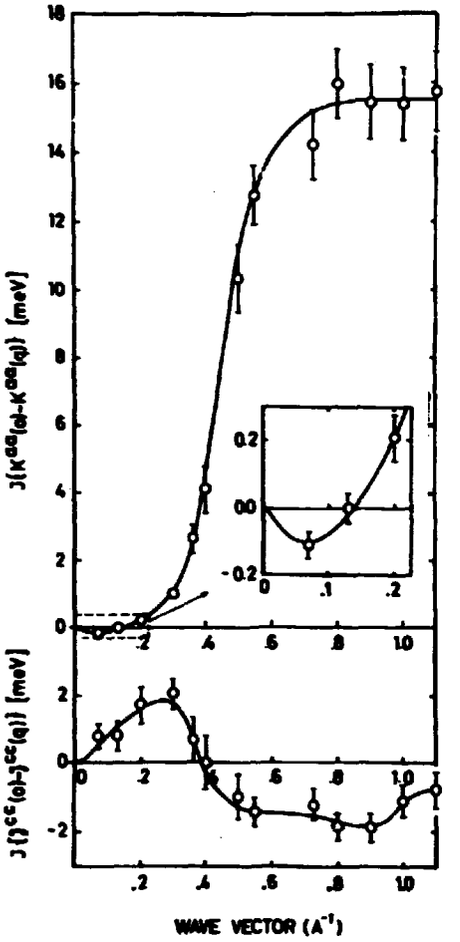

Fig. 4. The Fourier transforms of the effective two-ion coupling between moments, for the c-direction of Tb at 4.2 K.

The two sides of this equation are compared in fig. 3, and from their difference we can immediately deduce that the two-ion anisotropy is finite. Including B_q, we obtain from (8)

$$B_o - B_q = \left[\left(\frac{a_q}{2g\beta}\right)^2 - \epsilon^2(q)\right]^{1/2} \tag{18}$$

and from (16) and (18) find

$$J\,[J^{cc}(o) - J^{cc}(q)] = A_q + B_q$$

$$= \left[\left(\frac{a_q}{2g\beta}\right)^2 - \epsilon^2(q)\right]^{1/2} + \frac{a_q}{2g\beta} - (A_o + B_o) \tag{19}$$

and

$$J\,[K^{aa}(o) - K^{a}(\underline{q})] = A_{\underline{q}} - B_{\underline{q}}$$

$$= \frac{a_{\underline{q}}}{2g\beta} - \left[\left(\frac{a_{\underline{q}}}{2g\beta}\right)^2 - \epsilon^2(\underline{q})\right]^{1/2} - (A_o - B_o)\,. \qquad (20)$$

We note that the values of the single-ion anisotropy parameters enter these expressions only through A_o and B_o, which are directly deduced from the experiments at $q = 0$, and do not vary with $\underline{q}$.

The values of the Fourier transformed two-ion coupling parameters deduced from our measurements in the c-direction of Tb at 4.2 K, with a magnetic field along the easy direction, are shown in fig. 4. It is immediately obvious from this figure that the coupling between the moments is highly anisotropic, but whether this anisotropy arises primarily from anisotropic exchange or from two-ion magnetoelastic effects is not yet clear. Further experiments on the temperature dependence of the coupling between the moments should help to elucidate this question, while measurements with a field along the hard direction will allow the anisotropy in the plane to be studied.

6. CONCLUSION

These measurements have clearly demonstrated the efficacy of inelastic neutron scattering as a means for studying the mechanisms of anisotropy in magnetic materials. We have shown that magnetoelastic effects are of great importance in determining the anisotropy of Tb, and that the frozen-lattice model must be used in describing the dynamic magnon properties. The magnitudes of the single-ion anisotropy parameters and their temperature dependences have been deduced from the experimental results. A striking feature of this study is the revelation that the coupling between the moments on different ions, which has previously been tacitly assumed to be isotropic, is actually highly anisotropic. The detailed understanding of this phenomenon will require a substantial extension in the theory of the magnetic properties of the rare earth metals.

ACKNOWLEDGEMENT

The development of the facilities for neutron scattering experiments at the DR 3 reactor took place while Professor T. Bjerge was director of Risø. In appreciation of his understanding and support, this paper is gratefully dedicated to Professor Bjerge on his seventieth birthday.

REFERENCES

1) A.R. Mackintosh and H. Bjerrum Møller, Spin Waves. In: Magnetic Properties of Rare Earth Metals. Edited by R.J. Elliott(Plenum Press, London, 1972) chapter 5.

2) H. Bjerrum Møller and J.C.G. Houmann, Inelastic Scattering of Neutrons by Spin Waves in Terbium. Phys. Rev. Lett. 16 (1966) 737-739.

H. Bjerrum Møller, J.C.G. Houmann, and A.R. Mackintosh, Magnetic Interactions in Tb and Tb-10% Ho from Inelastic Neutron Scattering. J. Appl. Phys. 39 (1968) 807-815.

3) H. Bjerrum Møller, Neutron Spin Scattering by Spin Waves in Metals. In: Neutron Inelastic Scattering. Proceedings of a Symposium, Copenhagen, 20 - 25 May 1968, 2 (IAEA, Vienna, 1968) 3-27.

4) M. Nielsen, H. Bjerrum Møller, P.A. Lindgård, and A.R. Mackintosh, Magnetic Anisotropy in Rare-Earth Metal Phys. Rev. Lett. 25 (1970) 1451-54.

5) H.B. Callen and E. Callen, The Present Status of the Temperature Dependence of Magnetocrystalline Anisotropy, and the ℓ $(\ell+1)/2$ Power Law. J. Phys. Chem. Solids 27 (1966) 1271-85.

6) P.A. Lindgård, Field Dependence of the Spin Wave Energy in Rare-Earth Metals. J. Phys. (Paris) Colloq. 32 (1971) C1-238-240.

7) M.S.S. Brooks, Theory of the Temperature Dependence of the Spin-Wave Excitation Energies in the Rare-Earth Metals. Phys. Rev. B1 (1970) 2257-64.

8) J.J. Rhyne, Bulk Magnetic Measurements. In: Magnetic Properties of Rare Earth Metals. Edited by R.J. Elliott (Plenum Press, London, 1972) chapter 4.